LBL PUB-5303
SLAC-372
CALT-68-1715
UCRL-ID-106426
UC-IIRPA-91-01

An Asymmetric B Factory

Based on PEP

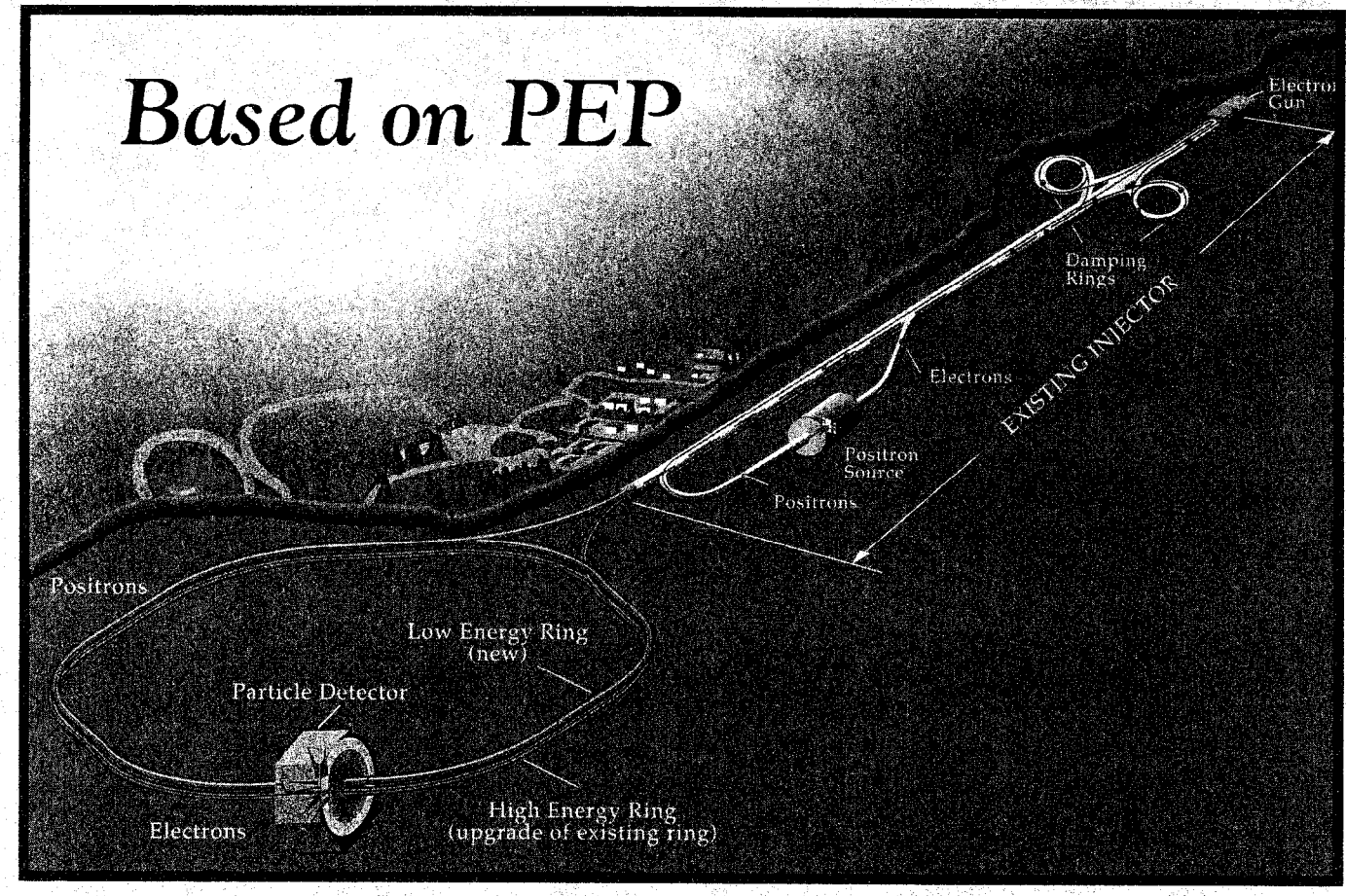

Conceptual Design Report

February 1991

Prepared for the U.S. Department of Energy under contract numbers
DE-AC03-76SF00098, DE-AC03-76SF00515, DE-AC03-81-ER40050, W-7405-Eng-48, and DE-AS03-76ER70285.

CONTENTS

1. Overview 1

2. Introduction 5
   - 2.1 Overview 5
   - 2.2 Characteristics of the 10-GeV Region—The Upsilon Family 8
   - 2.3 Physics Motivation 10
   - 2.4 Constraints Imposed on the Accelerator by the Detector 28
   - 2.5 Running Scenarios 31

3. General Description and Parameter Choices 33
   - 3.1 Design Overview 34
   - 3.2 Luminosity Considerations 39
   - 3.3 RF Considerations 43
   - 3.4 Reliability Considerations 45

4. Collider Design 47
   - 4.1 Lattice Design 48
   - 4.2 Estimation of Detector Backgrounds 93
   - 4.3 Collective Effects 139
   - 4.4 Beam-Beam Issues 166

5. Collider Components 197
   - 5.1 Magnets and Supports 198
   - 5.2 Vacuum System 246
   - 5.3 Survey and Alignment 309
   - 5.4 Power Supplies 314
   - 5.5 RF System 332
   - 5.6 Feedback Systems 354
   - 5.7 Instrumentation and Electronics 376
   - 5.8 Control System 382

6. Injection System 391
   - 6.1 Overall Approach and Specifications 391
   - 6.2 SLC Modifications 395
   - 6.3 Upgrade of the NIT and SIT Lines 400

6.4 Injection into the HER and LER 402
6.5 Optimum Time Between Fills 408
6.6 Summary 410

7. Conventional Facilities 411
7.1 Site and Utilities 411
7.2 Removals and Installations 416

8. Safety and Quality Assurance 423
8.1 Fire Safety 423
8.2 Radiation Safety 424
8.3 Nonionizing Radiation Safety 427
8.4 Electrical Safety 428
8.5 Construction 429
8.6 Emergency Preparedness 429
8.7 Environmental Protection 430
8.8 Detector Safety Issues 430
8.9 Quality Assurance 431

9. Cost and Schedule 433
9.1 Cost Estimate 433
9.2 Construction Schedule 435
9.3 Work Breakdown Structure 439

10. Summary 445

Acknowledgments 449

References 451

Appendix A: Parameters 459

Appendix B: Future Upgrades 483
B.1 Future Luminosity Improvements 483
B.2 Crab Crossing 487

1.

OVERVIEW

IT has become increasingly apparent in recent years that systems containing b quarks offer unique opportunities for studying the theoretical edifice of particle physics, the so-called "Standard Model." Although measurements with these b-quark systems offer a host of possibilities, the one that has riveted the attention of the particle physics community worldwide is the potential for understanding the origin of the phenomenon of *CP* violation—a small deviation in Nature's otherwise symmetric order that has been clearly observed but whose origins remain a mystery. The phenomenon of *CP* violation has cosmic consequences; in particular, it played a crucial role in the formation of our Universe. Thus, to understand it is one of the central goals in our quest to comprehend the orderly foundations of the natural world. The program of *CP* violation studies that we envision has great discovery potential; should the measurements disagree with predictions of the Standard Model, the observed pattern of *CP* violation will provide substantial and specific clues as to how the model should be extended.

Capitalizing on recent advances in detector technology and newly acquired information on the properties of the b quark, it is now widely accepted that a high-luminosity, asymmetric e^+e^- collider offers an ideal platform for an exhaustive study of *CP* violation. This fact was forcefully endorsed last year by HEPAP through the deliberations and recommendations of its subpanel on the U.S. High Energy Physics Research Program for the 1990s (the Sciulli panel, DOE/ER–0453P and the accompanying transmittal letter, April 1990). The thrust of HEPAP's recommendations was that the physics program of a B factory was compelling and that, given a technically sound proposal for construction of a machine, funds for such a facility should be sought with high priority.

While *CP* violation is the main motivation for the construction of a B factory, such a facility will also host a very exciting and broad-based program of bottom quark, charm quark, τ, and two-photon physics. Important tests of the Standard Model are possible in this program and many gaps in our knowledge are sure to be filled in. Because the number and range of distinct topics is very large, an asymmetric B factory will be an ideal facility for the training of young physicists, and we envisage more than 200 Ph.D. theses during the lifetime of the program (conservatively estimated at 15 years). The specific machine implementation discussed here has a single interaction region, though flexibility exists to expand this to two interaction regions, and therefore two detectors, should the user community consider this important enough to provide the extra funds. A

parasitic program of synchrotron radiation physics and nuclear physics would also be possible with additional funds.

A very large international particle physics community is committed to physics studies at an asymmetric e^+e^- B factory. A group of physicists numbering more than 150 Ph.D.'s has been involved with the PEP-based B Factory, both in developing the physics arguments and in designing an appropriate detector. This group includes investigators from more than 20 U.S. institutions, as well as physicists from Canada, Europe, Japan, and Israel. There are an equal number involved in other B factory efforts worldwide.

In early 1989, a group of accelerator and particle physicists from Caltech, LBL, SLAC, and the University of California began a study of the feasibility of an asymmetric e^+e^- collider based on an upgrade of the PEP storage ring at SLAC. A parallel study was conducted to examine in detail the physics capabilities of such a facility and to specify the luminosity required for a broad-based program aimed at understanding the origins of *CP* violation. The feasibility studies indicated that, with appropriate care, PEP could be upgraded to achieve the required luminosity of 3×10^{33} cm^{-2} s^{-1}. In November 1989, the SLAC Experimental Program Advisory Committee agreed that the B Factory program was indeed very compelling and encouraged the Directors of SLAC and LBL to move from a feasibility study to a conceptual design phase. It is the result of that conceptual design study that is contained in these pages. The Asymmetric B Factory design proposed here serves as a direct and wholly satisfactory response to the challenge set down by the Sciulli subpanel.

The goal of the conceptual design was to be a machine that would be both responsive to the physics needs and conservative in its approach to achieving high luminosity. The Asymmetric B Factory design we propose meets this goal. The facility consists of two independent storage rings, one located atop the other in the PEP tunnel. The high-energy ring, which stores a 9-GeV electron beam, is an upgrade of the existing PEP collider; it reutilizes all of the PEP magnets and incorporates a state-of-the-art copper vacuum chamber and a new RF system capable of supporting a stored beam of very high current. The low-energy ring, which stores 3.1-GeV positrons, will be newly constructed. Its design takes advantage of many of the machine component designs that have already proved successful at PEP.

Our approach to reaching the required luminosity of 3×10^{33} cm^{-2} s^{-1} is to use, in each ring, high circulating currents (approximately 2 A) separated into more than 1600 bunches. An advantage to this approach is that the parameters of individual bunches (current, length, emittance, etc.) are quite conventional and have been demonstrated in numerous successful colliders over many years. Thus, the design challenges are restricted to the high-current and multibunch arenas. These, in turn, are mainly engineering challenges, and—although they are by no means easy—they are amenable to standard engineering tools and approaches that assure us that the proposed solutions are workable, reliable, and conservative.

The PEP site offers an ideal location for the B Factory. SLAC has the world's most powerful positron injector, and the availability of the large 2.2-km-circumference tunnel greatly eases the problems associated with handling the intense synchrotron radiation power emitted by the high-current beams. This approach is not unique to the SLAC project; both DESY and KEK have now moved away from earlier plans to employ small storage rings and have adopted machine designs that place both rings in their large-radius

PETRA (2.3 km) and TRISTAN (3 km) tunnels. Moreover, the parameters of the B Factory high-energy ring match almost perfectly those of the present PEP; the project can benefit from the existing PEP infrastructure so that no conventional construction is required on the SLAC site.

SLAC and LBL have a long and very successful history of design, construction, and operation of e^+e^- storage rings. The original PEP project was a joint endeavor of these two laboratories. The staffs of both laboratories are enthusiastic about the prospect of an upgrade to this facility. Much of the expertise that conceived and built SPEAR and PEP remains within the laboratories, and new additions to the staff (for example, the team that is now completing construction of the ALS at LBL) have enhanced these strengths. The addition of LLNL as an institutional collaborator further strengthens the team that will build the Asymmetric B Factory.

In summary, we believe that the SLAC site is an ideal location for the construction of an Asymmetric B Factory that will provide the platform for a crucial component of the U.S. high-energy physics base program. The design presented here is flexible and fully capable of meeting the demands of a physics program that will exhaustively examine the question of *CP* violation. As soon as funds are available, we are ready to begin the construction and commissioning of this exciting facility and then to embark on studying one of the most important topics in high-energy physics today.

2.

INTRODUCTION

ON the following pages, we give an overview of the physics motivation for the Asymmetric B Factory. The overview includes a discussion of the advantages of the e^+e^- environment and a menu of the physics achievable at the B Factory. This chapter also offers a justification for the design luminosity for the machine and the asymmetric aspect of the collider, and it outlines a list of constraints on the machine design that arise from the physics goals (that is, tolerable background levels, maximum beam pipe radius, etc.).

2.1 OVERVIEW

We propose to construct a high-luminosity electron-positron colliding-beam accelerator that will operate in the 10-GeV center-of-mass energy ($E_{c.m.}$) regime; the majority of the physics running will be at the $\Upsilon(4S)$ resonance ($E_{c.m.} = 10.58$ GeV). The machine described in the following chapters has the novel feature of unequal beam energies, a configuration we call *asymmetric*. The luminosity goal is 3×10^{33} cm^{-2} s^{-1}; the electron and positron beam energies were chosen to be 9 and 3.1 GeV, respectively.

The main physics motivation for the B Factory is a full and exhaustive study of *CP* violation, using the rich spectrum of B meson decays. The goal is not simply to measure, for the first time, *CP* violation in the B meson system, but to mount a program sufficiently diverse to examine the more crucial issue of what constitutes the *origin of CP violation*. Such a program requires a machine that produces in excess of 10^7 neutral B mesons (B^0's) per year. The goal for the machine described in this proposal is 3×10^7 neutral B mesons per year.

The 10-GeV region was chosen so as to exploit the copious and exclusive production of B mesons at the $\Upsilon(4S)$ resonance; the level of asymmetry was chosen to optimize the measurement of *CP*-violating asymmetries in the decays of the B mesons. The full time-evolution of this phenomenon can be exposed by the use of the asymmetry, with the time-evolution measurements providing a comprehensive set of systematic cross-checks for the *CP* violation measurements.

The e^+e^- 10-GeV region has proved to be an ideal environment for the study of b quark physics. The $\Upsilon(4S)$ offers special advantages for the study of B hadron (meson and baryon) decays. The production of B hadrons at the $\Upsilon(4S)$ constitutes fully one-third of

the available cross section, and the availability of kinematic constraints further permits exceptionally clean isolation of the B physics. The background rejection is sufficient to allow a wide range of B meson decays, even decay modes with small branching fractions (10^{-4}–10^{-5}), to be reconstructed with high efficiencies and large signal-to-noise ratios. These include decay modes of high multiplicity and those that include final state π^0's. The ability to use the sign of the electric charge of both leptons and kaons to establish, accurately and with high efficiency, the difference between a B and a $\overline{B}$ meson is very powerful. These characteristics are especially advantageous for the study of *CP* violation. Programs at CESR and DORIS have provided a large amount of data for a detailed characterization of the Υ region. This, coupled with the rather simple nature of the e^+e^- environment, makes it possible to simulate the physics processes very reliably. Hence, one can attach considerable confidence to the estimates of the physics capabilities calculated for the B Factory. Indeed, as discussed below, the present proposal is based on very detailed modeling of the physics.

Besides bottom quark production, the B Factory will produce very large samples of charm quarks and τ leptons. The environment again favors high-efficiency, low-background studies of important physics processes associated with these fundamental constituents. Hence, the B Factory is more correctly viewed as a *Heavy Constituent Factory.*

Rounding out the possibilities offered by the B Factory is an exciting program of two-photon physics and the study of the spectroscopy of the Υ resonances. This spectroscopy reflects the underlying strong force that binds the quarks together and offers an opportunity for detailed and essential studies of this fundamental force.

Details of this compelling physics program are given below. As a measure of the power of the B Factory, we have tabulated in Table 2-1 the yields for $B\overline{B}$ and Υ that exist worldwide today and that will be available in a one-year run at the B Factory. Also tabulated are the annual yields of D mesons and τ pairs expected at the B Factory. The increase in statistical power is itself very impressive; what is not evidenced by the relative numbers is the level of accessibility to crucial physics that can only come with the Asymmetric B Factory.

The B Factory also offers the opportunity for an exciting parasitic program of synchrotron radiation and nuclear physics studies. The very high circulating current will generate x-ray beams of unprecedented brightness, permitting some experiments that will not be accessible even at the next generation of advanced light sources. Likewise, for certain QCD studies, a heavy-element gas-jet target intercepting the electron beam, along the lines proposed by the PEGASYS experiment [Van Bibber, 1989], would reach regions of phase space inaccessible at any other facility.

The U.S. is currently embarked on the SSC program, which will begin producing physics at the end of this decade. The U.S. particle physics program is in great need of additional facilities, particularly in the intervening years, both to maintain a balanced and vibrant program and to keep young people in the field. In this regard, the B Factory offers the nation an ideal opportunity. The SLAC site, with its existing powerful injector and large-circumference machine (PEP), provides a natural site for a high-luminosity Asymmetric B Factory. The B Factory constitutes an upgrade of the existing SLAC facility, with no conventional construction required. This has the advantage of saving both money and time. With proper financial planning, the U.S. program could have the

Table 2-1. Bottom, Υ, charm, and τ yields (1 yr = 10^7 s).

Channel	World sample (Jan. 1991)	B Factory $\mathcal{L} = 3 \times 10^{33}$ (per yr)
$B\overline{B}$	1×10^6	3×10^7
Υ(1S)	3.5×10^6	5×10^8
Υ(2S)	8.5×10^5	2×10^8
Υ(3S)	4.9×10^6	1×10^8
D^0	—	6.9×10^7
D^+	—	3.3×10^7
D_s	—	2.3×10^7
$\tau^+\tau^-$	—	2.8×10^7

SLAC-based B Factory operational for physics in 1996. The program has an expected lifetime for compelling physics of at least 15 years. While the SSC challenges the Standard Model by vigorously pursuing an understanding of the Higgs sector, the B Factory would provide a complementary pursuit of the Standard Model through the study of *CP* violation and the pattern of heavy-constituent decays. The B Factory physics program is exceedingly diverse, and the number of fully independent physics topics that can be studied is very large. This fact, coupled with the compelling nature of the physics, has brought together a very large community pushing for such a facility. (Based on current attendance at workshops and discussions with members of the worldwide community, we estimate that 300 particle physics Ph.D.'s will work at the B Factory.) The majority of this community has worked in e^+e^- collisions for many years and has a demonstrated ability to produce high-quality physics results. In addition, we envisage the B Factory as providing an exceptional training ground for young physicists: The number of interesting thesis topics far exceeds one hundred.

The rest of this chapter is organized to provide background for the nonspecialist; a more detailed discussion of physics measurements resumes in Section 2.3.4. Section 2.2 discusses the characteristics of the 10-GeV center-of-mass region as seen in e^+e^- collisions. Section 2.3 then discusses the physics motivation, including an outline of the Standard Model (Sections 2.3.1 through 2.3.3), a discussion of how *CP* asymmetries are measured at the Υ(4S) (Section 2.3.4), a justification of the machine asymmetry and luminosity (Sections 2.3.5 and 2.3.6), a discussion of sensitivity to non–Standard Model explanations for *CP* violation (Section 2.3.7), and outlines of B physics exclusive of *CP* violation, together with charm, τ, Υ, and two-photon physics (Sections 2.3.8 through

2.3.12). The chapter concludes with a discussion of the constraints imposed by the physics on the machine design and an outline of the likely scenario for choosing the operating energy of the machine.

2.2 CHARACTERISTICS OF THE 10-GEV REGION—THE UPSILON FAMILY

The cross section for producing hadrons in electron-positron collisions in the 10-GeV region is shown in Fig. 2-1. The rich resonance structure above the b quark threshold is called the upsilon (Υ) system. The first three prominent resonances are the lowest-lying S states of a bound $b\bar{b}$ quark system. These states are analogous to the bound states in an atomic system (such as positronium); in this case, however, it is the strong (color) force that provides the binding energy for the two constituents. The narrowness of the resonances reflects their stability against strong decays; the states have insufficient energy to decompose into a pair of mesons, each carrying a b quark. The fourth state, $\Upsilon(4S)$, has just sufficient energy to decay to a pair of B mesons (B and $\overline{B}$); this decay totally dominates the disintegration of the $\Upsilon(4S)$. The $\Upsilon(4S)$ is thus an ideal laboratory for the study of B decays, having the following important features:

- The $\Upsilon(4S)$ decays almost exclusively to pairs of B mesons. There are thus no extraneous particles that would provide background and reduce the sensitivity of the measurements.
- Since the $\Upsilon(4S)$ decays to only two particles, the daughter B mesons have a unique momentum in the $\Upsilon(4S)$ center-of-mass frame. In addition, the fraction of all events that contain a $B\overline{B}$ pair is 30%, significantly greater than at higher energies or in proton collisions. These two effects greatly limit contamination from backgrounds from the continuum of physics channels (non-b quarks) that accompany the $\Upsilon(4S)$.
- When the $\Upsilon(4S)$ decays, the two B mesons are coherently produced in a *P*-wave state. This guarantees that the two B mesons are nonidentical; that is, the one is a B^0 while the other is a $\overline{B^0}$. This feature is particularly advantageous for *CP* violation studies.
- The multiplicity of hadrons in the $\Upsilon(4S)$ decay is relatively small. When combining particles to reconstruct B meson states, this low multiplicity keeps combinatorial backgrounds at a reasonable level.

The B mesons produced in $\Upsilon(4S)$ decay (B_u, B_d) comprise a b quark and a lighter quark, either an up (u) or down (d) quark. It is also of considerable interest to study the decays of B mesons that contain a strange (s) quark (B_s). These studies must be done at the $\Upsilon(5S)$ resonance (see Fig. 2-1).

The majority of the B Factory program will be spent at the $\Upsilon(4S)$. As we have seen, this choice of energy provides a copious source of B_u and B_d mesons. Accompanying the resonant production of B mesons is the so-called continuum physics, the roughly 2.5 nb of cross section that comprises e^+e^- annihilation into pairs of light quarks (u, d, and s), pairs of light leptons (e^+e^- and $\mu^+\mu^-$), pairs of heavy quarks (charm quarks), and pairs of heavy leptons ($\tau^+\tau^-$). The light quark and lepton events are of little interest (save for

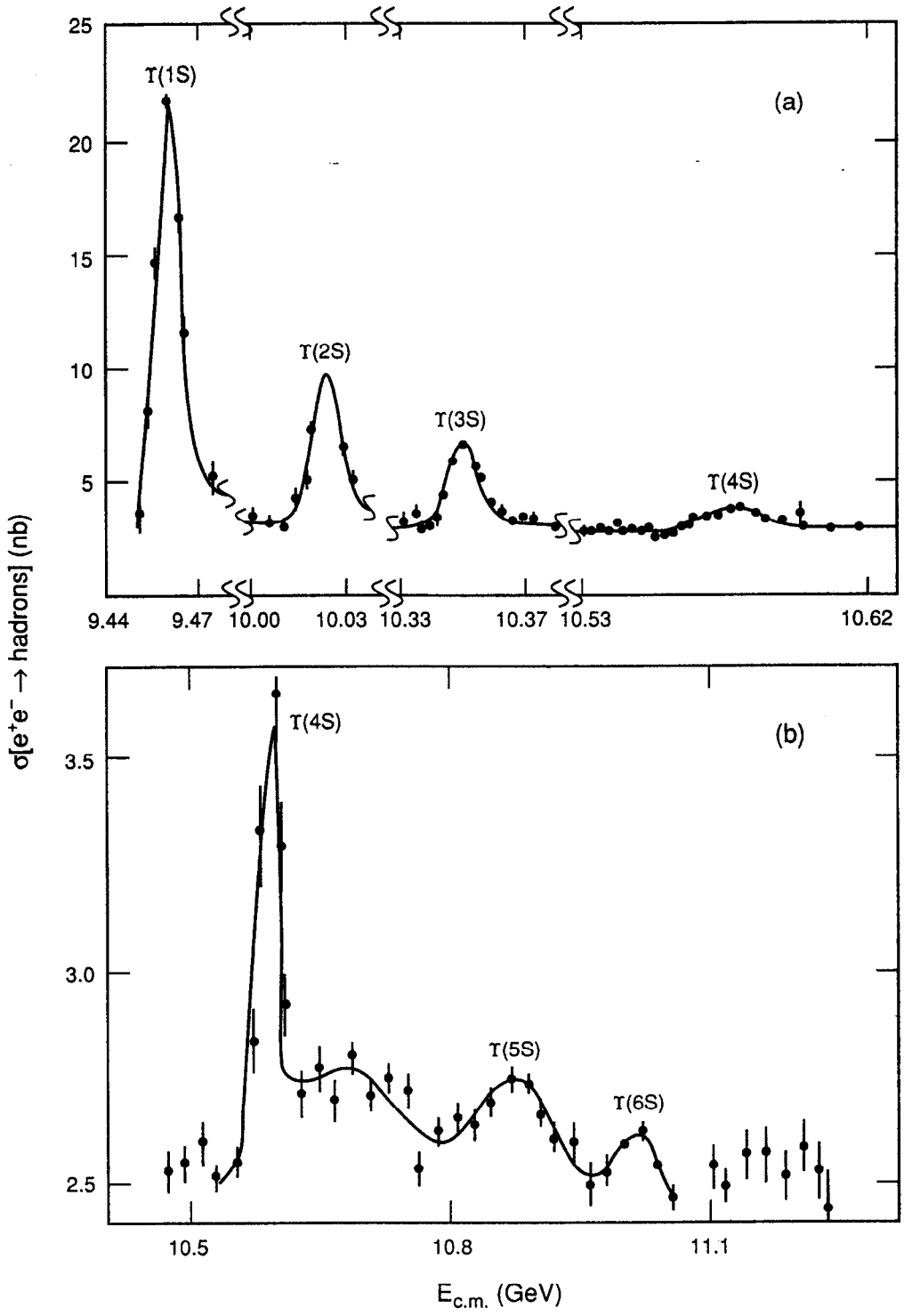

Fig. 2-1. The cross section for the production of hadrons in e^+e^- collisions in the center-of-mass energy region near 10 GeV. The data are characterized by a series of resonances, the Υ family, which herald the onset of the b quark threshold. The data in (a) are from the CUSB detector group; the data in (b) are from the CLEO detector group.

normalization of the experiment), but the heavy-constituent events are of considerable interest. The B Factory will produce very large samples of these heavy constituents, thereby assuring an interesting and diverse physics program.

2.3 PHYSICS MOTIVATION

We turn our attention now to the details of the particle physics program and how it relates to specifying the goals for the B Factory. We have studied this physics program very extensively and with great attention to detail in a series of workshops held over the past two years. The interested reader is encouraged to consult the proceedings of these workshops [Hitlin, 1989 and 1991] for more details. The earlier workshop covered the full spectrum of available physics (except two-photon physics), whereas the more recent one dealt much more extensively with the study of *CP* violation and also covered two-photon physics. The machine design goals all come from the B physics program and are dominated by the requirements for studying *CP* violation. [A rather similar set of goals arises from the study of B_s mixing, although, in this case, the experiment is done at the $\Upsilon(5S)$.] Happily, the requirements for the *CP* violation program do not conflict in any way with those of the rest of the physics program.

2.3.1 The Standard Model of Particle Physics

Our understanding of the interactions among Nature's basic building blocks, the quarks and leptons, is described by a theory called the *Standard Model.* This model successfully explains all experimental measurements as they pertain to the three forces seen by the constituents, the strong force, the electromagnetic force, and the weak force. There are no verified experimental anomalies between experiment and the Standard Model—a situation of unprecedented success. However, as a complete model of Nature, the Standard Model has several crucial shortcomings, and most particle physicists believe that it must one day be superseded by a more complete theory. It is widely acknowledged that progress toward this more satisfactory theory will almost certainly have to come from experiment (as opposed to new theoretical insights); the field is therefore greatly in need of verifiable data that is in solid *conflict* with the Standard Model.

Among the unsatisfactory elements of the Standard Model are its inability to predict many important numbers (such as the masses of the constituents, the masses of the force mediators, etc.) and the rather ad hoc (often called "unnatural") manner in which it handles certain essential elements, the leading example being the way particle masses are generated (the Higgs phenomenon). Whereas the well-established phenomenon of *CP* violation has a natural place within the Standard Model, it in no sense has an explanation. One of the strengths of the B Factory heavy-constituent program is the broad range of measurements that will directly confront the validity of the Standard Model. Many ways can be imagined in which this program could provide the first indication of where the Standard Model fails—in this sense, it provides possibly the best window to new physics of any currently proposed facility. Understanding the Higgs mechanism supplies the justification for the SSC; likewise, understanding the origin of *CP* violation is the central driving force for the construction of the B Factory.

The Standard Model describes the interactions of the building blocks of matter, the six quarks and the six leptons. These spin 1/2 constituents interact via three forces, each of which is mediated by spin 1 force carriers such as the photon (electromagnetic); the Z, W^+, and W^- (weak); and the gluons (strong). With these twelve constituents (and their antiparticles) and the force carriers, all physical phenomena are explainable (we ignore gravity in this discussion). The constituents come in three generations, or families. The lightest generation (the up and down quarks, the electron and the electron neutrino) plays a special role in our universe: All stable matter is made up of these four constituents. Yet, for reasons we do not understand (another shortcoming of the Standard Model), Nature has chosen to make two replicas of this lightest generation (see Table 2-2). The clearest distinction among the generations is the increase in mass; the higher the generation, the larger the constituent masses (save for the neutrinos, which so far appear massless). Hence, the τ lepton is the heaviest charged lepton, the top quark (as yet undiscovered, with a mass in excess of 90 GeV) is the heaviest charge 2/3 quark, and the b quark is the heaviest charge –1/3 quark. Whereas we do not understand the replication of the lowest-lying generation, there is no denying the existence of the second and third generations. Indeed, it is the richness of the quark generations that most likely holds the key to expanding beyond the Standard Model.

2.3.2 The Pattern of Quark Decays—The CKM Matrix

To understand this last statement, we must delve more deeply into the pattern of constituent decays. Here the apparently symmetrical role of the quarks and leptons breaks down. The lepton generations are distinct: No interactions couple them. In any physical process, lepton number is conserved separately *for each generation.* Thus, in the decay of a muon, three particles materialize: a muon neutrino, an electron, and an electron antineutrino. The first-generation lepton number is conserved by the balance of the electron and its antineutrino, while the muon neutrino is needed to balance the second-generation lepton number. This absence of cross-generation coupling appears to be absolute in the lepton sector, but not in the quark sector. Indeed, the s and b quarks would be entirely stable if they could not couple to quarks of a lower generation. Thus, quark decay involves a coupling of the generations: A b quark can cascade down to the charm quark (which is its predominant choice) or, less likely, to the up quark. This intergenerational mixing is summarized by the so-called Cabibbo-Kobayashi-Maskawa (CKM) matrix. This matrix represents the fact that the weak interaction does not couple directly to the quark mass eigenstates; rather the weak eigenstates (which couple to the W's) are admixtures of the mass eigenstates, the exact admixture being given by the elements of the CKM rotation matrix. The richness of the quark decay spectra is represented by the elements of the matrix:

$$\begin{pmatrix} V_{ud} & V_{us} & V_{ub} \\ V_{cd} & V_{cs} & V_{cb} \\ V_{td} & V_{ts} & V_{tb} \end{pmatrix}$$

Table 2-2. The particles of the Standard Model.

Leptons			
Name	Symbol	Mass (GeV)	Electric charge
Electron	e^-	0.000511	–1
Electron neutrino	ν_e	0	0
Muon	μ^-	0.106	–1
Muon neutrino	ν_μ	0	0
Tau	τ^-	1.784	–1
Tau neutrino	ν_τ	0	0

Quarks			
Name	Symbol	Mass (GeV)	Electric charge
Up	u	0.31	+2/3
Down	d	0.31	–1/3
Charm	c	1.50	+2/3
Strange	s	0.51	–1/3
Top	t	>90	+2/3
Bottom	b	5.0	–1/3

Carriers of force			
Force (carrier)	Symbol	Mass (GeV)	Electric charge
Electromagnetism (photon)	γ	0	0
Weak (weak vector bosons)	Z^0	92	0
	W^+	81	+1
	W^-	81	–1
Strong (gluon)	g	0	0

Higgs			
Name	Symbol	Mass	Electric charge
Neutral Higgs	H^0	?	0
Charged Higgs	$H^\pm$	?	±1

The CKM matrix can be completely characterized by four parameters: three real numbers and one complex phase. A commonly used parametrization is that due to Wolfenstein:

$$\begin{pmatrix} 1-\lambda^2/2 & \lambda & A\lambda^3(\rho-i\eta) \\ -\lambda & 1-\lambda^2 & A\lambda^2 \\ A\lambda^3(1-\rho-i\eta) & -A\lambda^2 & 1 \end{pmatrix}$$

where A, λ, ρ, and η are real parameters. When $\lambda = 0$, this matrix becomes the unit matrix, and there is no coupling among generations.

If the Standard Model were truly a complete theory of Nature, the CKM mechanism would have arisen naturally in the model, and all the values of the elements of the matrix would be specified. Instead, these numbers must be measured, and self-consistency must be established to check the validity of the model. *It is for this reason that the pattern of quark decays offers a powerful window onto the validity of the Standard Model.* In particular, the heavy-quark decays (those of charm and bottom, which are so profuse and so readily studied at the B Factory) provide a wealth of data for testing the Standard Model.

2.3.3 *CP* Violation in the Standard Model

We will now focus on the phenomenon of *CP* violation. The origin of *CP* violation has been one of the defining mysteries of particle physics since the violation was first discovered in the Nobel Prize–winning work of Cronin, Fitch, and collaborators [Christenson et al., 1964]. While the physical manifestations of this asymmetry are tiny, its ramifications are cosmic. Indeed, without the presence of this phenomenon, we would be hard-pressed to explain the presence of our universe. In the absence of *CP* violation, the equations that govern the behavior of particles created in the Big Bang are matter-antimatter symmetric. Under such circumstances, particle-antiparticle annihilation should have dominated, and no stable universe should have resulted. Yet we find ourselves living in a stable, matter-dominated universe. The tiny anisotropy generated by *CP* violation, the only known physical process that allows for an *absolute* determination of the sign of the electric charge, was sufficient to tip the balance away from total annihilation and permit the creation of a stable universe.

The lack of *CP* symmetry is experimentally well-demonstrated in the decays of K mesons. However, an explanation for the origin of the violation remains no more than conjecture; the K meson system provides too limited a set of measurements to fully fix the appropriate CKM parameters or to distinguish between competing models of the mechanism. It is the inclusion of the complex element (the phase η in the Wolfenstein representation) that provides a *mechanism* for *CP* violation in the Standard Model. It should be emphasized that *CP* violation is not a necessary consequence of the Standard Model; it is merely allowed. We have no experimental evidence for or against the idea that this mechanism of *CP* violation is in fact the correct one. Studies of *CP* violation in the decays of the B meson system, unlike those in the K meson system, provide the

diversity needed to over-constrain the Standard Model and hence establish once and for all whether this mechanism is correct.

Using the data from K meson measurements and the framework of the Standard Model, predictions for the size of the *CP* asymmetries in B meson decays can be made. Because our understanding of quark decays is not perfect, the size of these *CP*-violating effects cannot be precisely pinpointed; rather, a range of validity is predicted. Despite this uncertainty, for certain decays ($B^0 \rightarrow J/\psi K_s$ being the most studied), the Standard Model makes an unambiguous prediction of a large *CP*-violating asymmetry, in the range of 10–60%. (This can be contrasted with the asymmetries in the K meson system, which amount to two parts per thousand.) The physical effect we seek is thus large and easily measured, provided that sufficient events can be accumulated in the appropriate B meson decay modes. The branching fractions for these *CP*-violating decay modes tend to be small (typically 10^{-4}–10^{-5}), hence one needs to produce of the order of 10^7–10^8 B mesons to make statistically significant measurements of *CP* asymmetries. The desire to confront *CP* violation in this complete manner is what leads to the requirement of a very large integrated luminosity.

We shall now explore the range of the Standard Model predictions more quantitatively, because, if we are to fully test the validity of the Standard Model, we need to construct a machine capable of producing sufficient luminosity to cover this range completely. The CKM matrix is unitary, and therefore the following requirement must hold:

$$V_{ud}\,V^*_{ub} + V_{cd}\,V^*_{cb} + V_{td}\,V^*_{tb} = 0$$

This equation can be viewed as the closure of a triangle (the "Unitarity Triangle") in the complex (ρ,η) plane. Using the Wolfenstein representation, the triangle is as shown in Fig. 2-2. If *CP* violation in the B meson system were absent, then η would be zero and the triangle would collapse to a line on the real axis. As we stated above, the Standard Model predicts a range of *CP*-violating asymmetries in B decays and therefore a range of allowable angles α, β, and γ. This range is shown in Fig. 2-3 as a function of the t quark mass. It is this range of values that we must be capable of measuring if we are to ascertain whether the Standard Model can accommodate B meson *CP* asymmetries and

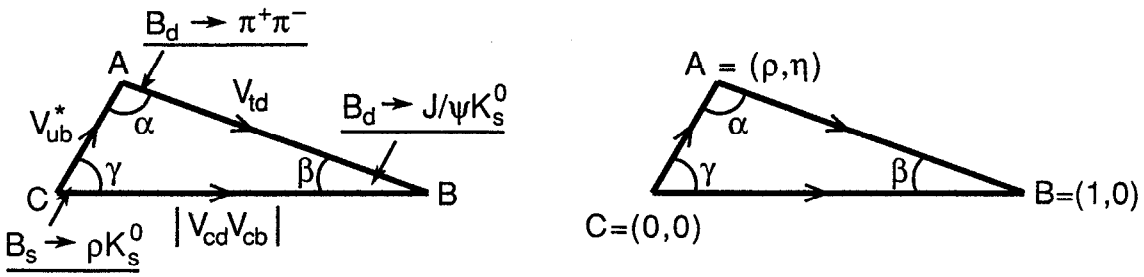

Fig. 2-2. The "Unitarity Triangle," along with definitions of the angles α, β, and γ and the prototypical self-conjugate CP eigenstates that are used to measure these angles. Closure of this triangle in the complex plane represents the unitarity of the CKM matrix. The parameters ρ and η, which appear in the Wolfenstein parametrization of the CKM matrix, are also shown here.

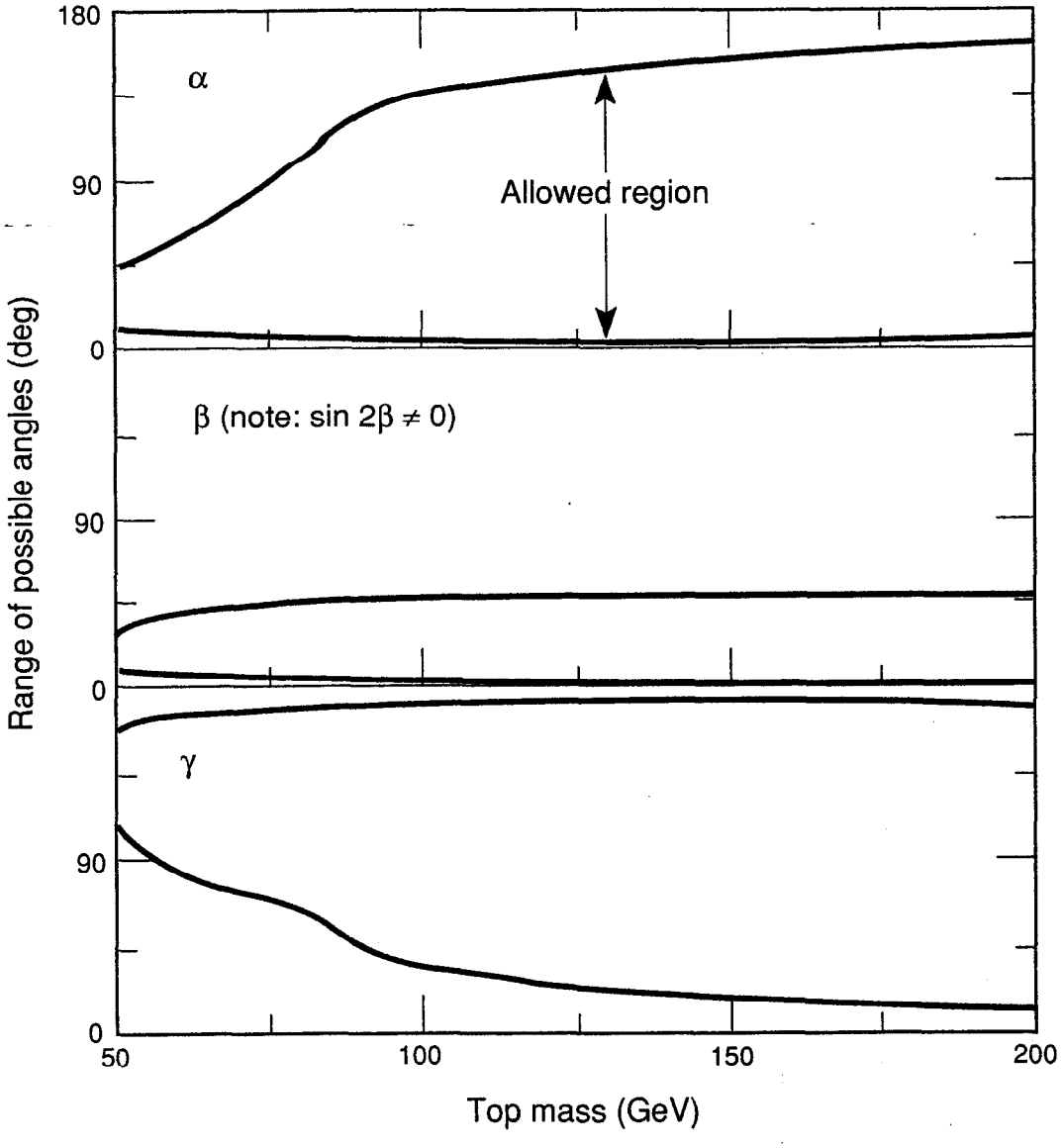

Fig. 2-3. The range of the unitary triangle angles allowed by the Standard Model (under reasonable assumptions for the model parameters), as functions of the top mass, currently thought to be above 90 GeV. Since the allowed range of β is never zero, the Standard Model unambiguously predicts finite asymmetries in decays characterized by sin 2β (like $J/\psi K_s$).

whether it is self-consistent. As indicated in Fig. 2-2, α, β, and γ are directly measurable from specific B meson decays to *CP* eigenstate final states, respectively indicated by a set of prototypical decays $B_d \rightarrow J/\psi K_s$, $B_d \rightarrow \pi\pi$, and $B_s \rightarrow \rho K_s$.

2.3.4 How *CP* Asymmetries Are Measured

To understand how the asymmetries are measured, we now return to our discussion of the $\Upsilon(4S)$ system and its decay into a $B^0\overline{B^0}$ pair. These B mesons are fairly long-lived (the B

meson lifetime is about 1 ps) and will propagate a measurable distance before they decay. The first B (we assume it to be a B^0; the argument is just reversed if it is a $\overline{B^0}$) will decay at time t_1 and, by the coherence referred to earlier, will force the second B to be a $\overline{B^0}$. This second B meson propagates further in time before it decays at time t_2. However, during the time interval $t_2 - t_1$, the $\overline{B^0}$ can change itself into a B^0 via the phenomenon of mixing. In fact, the Argus Group at DESY [Albrecht et al., 1987] first showed that mixing of neutral B_d mesons is large. Hence, it is possible to end up with either a $B^0\overline{B^0}$ final state or a B^0B^0 final state, depending on whether the second B meson has mixed or not. If we now arrange to detect one of the B's decaying to a *CP* self-conjugate eigenstate (like $J/\psi K_s$ or $\pi\pi$) and the other in a decay that distinguishes between a B^0 and a $\overline{B^0}$ (such as the sign of the charge of a lepton or kaon), it is possible to measure a *CP* asymmetry. The asymmetry arises from the fact that mixing has allowed two separate routes from the initial B meson to the final *CP* self-conjugate state (see Fig. 2-4), one without intermediate mixing and the other with mixing. If the interference between these two separate paths is different, depending on whether one starts from a physical B^0 or $\overline{B^0}$, a potentially measurable asymmetry is generated. The decay rate (Γ) of a time-evolved, initially pure $B^0\overline{B^0}$ into a B^0 ($\overline{B^0}$) and a self-conjugate *CP* eigenstate f_{CP} is given by

$$\Gamma(B^0\overline{B^0} \rightarrow B^0 f_{CP}) \propto e^{-\Gamma\Delta t}\,[1+ \sin 2\phi\ \sin \Delta m(t_2 - t_1)]$$

$$\Gamma(B^0\overline{B^0} \rightarrow \overline{B^0} f_{CP}) \propto e^{-\Gamma\Delta t}\,[1- \sin 2\phi\ \sin \Delta m(t_2 - t_1)]$$

where Δm is the $B^0\overline{B^0}$ mass difference, $\Delta t = t_2 - t_1$, and ϕ is α, β, or γ, depending on whether the *CP* eigenstate observed is $J/\psi K_s$, $\pi\pi$, or ρK_s.

There are four different measurable configurations:

$$n_1\colon f_B(t_1) f_{CP}(t_2)$$
$$n_2\colon f_{CP}(t_1) f_B(t_2)$$
$$n_3\colon f_{\overline{B}}(t_1) f_{CP}(t_2)$$
$$n_4\colon f_{CP}(t_1) f_{\overline{B}}(t_2)$$

where f_B signifies a B^0 tag, $f_{\overline{B}}$ signifies a $\overline{B^0}$ tag, and f_{CP} signifies a *CP* eigenstate. *CP violation produces a distribution in* $t_2 - t_1$ *that is different for* n_1 *and* n_4 *from that for* n_2 *and* n_3. In the absence of *CP* violation, the n_i distributions would be exponentials; in the presence of *CP* violation, they are measurably distorted by a sinusoidal oscillation with amplitude $\sin 2\phi$ and frequency Δm, as shown in Fig. 2-5.

A measurable asymmetry results from a proper summation of the number of events of each type:

$$A_{CP} = (n_2 + n_3 - n_1 - n_4)/(n_1 + n_2 + n_3 + n_4)$$

It is this asymmetry, as well as the detailed time distributions, that will be measured at the Asymmetric B Factory. As seen from Fig. 2-5, the advantage of the B Factory is the availability of the time-evolving distributions. Not only does this exhibit the *CP*

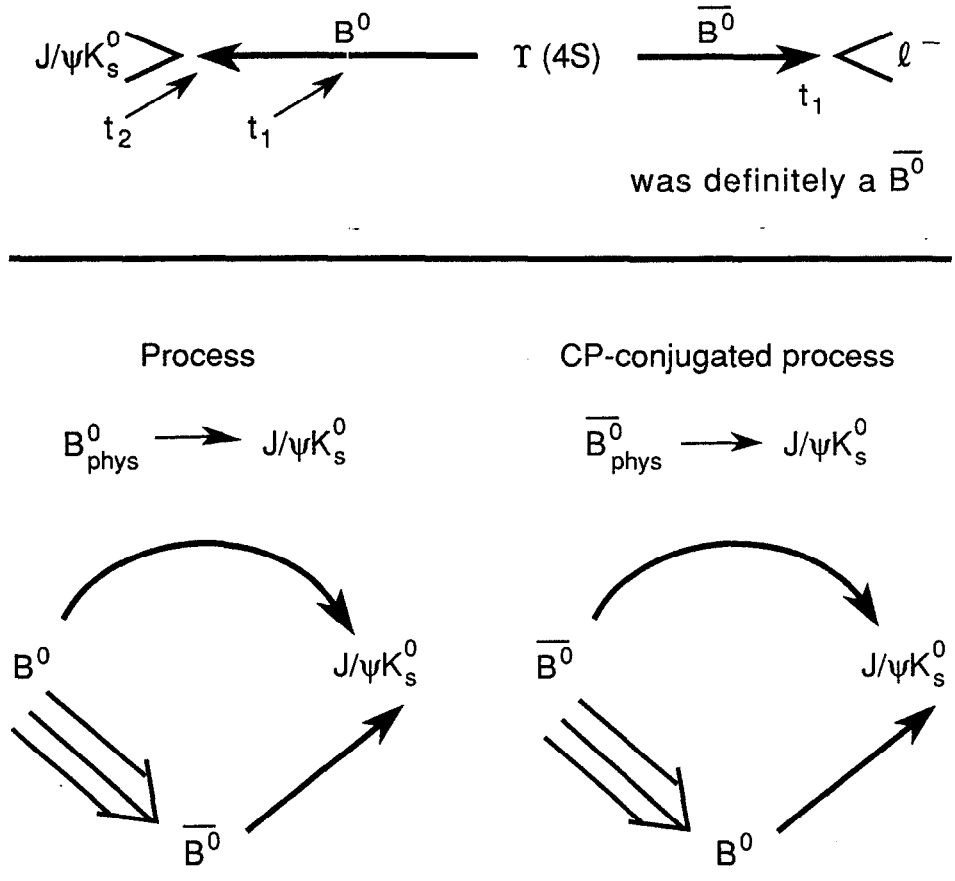

Fig. 2-4. An artist's rendition (upper diagram) of the topology used for measuring CP violation effects at the Υ(4S). One of the neutral B's is reconstructed in a CP self-conjugate state (the $J/\psi K_s$), while the identity of the other B (B^0 or $\overline{B^0}$) is established from the sign of the charge of a lepton (or K meson). The lower diagram illustrates how mixing is used to project out the CP violation effects. The B^0 can decay to $J/\psi K_s$ (bottom left) via two routes, one direct and one involving mixing. These two amplitudes will interfere, and this interference has a different magnitude when one begins with the CP-conjugated state $\overline{B^0}$ (bottom right). Thus, final states involving $J/\psi K_s/B^0$ and $J/\psi K_s/\overline{B^0}$ can be used to measure CP asymmetries.

violation to its fullest extent, but also the four time-evolved spectra provide two pairwise identical distributions, and the sum of the integrals under the four distributions should be zero (another way of saying that the time-integrated asymmetry must be identically zero). These constraints provide a valuable set of cross-checks on the correctness of the measurements.

The asymmetry A_{CP} is directly related to the angles of the Unitarity Triangle, according to

$$A_{CP} = \frac{x_d}{(1 + x_d^2) \sin 2\phi}$$

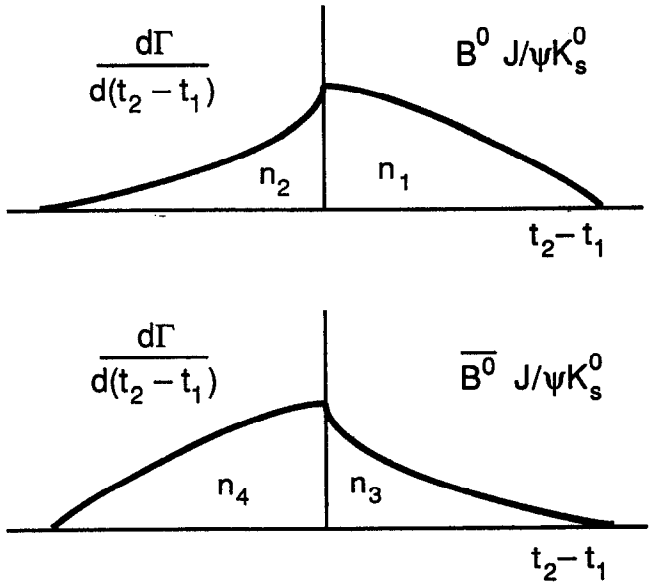

Fig. 2-5. The time-evolved decay distributions that are measured to yield the CP asymmetries. The n_i signify four different final-state topologies, as outlined in the text. It is the distortion of these spectra from exponentials that provide the information for measuring CP violations.

where ϕ is α, β, or γ, depending on whether the *CP* eigenstate observed is $J/\psi K_s$, $\pi\pi$, or ρK_s. Here x_d represents the strength of the B^0 mixing (measured to be 0.71), hence the dilution factor relating the measured asymmetry to the unitarity angle is known.

To summarize, then, the experiment involves measuring the time difference between the decay points of the two B mesons produced in the decay of the $\Upsilon(4S)$. In addition, one of the B final states must be established as a *CP* eigenstate, and the other must be tagged as either a B^0 or a $\overline{B^0}$. Establishing the identity of the two B mesons is readily done; this has a significant impact on the design of the detector but relatively little impact on the design of the accelerator. The time-difference measurement is faithfully represented by the measurement of the difference in the positions of the two decay points of the B mesons; it is the need to measure this difference that is responsible for the energy asymmetry of the accelerator.

2.3.5 Justification for the Energy Asymmetry

As suggested above, the crucial experimental ingredient is the ability to accurately measure the distance between the decay points of two B mesons. With modern vertex detectors using silicon technology, one is able to measure this distance with a resolution of about 50 μm. If a B meson facility is run with equal beam energies, the $\Upsilon(4S)$ is produced at rest in the laboratory and the two mesons do not propagate very far before they decay. The typical distance between the B meson decay points in this equal-beam-energy geometry would be about 30 μm, a distance too small to discern with today's detectors. The solution to this dilemma, first proposed by Oddone [1987], is to boost the

$\Upsilon(4S)$ in the laboratory frame by running the storage ring with *unequal beam energies*, hence the name Asymmetric B Factory. The asymmetry denotes the difference in energy between the electron and positron beams. For example, if one chooses 9 and 3.1 GeV for the two beam energies [$E^2_{\text{c.m.}} = 4E_{\text{low}}E_{\text{high}}$; the center-of-mass energy is thus that of the $\Upsilon(4S)$], then the average distance between the two B meson decays becomes 180 μm. Figure 2-6 shows the results of a detailed simulation (see Hitlin [1989], pp. 69–83) of a measurement of sin 2β, using the *CP* eigenstate $J/\psi K_s$ and kaons and leptons as tags. The distortion of the exponential decay distributions, arising from *CP* violation, is readily seen.

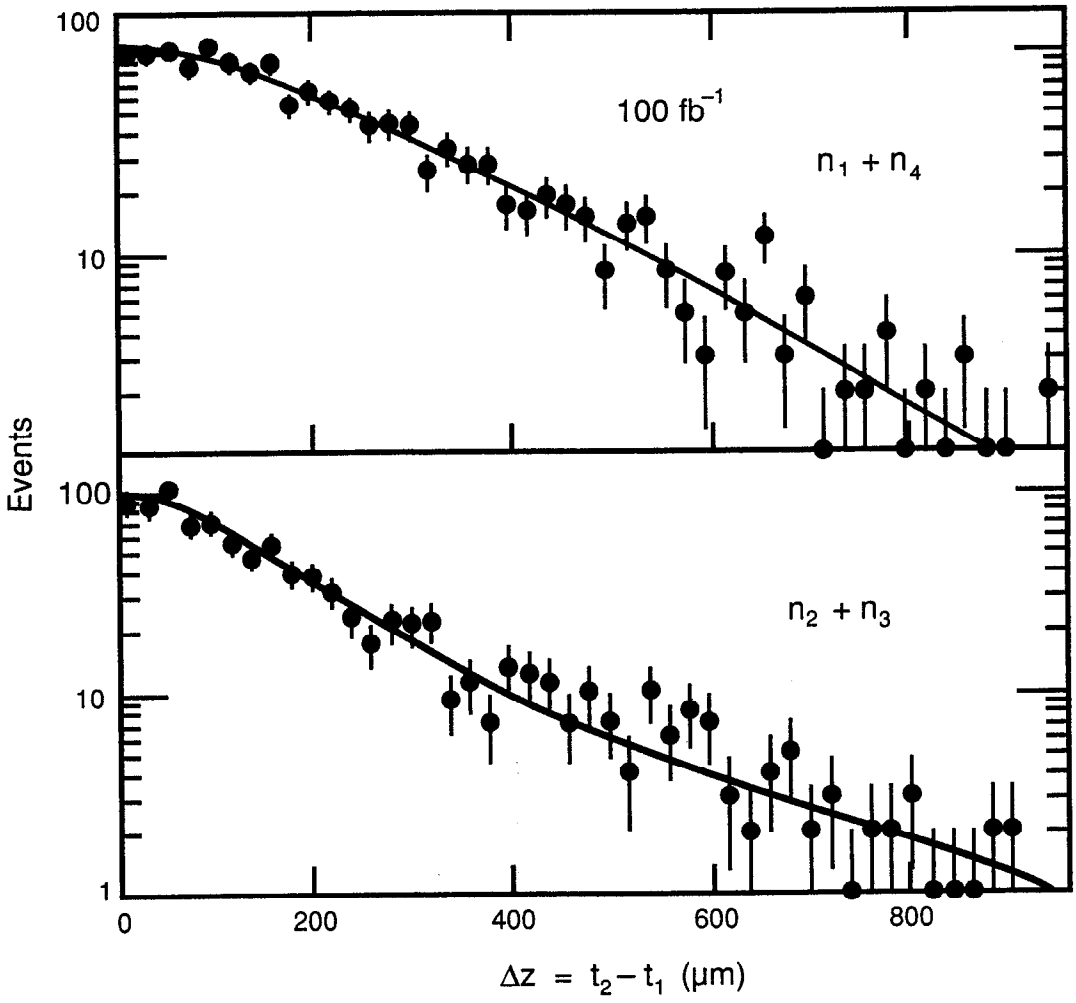

Fig. 2-6. A simulation of the decay length distributions for two classes of events. The upper plot includes events where the first B decays to $J/\psi K_s$ and the second B is tagged as a B^0, or the first B is tagged as a $\overline{B}^0$ and the second B decays to $J/\psi K_s$ (n_1 and n_4); the lower plot has the two complementary topologies (n_2 and n_3). For details, see Hitlin [1989], pp 69–83. The input value was sin $2\beta = -0.4$; a fit to the data yielded sin $2\beta = -0.408 \pm 0.023$ for the assumed 100 fb^{-1} of data.

The justification for an asymmetry in the beam energy is now clear: It is required to give the $\Upsilon(4S)$ system a sufficient Lorentz boost to provide a measurable $t_2 - t_1$ distribution. But how large does the asymmetry need to be? Figure 2-7 shows a simulation of the measurement error for sin 2β as a function of the energy of the high-energy beam. One sees a precipitous dependence on the asymmetry for energy choices below 8 GeV. To remain safely above this region, and to protect against a less optimal set of experimental conditions than those assumed in the simulation, we chose to set the high-energy beam energy at 9 GeV. This choice guarantees the full benefit of the asymmetric geometry.

2.3.6 Justification for the Design Luminosity

We now turn to the issue of what the machine design luminosity ought to be if we are to fully constrain the Standard Model within a reasonable period of time. A decision requires doing very detailed simulations of the measurements of *CP* asymmetries, using a realistic detector. Accordingly, simulations have been performed [Hitlin, 1989 and 1991] for a wide variety of final states. It turns out that it is possible to employ many more B^0 final states than the *CP* self-conjugate ones referred to above. A number of impressive studies have now shown that these final states also have measurable asymmetries, comparable to those expected for $J/\psi K_s$ and $\pi\pi$. These states are those of mixed *CP*, such as $J/\psi K^*$ and $D^{*+}D^{*-}$, as well as states that are not *CP* eigenstates, such as $\rho\pi$ or $a_1\pi$. Figure 2-8 shows the range of sensitivity to the angles α and β for an integrated

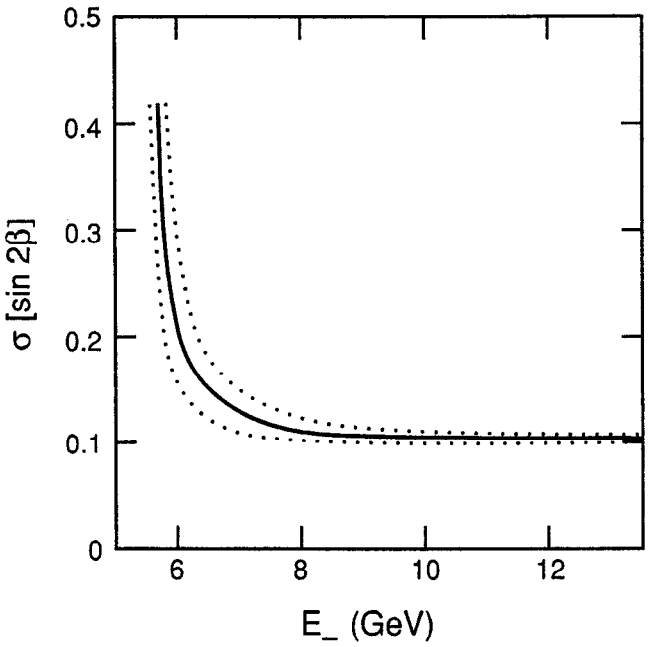

Fig. 2-7. The resolution for measuring sin 2β as a function of the energy of the electron (high-energy) beam. The upper (lower) dotted curve assumes a vertex resolution of 120 μm (50 μm); the solid line assumes 80 μm.

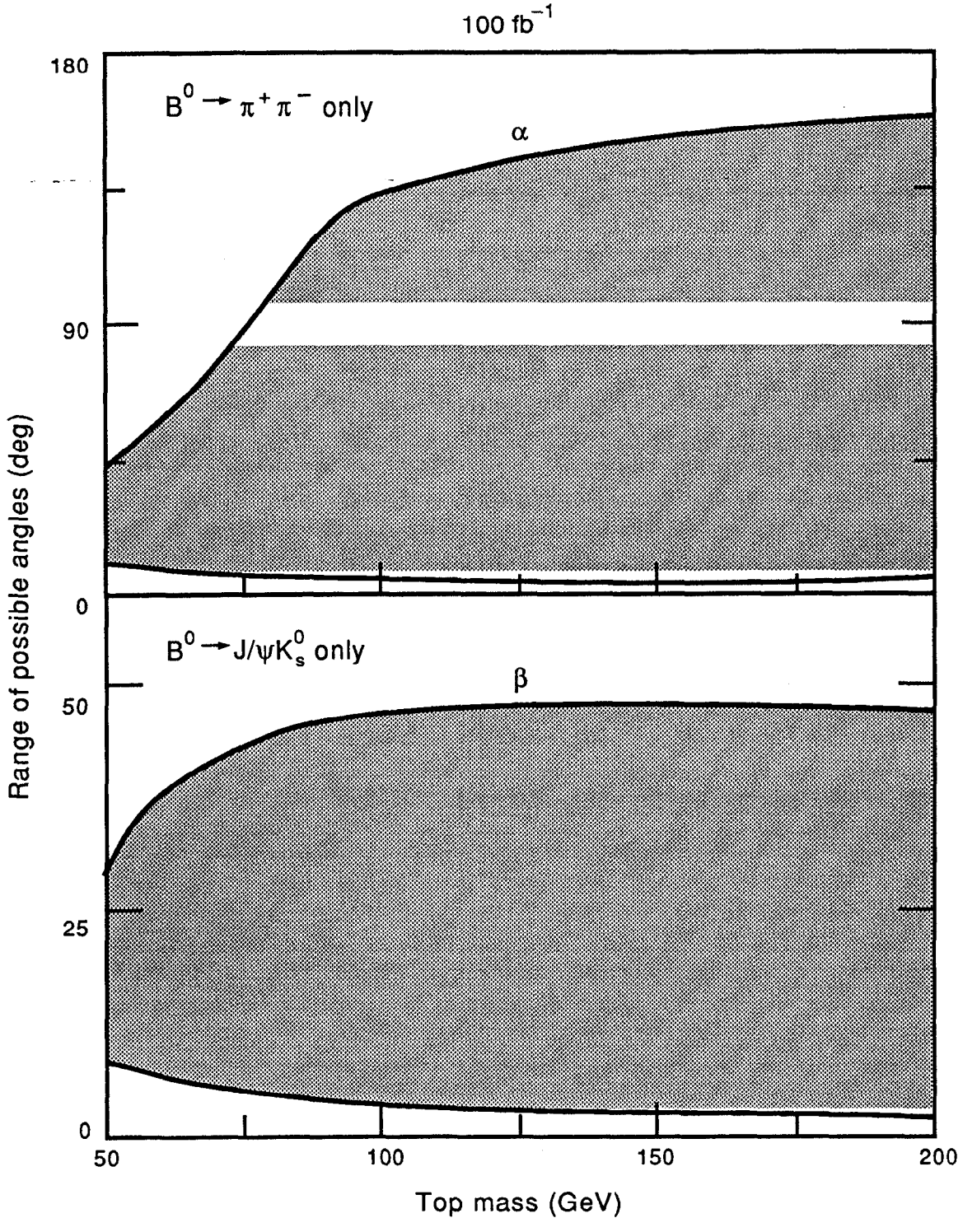

Fig. 2-8. The range of the Standard Model predictions for α and β. The shaded region represents the portion of this range covered (with 3σ precision) by measurements using the CP decay modes $J/\psi K_s$ (for β) and ππ (for α). A data set of 100 fb^{-1} was assumed.

luminosity of 100 fb^{-1}, using only the *CP* eigenstates $J/\psi K_s$ (for β) and $\pi\pi$ (for α). A data set of this size gives excellent coverage of the range of parameter space allowed by the Standard Model. Figure 2-9 shows what can be accomplished using the additional modes in Table 2-3, using a data set of 30 fb^{-1}.

It is important to emphasize here that the large integrated luminosities shown in Figs. 2-8 and 2-9 arise from the need to cover essentially the entire range of Standard Model predictions. It is entirely possible that a significant measurement of a *CP* violation asymmetry could be established with far less data. For instance, if the angle β were in the middle of the predicted Standard Model range, $\sin 2\beta = -0.4$, a 3σ measurement would be obtained with only 3 fb^{-1}. Likewise, if the Standard Model were wrong, and $\sin 2\beta$ were positive, a clear indication of such an effect would require relatively little data. It is for "less favorable" scenarios that the high luminosity is necessary.

Based on Figs. 2-8 and 2-9, we have concluded that an accelerator that delivers 30 fb^{-1} per calendar year has spectacular discovery potential and will cover the complete range of Standard Model predictions in a period of a few years. This then becomes the design goal for the storage ring. To convert this into a design luminosity for the B Factory, we use the "Snowmass convention" that a year has 10^7 seconds, taking into account accelerator and detector efficiencies and the difference between peak and average luminosities. We thus require a peak luminosity of 3×10^{33} cm^{-2} s^{-1} to log 30 fb^{-1} in one calendar year.

Information gathered at the $\Upsilon(5S)$ resonance on the angle γ is complementary to the measurements of α and β, but very large samples (several hundred fb^{-1}) are required to match the precision of the measurements done at the $\Upsilon(4S)$. For details, see Hitlin [1989], pp. 84–91.

2.3.7 Sensitivity to Nonstandard Origins for *CP* Violation

So far we have restricted ourselves to the use of *CP* asymmetries in the context of verifying the Standard Model. The asymmetries are actually much more powerful: They can provide deep insights in the event that the Standard Model proves to be incorrect.

The simplest statement that can be made is that, a priori, there is no reason to expect the Standard Model range for $\sin 2\beta$, namely $-1 \leq \sin 2\beta \leq -0.08$, to be any more probable than the rest of the physical range ($-0.08 \leq \sin 2\beta \leq 1$). Establishing that the Standard Model is wrong is therefore very direct and could take relatively little running time, even at luminosities significantly below the design level.

The B^0 meson *CP* laboratory is considerably richer than even this statement would suggest, as has been outlined by Nir and collaborators [1990a, b, and c]. When we make the predictions about *CP* asymmetries discussed above for the Standard Model, we make several essential assumptions. We assume, for instance, that the nontagging B^0 decay has contributions from only one W-mediated quark subprocess. Multiple subprocesses (such as penguin contributions) could significantly change the predictions of the Standard Model. (It is fortunate that this assumption is reliable for the prototypical decay $B^0 \rightarrow J/\psi K_s$, where contaminations are considered to be below the few percent level.) We also assume that both K-$\overline{K}$ and B-$\overline{B}$ mixing proceed via the Standard Model mechanism of a "box diagram." Both of these assumptions enter the calculations of the asymmetries in a

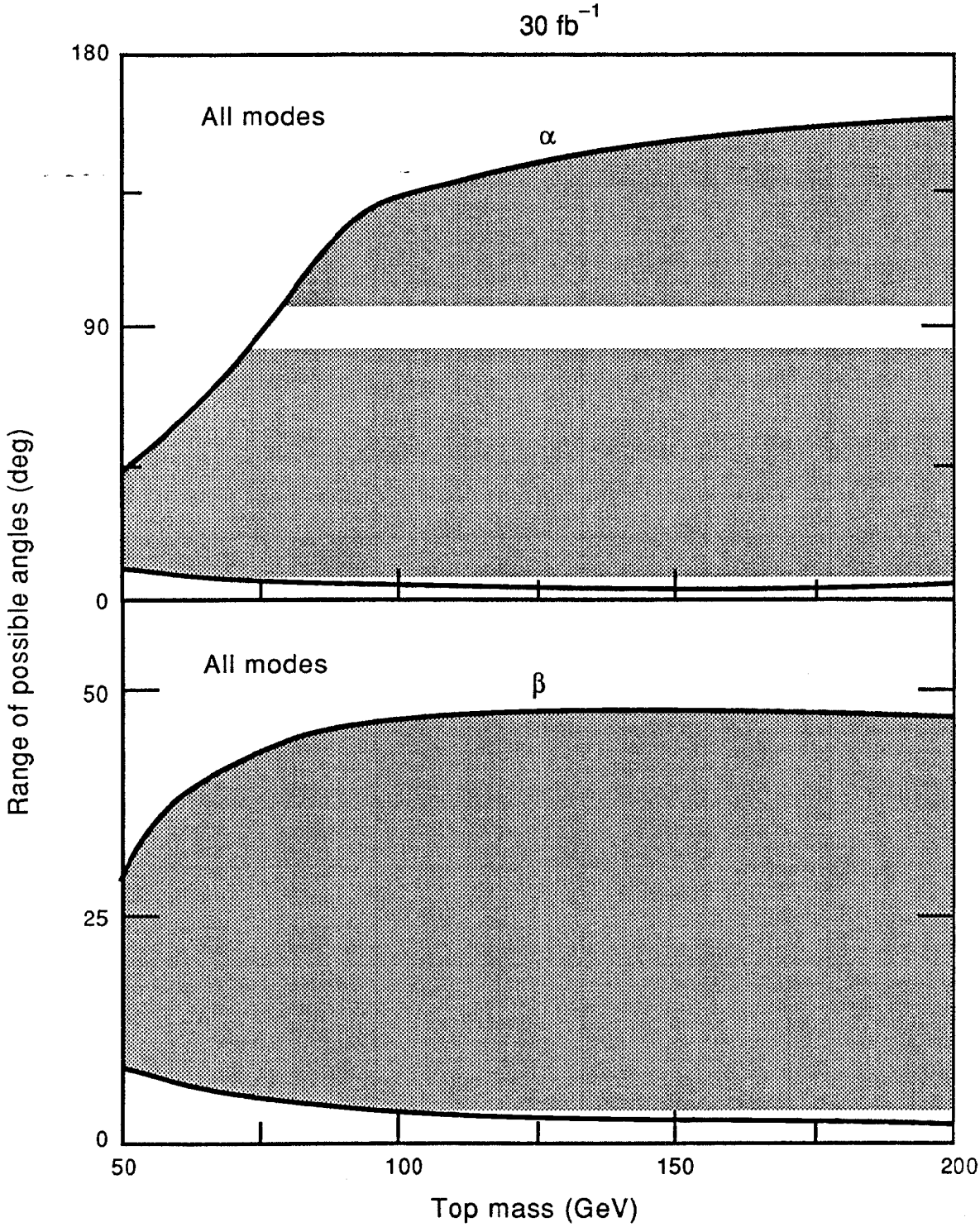

Fig. 2-9. The range of α and β predicted by the Standard Model that can be covered (3σ) by a 30-fb^{-1} data set, using a spectrum of CP decay modes (see Table 2-3).

Table 2-3. Summary of the assumptions used in the simulations of Fig. 2-9 to establish the measurement errors for sin 2 α and sin 2β (here generalized as sin 2ϕ). In addition, we have used as input a wrong-sign fraction of 8%, a $B\bar{B}$ cross section of 1.2 nb, and a neutral B fraction of 0.5.

Mode	Assumed branching fraction	Tagging efficiency (%)	Reconstruction efficiency (%)	σ (sin 2ϕ) (30 fb^{-1})
$B^0 \rightarrow J/\psi K_S$	7.4×10^{-4}	45	58	0.077
$\rightarrow D^+D^-$	6×10^{-4}	45	46	0.14
$\rightarrow J/\psi \bar{K}^{*0}$	12.5×10^{-4}	45	30	0.17
$\rightarrow D^{*+}D^{*-}$	16×10^{-4}	45	28	0.08
Combined (2β)				0.050
$B^0 \rightarrow \pi^+\pi^-$	2×10^{-5}	45	43	0.18
$\rightarrow \rho^{\pm}\pi^{\pm}$	6×10^{-6}	37	58	0.12
$\rightarrow a_1^{\pm}\pi^{\pm}$	6×10^{-5}	32	60	0.18
Combined (2α)				0.086

central way. What Nir and collaborators have shown is that experiments performed at the Asymmetric B Factory can, through a specific set of measurements, pinpoint directly which of these underlying assumptions is breaking down. For instance, in the Standard Model, the asymmetry measured in $B^0 \rightarrow J/\psi K_S$ must have the same value as that measured in $B^0 \rightarrow D^+D^-$: If these do not agree, the problem is uniquely with the assumption that K-$\bar{K}$ mixing proceeds via the box diagram. It has also been shown [Nir, 1990c] that in a model in which B-$\bar{B}$ mixing is predominantly due to Z-mediated flavor-changing neutral currents (rather than the familiar box diagram), the predictions for α and β can be completely different from those in the Standard Model; in fact, in this model, the Unitarity Triangle is actually a quadrangle. All these eventualities lead to striking departures from the Standard Model predictions—and they are all readily measurable at the Asymmetric B Factory.

It should also be reiterated that backgrounds in the reconstruction of B mesons in the $\Upsilon(4S)$ environment are small, making it uniquely suited to the reconstruction of a large number of B^0 decay modes with measurable *CP* asymmetries, even those of higher multiplicity and those that involve final state π^0's (see Table 2-3). This gives us the ability to make important cross-checks, as well as to reduce the luminosity required for the asymmetry measurements. Our simulations demonstrate that, for all the modes studied, large detection efficiencies are possible, with excellent signal-to-noise ratios.

2.3.8 Other B Physics

As outlined in Hitlin [1989], data taken at the $\Upsilon(4S)$ yield a rich B physics program beyond the area of *CP* violation. The production of several hundreds of millions of B mesons permits a sensitive search for rare and unexpected B decays. These rare decays also provide an important window to violations of the Standard Model. Processes involving yet-unseen penguin diagrams (an example of which is the decay $B^0 \rightarrow K^*\gamma$) will be accessible. It may also be possible to observe the decay $B^0 \rightarrow \tau\nu_\tau$, which would yield a measurement of the B decay constant f_B, a fundamental parameter. The B Factory will permit the search for rare decays at the level of 1 part in 10^8.

As pointed out earlier, the patterns of the heavy-quark decays are basic to an understanding of the weak interaction, and they determine directly the elements V_{ij} of the CKM matrix. A wide variety of $b \rightarrow c$ and $b \rightarrow u$ hadronic decays are available for study, as are $b \rightarrow c$ and $b \rightarrow u$ semileptonic decays.

Whereas we have measured mixing in the B_d^0 sector, mixing in the B_s^0 sector has not yet been observed. The mixing is expected to be more rapid: x_s is expected to be in the range 3–20 (compared with x_d, which is 0.71). Observing this mixing is a high-priority measurement. We have simulated a measurement of x_s using same-sign dilepton events observed in the decay of the $\Upsilon(5S)$. Requiring 10% measurement precision, x_s is measurable up to a value of 15 in a run of 30 fb^{-1}. This result assumes that the energy asymmetry at the $\Upsilon(5S)$ would be the same as at the $\Upsilon(4S)$; one gains rapidly in precision by increasing the energy asymmetry. In all likelihood, the $\Upsilon(5S)$ running will be a second-round experiment, following the first round of *CP* violation measurements done at the $\Upsilon(4S)$. It would seem prudent, then, when moving the energy up to the $\Upsilon(5S)$, to also reoptimize the interaction region geometry to provide a larger asymmetry. The machine design allows for such a change.

2.3.9 Charm Quark Physics

There is a long list of important topics in charm physics accessible at the B Factory by virtue of its high luminosity.

Mixing in the D^0-$\overline{D^0}$ system can be measured at a level several times smaller than the Standard Model prediction for this phenomenon. The expected limit on the mixing for a 30 fb^{-1} run at the $\Upsilon(4S)$ is less than 6×10^{-5}, compared with the Standard Model prediction of about 10^{-4} or larger. This means that if the Standard Model prediction is wrong the B Factory will have adequate sensitivity to establish this fact. The same measurement will yield information about *CP* violation in D decay, which is expected to be very small in the Standard Model. In a 30 fb^{-1} run at the $\Upsilon(4S)$, we will be able to search for *CP*-violating effects in the decays $D^0 \rightarrow K^+K^-$ and $D^0 \rightarrow \pi^+\pi^-$ at the 1% level. An effect this large would be uncommonly interesting, but is rather unlikely.

As with bottom quark decays, charm quark decays provide valuable input for the CKM matrix. Definitive measurements of both Cabibbo-allowed and Cabibbo-suppressed semileptonic decay modes are possible.

Two new areas of interest in charm physics are the spectroscopy of the $L = 1$ D** meson resonances and charmed baryons. This area of study has recently been initiated by CLEO and ARGUS with small numbers of events. There are 12 D** $L = 1$ states. Because this system is composed of one heavy and one light object (much like the hydrogen atom), the energy levels are sensitive to the details of the long-range (scalar) part of the potential. Mass splittings between the states are due to the spin-orbit interaction, rather than the more familiar spin-spin interaction. A large number of events are required to measure the masses, widths, spins and splittings in this system. Estimates have been made (see Hitlin [1989], Table 9.1, p. 236) of the number of events that would be observed in these 12 states. For a 30-fb^{-1} run, these numbers range from 700 to 20,000, with typical signal-to-noise ratios of better than 1 to 1. There is also a rich spectroscopy of charmed baryon states, few of which have been observed. The same 30-fb^{-1} run would yield thousands of these events per mode (see Hitlin [1989], Table 9.2, p. 239), with a signal-to-noise ratio of about 1 to 1.

2.3.10 Tau Physics

As far as we can discern, the τ lepton is a heavier version of the muon and electron, all three having properties strikingly consistent with the predictions of the Standard Model. The level of certainty of this statement is, however, experimentally not as great in the case of the τ as it is for the two lighter leptons, as our studies of τ decay involve statistical samples many orders of magnitude smaller. There are, in fact, several inconsistencies in the measurements of τ branching fractions. The B Factory will provide an increase in statistical power, relative to present studies, of about two orders of magnitude, thus allowing much more thorough tests of the sequential lepton hypothesis for the τ.

Many specific measurements have been considered in detail. The limit on the τ neutrino mass (currently less than 30 MeV) can be lowered to a few MeV. The Cabibbo angle in τ decay can be measured far more accurately than the current ±20%. Searches for second-class currents are possible at a level below the expectations of the Standard Model. Rare decays can be searched for at the 10^{-8} level. The structure of the τ-W-ν_τ vertex can be studied in detail. Both τ branching fractions and the τ lifetime can be measured with exquisite precision; these can then be combined to yield absolute decay widths. The current branching fraction puzzle in τ decays will either be resolved or shown to be an anomaly. The precision with which these measurements can be made is summarized in Table 2-4.

2.3.11 Upsilon Physics

Quarkonia, bound states of quark and antiquark, provide us with an excellent testing ground for QCD, both perturbative and nonperturbative. Bottomonium ($b\bar{b}$), the heaviest known system, is the most amenable to theoretical interpretation, as both relativistic corrections and higher-order QCD effects are much smaller than in the lighter quarkonia. The spectrum of bottomonium states is very rich, and although many of the states have been observed, a number of important spectroscopic measurements remain to be made.

Table 2-4. Summary of τ physics measurements.

Physics topic	$\int \mathcal{L}\, dt$ (fb^{-1})	Sensitivity	Backgrounds	Systematics
M_{ν_τ}	100	3 MeV @ 95% CL	None found	1.1 MeV; hadronic mass scale & M_τ
Cabibbo angle	30	0.5%	Small; from $\tau^+\tau^-$	0.4%; from background and cuts
Second-class currents	30	5σ signal if BF = 3×10^{-5}	From $\tau^+\tau^-$	
Rare decays ($\tau^+ \to \mu^+\mu^+\mu^-$)	100	BF $\leq 3 \times 10^{-7}$ @ 95% CL	Dominantly $\tau^+\tau^-$	
B_e/B_μ	30	0.2%	Dominantly $\tau^+\tau^-$	0.4%; from background
τ lifetime	30	0.14%	1%; from $q\bar{q}$	0.25%; from vertex detector position
Branching fracs ($\tau \to e\, \nu\, \bar{\nu}$)	30	0.3%	2%; from $q\bar{q}$	0.2%; from background
τ-W-ν_τ structure	30	$\rho, \eta\ O(0.1\%)$ $\xi, \delta\ O(1\%)$		

Much of this physics is only accessible with statistical samples of the size to be available at the B Factory.

Among these measurements, we single out a few for illustration. Transitions from the Υ(3S) and Υ(2S) states to the singlet S states (η_b) and to the lowest singlet P state could lead to the discovery of the pseudoscalar and pseudovector states and measurements of the hyperfine splittings. Detailed studies of the known triplet P states are needed. Enhanced studies of hadronic transitions between the Υ family are also much needed. High-statistics studies of radiative transitions will be performed, including searches for nonstandard Higgs particles. The Υ system can yield precise determinations of the strong coupling constant α_s from comparisons of B meson branching fractions to different final states.

These studies require that the machine be run at energies other than that of the Υ(4S). Relatively short runs (5–10 fb^{-1}) easily suffice to provide more than sufficient data for

these channels. These dedicated runs will be interspersed with $\Upsilon(4S)$ running: The accelerator will have sufficient energy tunability to allow movement among the Υ resonances.

2.3.12 Two-Photon Physics

The study of final states produced in e^+e^- reactions via the two-photon reaction (in contrast to the more prevalent one-photon exchange) has been actively pursued over the last ten years. Two-photon physics is now one of the primary sources of information about meson spectroscopy and QCD, and it serves as a unique laboratory for exotic meson searches. While a second generation of experiments is currently accumulating data, the much higher integrated luminosities available at the B Factory will make it an ideal place to study two-photon physics and will extend the range of results considerably beyond what could otherwise be achieved in the next few years.

The two-photon reaction permits detailed studies of the properties of charge-conjugation $C = +1$ mesons, which are not directly accessible in one-photon annihilation. The environment has many advantages for establishing the quantum numbers of these states; in the special case of spin 1 particles, the TPC group at PEP has demonstrated a unique method for determining the spin and parity of the states. The two-photon reaction probes the quark content of hadrons in a manner different from that of one-photon annihilation. The former has a rate proportional to the fourth power of the quark charges, whereas the latter has a rate proportional to the second power. This enhances sensitivity to the mesons containing up and charm quarks.

Two-photon reactions provide an ideal hunting ground for exotic meson states, those that cannot be formed by pairs of quarks. Such states might include four-quark states, states made from two quarks and a gluon, etc. Here, as with the $C = +1$ mesons, the high luminosity of the B Factory will provide sensitivity to particle masses well above anything current experiments will achieve.

The measurement of exclusive and inclusive hadron production in two-photon reactions allows access to many aspects of QCD that remain difficult to probe in other ways. Reaction rates and kinematic distributions yield important information on the distribution of quarks and gluons inside hadrons. One can probe regions of high Q^2 and large two-photon center-of-mass energy, where reliable perturbative QCD predictions exist. The total cross section yields information about the hadronic nature of the photon, while photon structure function measurements permit a definitive test of perturbative QCD.

2.4 CONSTRAINTS IMPOSED ON THE ACCELERATOR BY THE DETECTOR

The detector required for this physics program imposes certain constraints on the accelerator design, in addition to those of the energy asymmetry and the required luminosity. The main constraints involve requirements of solid angle coverage, the radius of the beam pipe, and the reduction of backgrounds.

The detector will closely resemble a conventional 4π detector for e^+e^- annihilation. It will not be inherently asymmetric, but there will be a premium on good charged-particle

and photon detection in the forward direction. Sensitivity to *CP* asymmetries suffers significantly if the solid angle for tracking is reduced, for example, from 95% to 85%. This leads to a requirement that the machine components not encroach beyond a ±300-mrad cone, measured relative to the beam direction. This stay-clear region must be maintained to a distance of ±2 m along the beam axis.

One would expect that an experimental program that depends so heavily on vertex detection for its success would require that a layer of vertex detector be at the smallest possible radius. There are many reasons for a small beam pipe radius, such as reducing the cost and improving many physics measurements, but they must be balanced against the fact that the detector backgrounds improve with a larger beam pipe radius. It is therefore fortunate that the measurement of the *CP*-violating asymmetries, which is the experiment motivating the entire facility, does *not* depend critically on this radius. Figure 2-10 shows the relative error on the measurement of sin 2α (using $B^0 \rightarrow \pi\pi$), as a function of the radius of the first vertex detector layer. One sees that providing a beam pipe with a radius in the region of 2–4 cm maintains resolution close to the best case, assuming an energy asymmetry of 3.1 on 9 GeV. (For B_s mixing, the story is somewhat different: Here it is indeed best to have the smallest possible beam pipe radius.)

Detector backgrounds have two deleterious effects: radiation damage to the devices and unacceptable occupancy levels. We have carefully studied the tolerance level for these two effects on the main elements of the detector. These backgrounds arise from two sources, namely, synchrotron radiation photons and lost particles ($e^{\pm}$)—either direct sources of electrons and positrons or those resulting from photon conversions

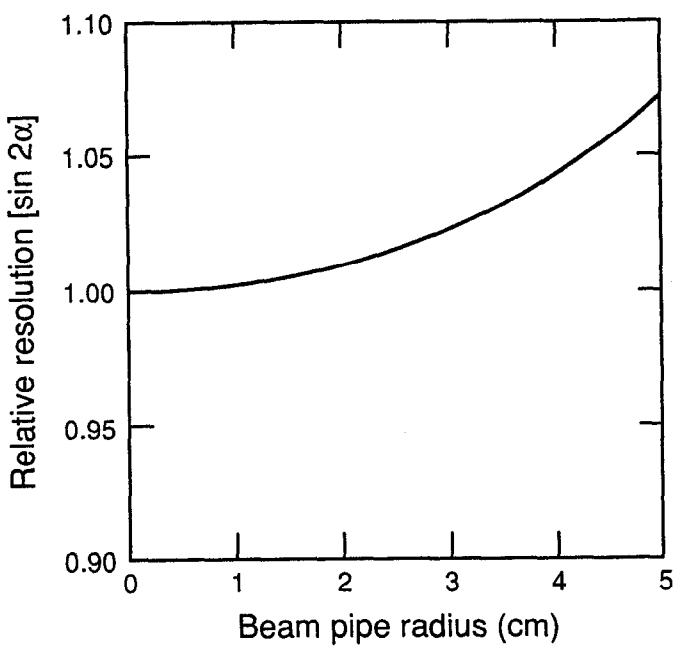

Fig. 2-10. The sensitivity of the measurement error for sin 2α, as a function of the radius of the beam pipe. The resolution worsens slowly as the beam pipe radius (that is, the radius of the first vertex detector layer) increases.

(independent of whether the photons are from synchrotron radiation or bremsstrahlung). Our detailed synchrotron radiation calculations were based on the appropriate photon spectrum, as generated in the background studies (see Section 4.2). Energy-loss mechanisms in the devices were also accounted for.

Tables 2-5 and 2-6 show the tolerance levels of the silicon vertex detector and the central drift chamber for these sources, as they pertain to detector occupancy and radiation damage. For the silicon, we assumed a radiation limit of 100 krads/yr, and for the occupancy limit, we assumed 10% in four strips. For the drift chamber, we took the radiation limit to be 0.5 C/cm of sense wire, and for the occupancy limit, we used 10%. For the calorimeter, we used the most conservative estimate available of radiation

Table 2-5. Silicon vertex detector background limits.

Source	Limit	Flux (particles/cm^2/μs)	Rate (particles/μs)
Synchrotron radiation photons	Occupancy	2	400
	Radiation damage	3	600
Lost particles ($e^{\pm}$)	Occupancy	1	200
	Radiation damage	0.1	20

Table 2-6. Drift chamber background limits.

Source	Limit	Flux (particles / cm^2/μs)	Rate (particles/μs)
Synchrotron radiation photons	Occupancy	1.0	30,000
	Radiation damage	2.0	60,000
Lost particles ($e^{\pm}$)	Occupancy	0.0003	11 (1st sense wire layer)
	Occupancy	0.0003	28 (middle sense wire layer)
	Radiation damage	0.002	50 (1st sense wire layer)

damage limits for CsI: 5 krads/yr. For this limit, the corresponding guideline is to keep the radiation below 10^4 MeV/μs in the barrel region. We see that, in reality, the calorimeter radiation requirements are less stringent than those for the other two devices.

It is against these criteria that the estimates of backgrounds in Section 4.2 must be measured.

2.5 RUNNING SCENARIOS

It is worthwhile in conclusion to summarize the energy settings for the machine that we envision providing the proper balance for the physics program.

The physics running will commence at the Υ(4S); most of the running in the first few years will be at this energy. This running will be interspersed with short (1–3 month) runs on the Υ(1S), Υ(2S), Υ(3S), and Υ(5S) resonances. After sufficient data have been accumulated to establish the *CP* program, a dedicated one-year program could be run at the Υ(5S), the primary motivation being to measure B_s mixing. The interaction region components will likely be reoptimized for this run, so as to obtain a smaller beam pipe radius and perhaps a larger energy asymmetry.

3.

GENERAL DESCRIPTION AND PARAMETER CHOICES

IN this chapter, we give a general overview of the Asymmetric B Factory collider. First, we summarize the performance goals of the collider, based on the physics considerations outlined in Chapter 2. Then, we briefly describe a design that meets these requirements. To carry out the physics program of a B Factory, the luminosity of the facility must be improved by a factor of 30 over that of currently operating e^+e^- colliders. It is clear, of course, that this is a challenging goal, and one that is inherently at odds with maintaining a "conservative" design in all areas. On the other hand, we are convinced that a successful project must take seriously the concept of a "factory," that is, the machine must be designed—insofar as possible—to be highly reliable.

As might be imagined, there are various possible machine configurations that could be considered to achieve our performance goals. Therefore, it is necessary to make certain choices from the outset to focus the design process. Such choices might be based on the advantages (or disadvantages) of a particular site, on the experience and expertise of the design team, or on judgments about the degree of reliability and/or flexibility inherent in particular approaches. To put our parameters in context, we include in this chapter a discussion of the rationale for each of the major choices made in arriving at the B Factory configuration described in this report.

We have restricted ourselves to consideration of a B Factory based upon storage ring technology. At the present time, alternative approaches, such as linac-on-linac or linac-on-storage-ring scenarios, are felt to be more speculative than the approach taken here. For example, the technology of high-power, high-repetition-rate, high-brilliance linacs is still in its infancy. Moreover, it does not appear that these alternative approaches offer significant advantages over the more straightforward approach of extrapolating the relatively well-understood performance of storage rings. This outlook is clearly shared by many other groups worldwide that have actively pursued the design of a B Factory collider, all of whom have based their work on asymmetric storage rings [Funakoshi et al., 1990; Hartill, 1990; Rivkin, 1990; Zholents, 1990].

3.1 DESIGN OVERVIEW

The primary performance goals for the collider, based on the discussion in Chapter 2, are as follows:

- Achieving a peak luminosity of 3×10^{33} cm^{-2} s^{-1} in a reliable fashion
- Operating with an energy asymmetry of about 1:3 in the vicinity of the $\Upsilon(4S)$ resonance, $E_{c.m.} = 10.58$ GeV
- Storing high beam currents (1–2 A) stably and with adequate lifetime
- Maintaining acceptable detector background conditions
- Providing flexibility to accommodate both modifications to the assumed beam-beam interaction parameters and optics changes near the interaction point required by background considerations

The Asymmetric B Factory design described in this report meets all of these requirements. Key features of the design are summarized below:

- Low β_x^* values at the interaction point
- Head-on collisions
- Flat beams ($\sigma_x/\sigma_y = 25$)
- Many bunches ($k_B = 1658$ in each ring)
- Two rings (9-GeV e^- in PEP; 3.1-GeV e^+ in a new low-energy ring)
- Well-cooled, low-impedance vacuum chambers
- Wigglers to control the emittance and damping time of the low-energy ring
- Single-cell, room-temperature RF cavities
- Feedback systems for controlling multibunch instabilities
- A powerful injection system (the SLC linac)

The B Factory collider is an upgrade of the existing PEP ("Positron-Electron Project") collider at the Stanford Linear Accelerator Center (SLAC); its major parameters are collected in Table 3-1. To optimize the physics potential of the facility, we have adopted an *asymmetric* design in which a high-energy electron beam of 9 GeV collides with a low-energy positron beam of 3.1 GeV. We thus require a two-ring configuration, where each beam circulates in its own vacuum chamber and is controlled by independent optical elements, except in the interaction region (IR) where the beams collide. The high-energy beam will circulate in the (upgraded) PEP ring; the low-energy beam will circulate in a newly constructed ring.

Both the high-energy ring (HER) and the low-energy ring (LER) are located in the existing PEP tunnel; a site plan for the facility is shown in Fig. 3-1. The tunnel has a hexagonal geometry and accommodates a ring having a circumference of 2200 m. The

Table 3-1. Main B Factory parameters.

	Low-energy ring	High-energy ring
Energy, E [GeV]	3.1	9.0
Circumference, C [m]	2199.32	2199.32
Emittance, $\varepsilon_x/\varepsilon_y$ [nm·rad]	96.5/3.9	48.2/1.9
Beta function, β_x^*/β_y^* [cm]	37.5/1.5	75.0/3.0
Beam-beam tune shift, $\xi_{0,x}/\xi_{0,y}$	0.03/0.03	0.03/0.03
RF frequency, f_{RF} [MHz]	476	476
RF voltage, V_{RF} [MV]	9.5	18.5
Bunch length, σ_ℓ [cm]	1.0	1.0
Number of bunches, k_B	1658	1658
Bunch separation, s_B [m]	1.26	1.26
Damping time, τ_E/τ_x [ms]	18.4/36.4	18.4/37.2
Total current, I [A]	2.14	1.48
Synch. rad. loss, U_0 [MeV/turn]	1.24	3.58
Luminosity, $\mathcal{L}$ [cm^{-2} s^{-1}]	3×10^{33}	

six straight sections in the PEP tunnel are each 110 m long; this provides generous space not only for the IR but also for the various utility functions (RF, injection, etc.).

Because the PEP tunnel was originally sized to house a second (proton) ring, there is ample room for the LER to be mounted above the HER, as illustrated in Fig. 3-2. This design choice, which leads to equal circumferences for the LER and HER, has several advantages. First, it eliminates the need for the major conventional construction that would result if a smaller-circumference LER were chosen. Second, it permits the same number of beam bunches in each ring, thus avoiding possible concerns about coherent beam-beam instabilities. Finally, the large circumference increases the luminosity lifetime, compared with that in a smaller ring, by storing more particles (which are lost at a constant rate in the beam-beam collisions) for a given luminosity. (To take full advantage of the last benefit, it must be possible to fill the large ring quickly. As we will discuss below, the linac injector available at SLAC is ideal for this purpose.)

Reutilizing the PEP tunnel has the added benefit of making many of the installed utilities available for the B Factory, including power and water distribution, cable ways, etc. This is advantageous not only in terms of costs, but also in terms of minimizing the construction time for the facility. We also intend to reuse essentially all of the existing

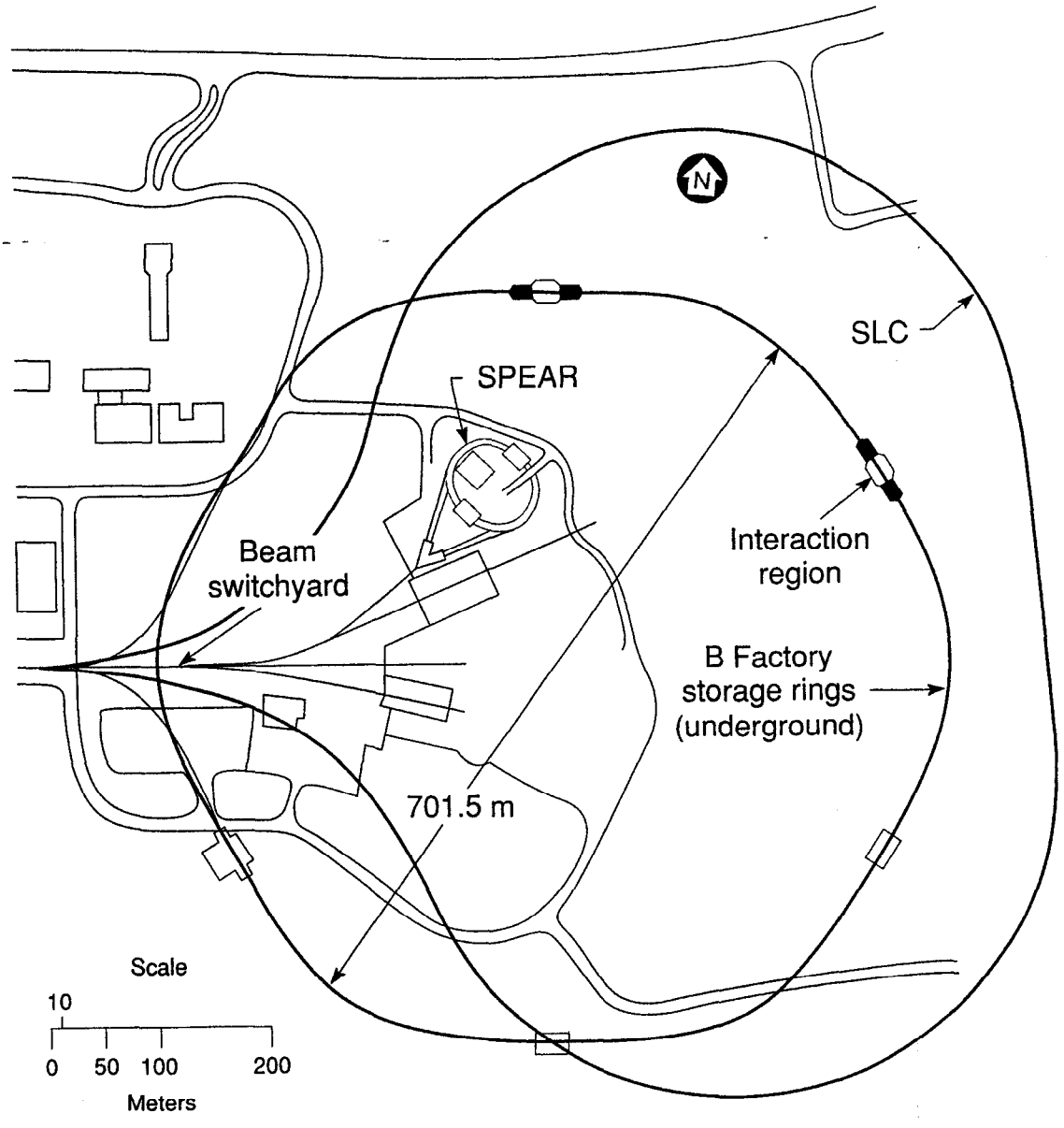

Fig. 3-1. SLAC site plan showing the general configuration of the B Factory. The linac beam enters the rings from the beam switchyard at the left. The SLC arcs are at a different elevation from the PEP tunnel and thus do not intersect it.

PEP magnets for the HER. This too will yield significant cost and schedule benefits, with no compromise on the performance of the B Factory.

PEP was built to operate at beam energies up to 18 GeV; therefore, its magnet parameters are fully compatible with the requirements for the HER of the Asymmetric B Factory collider. For example, the PEP bending magnets have a magnetic radius of ρ = 165 m at 9 GeV, which considerably reduces the synchrotron radiation power emitted by the high-energy beam in the B Factory, compared with that from a smaller ring. Thus, we will be able to maintain a high beam current and a suitable asymmetry without prohibitively high synchrotron radiation power losses. The natural emittance required for

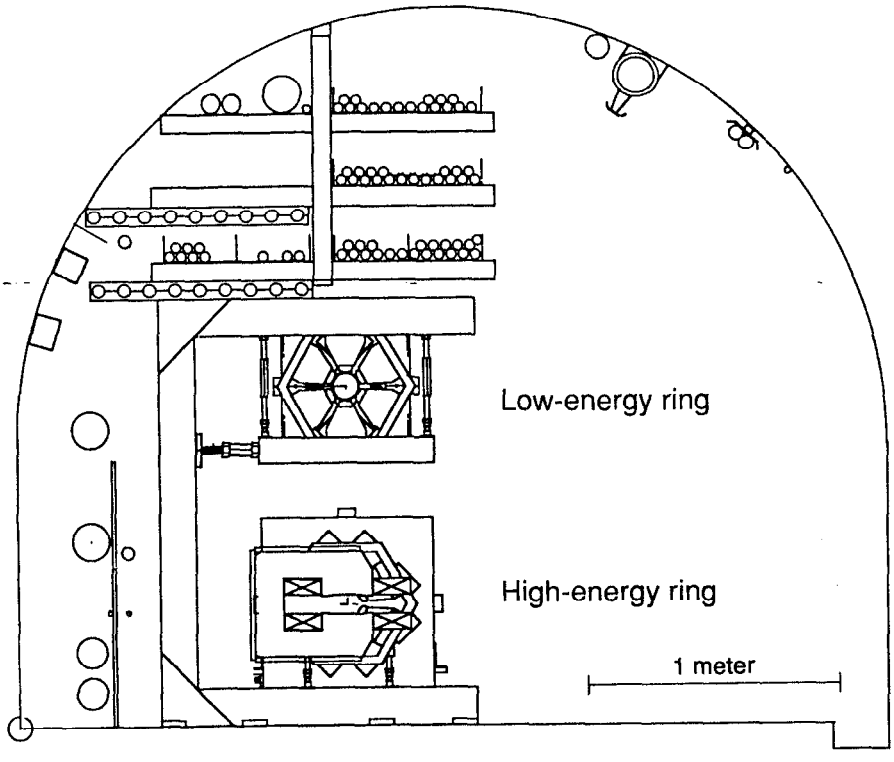

Fig. 3-2. Cross section of the PEP tunnel, showing the locations of the two B Factory rings and installed utilities.

the B Factory HER is essentially that of the standard PEP lattice. Moderate adjustments to the emittance, such as might be dictated by beam-beam considerations, can be accommodated either by mismatching the dispersion function or by trimming the phase advance in one or more sextants of the ring.

In the case of the LER, relatively short (1 m) bending magnets having a magnetic radius of $\rho = 30.5$ m are used. Despite this choice, the natural emittance generated in the ring dipoles alone would be considerably lower than the emittance called for in Table 3-1. To handle this, we make use of wigglers in two straight sections to give us independent control of emittance and damping times. This approach provides a great deal of flexibility to select the operating parameters of the LER in an optimum fashion.

The injection system for the collider is based upon the existing SLC linac injector, as illustrated in Fig. 3-3. It is assumed here that the SLC experimental program will be completed prior to the time the B Factory becomes operational, although it is likely that the injector complex will still play a part in various R&D activities (for example, as injector for the Final Focus Test Beam or, possibly, for a test section of the so-called Next Linear Collider), in addition to its primary role as the B Factory injector. Thus, the SLC damping rings and positron-production target will be available for the B Factory. We will see in Chapter 6 that this combination is very powerful and provides an ideal injector for the B Factory. With the injection system operating at only 10% of routine SLC intensity, the top-up time for *both* collider rings is about 3 minutes.

To summarize, we note that from many viewpoints the PEP site at SLAC is an ideal location for the construction of an Asymmetric B Factory collider:

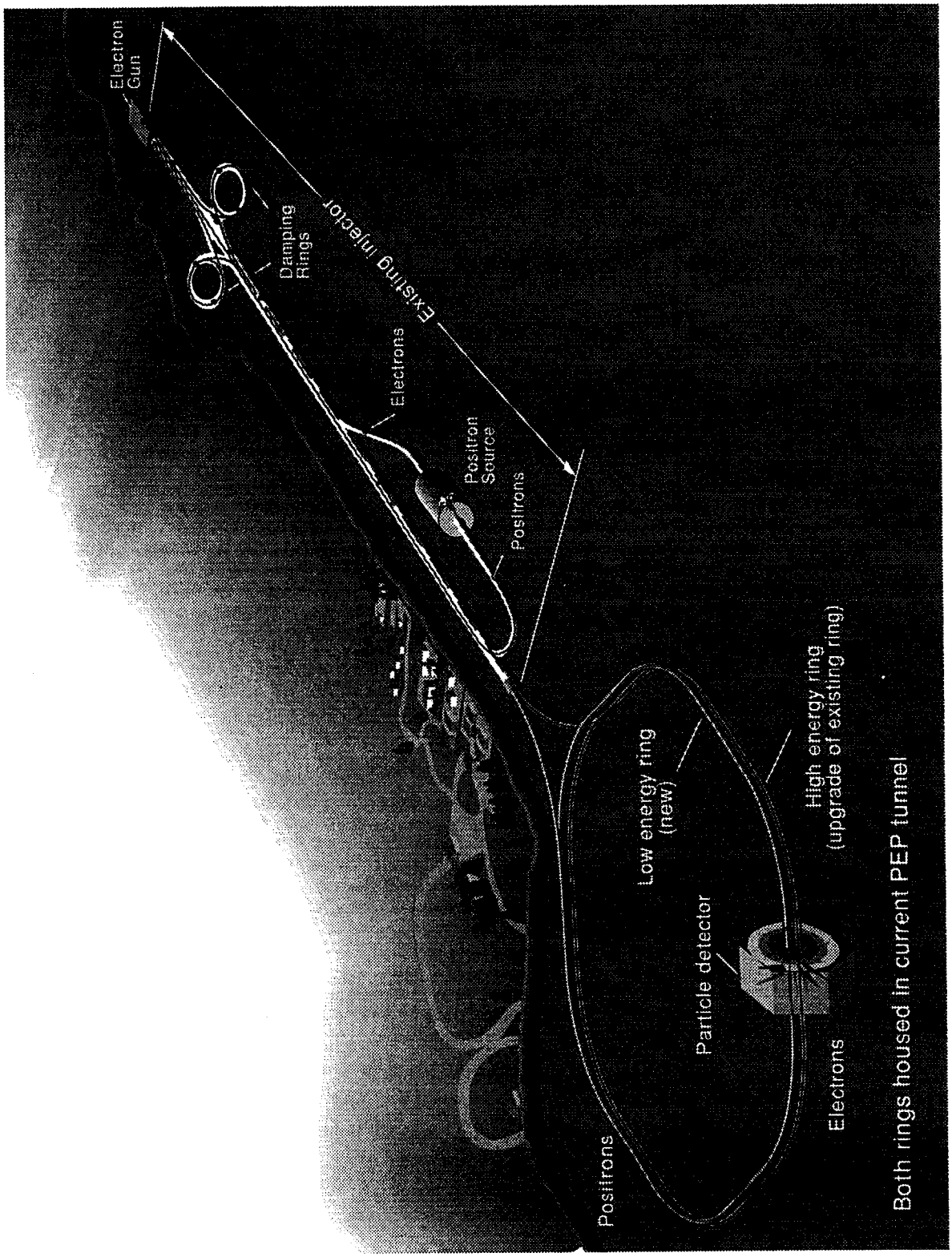

Fig. 3-3. Schematic illustration of the B Factory, showing the existing injector system.

- The availability of a large-circumference tunnel offers maximum flexibility in the choice of collider parameters.
- The existence of a powerful positron injector facilitates rapid commissioning and ensures a high *integrated* luminosity.
- The existing PEP infrastructure permits the rapid construction and commissioning of the facility.

In addition, the considerable accelerator design expertise and engineering strengths of SLAC, LBL, and LLNL will ensure the successful and reliable operation of the facility at its design luminosity.

3.2 LUMINOSITY CONSIDERATIONS

The first four of the key B Factory design features listed earlier are dictated primarily by the luminosity limitations associated with the beam-beam interaction. The physics issues will be discussed in detail later (in Section 4.4), but here we will introduce the topic in the context of parameter choices for the B Factory.

The general expression for luminosity in an asymmetric collider is cumbersome, involving various parameters of both beams at the interaction point (IP). To simplify the choices and to elucidate the general issues of luminosity for any B factory, it is helpful to write the luminosity in an energy-transparent way. In this section, we express the luminosity in terms of a single beam-beam tune shift parameter ξ, common to both beams, along with a combination of other parameters taken from *either* the high-energy (e^-) or low-energy (e^+) ring, irrespective of energy.

With a few plausible assumptions (for example, complete beam overlap at the IP and equal beam-beam tune shifts for both beams in both transverse planes), such parameters as energy, intensity, emittance, and the values of the beta functions at the IP may be constrained to satisfy certain scaling relationships. (Details of this approach are presented in Section 4.4.) It then becomes possible to express luminosity in a simple, energy-transparent form [Garren et al., 1989]:

$$\mathcal{L} = 2.17 \times 10^{34}\, \xi (1 + r) \left(\frac{I \cdot E}{\beta_y^*} \right)_{+,-} \quad [\mathrm{cm}^{-2}\, \mathrm{s}^{-1}] \tag{3-1}$$

where

- ξ is the maximum saturated dimensionless beam-beam interaction parameter (taken to be the same for both beams, and for both the horizontal and the vertical transverse planes).
- r is the aspect ratio characterizing the beam shape (1 for round, 0 for flat).
- I is the average circulating current (in amperes).
- E is the energy (in GeV).
- β_y^* is the beta function at the IP (in cm).

The subscript on the combination $(I{\cdot}E/\beta_y^*)_{+,-}$ means that it may be evaluated with parameter sets taken from either ring.

The scaling relations derived in Section 4.4 were used to produce a self-consistent set of parameters that have been used in this report. After a few basic parameters are chosen, such as the energies, the currents, the aspect ratios, and the lowest beta value at the IP for each ring, most of the other parameters, including the luminosity $\mathscr{L}$, follow. To a certain extent, the choice of which parameters are specified and which are derived is arbitrary. Nonetheless, as discussed below, there are many practical considerations that limit the degrees of freedom in maximizing the luminosity.

Energy. The energies $E_{+,-}$ are not entirely free parameters; they are constrained kinematically. To take advantage of the cross section enhancement at the $\Upsilon(4S)$ resonance, the collider center-of-mass energy must be 10.58 GeV. Precise determination of the decay vertices with a reasonable detector geometry then limits the energy ratio to the range of about 1:3 to 1:5. Simulations of the beam-beam interaction (both our own and those of others [Hirata, 1990]) argue for approximately equal damping times per collision ("damping decrement") in the two rings, which is more easily accomplished when the energy asymmetry is reduced. On the other hand, magnetic separation becomes easier when the energy asymmetry increases. Taken together, these considerations lead to an optimum energy of the high-energy beam of $E \approx 8$–12 GeV, and the corresponding energy of the low energy beam is thus $E \approx 3.5$–2.3 GeV. For the B Factory design, we have adopted energies of $E_- = 9$ GeV and $E_+ = 3.1$ GeV.

Beam-beam tune shift. The beam-beam tune shift parameter ξ is not really a free parameter; it is determined intrinsically by the nature of the beam-beam interaction. The range of maximum beam-beam tune shifts achieved in existing equal-energy e^+e^- colliders is $\xi \approx 0.03$–0.07. We chose a moderate value of $\xi = 0.03$ as the basis of our nominal luminosity estimates. (For simplicity, we assume at this point that the ξ values of both beams, in both transverse planes, are equal. Less restrictive assumptions would lead to a parameter dependence similar to that in Eq. 3-1, as discussed in Section 4.4.) Insofar as considerably higher tune-shift values than this have already been observed at PEP—even with multiple IPs—we consider the value of 0.03 to be reasonable for estimating the performance of an asymmetric collider.

One implication of the tune-shift limitation is that increased luminosity must perforce come from decreasing the bunch spacing s_B, that is, increasing the number of bunches. The push toward small bunch spacing has a significant impact on the design of the IR, which must separate the beams sufficiently to avoid unwanted collisions. (As will be discussed in Section 4.4, including the effects of parasitic crossings makes the ξ value we have adopted less conservative.) The close spacing also exacerbates the problem of controlling coupled-bunch beam instabilities, because it increases the bandwidth requirements of the feedback systems.

There is evidence from computer simulations [Krishnagopal and Siemann, 1990] that the maximum achievable ξ may depend on the beam aspect ratio: $\xi = \xi(r)$. This is a controversial issue, now being debated, but it is known that an enhancement in ξ (for round beams) of at best a factor of two can be obtained. As will be discussed below, there are significant difficulties associated with round beams, having nothing to do with the beam-beam interaction, that make this option unattractive even if the tune-shift enhancement proves to be correct.

Beam Aspect Ratio. The aspect ratio r is free to the extent that one can create round beams. However, the physics of the beam-beam interaction is sensitive to the method (coupling resonances, wigglers, etc.) used to make the beams round. Although the use of coupling resonances is a straightforward way to obtain a round beam, it is not clear that applying such a constraint in tune space—where the nonlinear effects of the beam-beam interaction manifest themselves—is the best thing to do. The use of wigglers or phase-plane rotators offers the potential advantage of producing round beams via a noiselike excitation that should not correlate with the subtleties of the nonlinear tune-space behavior.

In the LER, one could imagine the use of wigglers to create a large vertical emittance corresponding to $r = 1$. In the case of the HER, where the synchrotron radiation emission in the horizontal bending magnets is already very large, the addition of sufficient wigglers (in an intentionally created vertically dispersive region) to produce a round beam is nontrivial, although it is certainly conceptually possible. This technique may, however, be impractical from the viewpoint of synchrotron radiation power. Therefore, optics changes (via skew quadrupoles) would likely be the preferable way to create round beams in the HER.

If there is no increase in the beam-beam tune shift, the maximum enhancement from the use of round beams is a factor of two, that is, $r = 1$ gives $(1 + r) = 2$ in Eq. 3-1. (As discussed below, however, the limit on β_y^* is lower in the flat-beam case, so the geometrical gain does not appear to be realizable in practice.) If the tune shift itself increases, a luminosity improvement by another factor of two might result. Such enhancements potentially permit the same luminosity to be reached with a twofold or fourfold decrease in the required beam current.

The fundamental disadvantage of round beams lies in the optics required to focus them. Near the IP, very strong quadrupoles are required. Because of the magnetic separation scheme, at least one of the beams must be off-axis in the quadrupoles, which results in the production of copious synchrotron radiation very close to the detector. In our earlier attempts [*Feasibility Study for an Asymmetric B Factory Based on PEP,* 1989; *Investigation of an Asymmetric B Factory in the PEP Tunnel,* 1990] to explore the round-beam case, up to 750 kW of synchrotron radiation power was emitted within a few meters of the IP. To handle this power, and the photon background that comes with it, in such a spatially constrained region appears at best to be very difficult.

Flat-beam optics, in contrast, produce an order-of-magnitude less synchrotron radiation power near the IP. In this case a masking and cooling scheme is practical, though still difficult. The flat-beam solution we adopted is described in detail in Section 4.2. It is worth noting here that, even taking account of the possible reductions in beam current enhancements from the use of round beams, the synchrotron radiation power near the IP in the round-beam case would be at least twice that of the flat-beam solution adopted here.

For the flat-beam case, there are some constraints on how low the aspect ratio can be. In the LER, the need to displace the beam vertically in the IR contributes to vertical emittance. For the HER, there is no such limit. In any case, we are concerned that the independent optics in the two rings could lead to a tilt of the two "ribbon beams" at the IP, such that the luminosity degrades quite substantially. The beam separation scheme gets easier if the aspect ratio of the beams is large (due to the lower angular spread of the

beams at the IP), so it is to the designer's advantage to postulate as large a ratio as possible. The Asymmetric B Factory design is based upon an assumed aspect ratio of $r = 0.04$; this value, conservative from the standpoint of ensuring a good collision geometry, makes the requirements on beam separation more stringent. (Because the limit associated with the weak LER vertical bends is only $r = 0.001$, we have considerable margin for improvement. This has *not* been taken into consideration in assessing the efficacy of the separation scheme discussed in Section 4.2.)

Beam Intensity. The average beam current I is a relatively free parameter, but not absolutely so. It is determined by various current-dependent coherent effects. The storage rings must accept the chosen currents, given certain impedances in the paths of the beams. There are several intensity-dependent issues with which we must be concerned:

- Longitudinal microwave instability, which causes individual beam bunches to grow both in length and in momentum spread; both the increased bunch length and the increased center-of-mass energy spread can reduce the effective luminosity
- Transverse mode-coupling instability, which limits the maximum current that can be stored in a single beam bunch
- Touschek scattering, which causes particle loss (from large-angle intrabeam scattering) and reduces the beam lifetime
- Coupled-bunch instabilities, which, unless controlled by feedback, can lead to unstable longitudinal or transverse motion and thus to either beam loss or luminosity loss
- Synchrotron-radiation-induced gas desorption, which can lead to very high background gas pressure and thus to beam losses from gas scattering
- Synchrotron radiation heating of the vacuum chamber wall, which can lead to melting of the chamber if the power density is sufficiently high

As will be discussed in Section 4.3, for our chosen parameters, the first three issues listed above are not expected to limit the performance of the B Factory. Based on our present estimates, the issues of most concern to the B Factory design are coupled-bunch instabilities (driven by parasitic higher-order modes of the RF system), synchrotron radiation heating, and synchrotron-radiation-induced gas desorption. Means to deal with the first issue are discussed in Sections 5.5 and 5.6. Problems arising from the synchrotron radiation emission require innovations in vacuum chamber design; our approach, based on a copper vacuum chamber, is described in Section 5.2. To provide a safety margin and to permit some room for future improvements, we have considered a maximum beam current of 3 A in the design of the vacuum systems for both the HER and the LER.

Beta Function at the IP. The beta function at the IP, β_y^*, is a free parameter and is easily variable down to a few centimeters, subject to the bunch-length condition $\sigma_\ell \leq \beta_y^*$ that arises from considerations of the beam-beam interaction. (Specifically, we wish to avoid luminosity loss resulting from either the increase in beam size away from the IP or the excitation of synchrobetatron resonances.) As the beta functions are reduced, of course, it becomes difficult to reduce the bunch length accordingly. Either the RF

voltage becomes excessive or the IR optics become unmanageable owing to the increased chromaticity. We have taken a bunch length of $\sigma_\ell = 1$ cm, which then restricts the value of β_y^* to the range of 1–3 cm.

It turns out that, for round-beam optics, the chromaticity tends to be about twice that of flat-beam optics. Thus, whatever chromaticity is tolerable in the round-beam case can be reached equivalently with flat-beam optics in which the β_y^* value has been reduced by a factor of two. This means that, in practice, the factor of two increase in luminosity implied by Eq. 3-1 is largely illusory.

From Eq. 3-1, it is clear that the luminosity is maximized with high currents and low β_y^*. What are the implications regarding these parameters for a luminosity goal of 3×10^{33} cm^{-2} s^{-1}? Following a conservative route, we use a typical low β_y^* of a few centimeters (1.5 cm in the LER, 3 cm in the HER), $\xi \approx 0.03$, and flat beams ($r = 0.04$). These choices imply an average circulating current I of several amperes (2.14 A in the LER, 1.48 A in the HER). As mentioned above, those portions of the vacuum chambers that would be difficult to upgrade later in the project have been designed to handle up to 3 A of beam current.

As a final point, we note that, for the initial phase of the project, we have adopted a design based upon a head-on collision geometry. This configuration has been employed successfully in many colliders and is therefore felt to be a prudent choice. It is likely, however, that detector backgrounds could be reduced by going to a nonzero crossing angle geometry in which the bunches are tilted transversely with respect to their direction of motion (a so-called "crab-crossing" scheme) to avoid the excitation of synchrobetatron resonances. To permit reaching higher luminosity values in the future, therefore, we do not wish to preclude this alternative now. Fortunately, because the separation scheme adopted here operates in the horizontal plane, the proposed layout lends itself quite well to later modification to a crab-crossing scheme. This possibility, discussed in Appendix B.2, is *not* part of the present project but could be considered as a future upgrade.

3.3 RF CONSIDERATIONS

There are two important choices to be made in the design of the RF system: frequency and technology (room temperature vs superconducting). The issues involved are discussed below.

3.3.1 Choice of Frequency

The choice of frequency is influenced by a number of intertwined issues. We have already discussed the need for obtaining short bunches, $\sigma_\ell = 1$ cm, to avoid a loss in luminosity. To obtain short bunches, it is necessary to increase the longitudinal focusing of the RF system, which can be accomplished with either additional voltage or higher frequency. Indeed, in the limit where the applied voltage is large compared with the synchrotron radiation energy loss (that is, $\cos \phi_s \rightarrow -1$), the two parameters are essentially equivalent and $\sigma_\ell \propto (V_{RF} f_{RF})^{-1/2}$.

The aperture of the accelerating cavities must be sufficient to avoid reducing the beam lifetime and to avoid introducing excessive transverse beam impedance into the ring. In practice, these constraints limit the choice of frequency to only a few frequency "islands" ($f \approx 350$ MHz and 500 MHz) for which high-power (1 MW) klystrons are commercially available. Because we must provide 1-cm bunches, we find that—even with equal apertures—the upper frequency range, near 500 MHz, offers lower power and lower cost; it is thus the preferred choice.

To pick the exact frequency, we must bring in additional considerations. The injection system timing requirements are best handled by having the linac and storage ring RF systems phase-locked, which is most easily accomplished if the two frequencies are harmonically related. The advantage of phase-locking the two RF systems is expected to show up primarily in the feedback system requirements. Any phase jitter at injection will initiate oscillations that must be controlled by the longitudinal feedback system. Such injection jitter can easily dominate the feedback system design, in the sense of determining the power required by the system. Because the SLAC linac operates at a frequency of 2856 MHz, the possible harmonically related choices are 357 MHz and 476 MHz. As mentioned, we prefer a higher frequency to reduce the voltage requirement, so we have adopted 476 MHz for the Asymmetric B Factory RF system.

3.3.2 Choice of Technology

The choice of room-temperature or superconducting RF is also a complicated issue. Given the parameters of the Asymmetric B Factory, superconducting technology would not be of much benefit in reducing the power requirements of the facility. Even for room-temperature cavities, only about one-third of the RF power will be dissipated in the walls, and the power associated with cryogenics for a superconducting RF system would consume a significant fraction of the potential savings. Thus, the choice is not dominated by operating cost considerations.

The potential benefit of a superconducting RF system is that it can provide a high voltage with relatively few cavities. This is important because the most serious beam instabilities in the B Factory (the coupled-bunch instabilities; see Section 4.3) are driven primarily by the higher-order-mode (HOM) impedance of the RF cavities. Reducing the number of cavities lowers the instability growth rates proportionately, which in turn reduces the feedback system power requirement quadratically (unless the power is already limited by injection jitter).

As mentioned, in the case of a B Factory, the RF power requirements are dominated by beam loading; that is, the majority of the power put into a cavity goes to the beam itself, even in the case of a room-temperature system. The limit on the number of cavities, then, is dictated by the power-handling capability of the RF input coupler. In the B Factory design, a 20-cavity room-temperature RF system requires nearly 500 kW per cavity, of which about two-thirds goes into the beam. If the difficulty of designing a reliable high-power input coupler were the same in a superconducting environment as it is in a room-temperature environment, then the number of cavities could possibly be reduced by one-third in the superconducting case. A moderate derating of the input

power capability in the (presumably more difficult) superconducting case, however, would lead to roughly equal numbers of cavities in the two scenarios.

A difficulty with superconducting cavities that requires new technology arises from the need to remove the HOM power deposited in the cavity by the high-current beam. For the room-temperature case, solutions for this problem have been demonstrated in test cavities and can be implemented in a reasonably straightforward manner (see Section 5.5). The problem of removing hundreds of kilowatts from the cryogenic environment, however, has not been solved. At present, the Cornell RF group [Padamsee et al., 1990] is working on this problem, and it may be solvable with suitable R&D.

On balance, superconducting RF technology for a high-luminosity collider seems to require a significantly larger performance extrapolation than does room-temperature technology, and it is not judged by us to be a sufficiently mature platform on which to base a "factory" at present. Therefore, the present proposal is based on a conventional room-temperature RF system, as described in Section 5.5.

3.4 RELIABILITY CONSIDERATIONS

The physics requirements for the Asymmetric B Factory are associated with a large *integrated* (as opposed to peak) luminosity. Therefore, it will be necessary to pay attention to reliability issues from the outset. Several approaches can be used to improve the reliability of the facility:

- Provide safety margins in the initial design parameters
- Design the control system to facilitate failure diagnosis
- Design the hardware in a modular fashion to facilitate repairs
- Maintain adequate spares
- Use a powerful, fully automated injection system to recover quickly from beam loss
- Design the detector for rapid turn-on and turn-off during injection

All of these approaches will be taken for the B Factory collider. As a goal, the collider will be designed to be in collision mode 85% of its scheduled operating time. Initial guidelines for the allocation of operating time are as follows:

Filling or top-up	5%
Detector switch-on, switch-off, tune-up	5%
Scheduled and unscheduled maintenance	5%
Collisions	85%

While we recognize that it will not be possible to reach this goal immediately, it is clear that highly reliable operation of a B Factory mandates a careful and conservative design approach. This has been our guideline for the design presented here.

4.

COLLIDER DESIGN

IN this chapter, we describe the physics designs of the two storage rings that make up the B Factory. The concepts described here have evolved over the past several years and are based on numerous interactions among the lattice designers, detector designers, and engineering staff. More than has been true for most past colliders, the B Factory design has, from the outset, focused heavily on the issues of flexibility and reliability. In addition, it was recognized that the success of the B Factory project, measured in terms of its ability to produce the requisite physics data, would depend on special attention being paid to the machine-detector interface. The issue of background suppression is so central to the project that it quite strongly influenced the lattice design.

In what follows, we first describe the lattice designs themselves and the beam focusing and separation solutions we have adopted. Thereafter, we describe the detailed background and masking studies we have undertaken. The design we have arrived at has considerable safety margin in terms of expected vs tolerable background levels, based on careful and systematic examination of all background sources. Because of the high beam intensity required for the B Factory, it is important to examine the influence of collective effects on the ring performance. These are discussed in Section 4.3. Our choice of many relatively low-current bunches results in there being no single-bunch thresholds that lead to performance limitations. Coupled-bunch instabilities are important, however. We have developed means to deal with this problem by damping the cavity HOMs and by feedback. These solutions are described in Sections 5.5 and 5.6. Beam lifetimes have been examined for both rings and found to be acceptably long. Because we wish to achieve a very high luminosity, we have looked carefully at the performance limitations imposed by the beam-beam interactions. Detailed results of our simulations appear in Section 4.4.

4.1 LATTICE DESIGN

4.1.1 High-Energy Ring

The design of the lattice for the high-energy ring (HER) has been influenced by the following criteria:

- It must meet all the conditions necessary to obtain the desired luminosity of 3×10^{33} cm^{-2} s^{-1}. These conditions require that the beta functions at the collision point be correct; that the horizontal emittance, energy spread, and momentum compaction factor be brought to their proper values; and that the dynamic aperture of the ring be adequate.
- It must fit in the PEP tunnel, leaving space for existing services and enough aisle space for the passage of magnet trolleys, etc., and it must have the correct circumference for the chosen RF frequency and harmonic number.
- It must be arranged in the tunnel such that it is easily supported and aligned.
- It should be designed such that existing PEP components and services are used as much as possible (provided that the design is not compromised by doing so).

The lattice we have adopted meets all the criteria outlined above. In Fig. 4-1 we show a layout of the PEP tunnel. The straight sections of the hexagonal ring are labeled according to the clock. (The straight sections have even numbers, and the arcs connecting them are odd-numbered regions.) Figure 4-2 shows the lattice functions of the HER, β_x, β_y, and D_x, starting and ending at the center of the straight section in region 8. Collisions take place in the center of the straight section of region 2, which is shown in the center of the figure. In the straight section of region 8 (and also in region 6) the beta functions are seen to be somewhat uneven. This is because these straights are used to adjust the betatron tunes of the lattice. In arcs 9, 5, 7, and 11, the horizontal dispersion function is mismatched. This (controllable) mismatched dispersion function is used to adjust the horizontal emittance of the beam. Region 10 is the injection straight where the beta functions are tailored to optimize the injection process. Arcs 1 and 3 have a regular dispersion function to make it easier to match the chromatic properties of the interaction region by adjustment of sextupoles. The design of the lattice is modular, and the individual modules can be adjusted with little or no effect on the remainder of the lattice. The basic modular building blocks of the lattice are regular arcs, dispersion suppressors, and straight sections. Details of each of these lattice modules are discussed below.

4.1.1.1 Choice of Cell Length. Before design can start in earnest, the length of the standard arc cell must be chosen. One obvious choice of cell length would have been to leave the layout of the ring components exactly as it is in PEP, so that PEP essentially becomes the HER. Consideration of this possibility, however, showed that such a layout

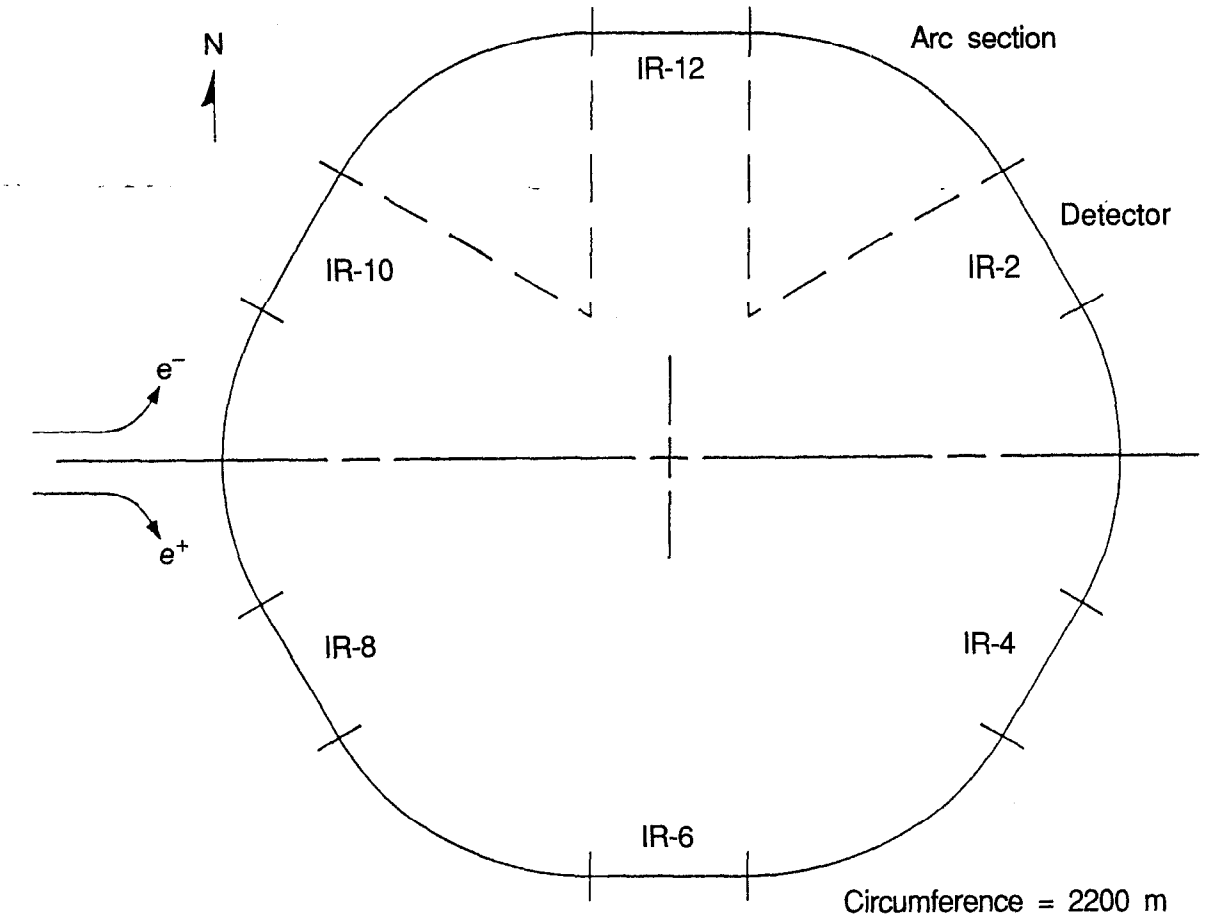

Fig. 4-1. Layout of the PEP tunnel. The numbering system follows the clock, with the straight sections being even numbers; IR = interaction region.

would not suffice and that the cell length would have to be changed. There are three factors that enter:

- The HER is located closer to the tunnel floor than the PEP ring, so that the low-energy ring (LER) can be mounted above it while still providing sufficient space for cable trays, etc. Therefore, the present support structure will have to be replaced.
- The circumference of the ring has been changed to match the new RF frequency chosen for the B Factory. The circumference of PEP is 2200.0004 m, whereas the B Factory HER circumference will be 2199.318 m. The harmonic number of the HER is 3492, compared with 2592 for PEP.
- The new (copper) vacuum chambers cannot be fabricated in sections as long as the PEP (aluminum) chambers, so extra space is needed for additional flanges. Therefore, the cell length must be longer than the present 14.35 m of the PEP cell.

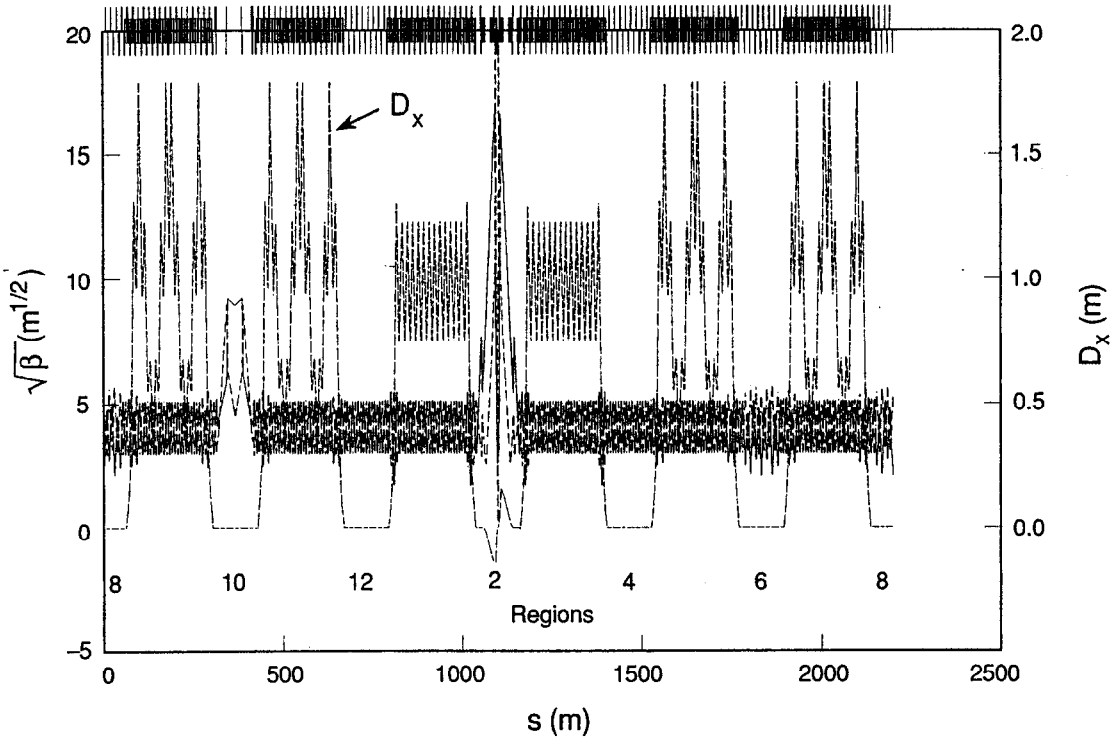

Fig. 4-2. Lattice functions $\sqrt{\beta_x}$, $\sqrt{\beta_y}$, and D_x (horizontal dispersion function) for the complete HER, starting at region 8. The collision region (region 2) is shown in the center of the figure.

To accommodate the longer cell, we must remove the short (symmetry) straight sections located at mid-arc in the present PEP lattice. A half-sextant of PEP is made up of a long straight section of just over 60 meters, followed by an arc section and terminated by a short straight section of about 2.5 meters. This short straight section was used as a utility straight and was tailored to the needs of PEP. For the B Factory, however, the utilities are more usefully placed in the long straight sections.

PEP has 192 main dipole magnets, 16 in each half-arc, 2 per standard FODO cell. Keeping this structure, a range of cell lengths was investigated for two different types of dispersion suppressor. The missing-magnet type of dispersion suppressor was found to be unsuitable for the HER, because the "gap" in the bending makes the central orbit too different from the present PEP central orbit, giving layout problems in the tunnel. A dispersion suppressor consisting of two cells, each of approximately 90° phase shift gave an acceptable geometry for the beam orbit. These cells must be slightly longer than the regular cells to match both the beta functions and dispersion function properly.

A computer code was developed to plot the deviation of the central orbit of the beam relative to the central orbit of a smooth version of PEP. (A "smooth PEP" consists of straight sections of the appropriate lengths sandwiching an arc of constant radius.) The results of the survey of cell lengths are shown in Fig. 4-3.

In Fig. 4-3, three parameters are plotted as a function of cell length: The straight lines, labeled "mid-arc" and "mid-straight," show the deviation of the orbit from the smooth PEP orbit at the symmetry point (mid-arc) and at the original PEP interaction

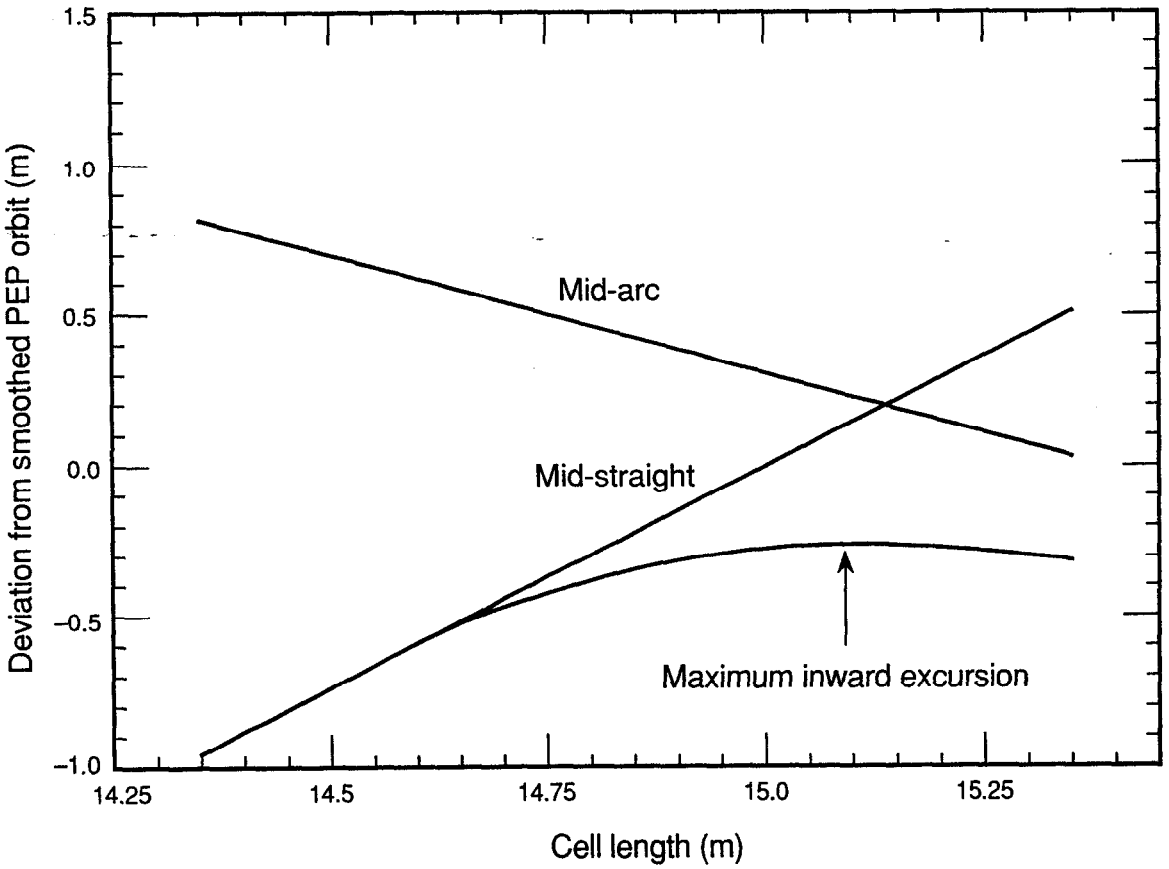

Fig. 4-3. Results of computations to find the optimum length for the regular arc cells. The radial displacement from the smooth PEP orbit is plotted as a function of cell length. The displacement is plotted for mid-straight, mid-arc, and the greatest excursion inside the PEP orbit.

point (IP, in the center of a long straight section). The curve shows the maximum deviation of the orbit in the arc toward the inside of the smooth PEP orbit. It is seen that a cell length of 15.125 m gives an orbit closest to the original PEP orbit and thus minimizes layout problems in the tunnel. This cell length is also long enough to meet the spatial requirements given by mechanical engineering considerations and is thus a good choice on that basis as well.

With this choice of cell length, the long straight sections can be segmented into eight cells of the same length as the regular arc cells. The various cell lengths of the HER modules are summarized in Table 4-1.

The geometry of a normal sextant of the HER is shown in Fig. 4-4, where the ordinate denotes the radial position of the beam orbit relative to the smooth PEP orbit. The curve close to the zero position is the actual PEP orbit, the small wiggles being due to the nonuniform bending in a PEP cell (due in turn to the fact that the dipoles occupy most, but not all, of the length). The other curve shows the deviation of the orbit of the HER from the smooth orbit. At the ends (symmetry points in the arcs), the HER orbit is just over 20 cm outside of the smooth orbit; in the long straight section (center section of the plot), the orbit is just less than 20 cm outside the PEP orbit; and in the arcs, the orbit

Table 4-1. Lengths of HER lattice modules.

Module	Cell length (m)
Arc	15.125
Straight section	15.125
Dispersion suppressor	16.013

comes inside the PEP orbit by about 26 cm. With this layout for the HER, there is enough clearance on the inside for the existing PEP services, and there is enough space in the outer aisle for magnet trolleys to pass.

4.1.1.2 Normal Sextant. A phase shift of 60° per cell was chosen to obtain a beam emittance slightly below the emittance required for the design luminosity. As will be

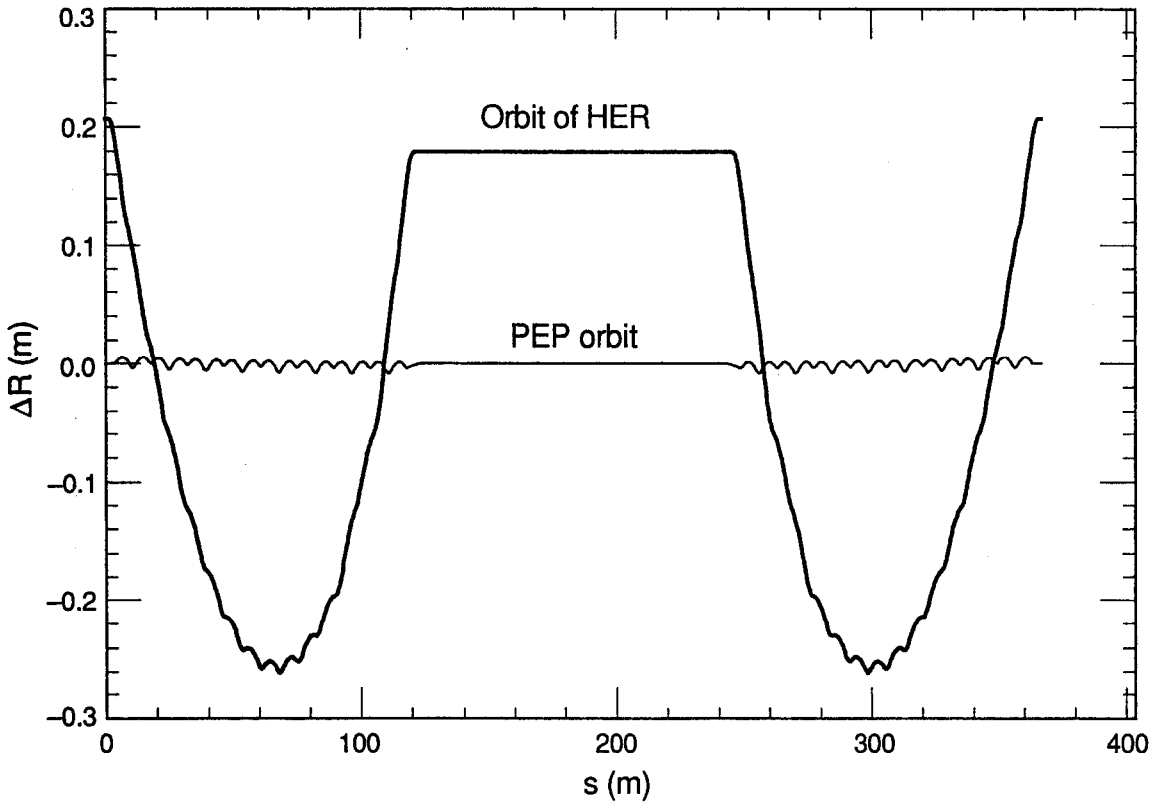

Fig. 4-4. Geometry of the HER orbit in the PEP tunnel relative to that of a smooth PEP orbit. The radial displacement of the orbit is plotted as a function of distance along the orbit from mid-arc to mid-arc. Negative ΔR values correspond to being inside the smooth PEP orbit. A different geometry applies in the special case of the collision sextant (cf. Fig. 4-13).

discussed shortly, the emittance can be changed, in a controlled fashion, above and below the design value. The phase advance of 60° per cell is also optimal for the control of the chromatic properties of the lattice by sextupole compensation. The lattice functions for a normal sextant are shown in Fig. 4-5. It can be seen that the lattice is quite well-matched; the dispersion function is zero in the straight section and the beta functions are regular throughout, except for a small beating in the dispersion suppressor cells. Beta function values are moderate in the straight section, making it a suitable place for locating the RF accelerating cavities.

4.1.1.3 Emittance Control Sextant. The HER beam emittance is controlled by adjusting the dispersion function at the position of the main dipoles, where most of the synchrotron radiation is generated. It is, of course, possible to have a portion of the lattice with a phase shift per cell different from 60°. (As the phase shift per cell decreases, the dispersion function increases and therefore the emittance increases.) Adjustment in this fashion is workable, but has the disadvantage of increasing the

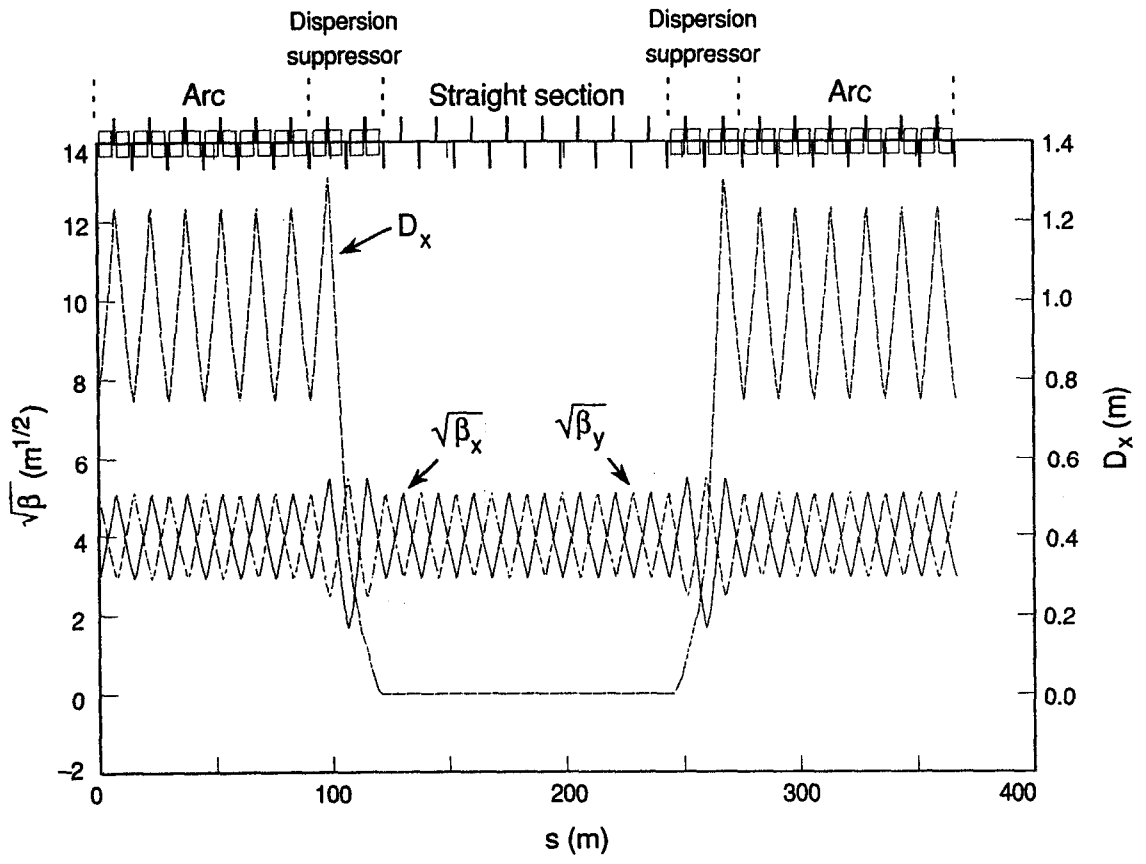

Fig. 4-5. Lattice functions for a normal sextant of the HER, plotted as a function of position in the sextant, from mid-arc to mid-arc. Dispersion is matched to zero in the straight sections.

momentum compaction factor α. This means that additional RF accelerating voltage would be needed to maintain the desired 1-cm bunch length. Instead of this phase adjustment, we have chosen to use a mismatched dispersion function in the arcs of four of the six sextants. Similar to an orbit bump, the dispersion mismatch is confined to the arc, with the dispersion in the adjoining straight sections remaining at zero. Although the average value of D remains unchanged by this modulation, it is the square of the dispersion function that determines the increase in emittance. Figure 4-6 shows an emittance control sextant that is mismatched sufficiently to increase the emittance from 40 nm rad to 48 nm rad. (In reality, there is no sextant exactly like the idealized version in Fig. 4-6, because the straights adjoining these arcs are all special.) The modularity of our lattice design allows "plugging in" sections in a mix-and-match manner without having to do any lattice rematching, apart from possibly having to restore the betatron tune.

4.1.1.4 Injection Sextant. The injection sextant provides lattice functions suitable for the injection scheme presently envisaged, and it provides great flexibility in adjusting the lattice functions to whatever is required to optimize the injection process. Figure 4-7 shows a nominal design having beta functions of 80 m in the horizontal plane and 20 m in

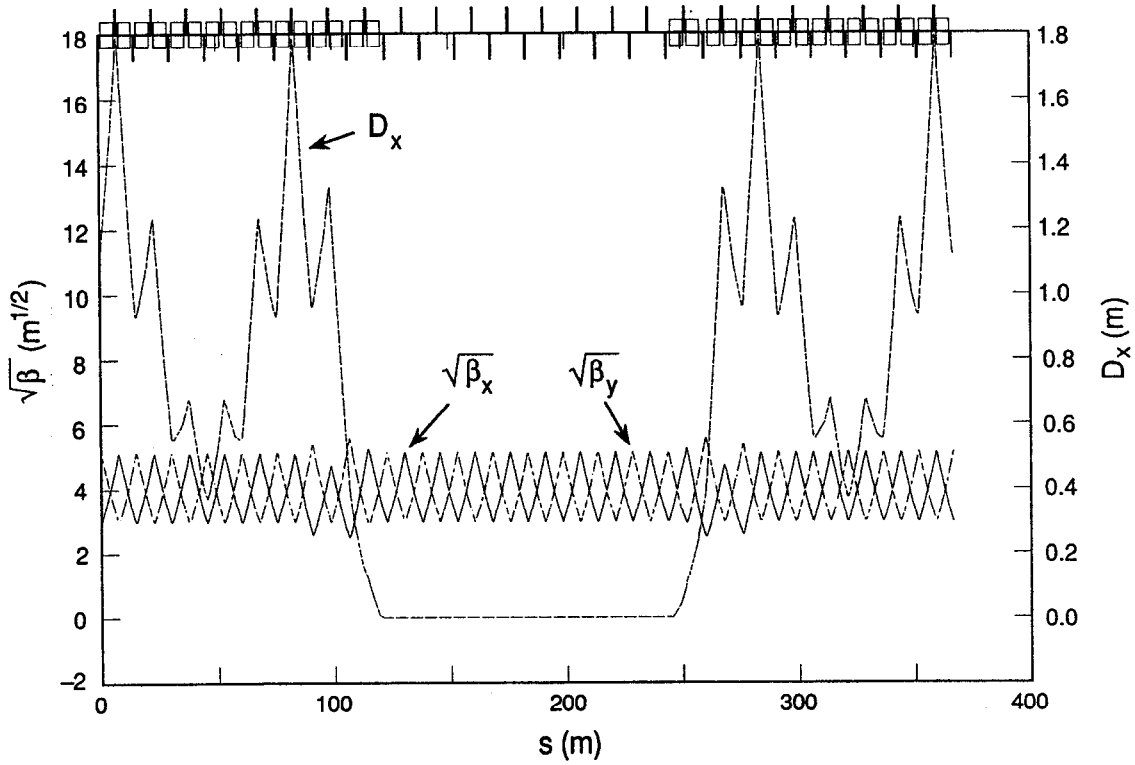

Fig. 4-6. Lattice functions for an emittance control sextant of the HER. The dispersion function mismatch is confined to the arcs, the dispersion function being zero in the straight section.

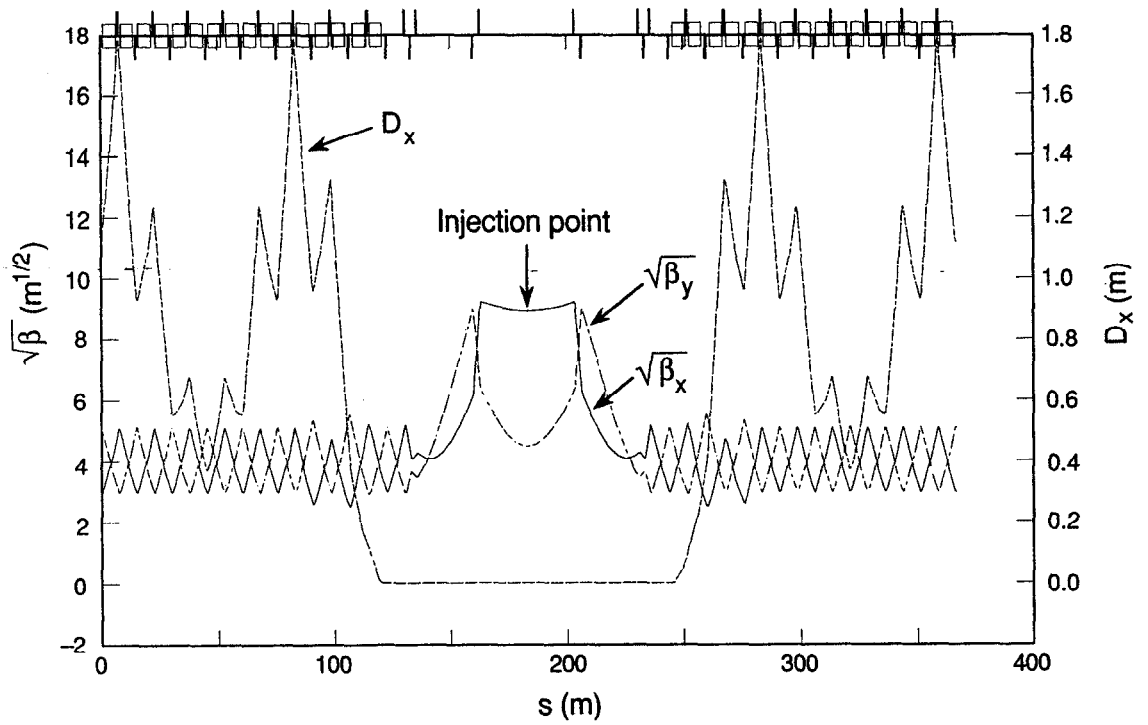

Fig. 4-7. Lattice functions for the injection sextant of the HER. The beta functions at the injection point in the center of the straight section are adjustable. Nominal values correspond to $\beta_x = 80$ m, $\beta_y = 20$ m.

the vertical plane. If another injection scheme were considered, the appropriate lattice module could be very quickly fitted into the straight section.

4.1.1.5 Phase Control Sextant. The straight sections of two sextants will be used to change the betatron tune of the HER. Even a single phase-control sextant would probably have enough range to be acceptable, but the choice of two sextants improves the beta functions at the extremes of the required tune range. The phase control straight sections are located in regions 6 and 8. The optical functions of a phase control sextant are shown in Fig. 4-8.

4.1.1.6 Interaction Region Sextant. The IR sextant is very special and is considerably more complicated than the other sextants. The IR, described in Section 4.1.2, is at its center. The arcs on either side have matched dispersion functions so as to facilitate the correction of chromatic aberrations produced by the IR focusing. Between the IR and the arcs are the matching elements. The matching of the HER is fairly simple owing to the fact that the ring lies in a plane (that is, there are no vertical bends). The lattice functions for the collision sextant and right-hand half-sextant are shown in Figs. 4-9 and 4-10, respectively. In Fig. 4-9 notice the antisymmetry of the dispersion function caused by the S-bend geometry.

Figure 4-11 shows the first 10 m from the interaction point (IP). The dipole B1 initiates the separation of the beams, the separation being aided by the offset quadrupoles

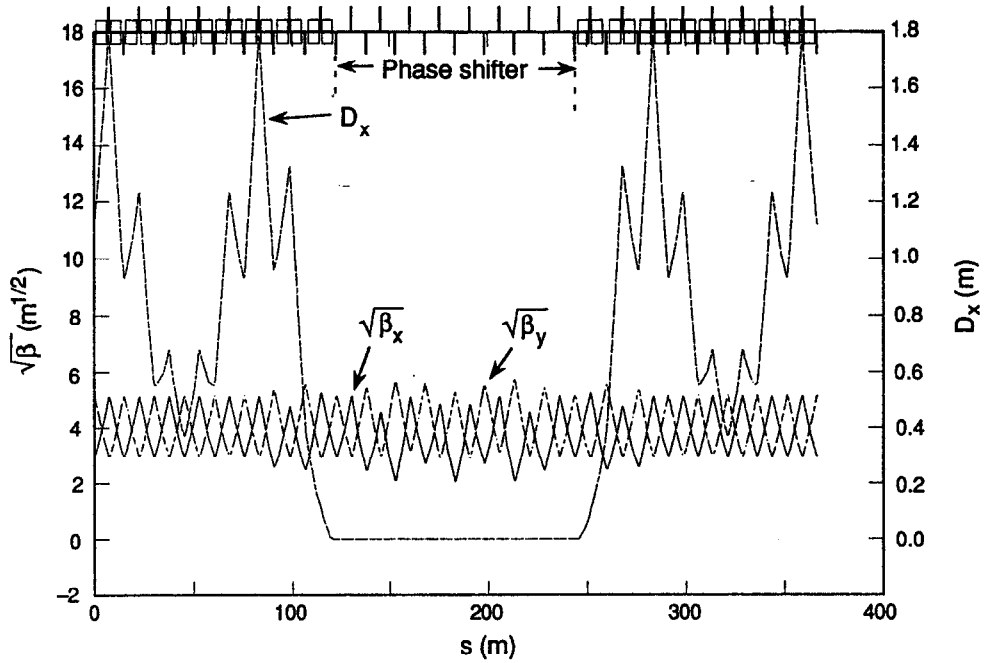

Fig. 4-8. Lattice functions for the phase control sextant of the HER. The beta functions are almost regular in the straight section where the phase shifter is located.

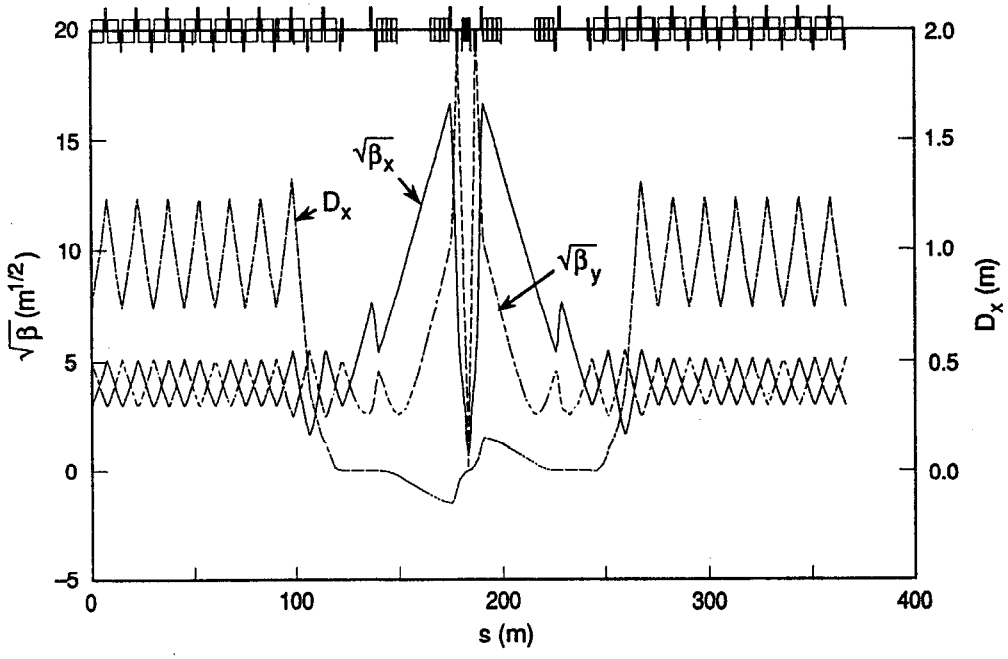

Fig. 4-9. Lattice functions for the collision sextant of the HER. Note the symmetry of the beta functions and the antisymmetry of the dispersion function in the straight section.

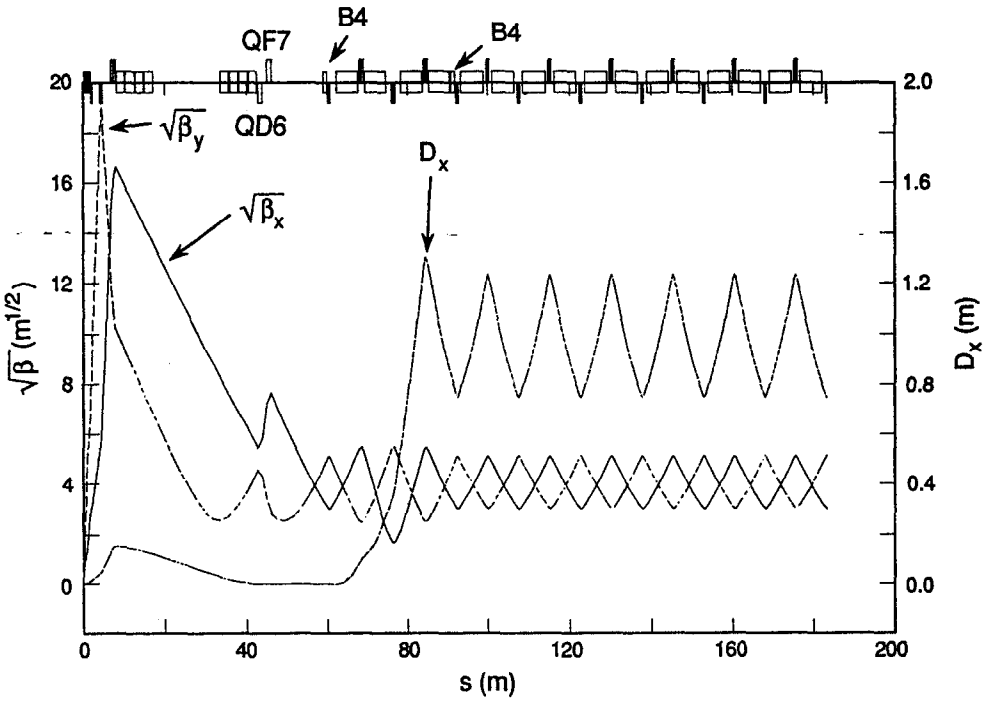

Fig. 4-10. Lattice functions for the right-hand half of the collision sextant of the HER. The B4 magnets that steer the orbit into the arcs are shown here.

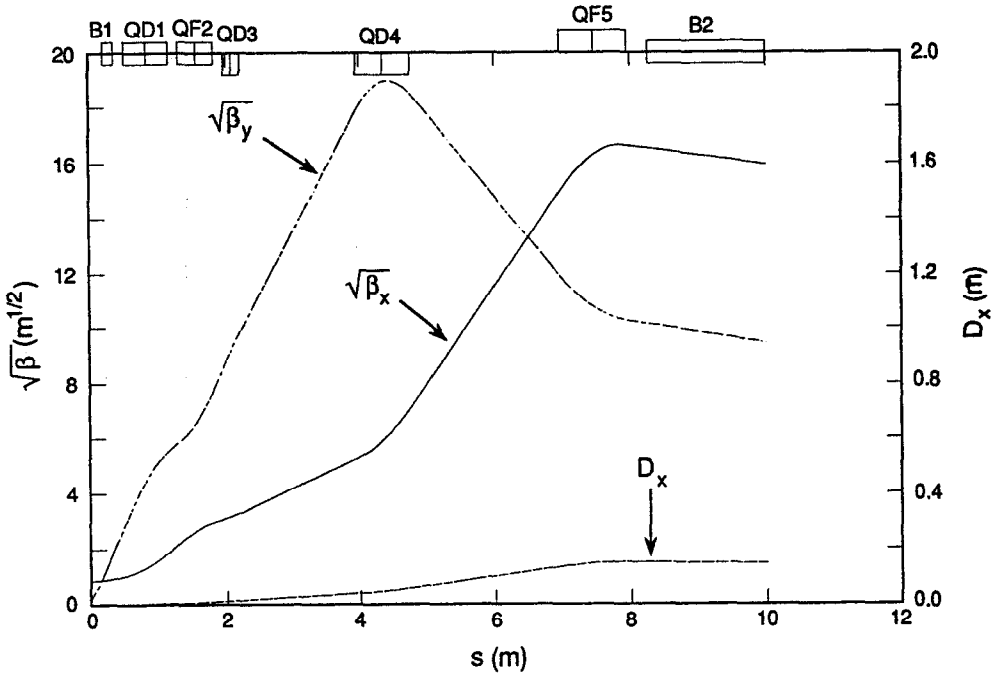

Fig. 4-11. Lattice functions for the first 10 m of the IR straight section of the HER. Note the prefocusing of the beta functions of the HER by the first triplet.

QD1 and QD3. Quadrupole QF2 actually hinders the separation somewhat, but is necessary for the horizontal focusing of the low-energy beam. Quadrupole QF2 is centered on the low-energy beam and thus acts as a combined-function dipole for the high-energy beam; it is thus shown in the figure as a dipole. Quadrupole QD1, although centered on the high-energy beam, is tilted with respect to it and therefore bends the beam slightly (essentially a mini-S bend). As a consequence, it too is shown as a dipole. The quadrupoles QD1, QF2, and QD3 are common to both beams. Their primary purpose is to focus the low-energy beam, but they also have a quite useful focusing effect on the high-energy beam, reducing considerably the beta functions at the high-energy beam focusing elements QD4 and QF5, compared with the values they would have had in the absence of the prefocusing.

QD4 is the first of the high-energy beam focusing elements. It is a septum quadrupole, vertically focusing for the high-energy beam while acting as a field-free region for the low-energy beam. This is a strong quadrupole with a large aperture requirement. Both a superconducting and a conventional design are being considered, as discussed in Section 5.1.3.

As Fig. 4-11 shows, QD4 and QF5 serve to turn over the beta functions coming from the IR and reduce the slope of the dispersion function to near zero. The dispersion function produced by the bending in the IR should be corrected before matching the IR into the arc region. (Strictly speaking, this is not necessary, but to keep the design modular it is advantageous to insist on it.)

Figure 4-12 shows the 60 m from the IP to the start of the arc (that is, to the entrance of the dispersion suppressor). The dispersion function and its slope are brought to zero

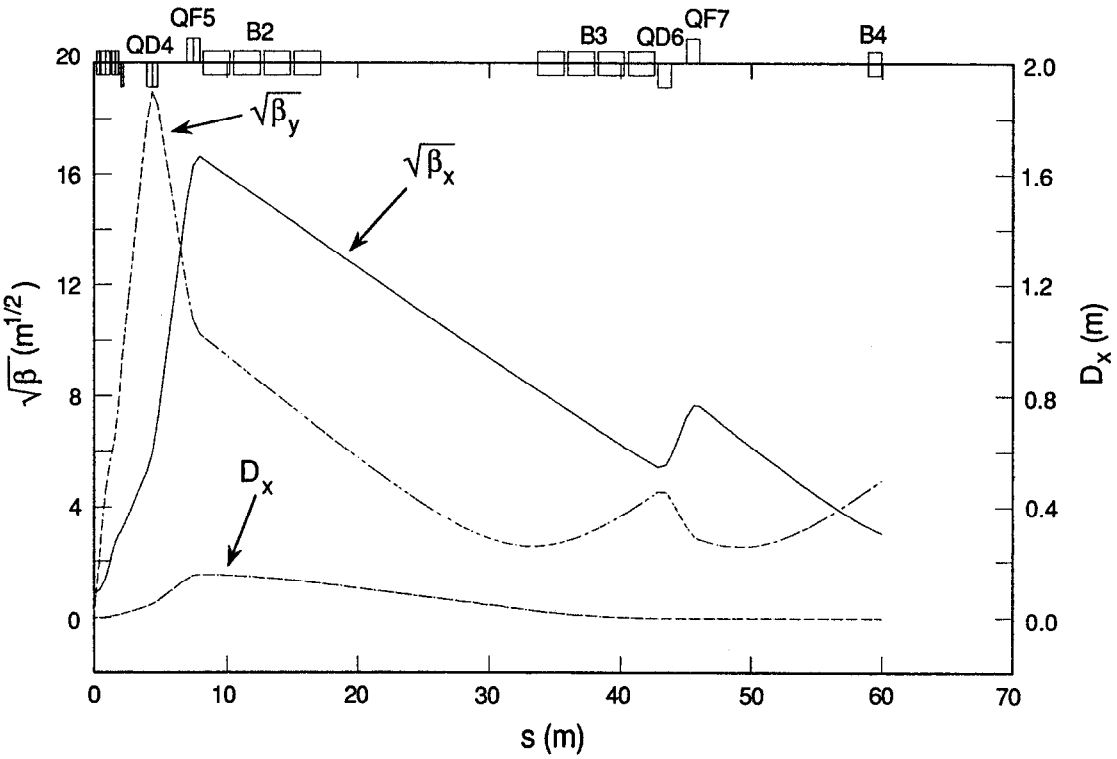

Fig. 4-12. Lattice functions for the first 60 m of the IR straight section of the HER. The B2 and B3 dipoles match the dispersion function to zero.

by the dipole combination B2 and B3. These are very weak dipoles, each made up of four of the PEP low-field bends. The bending is purposely kept very weak to avoid problems with synchrotron radiation shining into the IR. The dipoles B2 and B3 are followed by a pair of matching quadrupoles QD6 and QF7 that, in conjunction with QD4 and QF5, match the beta functions into the dispersion suppressor.

The dispersion suppressors in the arcs adjacent to the IP are slightly different from the others. There is a pair of small dipoles, B4, situated 180° apart in betatron phase (see Fig. 4-10), that match the angles of the orbits from the IP to the arcs. These pairs of dipoles on the two sides of the IP are powered antisymmetrically, as is the B1 dipole. The quadrupoles QD1, QF2, and QD3 are also offset antisymmetrically. The B4 dipoles make an adjustment to the beam trajectory such that the center of the IP lies at the point where the center of the straight section of a normal sextant would be. The angle of the high-energy beam at the IP is not zero with respect to this line, however. The LER has to match the angle of the low-energy beam to this same angle, 13.5 mrad. The IR geometry is illustrated in Fig. 4-13.

4.1.1.7 Dispersion Suppressors. The dispersion suppressors consist of two 90° cells, each slightly longer than the regular cells. All five quadrupoles of the suppressor are independently adjustable to give flexibility in matching, although two pairs are almost identical in strength. As mentioned, the dispersion suppressors surrounding the IR have additional dipoles B4 in them to adjust the position of the IP. Dispersion suppressors in

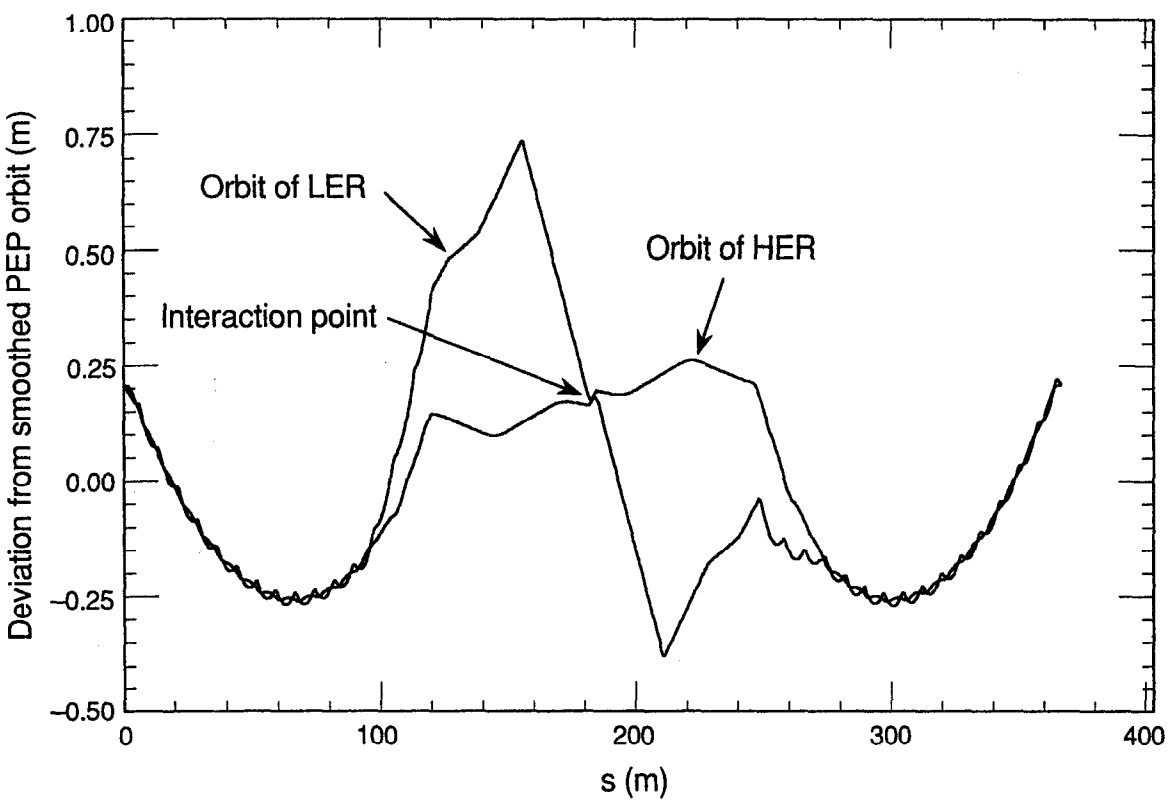

Fig. 4-13. Geometry of the collision sextant, showing how the orbits of the LER and HER deviate from the orbit of PEP. The orbits at the collision point are tilted 13.5 mrad with respect to the straight-section axis.

the emittance control sextants are the same as those for the normal sextants, but they have their quadrupoles powered differently to produce the dispersion function mismatch in the arcs. To match so that the dispersion function is zero in the arcs for this mismatched dispersion case, it is necessary to adjust the strength of the first QF quadrupole in the regular arc cells. This causes only a minor perturbation to the sextupole correction scheme for the achromats in the arcs.

4.1.2 Low-Energy Ring

The LER is designed to satisfy the design parameters discussed in Chapter 3. Key features of the LER include

- Head-on collision optics
- Flat beams with 25:1 horizontal-to-vertical aspect ratio and $\beta_y^* = 1.5$ cm
- Zero dispersion in both planes at the IP
- Bunch separation of 1.26 m
- Beam separation in the IR first horizontally and then vertically
- Wigglers to permit adjustments of emittances and damping times

4.1.2.1 Overall Ring Configuration. The LER has a circumference of 2199.318 m and is designed to operate at 3.1 GeV. As illustrated schematically in Fig. 4-14, the ring has the hexagonal shape of PEP, with six long straight sections and six arcs. One of the long straight sections contains the IR with its low-beta optics; on the opposite side of the ring, the straight section is configured for injection. Two straight sections contain wigglers; two others, one containing the RF cavities, are used for tune adjustment. Figure 4-15 shows the layout and lattice functions of the LER. The beam circulates in a counter-clockwise direction as seen from above the ring. (Note, however, that the optics figures, such as Fig. 4-15, are arbitrarily drawn in the clockwise direction.)

The LER is situated 89.5 cm above the HER in the PEP tunnel, except in the IR straight section, where the two beams collide head-on. There are small radial offsets of the two rings in the arcs, and in the RF and injection straight sections, and larger offsets in the IR and wiggler straight sections.

4.1.2.2 Arcs. The six arcs of the LER are identical. Each contains nine regular FODO cells in the center and has a dispersion suppressor at each end, consisting of 3-1/2 cells with modified gradients. The ring circumference is quantized with two distinct half-cell lengths: that of the regular cells, $LC_{1/2} = 7.5625$ m, and that of the two suppressor cells closest to the straight section, $LD_{1/2} = 8.00625$ m. Each long straight section has a half-length equal to that of four regular cells: $LS_{1/2} = 8\ LC_{1/2} = 60.5$ m. As described in Section 4.1.1, the HER circumference is divided in exactly the same way. The overall geometrical layouts of the two rings are rather close, but there are notable differences in the optics.

Each FODO half-cell in the LER contains one 1-m dipole, one 0.726-m quadrupole, and one sextupole, and has length $LC_{1/2} = 7.5625$ m. The optics of one cell, shown in

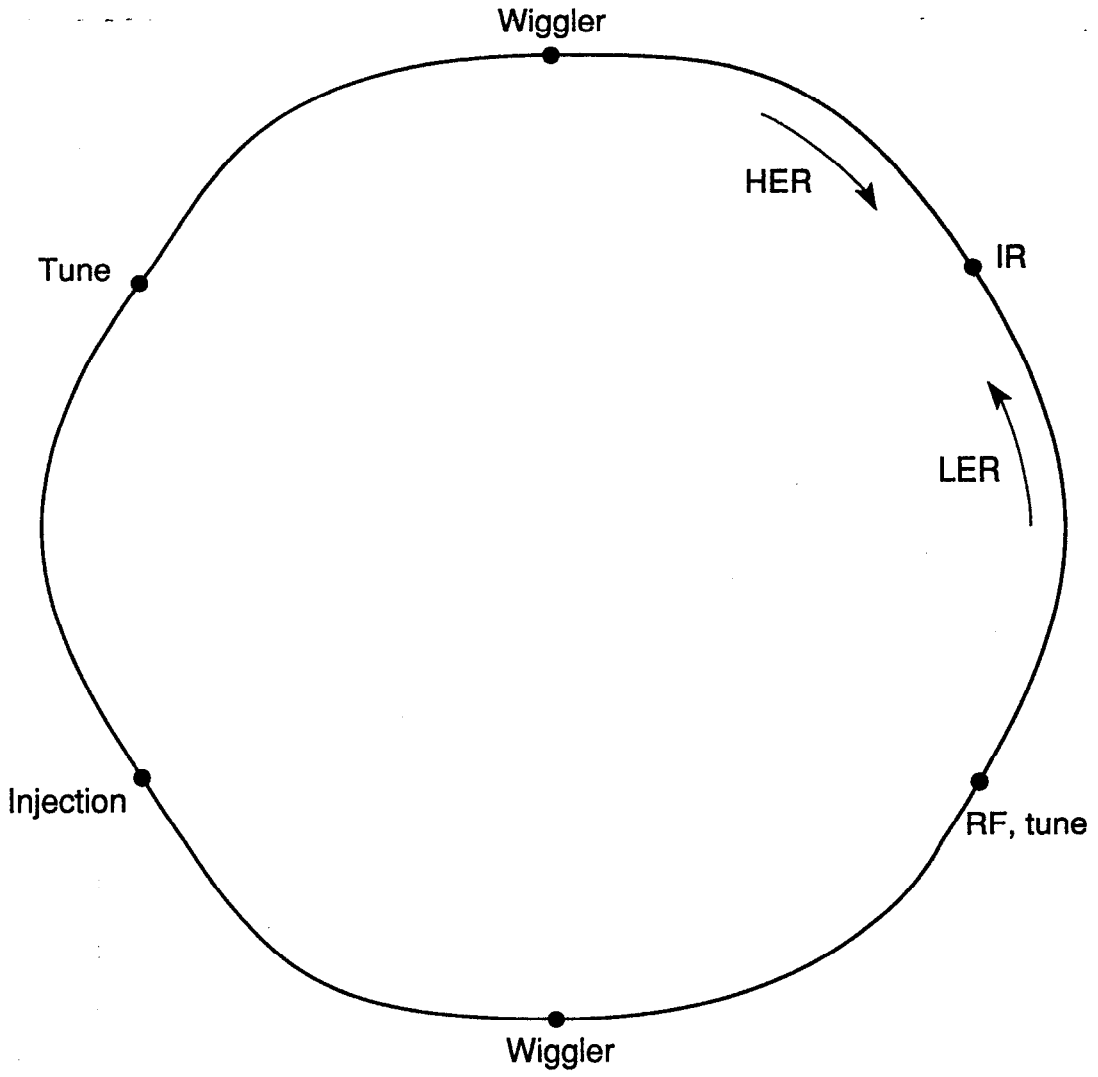

Fig. 4-14. Schematic layout of the LER, which will be located above the HER in the sixfold symmetric PEP tunnel.

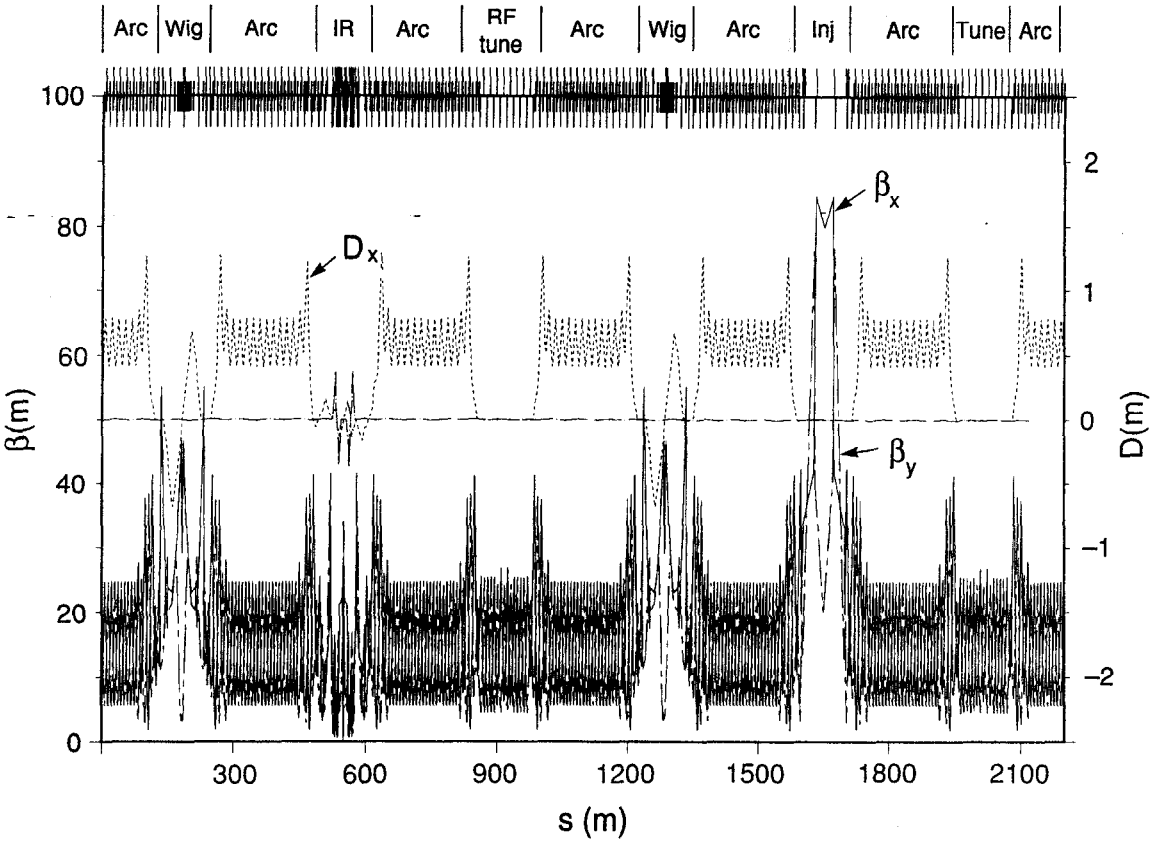

Fig. 4-15. Layout and optics functions for the LER. The lattice for the full ring is shown, starting and finishing at mid-arc in region 11.

Fig. 4-16, are adjusted to give a phase advance of 80° in each transverse plane; hence, the nine regular cells constitute an achromat with a tune of two units. The dipoles are offset 2.24 m upstream from the half-cell center, both to prevent the synchrotron radiation generated by them from striking the adjacent magnets and to facilitate the mechanical support system of the two rings. In plan view, the arc quadrupoles of the LER are almost coincident with those of the HER. The reason the cell phase advance is higher in the LER than in the HER (where it is 60°) is to avoid having too large a value for the momentum compaction factor α. If α gets too large, a very large RF voltage is required to hold the bunch length to a value consistent with the low value of β_y^*. Unfortunately, for geometrical reasons, this difference in phases prevents use of the more elegant type of dispersion suppressor used in the HER.

4.1.2.3 Dispersion Suppressors. The dispersion suppressors on the left and right sides of the long straight sections (or right and left sides of the arc) are shown in Figs. 4-17 and 4-18. As shown in Fig. 4-17, the left suppressor is bordered on the left by the regular cells and on the right by the long straight section. It has seven half cells, the first three of which are the same as those of the regular cells except that the quadrupole gradients are different and the sextupoles are missing, while the last four half cells have the length $LD_{1/2}$ = 8.00625 m. The gradients are irregular in these longer half cells as well, and

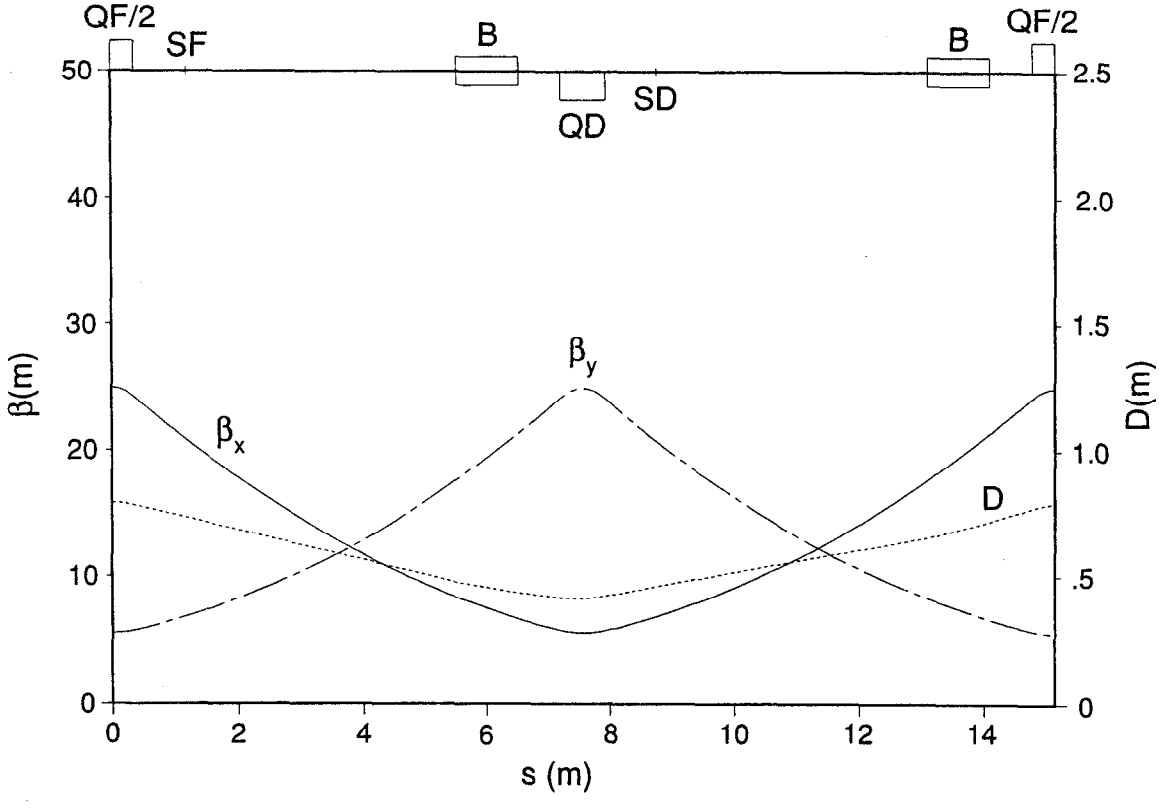

Fig. 4-16. Layout and optics functions for the standard arc cell of the LER. The dipoles B are offset from the center of the half cells so that synchrotron radiation from the beam, traveling from right to left, is absorbed in the longer straight sections between B and QF or B and QD.

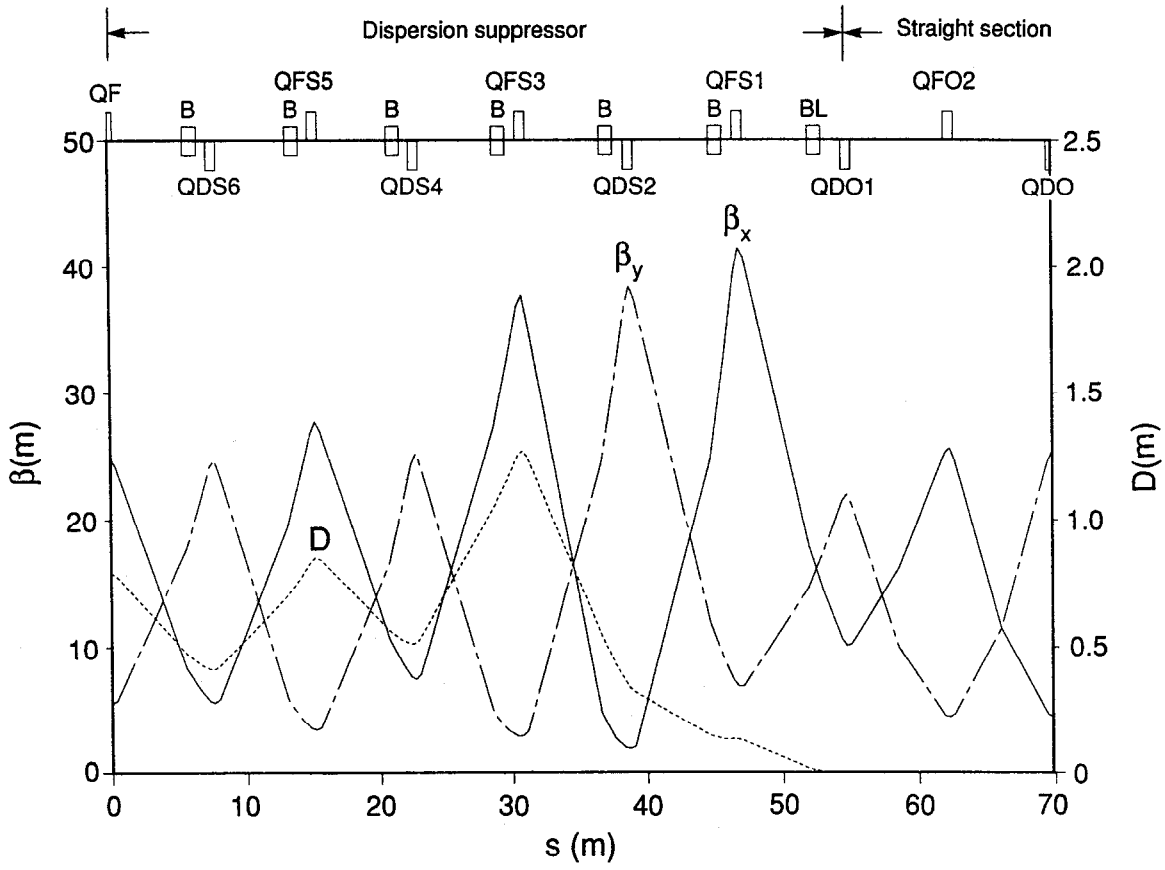

Fig. 4-17. Layout and optics functions for a left-hand dispersion suppressor of the LER. The strength and position of the dipole BL compensates for the fact that the LER dipoles are not symmetric about the arc center. It steers the orbit to the center of the straight section.

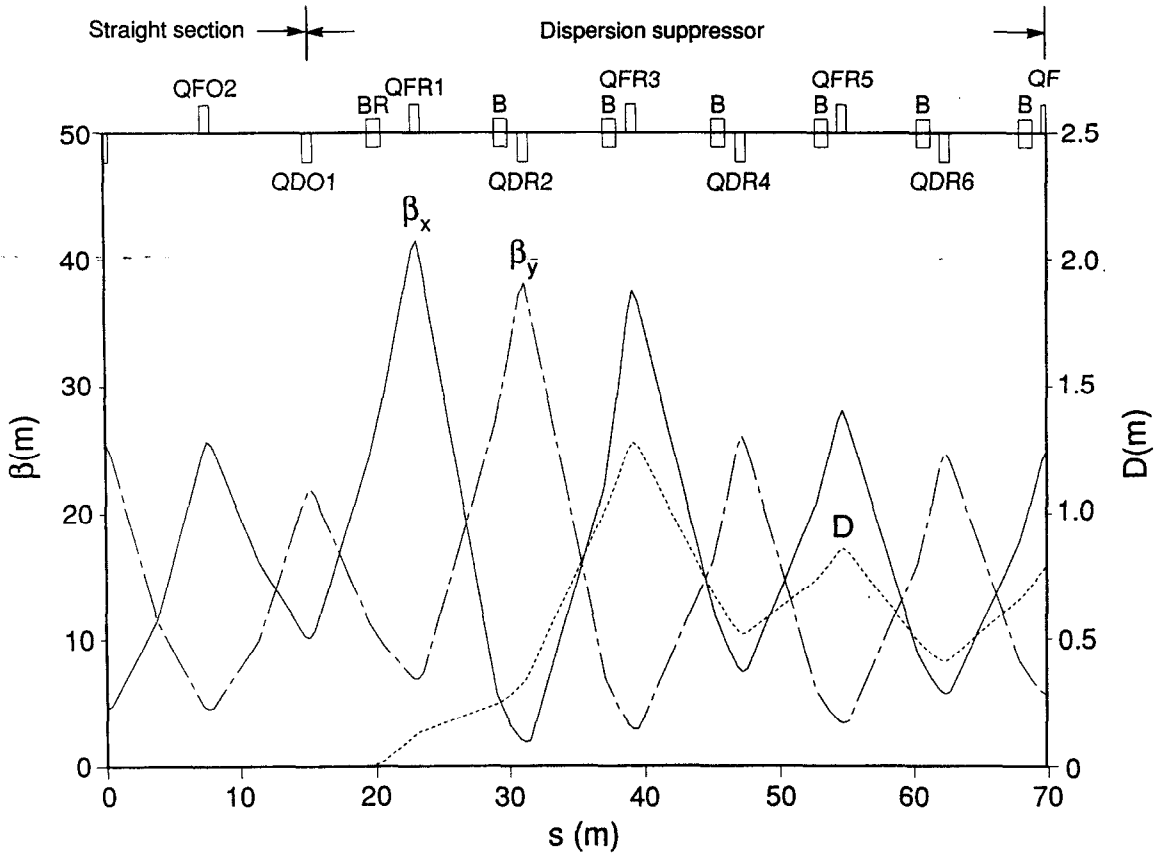

Fig. 4-18. Layout and optics functions for a right-hand dispersion suppressor of the LER. The dipole BR corresponds to BL in Fig. 4-17.

their dipole longitudinal offsets are scaled with the half-cell length in order to keep the quadrupoles lined up vertically with those of the HER. The dipoles in the suppressor cells are the same as those of the regular cells, except for those immediately adjacent to the long straight section, which are adjusted in position and strength in such a way as to steer the LER beamline into horizontal coincidence with that of the HER in the long straight sections.

Each suppressor is matched optically at one end to the orbit functions of a regular cell in the center of a QF quadrupole, and at the other end to those of a 90° normal-length cell without dipoles, with the dispersion being zero at that end. Because the dipole positions do not have reflection symmetry between the left and right suppressors, the quadrupole gradients are slightly different in the two cases.

4.1.2.4 Normal Sextants. We consider each sextant to begin and end at the center of an arc; that is, the long straight section lies in the center of the sextant. There are four straight section types and four corresponding types of sextant. The normal long straight section consists of eight 90° normal-length FODO cells without dipoles; the last two quadrupoles at the ends of each straight section (QDO1, QFO2) have different gradients and are actually part of the dispersion suppressor matching system. The optics and lattice arrangement of a normal long straight section with its adjacent dispersion suppressors are

shown in Fig. 4-19. A normal sextant is shown in Fig. 4-20. The near geometrical coincidence of the HER and LER in plan view, achieved by the dipoles BL (see Fig. 4-17) and BR (see Fig. 4-18), is shown in Fig. 4-21, which shows the radial offset of the two rings from the PEP centerline.

The two normal straight sections are used for adjustment of the global betatron tunes; one also houses the RF system. For the former purpose, the seven quadrupoles in the center of the straight section are varied symmetrically in such a way as to change the two tunes independently, while preserving the beta-function matching to the regular empty (dipole-free) cells. Figure 4-22 shows a normal long straight section with such a "phase trombone" activated.

4.1.2.5 Wiggler Straight Sections. Two of the long straight sections contain wiggler magnets, which are used to adjust the emittance of the LER and also to permit the damping time of the LER to be reduced to a value as low as that of the HER, if desired. Figure 4-23 shows the layout and optics of a wiggler straight section. Four blocks of 6-m wigglers are placed in each wiggler straight section along the length of a horizontally tilted line. The zig-zag beamline pattern serves both to deflect the synchrotron radiation away from the main beamline and to increase the dispersion in the wigglers (which in

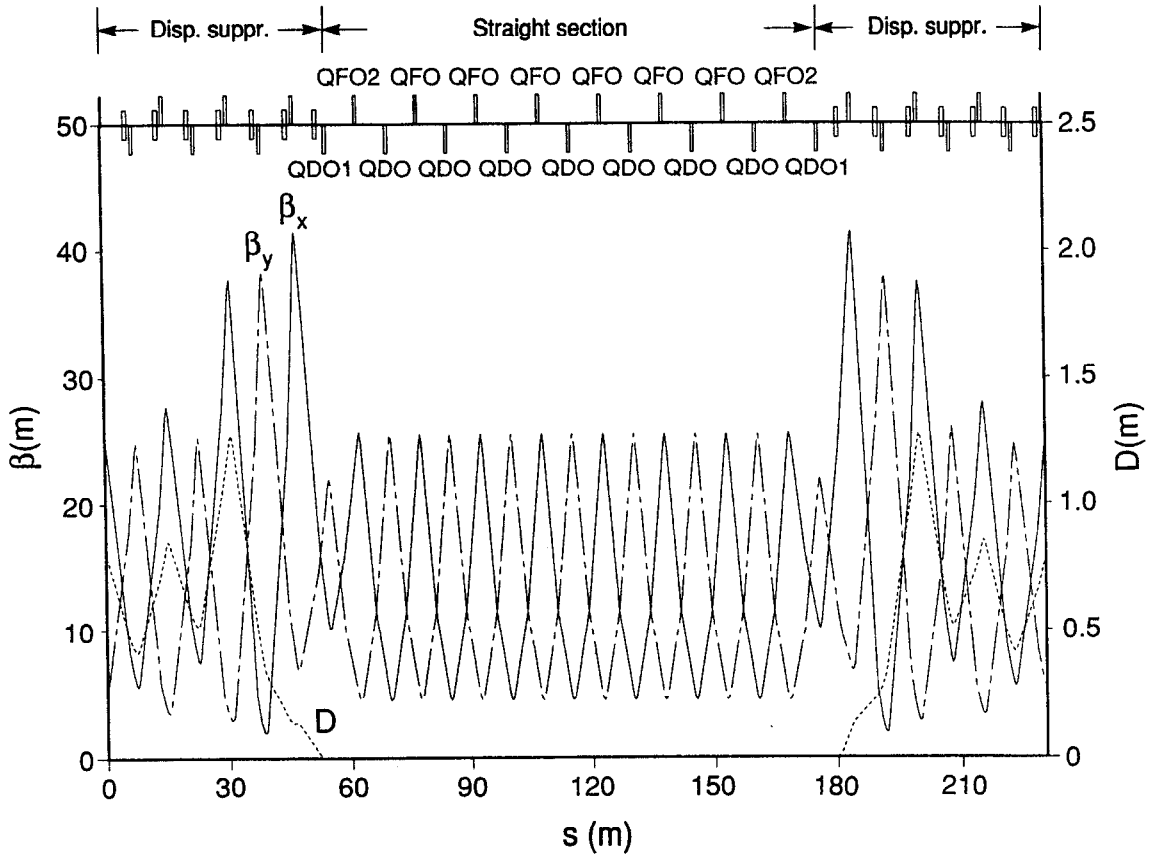

Fig. 4-19. Layout and optics functions for a normal long straight section of the LER.

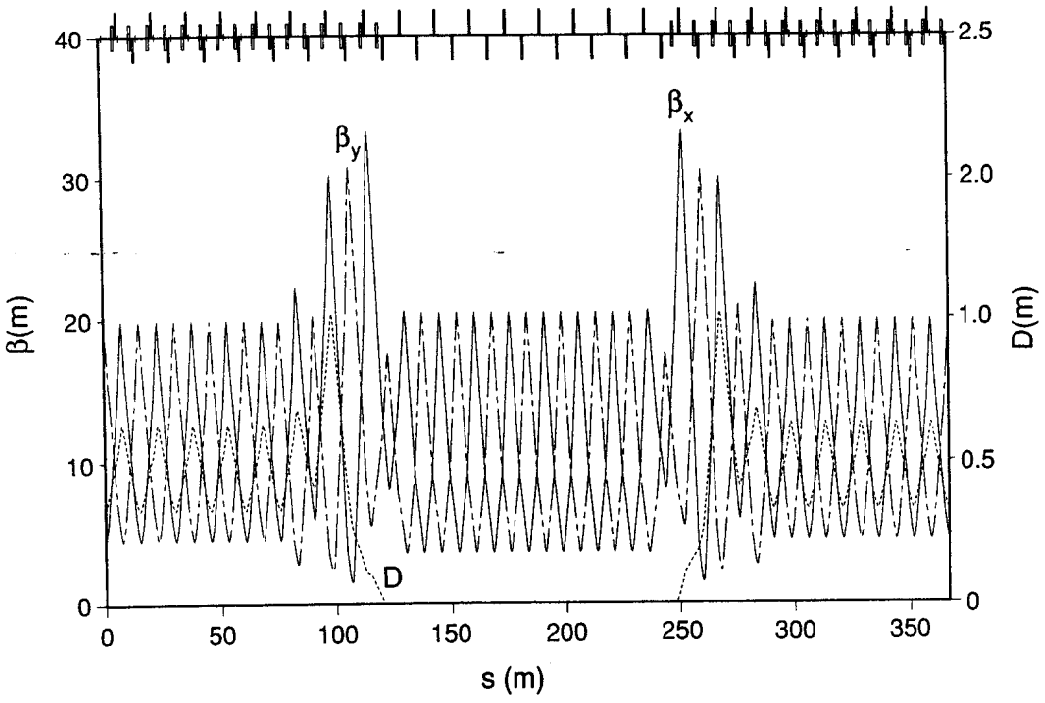

Fig. 4-20. Layout and optics functions for a normal sextant of the LER.

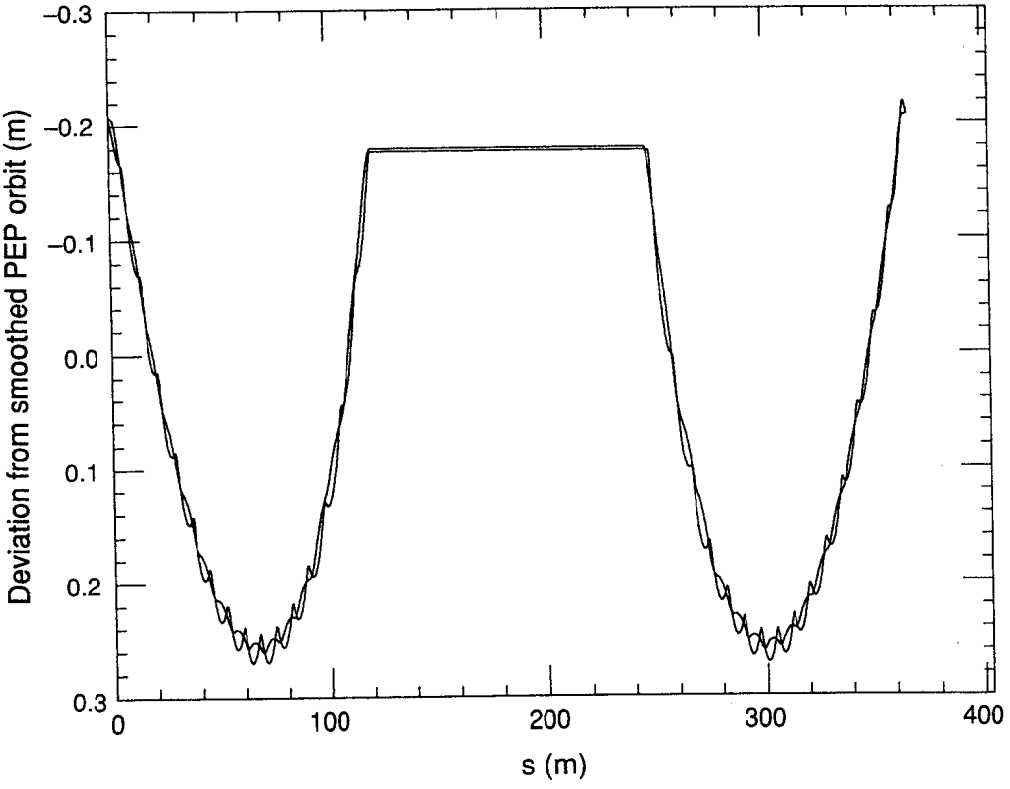

Fig. 4-21. Plot showing the radial offsets of the LER and HER in a normal sextant, with respect to the PEP centerline. The maximum excursions, 26 cm to the inside and 21 cm to the outside of the PEP orbit, fit well in the PEP tunnel.

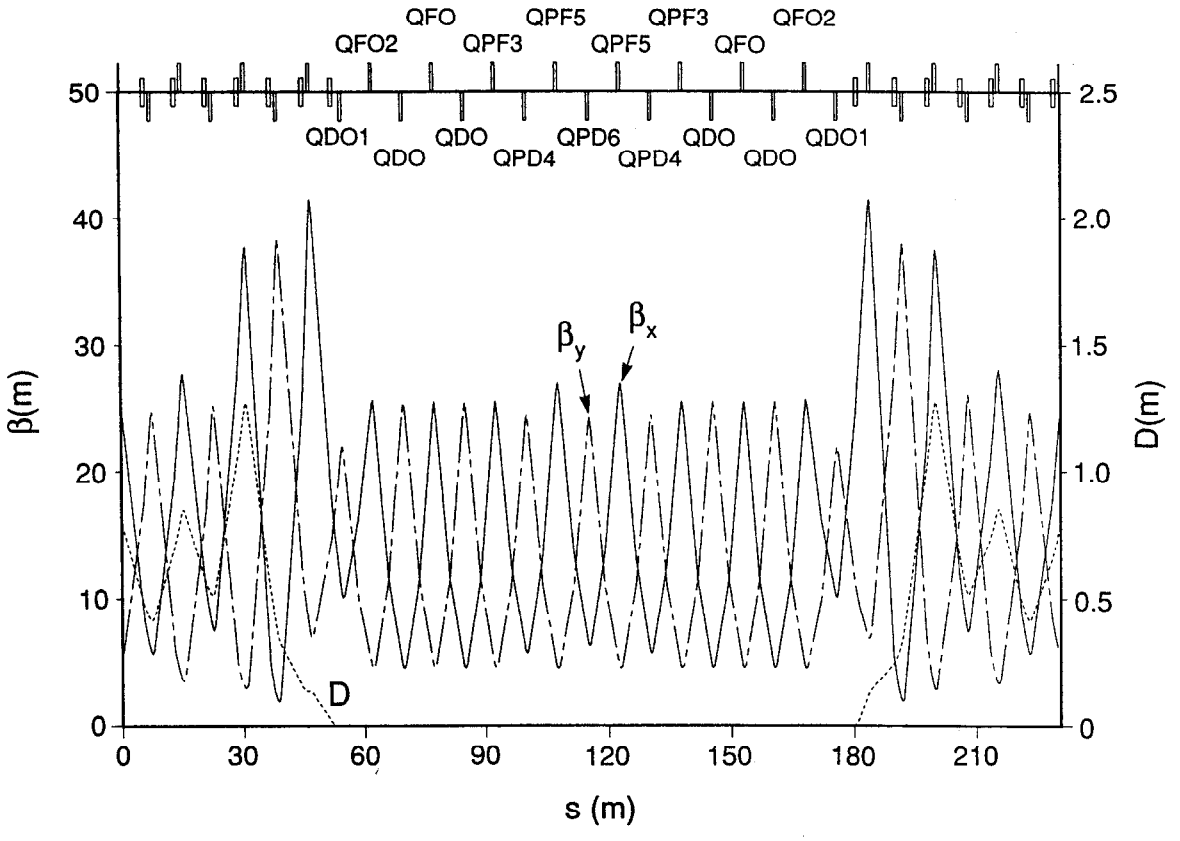

Fig. 4-22. Layout and optics functions for a phase control straight section containing "phase trombone" quadrupoles. The many independently adjustable quadrupoles permit smooth beta functions in a region where RF cavities may be placed.

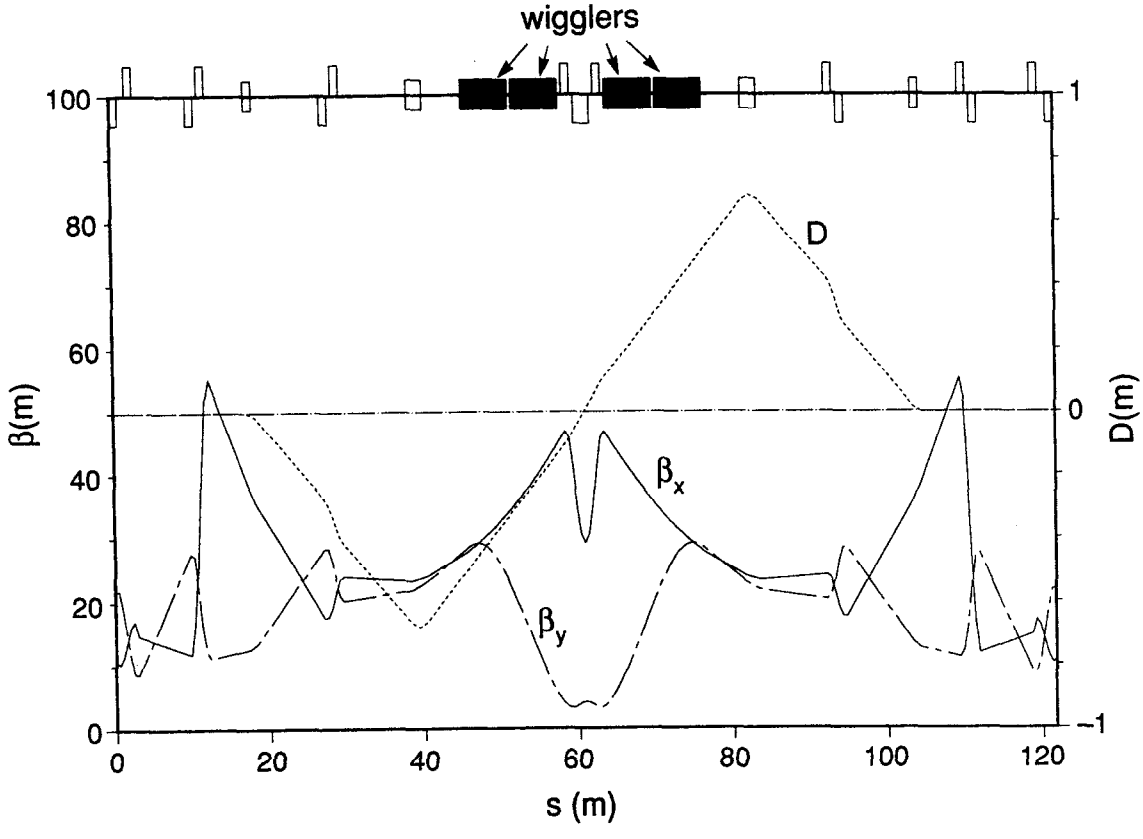

Fig. 4-23. Layout and optics functions for the wiggler straight sections of the LER. In conjunction with the dispersion function D, and its derivative, the wigglers increase the emittance of the low-energy beam. In addition, the wigglers can decrease the damping time of the low-energy beam so that it is equal to that of the high-energy beam.

turn causes a growth of horizontal emittance). By adjusting the strength of the bends that constitute the dogleg, the emittance is brought to the design value.

The optics shown in Fig. 4-23 correspond to the case where the damping times of the two rings are equal. Each 6-m block contains nine wiggler periods, each 60% full of 1.63-T dipoles. Figure 4-24 shows the radial offset of the two rings in a wiggler sextant and shows that the radiation is directed from right to left radially outward. The optics of the wiggler straight is symmetric. Seven independent quadrupoles produce a beam waist at the center and bring the dispersion to zero there, causing both the dispersion and its slope to be zero at either end of the straight section.

4.1.2.6 Injection Straight Section. The straight section opposite the IR straight section is used for injection into the LER. It is configured in the same way as that of the HER, with a 40-m-long free space in the center having $\beta_x = 80$ m. The layout and optics of this straight section are shown in Fig. 4-25.

4.1.2.7 Interaction Region and Beam Separation. The most difficult part of the design of a collider is that of the IR, and that is especially true in the case of a high-luminosity

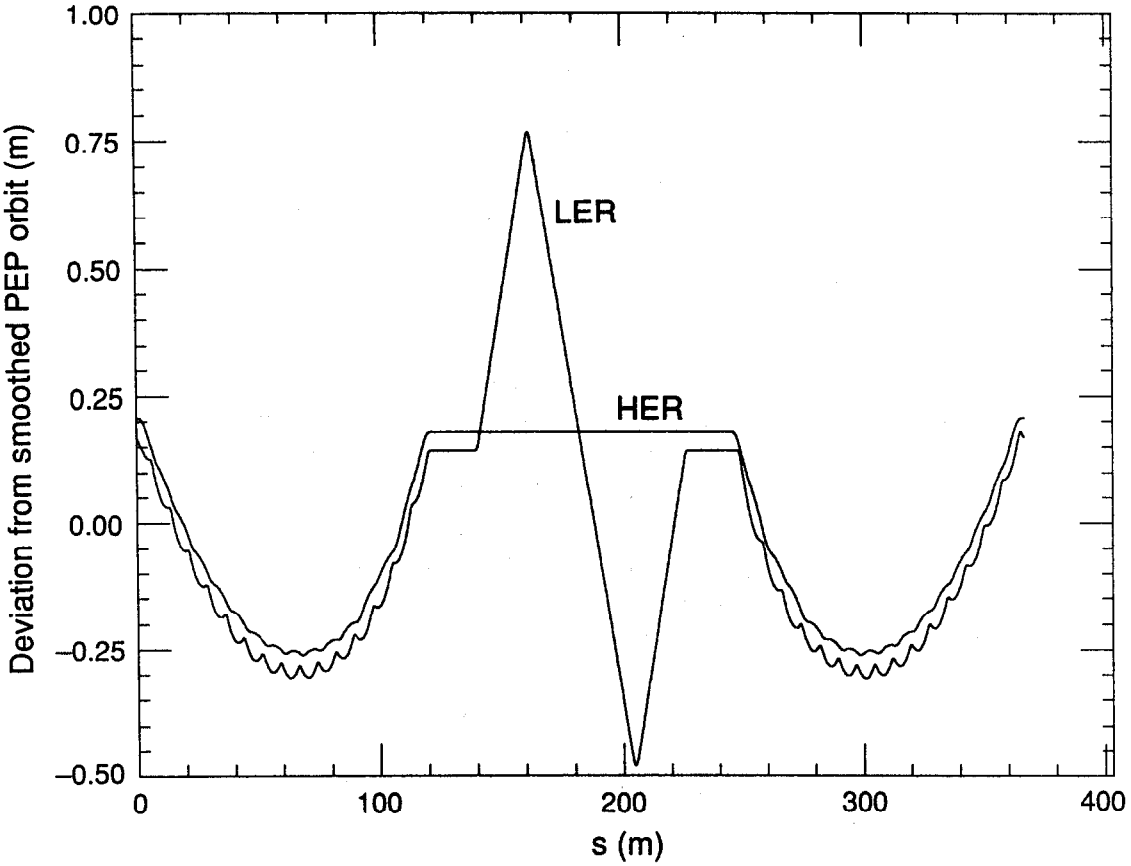

Fig. 4-24. Plot showing the radial offsets of the LER and HER in the sextant containing the wigglers, with respect to the PEP centerline. Note that, with the low-energy beam traveling from right to left, synchrotron radiation from the wigglers is directed to the outside of the ring.

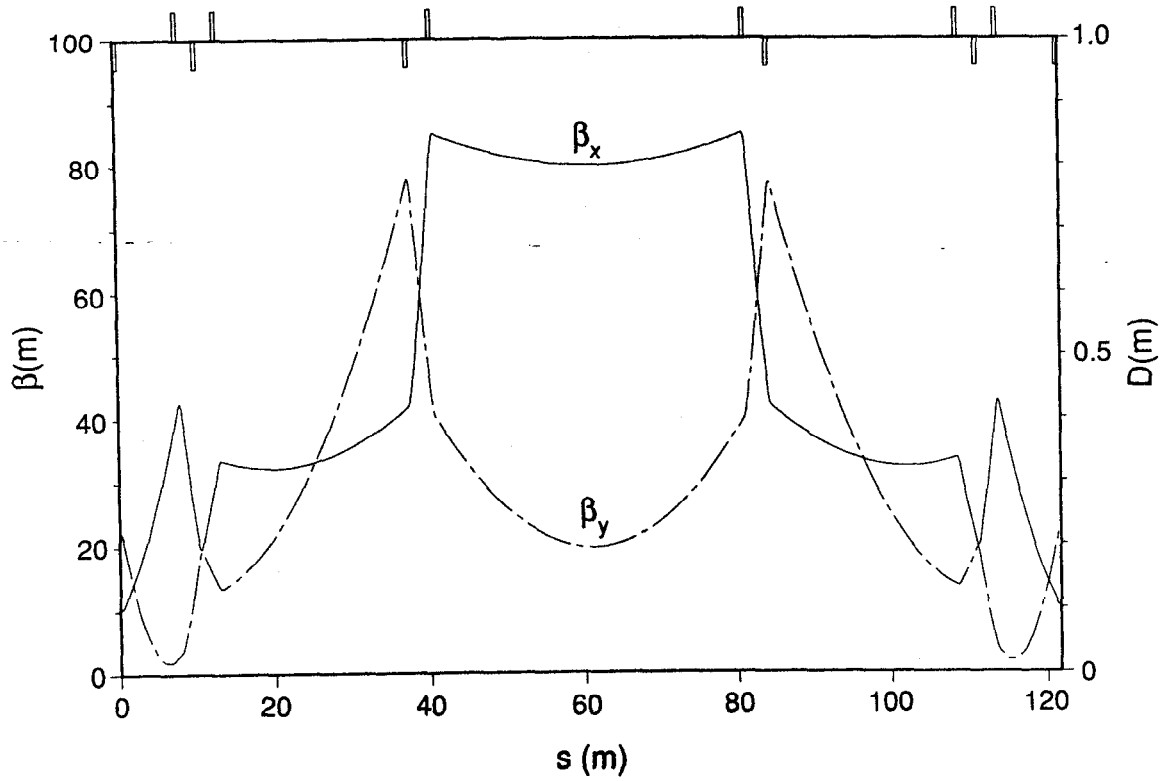

Fig. 4-25. Layout and optics functions for the injection straight section of the LER. The injection point is at the center of the figure, in the middle of the long straight section. Beta functions in this region are easily adjustable to match injection requirements.

asymmetric machine. The energies and beta functions of the two rings are different, the bunches are closely spaced, and the synchrotron radiation from the magnetic separation is large. Optics, separation, masking, and experimental detectors must all coexist in a very small region, so that neat, modular designs are elusive or nonexistent.

As discussed earlier, the scheme adopted for this design is horizontal separation using a separating dipole, a quadrupole triplet common to both beams (with offsets to enhance the separation), a septum quadrupole to focus the high-energy beam, followed by a vertical septum magnet that begins the step that brings the LER beamline 89.5 cm above that of the HER. The horizontal bending pattern is antisymmetric about the IP, which produces an S-bend beamline—a geometry that is conducive to extracting the synchrotron radiation. Figure 4-26a shows an anamorphic diagram of the IR in plan view. The beamlines are shown solid, and the $15\sigma_x$ envelopes are dashed. The polarities of the quadrupoles are indicated, as usual, by the names QF or QD, and (H) or (L) indicates that the magnet is centered on the HER or LER beamline, respectively.

The horizontal separation is produced by B1 and the common triplet QD1, QF2, QD3 with the offsets shown in the figure. These are permanent magnets. The separated beams then traverse the septum quadrupole QD4H, which focuses the high-energy beam only. Figure 4-26b shows the displacements of the low-energy beam from the IP through the horizontal and vertical separation systems. The low-energy beam is transported from the

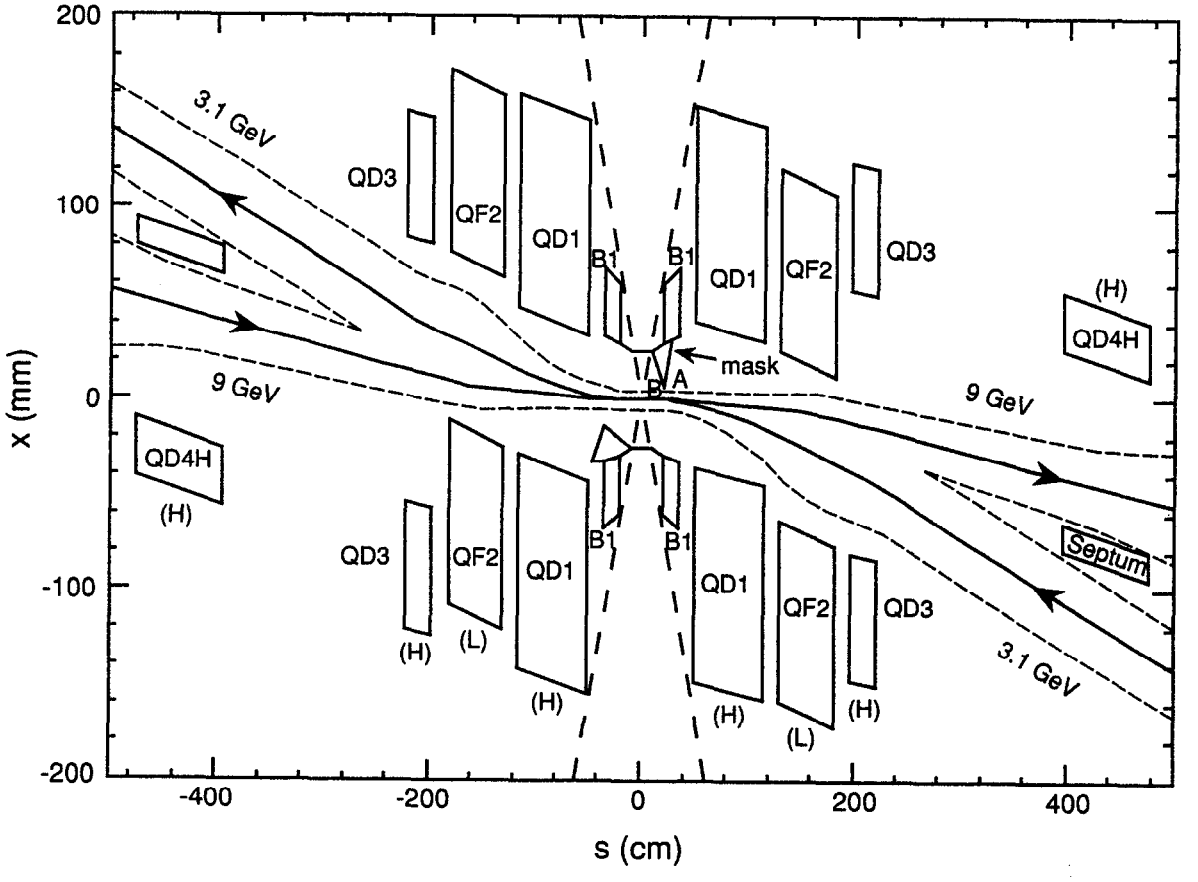

Fig. 4-26a. Anamorphic plan view of the IR.

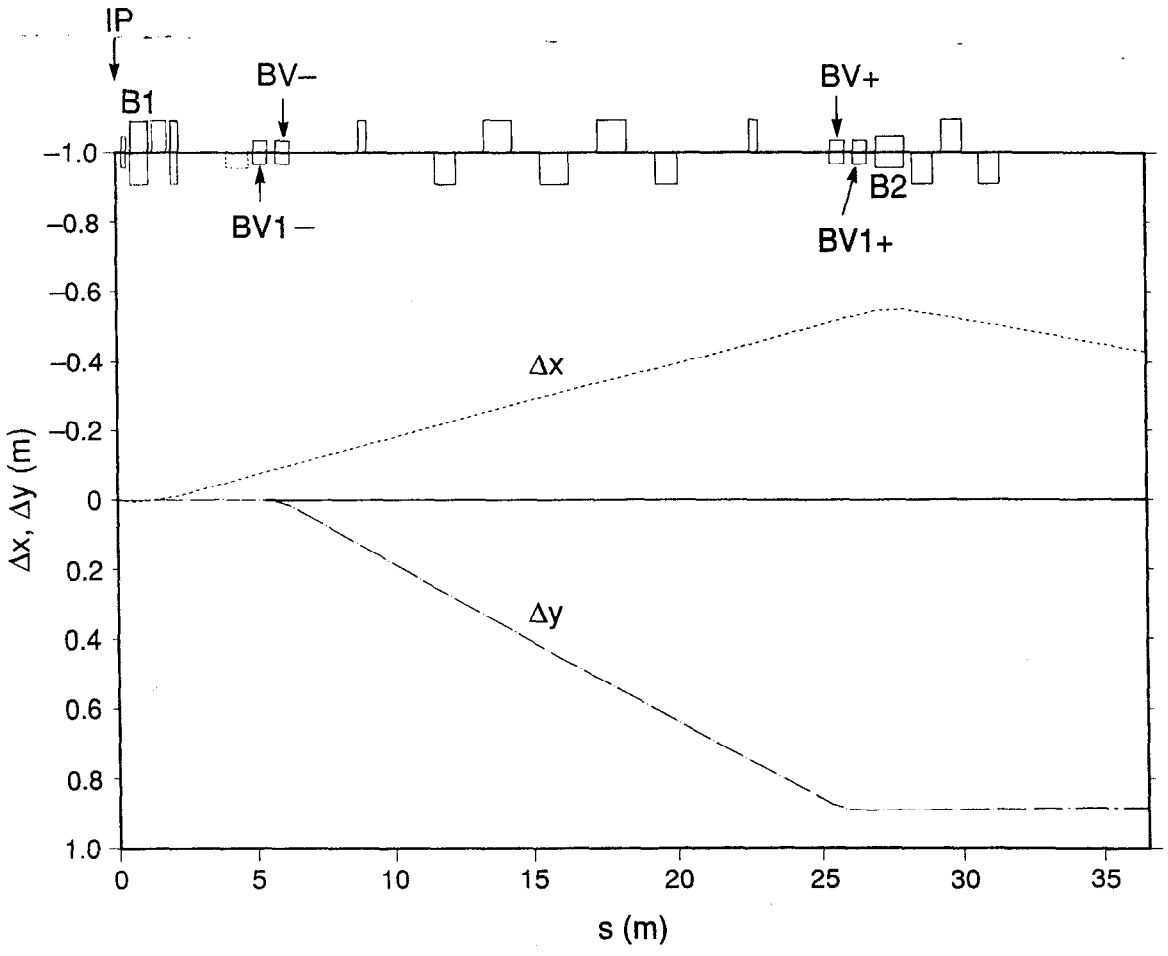

Fig. 4.26b. Plot showing the horizontal and vertical displacements of the low-energy beam in the separator systems. Note the inverted scale for Δx and Δy. The dashed quadrupole represents QD4H, which acts only on the high-energy beam.

collision plane to one 89.5 cm above by the action of the four vertical bending magnets BV1–, BV–, BV+, BV1+, the first of which is a Lambertson septum magnet.

The optics of the LER in the horizontal separation region is shown in Fig. 4-27. The low-energy beam proceeds from a waist at the IP with $\beta_x^* = 37.5$ cm, $\beta_y^* = 1.5$ cm. The first parasitic bunch-crossing point occurs 0.63 m from the IP, just inside of QD1, where the beamlines are separated by $7.5\sigma_x$. The quadrupole apertures allow for $15\sigma_x$ and $15\sigma_y$ beams (the fully coupled vertical emittance is used to calculate the vertical beam size), plus 5 mm for the beam pipe and trim coils and a 2-mm closed-orbit distortion allowance, as well as the additional aperture required by the synchrotron radiation fans. These factors set the inner radii; the outer radii are controlled by the need to maximize the detector solid angle. These dimensions, and an assumed remanent field of 1.05 T give the gradients. The lengths are then adjusted to achieve the desired low-energy beam optical behavior, as shown in Fig. 4-27. Although many iterations were needed to make this process self-consistent, the outcome of these iterations was a conservative and robust design. The discussion of the background issues is covered in Section 4.2. It is worth reiterating here that the high-energy beam benefits significantly from the focusing

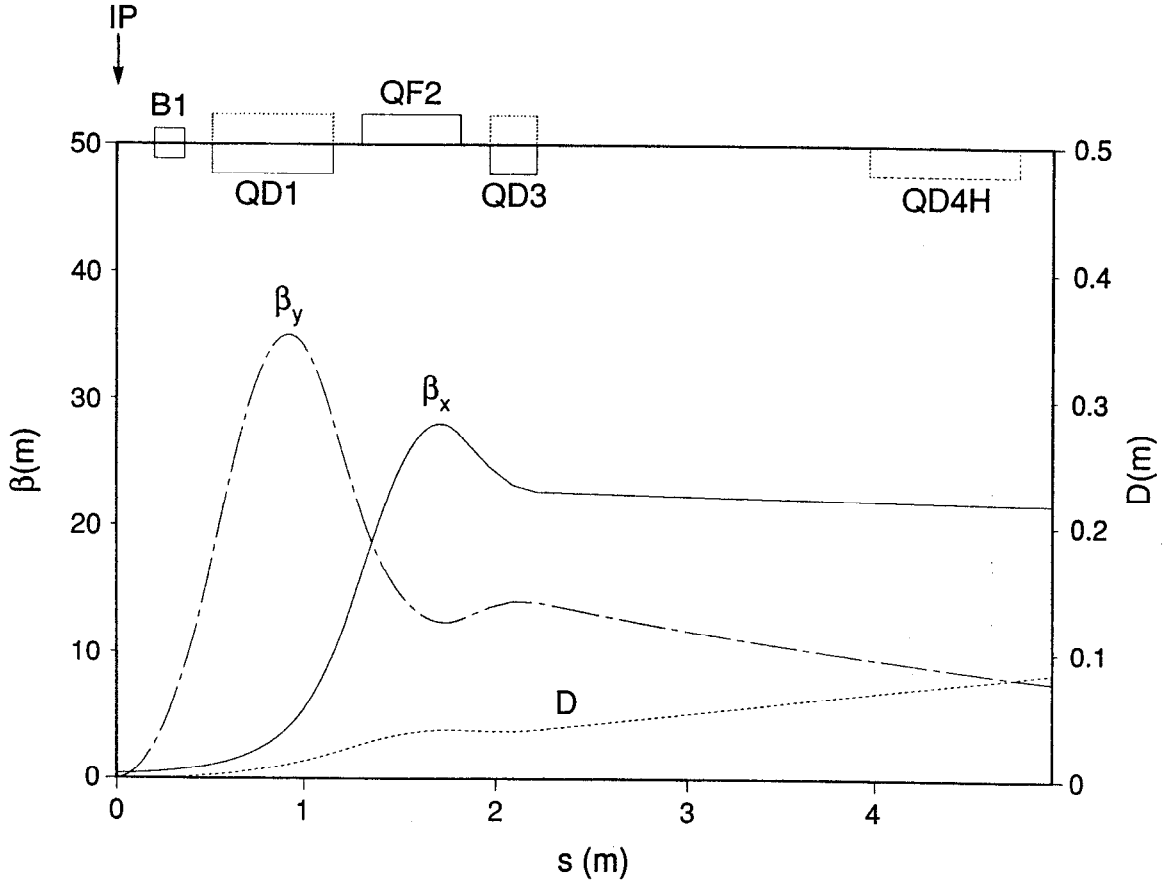

Fig. 4-27. Layout and optics functions for the horizontal separation region of the LER. The dipole B1 and the offset quadrupoles of the triplet, QD1 and QD3, separate the beams. The triplet focuses the low-energy beam to a nearly parallel condition; it then passes through the field-free region of the HER quadrupole QD4H.

of the triplet. Although substantial focusing of the high-energy beam takes place mainly in QD4H, the $\beta_{y,-}$ value in this quadrupole is sufficiently low that the resultant chromaticity contribution to the HER is actually lower than that of the corresponding quadrupole at PEP.

The optics through the horizontal and vertical separation regions is shown in Fig. 4-28. The common triplet is adjusted to produce a beam waist at the entrance to QF4 and a low enough β_x value to permit the low-energy beam to clear the septum in QD4H. The seven quadrupoles, which are located symmetrically about the center of the vertical step, are adjusted to bring D_y and its slope to zero at the end of BV1+, to bring D_x to zero in the center of B2, and to prevent large beta values in between. The B2 dipole is centered on the point where D_x is brought to zero by the quadrupoles to its left; as part of the design process, its strength was initially adjusted to bring both D_x and the slope of D_x to zero at the end of B2. Later, its strength was incremented, along with those of the dipoles B3–B6, in such a way as to steer the low-energy beam from the arc to the IP with the correct radial position and slope, while preserving the dispersion matching.

The remaining optical matching of the IR straight section is shown in Fig. 4-29. It is done with the quadrupoles QD8 through QF13, which produce the characteristic β and α functions at the center of the QDO1 quadrupole. This point marks the beginning of the

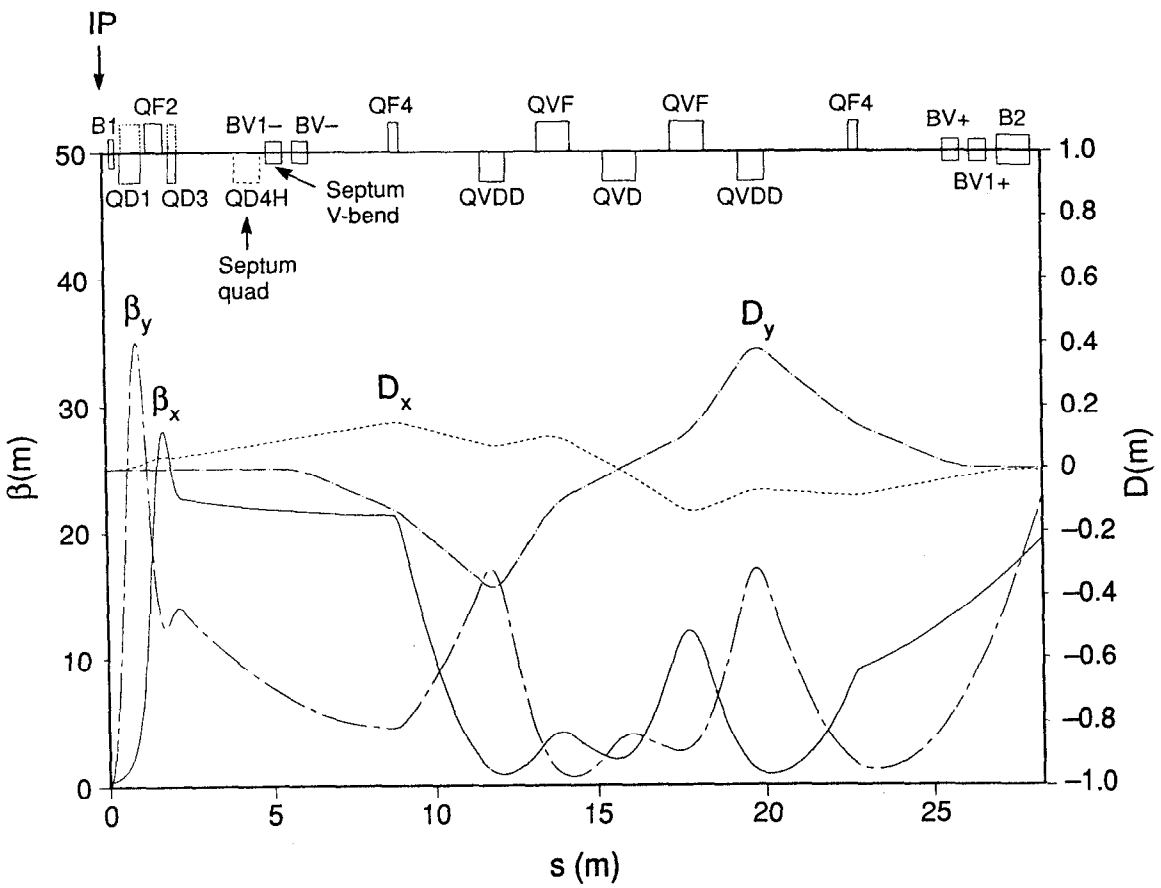

Fig. 4-28. Layout and optics functions for the horizontal and vertical separation regions of the LER. To avoid coupling of the horizontal and vertical motion, the vertical bending is confined to a region that is free of horizontal bends.

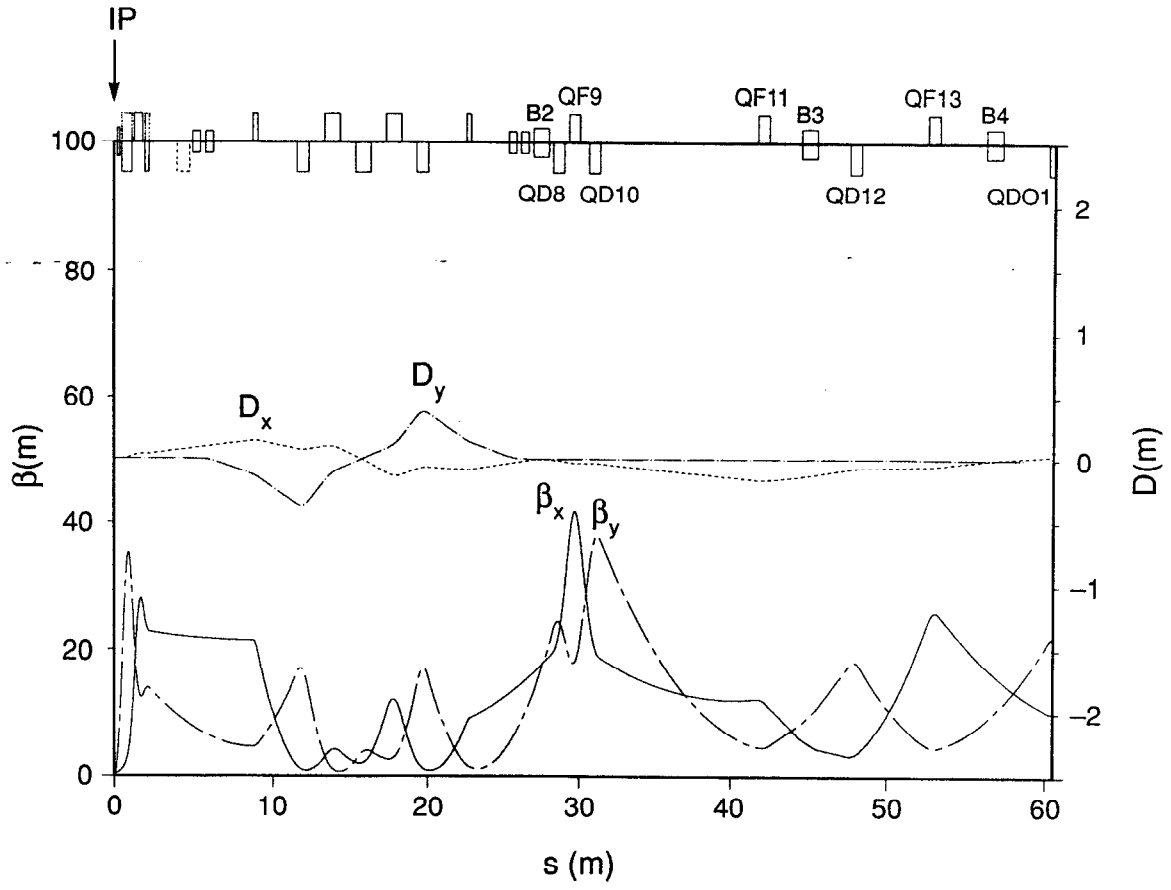

Fig. 4-29. Layout and optics functions for the right-hand half of the IR straight section of the LER. The quadrupoles QD8 through QF13 match the beta functions into the dispersion suppressor.

arc. Figure 4-30 shows the optics from the IP, through the right half of the IR straight section and the right dispersion suppressor, to the beginning of the regular cells. In this figure the bends B2–B6 are set as described above. The radial displacement of the LER compared with that in a normal sextant is shown in Fig. 4-31, while Fig. 4-13 shows both the LER and HER displacements relative to PEP in the IR sextant. Figures 4-32 and 4-33 show the optics of the right side and of the complete IR sextant of the LER. The maximum beta functions generated by these optics, even with $\beta_y^* = 1.5$ cm, are quite moderate.

4.1.3 Tracking Studies

4.1.3.1 High-Energy Ring. Here we present results of the dynamic aperture studies for the B Factory HER. The lattice actually studied is a slightly earlier version of the lattice presented in Section 4.1.1. At present, only a single tune configuration, $\nu_x = 25.29$, $\nu_y = 24.19$ has been analyzed.

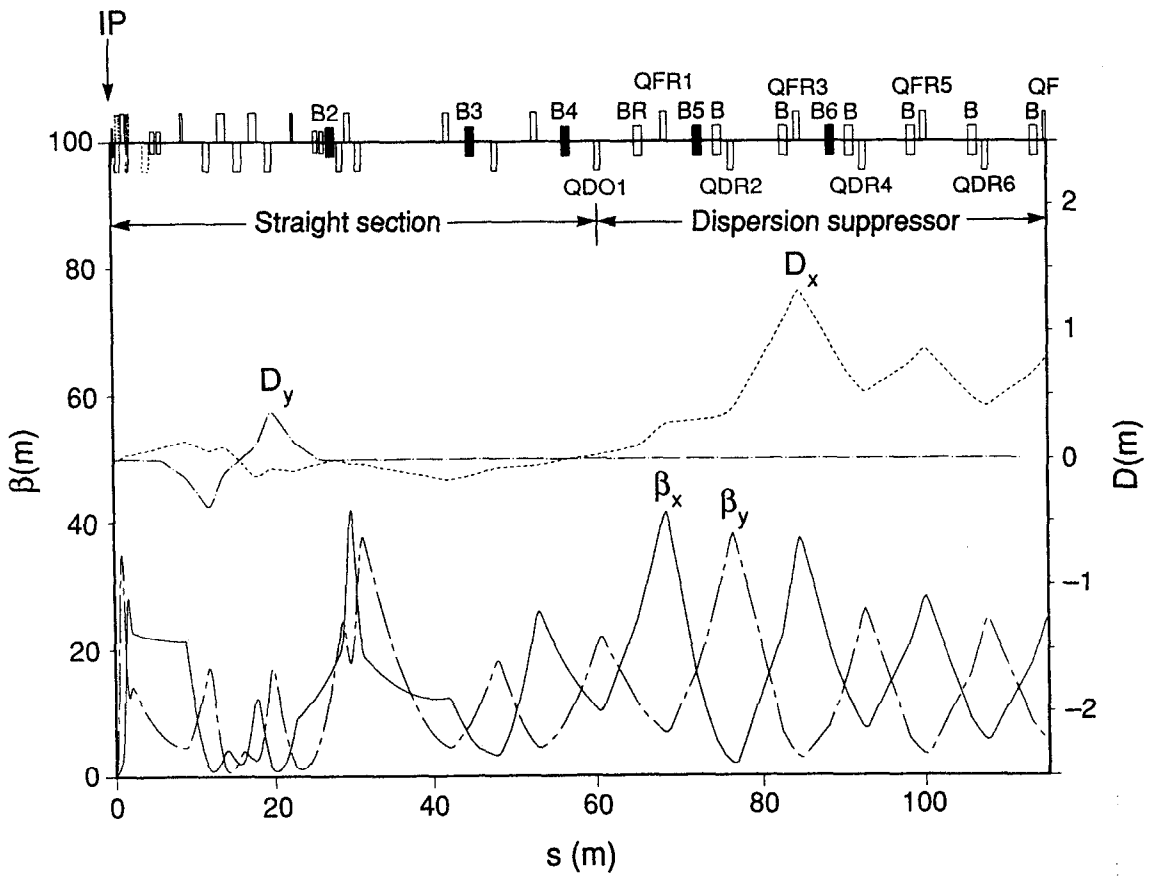

Fig. 4-30. Layout and optics functions from the IP to the beginning of the normal cells of the LER. The dipoles B2 through B6 correct the horizontal dispersion function and steer the beam into the arcs. The steering is needed to place the IP at the center of the straight section and to match the beam angle at the IP to that of the high-energy beam.

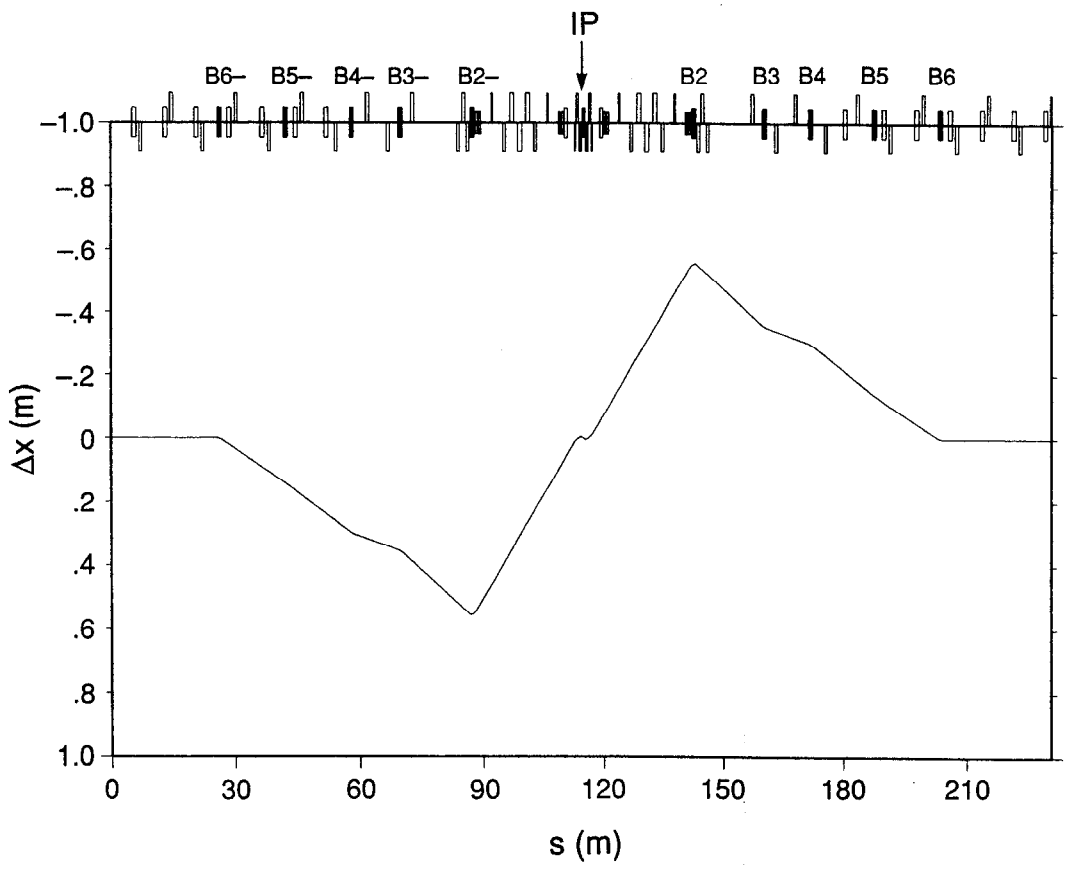

Fig. 4-31. Radial displacement of the low-energy beam in the IR sextant, compared with that in a normal sextant.

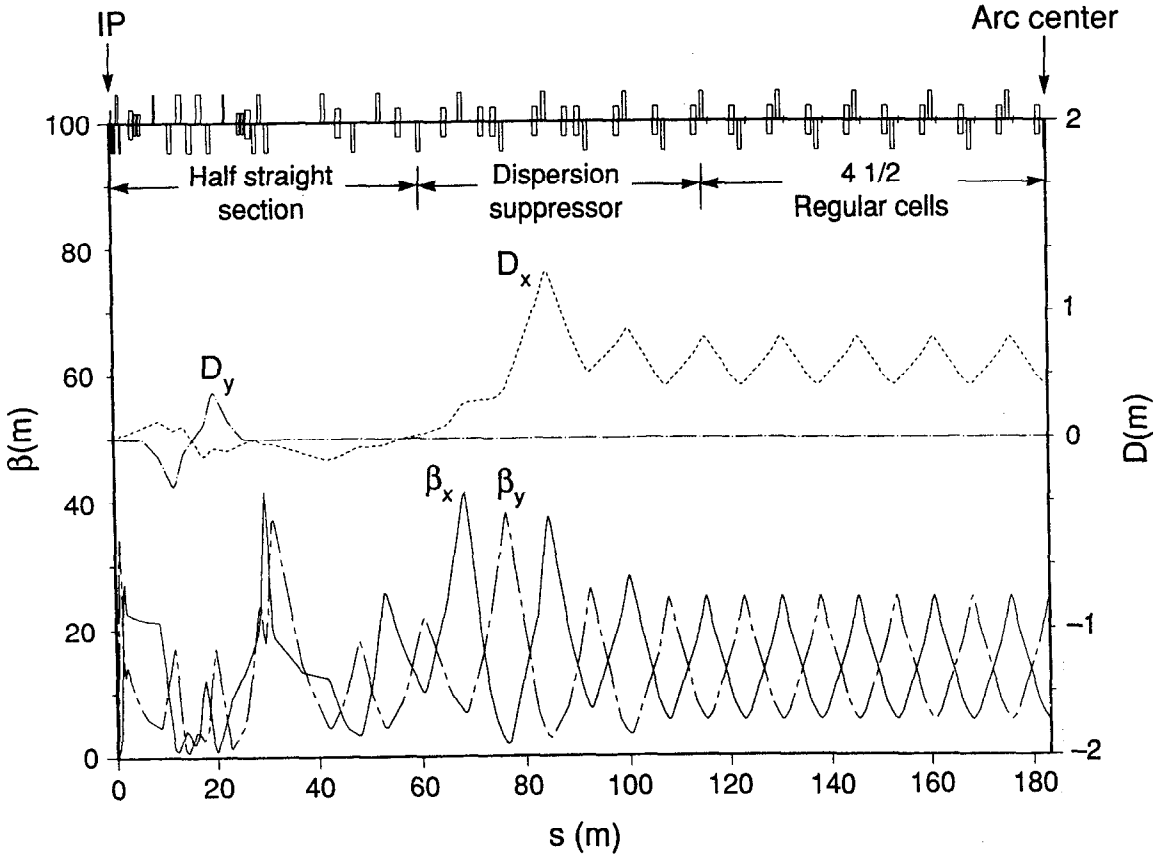

Fig. 4-32. Layout and optics functions for the right-hand side of the IR sextant in the LER.

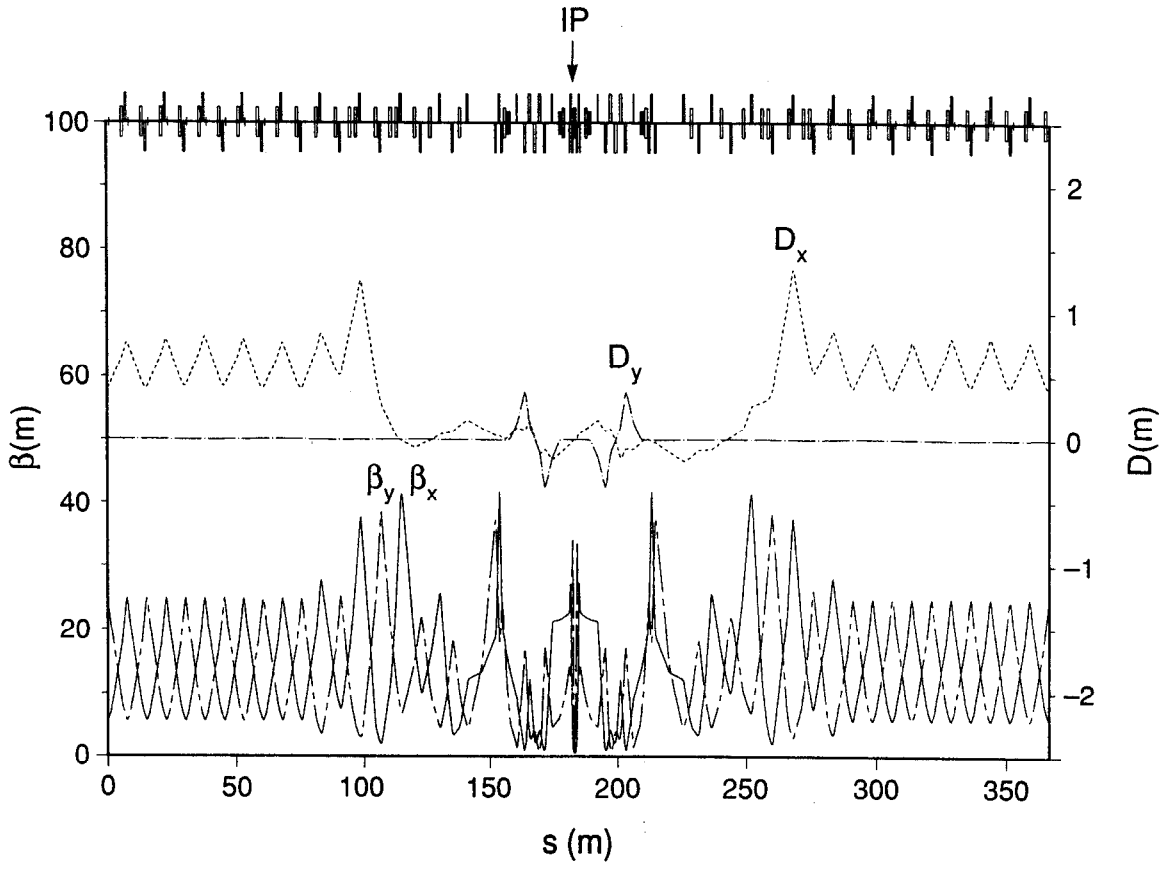

Fig. 4-33. Layout and optics functions for the complete IR sextant in the LER. Note the symmetry of the vertical dispersion function and the antisymmetry of the horizontal dispersion function.

Chromatic Correction Scheme. For this study we adopted a rather straightforward chromatic correction scheme. First, one family of sextupoles for each plane (SFA, SDA) was distributed inside the pseudo-achromats in the arcs. This accounts for 12 sextupoles of each family in each regular arc section and eight per family in the emittance control arcs. These sextupoles are set to completely correct the chromaticity of the entire ring.

Then four sextupoles, SD1, and two sextupoles, SF1, replace selected SDA and SFA sextupoles in the two pseudo-achromats that surround the IR. The sextupoles SDA, SFA, SD1, and SF1 are then set to completely correct both the chromaticities and the momentum dependence of the beta function ($d\beta/d\delta$) at the IP. The positions of the SD1 and SF1 sextupoles are chosen to minimize the sextupole strengths required.

Alignment Tolerances. The alignment errors taken for the magnetic elements are summarized in Table 4-2. For the present study, the errors for the IR quadrupoles were taken as 100 μm transverse error and a field error of 0.0001. This aspect will be revisited after the detailed designs of the IR magnets are available.

For tracking purposes, sets of horizontal and vertical correctors and beam position monitors were distributed around the ring to provide a closed-orbit correction scheme. The scheme chosen works well, although it is not necessarily the one that will be adopted on the real machine. After correction, the rms orbit errors were 650 μm in both planes, with a maximum displacement below 2 mm. In the orbit-correction procedure, it was assumed that BPMs had rms errors of 300 μm in displacement and 1 mrad in roll angle.

Magnetic-Field Errors. Dipole field errors are based on measurements of prototype PEP magnets and include only multipoles up to sextupole. As part of the removals process, a number of actual magnets will be measured to provide additional input for future tracking studies. The values used in the present case are given in Table 4-3.

For the arc quadrupoles, errors are available as values of b_n/b_1 at a radius of $r = 0.05652$ m, where b_n is the multipole n-field and b_1 is the quadrupole field at that radius. The k_n and k_1 are defined by:

$$k_n = \frac{b_n}{B\rho \cdot r^n} \tag{4-1}$$

Table 4-2. Positioning and strength errors taken for tracking runs. All errors are rms values, truncated at 2σ.

Transverse displacements	$\Delta x = 300$ μm; $\Delta y = 300$ μm
Longitudinal displacement	$\Delta z = 1$ mm
Roll angle (quadrupoles)	$\Delta\theta = 1$ mrad
Field setting error (dipoles)	$\Delta B/B = 0.001$
Gradient error	$\Delta k/k = 0.001$

from which it follows that

$$\frac{k_n}{k_1} = \frac{b_n}{b_1} \frac{1}{r^{n-1}} \tag{4-2}$$

Table 4-4 summarizes the systematic and random values of b_n/b_1 used in the tracking.

Table 4-3. Dipole field errors; tabulated values are rms errors, truncated at 2σ.

Multipole	Systematic	Random
Quadrupole, k_1 [m^{-2}]	0	1.1×10^{-5}
Sextupole, k_2 [m^{-3}]	2×10^{-4}	3×10^{-4}

Table 4-4. Summary of multipole errors in quadrupoles; tabulated values are rms errors, truncated at 2σ.

n	(b_n/b_1) (systematic)	(b_n/b_1) (random)
2	1×10^{-3}	0.5×10^{-3}
3	2×10^{-4}	1×10^{-4}
4	1.5×10^{-4}	0.75×10^{-4}
5	1×10^{-3}	—
6	0.5×10^{-4}	0.25×10^{-4}
7	1.5×10^{-5}	0.75×10^{-5}
8	2.5×10^{-5}	1.25×10^{-5}
9	5.0×10^{-4}	—
10	2×10^{-5}	1×10^{-5}
11	1.5×10^{-5}	0.75×10^{-5}
12	1.5×10^{-5}	0.75×10^{-5}
13	5×10^{-5}	—
14	1×10^{-5}	0.5×10^{-5}

The quadrupole data come from the measurement of one prototype magnet. Allowed harmonics were assumed to have no random component; for nonallowed multipoles, the measured values were (arbitrarily) ascribed to be half random, truncated at 2σ. During the disassembly of PEP, we will measure a sample of quadrupole magnets to obtain a better estimate of the errors for future tracking studies. These selected magnets will be measured again after reassembly to ensure that no changes have taken place.

Dynamic aperture runs were made with varying amplitudes for these errors. Multiplicative factors f_s and f_r were used to adjust (independently) the systematic and random errors, respectively.

Dynamic Aperture Determination. The HER dynamic apertures were determined by tracking particles for 1000 turns. The basic rms emittance values were taken as $\varepsilon_x = 50 \times 10^{-9}$ m·rad and $\varepsilon_y = 25 \times 10^{-9}$ m·rad, the latter corresponding to a fully coupled beam in the vertical plane. Particle starting amplitudes of 10, 15, 20, 23, 26, and 28σ in both planes were tracked. A summary of the results for the working point $\nu_x = 25.29$, $\nu_y = 24.19$ is presented in Table 4-5.

For the canonical error values $f_s = f_r = 1$, the dynamic aperture remains quite large. However, the present set of errors is relatively small and, for example, does not contain information in the higher multipoles in the dipoles. When either f_s or f_r is set to 20, the dynamic aperture collapses to well below 10σ. On the other hand, it is worth pointing out that the quadrupole errors are measured at a radius of 56 mm, whereas the 30σ beam envelope in the HER is only about 30 mm. Thus, the beam does not really experience the high-order multipole components of the field very strongly. The results obtained here are consistent with this consideration.

Table 4-5. Dynamic apertures, given in units of the normal rms beam size.

$\delta p/p$ (10^{-3})	$f_s = 1$ $f_r = 0$	$f_s = 1$ $f_r = 1$	$f_s = 1$ $f_r = 10$	$f_s = 10$ $f_r = 1$	$f_s = 5$ $f_r = 10$
0	28	28	26	15	15
2	28	28	23	15	15
–2	28	28	20	15	15
4	28	28	23	15	15
–4	28	28	23	15	20
6	28	28	23	15	15
–6	28	28	23	15	20
8	20	28	23	15	20
–8	23	15	26	23	23

No assessment has yet been made of the field quality needed for the IR quadrupoles. Insofar as the beta functions here are lower than now used at PEP, it is likely that tolerances will be relaxed compared with the present PEP IR quadrupole tolerances, but the degree to which this is true must be determined.

We conclude from the work to date that the HER ring can operate satisfactorily with the existing PEP magnets.

4.1.3.2 Low-Energy Ring. An initial study of the LER lattice has been carried out based on the same errors (summarized in Tables 4-3 and 4-4) used for the HER results quoted above. The phase advance adopted here, 80°, was selected after earlier investigations of an LER lattice with strings of 12 cells tuned to 90°. The on-momentum dynamic aperture in that case was found to be near $10\sigma_x$; this left us with a very small safety margin for the errors.

A lattice with 90° phase advance per cell is often selected when chromatic effects are to be minimized. To maximize the dynamic aperture, the cells with sextupoles are put together in groups of four, which produces a second-order achromat. To be more technical, one can say that the map for four cells will contain only second-order terms generating chromaticities and quadratic momentum compaction. However, the cubic part of the map can be more of a problem in a 90° lattice than in a 60° lattice, for example. Indeed, the cubic part will generate potentially harmful resonances, such as the $4\nu_x$ and the $2\nu_x + 2\nu_y$ resonances, in addition to the tune shifts and the $2\nu_x - 2\nu_y$ resonance found in the 60° lattice.

The dynamic aperture of the 80° ideal lattice adopted for the B Factory LER is shown in Fig. 4-34. The tracking runs were carried out with a fully six-dimensional code, including synchrotron oscillations.

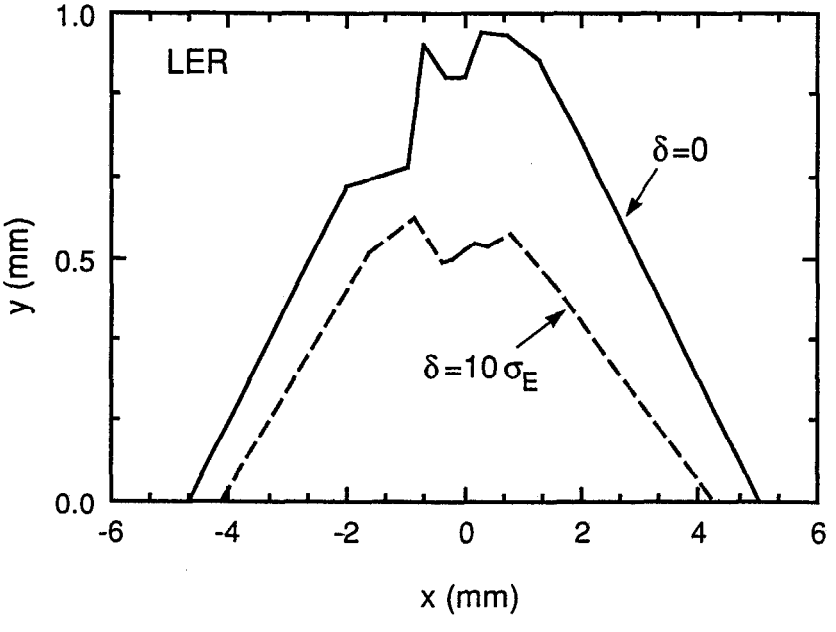

Fig. 4-34. Dynamic aperture of the 80° ideal lattice for the LER. At the tracking point, $\sigma_x = 0.2$ mm, $\sigma_y = 0.03$ mm, the vertical beam size being evaluated with the fully coupled vertical emittance.

It is clear that the LER lattice ($\nu_x = 32.29$, $\nu_y = 35.19$) provides a good starting point. At present only two families of sextupoles are being used, and these were always adjusted so that the chromaticities were near zero (within a unit). Particles are launched at the IP with initial conditions of the form $(x,0,y,0,0,\delta)$ and tracked for 400 turns.

Simulations with Errors. Next we introduced errors into the ideal lattice. For technical reasons having to do with the present status of the simulation code, we did not correct the closed-orbit distortions. Instead, the errors were reduced so as to produce an average distortion around a few tenths of a millimeter, typical of an orbit after proper correction. The multipole errors used are given in Tables 4-3 and 4-4. These were applied to all magnets in the lattice, including the permanent magnet quadrupoles in the IR. Strength errors of $\Delta B/B = 0.001$ for dipoles and $\Delta k/k = 0.001$ for quadrupoles and sextupoles, and a roll angle of 1 mrad were also included in the simulations. The resulting dynamic aperture is given by Fig. 4-35. Although there is some loss compared with the ideal lattice, the apertures are still quite acceptable.

To get a feeling for the tolerance of this 80 ° lattice, we augmented first the random and then the systematic multipole errors by a factor of 10. Figure 4-36 shows the dynamic aperture for the case of amplified random errors. Even in this case, the apertures are still quite large. This gives us some confidence that the lattice behavior is acceptable, despite the preliminary nature of these simulations. Figure 4-37 shows the aperture for the case of amplified systematic errors. For this case, the $10\sigma_E$ particle has a significantly reduced aperture; it is likely that this can be improved by using additional sextupole families, as was done for the HER. Even if the systematic errors turn out to be small,

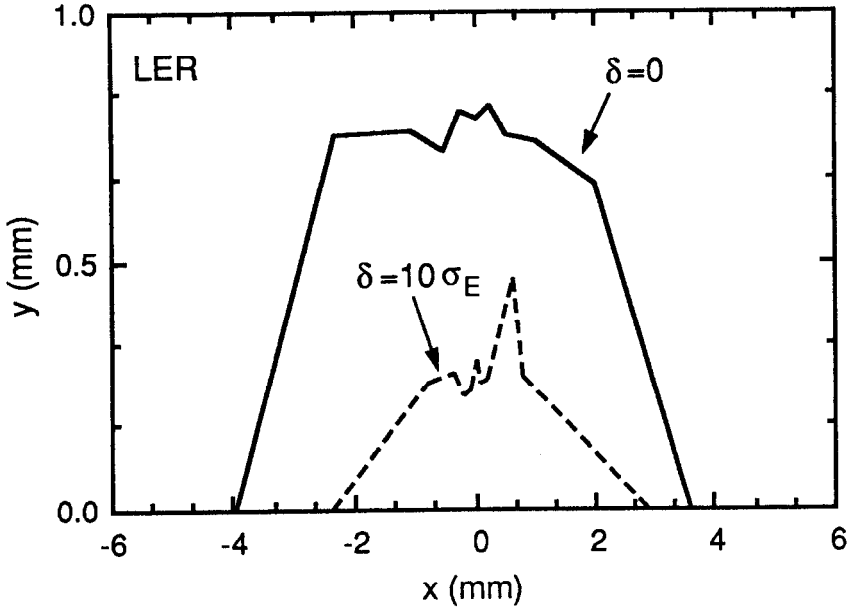

Fig. 4-35. Dynamic aperture of the LER lattice, with multipole errors included in the simulation.

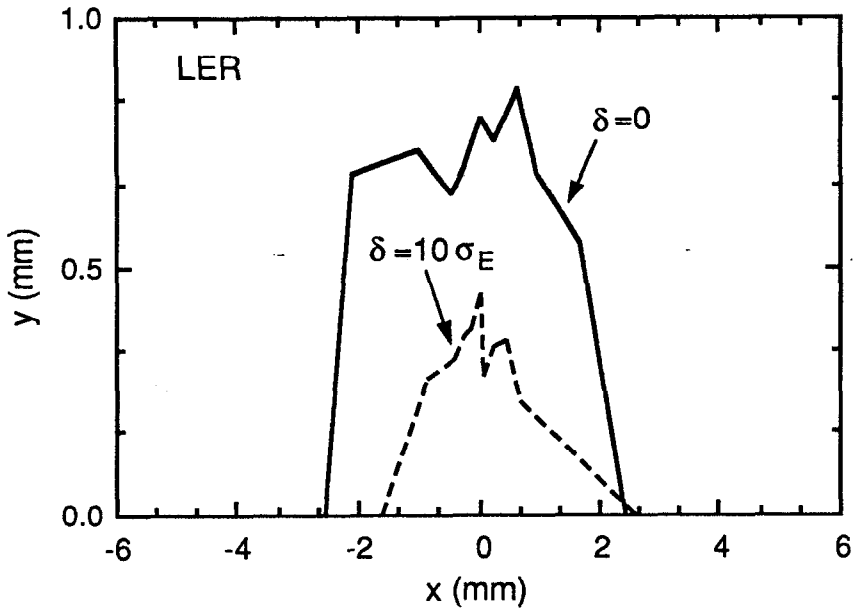

Fig. 4-36. Dynamic aperture of the LER lattice with amplified random errors.

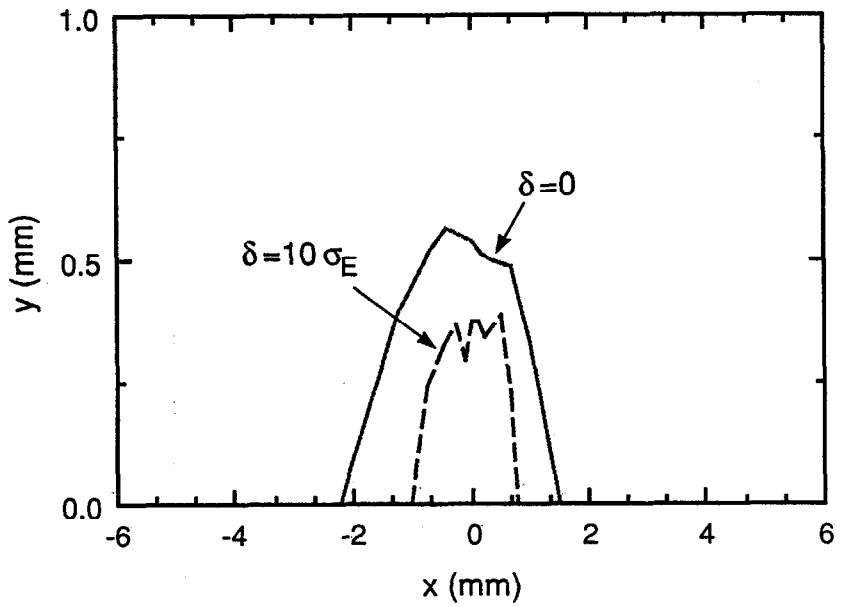

Fig. 4-37 Dynamic aperture of the LER lattice with amplified systematic errors.

future simulations done in conjunction with the beam-beam studies might lead us to modify the tunes and the chromatic behavior of the linear lattice functions. This can be accomplished with the use of additional families of sextupoles distributed, for example, as described earlier for the HER.

Initial tracking studies for both rings, based on errors from prototype PEP magnets, show that the dynamic aperture is adequate for injection and beam lifetime. Future work, using more realistic errors and possibly additional sextupole families is expected to improve the dynamics further.

4.1.3.3 Injection Studies. In many present-day colliders, much of the total radiation damage to the detector components comes during the injection process. For example, it has been estimated by Billing [1990] that at CESR about half of the total radiation dose to the detector occurs during injection. Because the B Factory will undergo injection relatively often, albeit for short periods of time, we have adopted a "graded-aperture" approach to the IR design.

As described in Section 4.2, the B Factory rings have been designed such that the beam-stay-clear aperture near the detector is given by $15\sigma + 2$ mm, whereas it is limited to 10σ elsewhere in the arc sections by means of movable collimators. (To be safe, the horizontal beam-stay-clear aperture is evaluated with the uncoupled emittance and the vertical beam-stay-clear aperture is evaluated with the fully coupled emittance.) These aperture choices are meant to ensure that the limiting aperture occurs at a well-defined location that is far away from the detector. To explore the efficacy of this graded approach, we have performed tracking studies of the injection process to see where the lost particles are stopped. Thus far, only the LER has been studied, but it is clear that the behavior of the HER will be similar.

Injection takes place in the middle of a special high-beta injection straight section, as discussed in Section 6 (see Figs. 4-25 and 6-8). For the purposes of tracking, we have kept the septum location fixed at $10\sigma_x$, that is, at 27 mm; this serves to define the limiting aperture of the ring. (In the actual design, specially designed movable collimators located upstream of the injection septum define the limiting aperture.)

In the initial simulations, we tracked the phase-space distribution of particles (at the injection point) shown in Fig. 4-38. The nominal launch point of the injected beam is at $8\sigma_x = 21.6$ mm from the closed orbit of the stored beam, so the phase-space distribution is centered at this location. For each initial condition, particles were launched with energy offsets (shown from left to right in each triplet of points) of $\delta = -1\%$, 0, and $+1\%$. As in the dynamic aperture studies discussed in Section 4.1.3.2, particles were tracked in six dimensions, that is, including synchrotron oscillations. The errors used were the same as those listed in Tables 4-3, and 4-4. To permit realistic long-term tracking, radiation damping effects were also included, using damping coefficients of $\alpha_x = \alpha_y = 2 \times 10^{-4}$ turn^{-1} and $\alpha_E = 4 \times 10^{-4}$ turn^{-1}. The aperture limitation in the arcs was taken as $x = \pm 40$ mm and $y = \pm 25$ mm; near the IP, we took the limiting aperture to be $x = y = \pm 25$ mm, and in the straight sections, we used $x = y = \pm 50$ mm.

The results are summarized in Fig. 4-38, where particles that survived for 20,000 turns are represented by filled circles and lost particles by open circles. All particles with an energy offset of $\delta = +1\%$ were lost in the first turn at a high-dispersion point, for

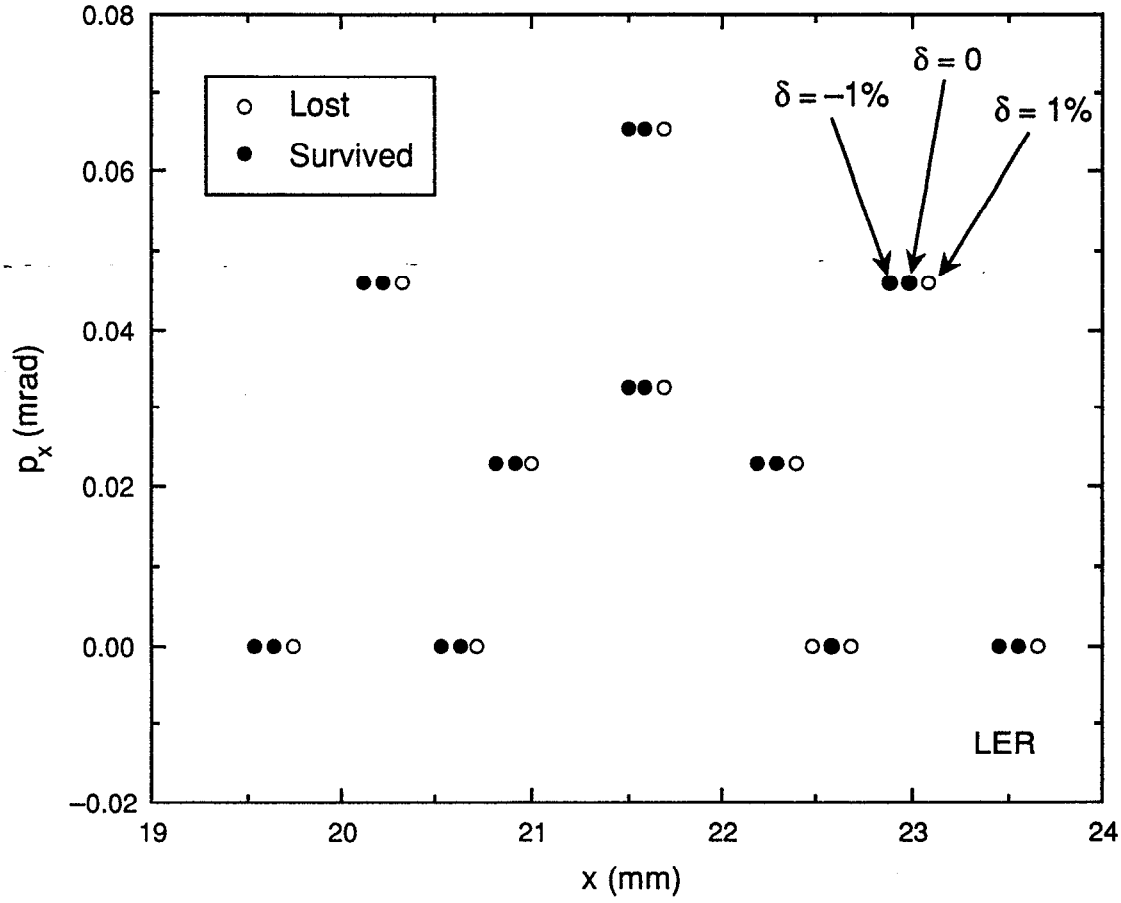

Fig. 4-38. Phase-space distribution at the injection point of particles tracked in the injection simulations with nominal lattice errors. Particles that survived for 20,000 turns are indicated by filled circles; lost particles are represented by open circles. Each triplet of points represents three different energy offsets, as indicated. The normal injection point, corresponding to $8\sigma_x$, is 21.6 mm. All lost particles stopped at a high-dispersion point, and none was lost near the IP.

example, the QFR3 quadrupole (see Fig. 4-30). Only one of the particles launched with $\delta = -1\%$ was lost, and it was lost at the $10\sigma_x$ aperture limitation represented by the septum. Although the physical aperture near the IP is smaller than in the arcs, no particle was lost in this region after 20,000 turns.

To ensure that this result is not strongly influenced by the choice of errors, we repeated the study for a lattice having large errors; these were obtained by increasing both the random and systematic errors by a factor of 10 from their nominal values. The resultant dynamic aperture (projected to the standard tracking point at the IP) is shown in Fig. 4-39. For on-momentum particles, the dynamic aperture has decreased below $10\sigma_x$; for off-momentum particles, the degradation is even more severe, down to about $5\sigma_x$.

To determine where the on-momentum particles are lost, starting amplitudes of the tracked particles were increased to cover a larger range, as shown in Fig. 4-40. For completeness, both positive and negative p_x values were tracked. Again, we indicate the surviving particles (followed for 20,000 turns) with closed circles and the lost particles

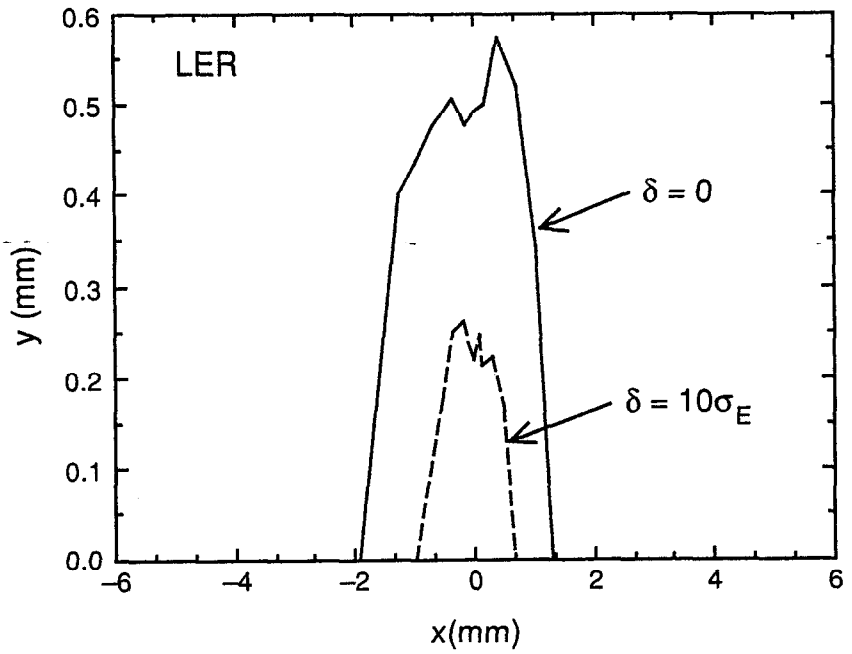

Fig. 4-39. LER dynamic aperture (at the IP) corresponding to the enhanced errors used in the injection simulation shown in Fig. 4-40.

with open circles. Despite the increased errors and larger starting amplitudes, we still see that most of the on-momentum particles survive. Of those that do get lost, all are stopped at the $10\sigma_x$ aperture, and none is lost near the IP. Results for the off-momentum particles remain the same as before; that is, they are lost in the dispersion suppressor in the region near QFR3.

From these studies, we see that a collimator located in the dispersion suppressor cell downstream of the injection point suffices to stop the off-momentum lost particles. On-momentum lost particles can be stopped in the injection straight section itself, using a collimator located upstream of the septum at a $10\sigma_x$ aperture. In reality, of course, all lost particles will not be stopped cleanly by a single collimator. At least one additional collimator will be located at a suitable distance downstream from the primary collimator to deal with edge-scattered particles.

To summarize, we conclude from this initial investigation that the use of a larger effective aperture in the IR than in the arcs ($15\sigma_x$ compared with $10\sigma_x$) is successful in eliminating the loss of particles near the IP during the injection process.

4.1.3.4 Compensation of the Detector Solenoid. One aspect of the lattice design not covered elsewhere is that of compensating for the optical effects of the detector solenoid. To explore the feasibility of restoring the ring optics in the presence of the solenoidal field from the detector, we performed a series of calculations for the LER lattice. For this purpose, it suffices to use a rather simple model of the solenoid. We therefore considered a constant-field solenoid set at $B_z = 1$ T for our initial study. If we denote the map of a solenoid of length l and field B by $S(l,B)$, then we can create a zero-length insertion, $I(l,B)$, by using the elements $I(l,B) = S(-l/2,0)\ S(l,B)\ S(-l/2,0)$.

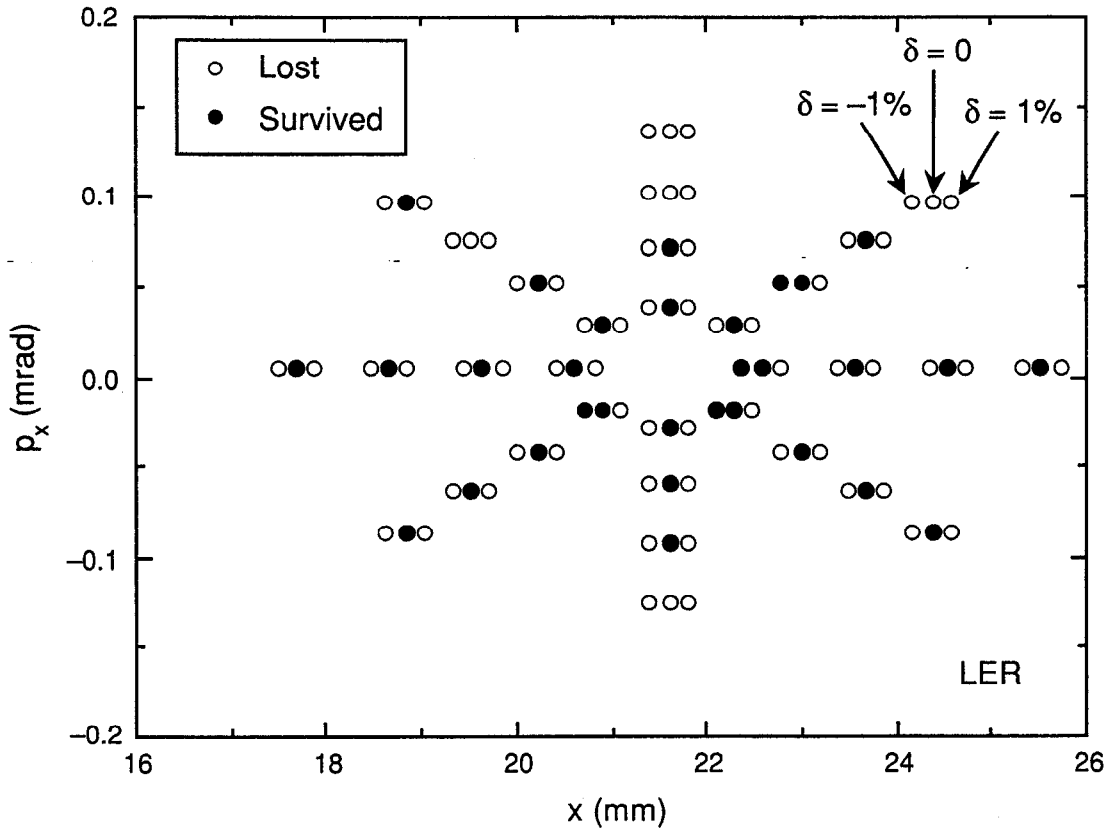

Fig. 4-40. Phase-space distribution at the injection point used in the injection simulations with enhanced errors. On-energy lost particles were stopped at a 10σ aperture; off-energy particles were stopped at a point of high dispersion in the dispersion suppressor cells. No particles were lost near the IP after 20,000 turns.

In the actual calculations, we used this approach to mimic the effect of the solenoid over an extended region near the IP by utilizing four such insertions $I(l,B)$ with $l = 0.5$ m and $B = 1$ T, located as follows (see Fig. 4-27 for the layout; all drifts are not identical):

QD4H, drift, $I(l,B)$, drift, QD3, drift, QF2, drift, QD1, drift, B1, $I(l,B)$, drift
+ mirror symmetric beamline

Because a 4 × 4 simplectic matrix can be generated by a quadratic Hamiltonian having four variables, we require 10 adjustable parameters to match the transverse optics. In other words, with 10 "knobs" we can restore a coupled, mismatched map to its original conditions. As a first attempt to do this, we placed correctors as close as possible to the IP without encroaching on the solenoid region itself. The setup employed is denoted symbolically as follows (where underlined quadrupoles are normal elements and quadrupoles marked with an asterisk have an adjustable skew component as well; again, all drifts are not identical):

QVD, drift, QVF, drift, QVD*, drift, QVF*, drift, QVD*, drift, QF4*, drift,
BV–, drift, BV1–, drift, QD4H, drift, *I*(*l*,*B*), drift, QD3, drift, QF2, drift, QD1,
drift, B1, *I*(*l*,*B*), drift, IP
+ mirror symmetric beamline

With these magnets, the map was restored to its original value, that is, one without a solenoidal field. Unfortunately, this approach does not suffice to restore the beam conditions at the IP; beam sizes in both transverse planes were roughly double their original values. An examination of the beam behavior in the rematched lattice indicates why this occurs: It is due to the fact that the dispersion has not been properly rematched by this technique. The resultant mismatched dispersion propagates around the lattice and is large enough in the wiggler sections to give rise to considerable growth in beam emittance.

We conclude from this attempt that it is not sufficient merely to reduce the dispersion at the IP to a low value. It is also necessary to match the dispersion and its slope in each transverse plane, which requires an additional four adjustable parameters. Therefore, we must add another set of quadrupoles, located in a dispersive region, to our matching parameters. After doing so, we found that the resultant solution works perfectly. With additional quadrupoles in the dispersion suppressor cells adjacent to the IP, we were able to fully restore the optics in the presence of the solenoidal field. Although we have not yet attempted to optimize the correction scheme, we conclude from the work to date that it is possible to provide sufficient parameters to do so.

4.1.4 Energy Tunability

Because the LER optics are based on permanent magnet technology and are thus not easily adjustable, some care must be taken to ensure suitable optics flexibility.

The majority of running at the B Factory will be at the $\Upsilon(4S)$ resonance. This is where the *CP* violation physics is done; the remaining physics topics, except for the Υ resonance and B_s mixing studies, are also best done at the $\Upsilon(4S)$. It will nevertheless be desirable to intersperse short runs (1–3 months) at the other resonances, the $\Upsilon(1S)$, $\Upsilon(2S)$, $\Upsilon(3S)$, and $\Upsilon(5S)$ (see Fig. 2-1). For such studies, these short runs will generate enormous increases (factors in excess of 100; see Table 2-1) over the size of data-sets currently available. In addition to a short run at the $\Upsilon(5S)$, a longer dedicated run (on the order of 30 fb^{-1}) will be needed for studies of B_s mixing; for this, it may well be prudent to reoptimize the IR region, increasing the machine asymmetry and reducing the radius of the first layer of the silicon vertex detector. This experiment is not foreseen early in the program; it will commence after a comprehensive *CP* violation program has been established.

The Asymmetric B Factory has been designed to accommodate this program. The collision energy is tunable over the full range of energies from the $\Upsilon(1S)$ to the $\Upsilon(5S)$. The strategy for covering the range from the $\Upsilon(2S)$ to the $\Upsilon(5S)$ is to change both the electron and positron beam energies, keeping their ratio constant. Scaling the fields in the accelerator lattice magnetic elements and in the trim coils (see Section 5.1.3) of the samarium-cobalt IR magnets accordingly (±4%), the particle orbits are kept identical and the change is transparent to the accelerator environment.

To run at the $\Upsilon(1S)$, the positron energy is kept constant at 2.942 GeV and the electron energy is lowered by 11% to 7.6 GeV. The currents in all the magnets in the HER are scaled in proportion to the electron beam energy. The trajectories are restored to within a few millimeters of their nominal positions by adjusting the magnetic field in B1, the position and angle of the incoming beams, and the position of the IP itself. We have assured ourselves that the beam trajectories in this case—as at higher center-of-mass energies—remain within our conservatively defined stay-clear region of $15\sigma + 2$ mm.

The B Factory has been designed to deliver a luminosity of 3×10^{33} cm^{-2} s^{-1} at the $\Upsilon(4S)$. It is, of course, desirable to maintain this maximum luminosity for the short Υ-physics runs; by the very nature of the large increase in statistics these runs will bring, however, moderate reductions in machine luminosity pose no problems.

The luminosity of the B Factory at different center-of-mass energies can be derived in a straightforward way from the scaling of a single-ring circular collider. In going from the $\Upsilon(4S)$ to the $\Upsilon(5S)$, the beam energies must be raised by 2.4%. In a conventional electron-positron collider, most of the RF power is devoted to producing the cavity voltage at the design energy. Above this energy, the voltage required is proportional to the synchrotron radiation loss (the well-known γ^4 law), so the cavity dissipation scales as γ^8. Since the tune shift is proportional to γ, the luminosity scales as γ^7. In the case of the B Factory, the cavity wall losses are only about one-third of the total power; the existing spare capacity can therefore be used to keep the luminosity approximately constant up to the $\Upsilon(5S)$.

In the regime below the nominal energy, and with fixed optics, the beam dimensions are proportional to γ. (In this regime, the RF power needed to restore synchrotron radiation is always less than at the design energy.) The current per beam is then limited by the beam-beam tune shift equation, scaling as γ^3. The luminosity then scales as γ^4. In the B Factory, as in most modern storage rings, the emittance can be optimized by using wigglers or dispersion mismatching. In this case, it is possible to keep the beam dimensions constant as the energy varies. Under these conditions, the luminosity varies as γ^2, giving a 10% reduction in luminosity at the $\Upsilon(1S)$.

4.2 ESTIMATION OF DETECTOR BACKGROUNDS

The problem of machine-related backgrounds is one of the leading challenges in the B Factory project: The detector must be sufficiently well-protected to prevent either excessive component occupancies or deterioration from radiation damage. In effect, what is required is to achieve background rates similar to those of existing colliders, but at beam currents an order of magnitude higher. There are three primary sources of backgrounds:

- Synchrotron radiation photons produced in the machine magnetic elements
- Off-energy electrons and photons produced in bremsstrahlung interactions with background gas molecules
- Elastically (Coulomb) scattered, off-angle electrons produced in interactions with background gas molecules

These background sources can give rise to primary particles that can either enter the detector directly or generate secondary debris that ultimately reaches the detector.

We have carefully simulated, in great detail, the effects of these backgrounds. It is probably fair to say that the interaction of machine backgrounds and the detector environment has never been so exhaustively studied for any previous accelerator. This level of detail is mandatory in the case of a B Factory design, because the consequences of underestimating the effects of the background are so serious. Thus, we view the considerations described in this section to be the sine qua non of the Asymmetric B Factory design.

In what follows, we try to convey the breadth of the considerations and the level of detail that were incorporated in the simulations. Before delving into the details of the calculations, however, it is useful to provide an overview that describes the thrust of our approach to the machine optimization.

The attraction of head-on collisions and magnetic separation of the heteroenergetic beams was discussed in Chapter 3. As indicated there, we believe that this strategy provides the most conservative approach to achieving high luminosity in an asymmetric collider. Magnetic separation (as opposed to using a nonzero crossing angle) does come at a price, however. The separating elements (dipoles and quadrupoles) generate high levels of radiated power and consequently a large flux of synchrotron radiation photons. Two issues thus dominate the optimization of the interaction region (IR) optical design: controlling the resultant backgrounds and effectively managing the absorption of the power. Achieving these goals simultaneously is quite difficult. Indeed, we generated many attractive IR geometries that were ultimately rejected because one or both of these criteria could not be met.

It is also crucial to subject each promising design to the stringent test of a realistic engineering solution for the IR elements (magnets, masks, etc.). Both the limiting of backgrounds and the ability to engineer all the beamline elements in the IR must be demonstrated before the design can be deemed acceptable. We believe that what follows in this section (management of backgrounds) and the detailed engineering considerations

for all the IR mechanical elements, covered in Sections 5.1.3 and 5.2.7, represent a robust and completely satisfactory solution.

Our design strategy was to choose the placement and apertures of the IR magnetic elements in such a way as to ensure that most (about 90%) of the radiated power produced close to the interaction point (IP) is absorbed on downstream surfaces far away from the detector. This is the key ingredient in the success of the design, because it ensures that local sources of secondary interactions are greatly limited. Our strategy requires a careful evaluation of all the material required for the machine elements and for their support, as well as a generous space allowance between the radiation fans and any such material. Realistic evaluations of the space required for the IR elements have been based on the detailed engineering designs discussed in Section 5.1.3; appropriate clearances, including an allowance for displacement of the beam orbit, have been incorporated. It has also proved important to provide a low gas pressure (1 nTorr) in the section of beam pipe in each ring that immediately precedes the IR. Because this region is relatively free of machine components, this vacuum requirement is not technically difficult.

In addition to paying attention to these engineering details, sufficient care must also be taken with the simulations of the absorption, scattering, and reemission of radiation incident on masks, beam pipe walls, magnets, etc. In our simulations, all primary sources (both electrons and photons) were propagated from their creation to the point where they are intercepted by a machine element. For charged particles, the effects of all magnetic elements were taken into account. The EGS electromagnetic shower simulation code was used to track the debris of the showers. This code includes the material properties appropriate to each intercepting element, the incidence angle and energy of the showering particle, and the geometry of the scatterer (particularly thin, sharp edges or "tips"). The shower process is followed until an inventory, in terms of both energy and number, of all electrons, positrons, and photons hitting each detector element has been established. The appropriate material, geometry, and magnetic effects of the detector are incorporated in establishing this inventory.

In what follows, we turn first to the details of the synchrotron radiation backgrounds (Section 4.2.1), next to the inventory of where all the synchrotron radiation power is deposited (Section 4.2.2), and finally to the consideration of lost-particle backgrounds (Section 4.2.3). We will see that the design we adopted provides a considerable safety margin between the occupancy and radiation-tolerance levels of the detector components and the estimated levels of detector backgrounds.

4.2.1 Synchrotron Radiation Backgrounds

Several sources must be considered in the investigation of synchrotron radiation backgrounds:

- Direct synchrotron radiation (primary masks must be placed to prevent such radiation from striking the detector beam pipe, at the same time keeping the number of photons striking their tips to an acceptable level)
- Photons that scatter through a mask tip

- Sources of synchrotron radiation from elements far upstream of the IP
- Sources of backscattered photons from downstream surfaces

These issues are taken up here, along with a discussion of the calculational procedure used for predicting detector backgrounds. Our conclusions are that synchrotron radiation background rates are 100 times lower than the allowable detector occupancy and radiation damage limits.

A detailed tracing of all the synchrotron radiation power must also be undertaken to make sure that no background problems arise from surfaces where the power is absorbed. This study is described in Section 4.2.2.

Separating the unequal-energy beams by the use of bending magnets and offset quadrupoles generates several fans of synchrotron radiation. The geometry of the IR optics, however, is designed to minimize the amount of synchrotron radiation that strikes nearby surfaces. In particular, the "S-bend" geometry of the beamlines (see Fig. 4-41)

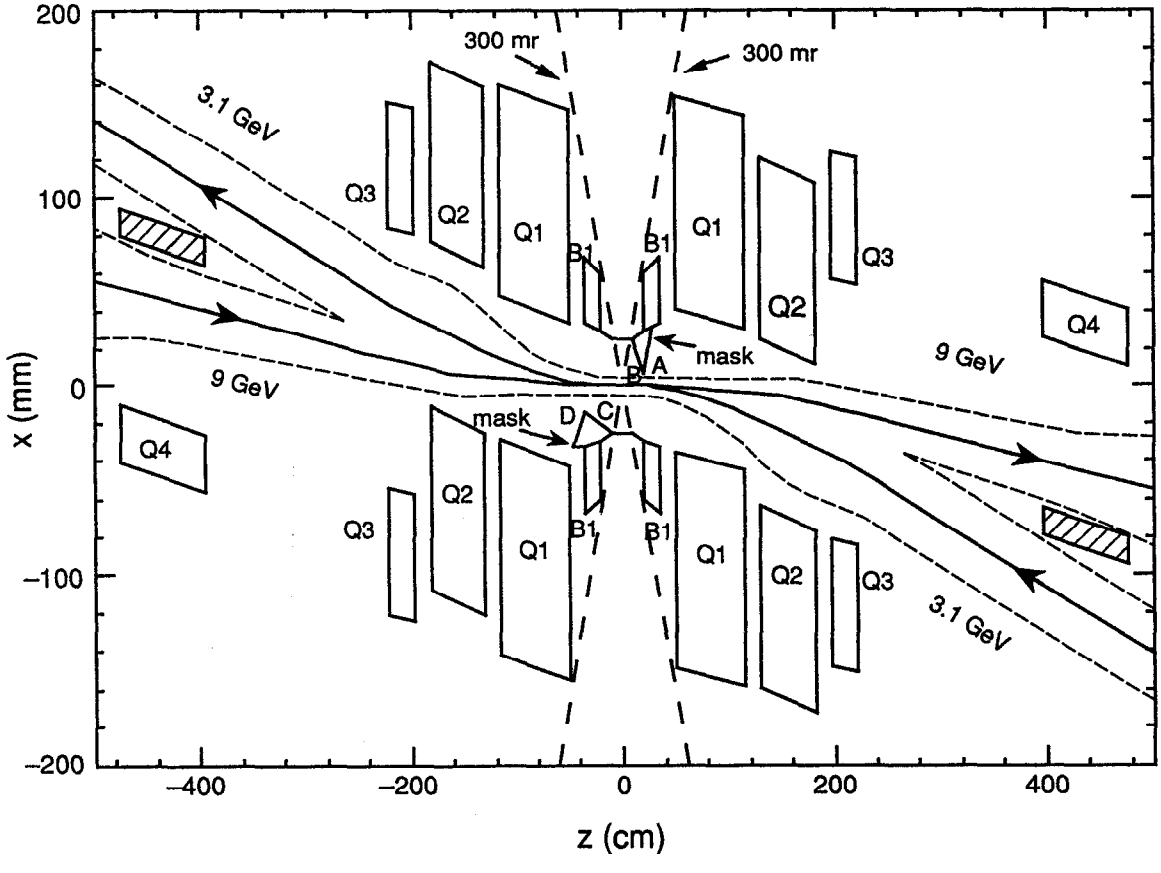

Fig. 4-41. General layout of the interaction region. The vertical scale is highly exaggerated. The dashed lines are the beam-stay-clear envelopes. The masks labeled AB and CD shield the detector beam pipe from direct synchrotron radiation. The mask surfaces A and D are sloped so that incoming photons striking these surfaces cannot scatter directly onto the detector beam pipe.

allows most of the synchrotron radiation generated by magnetic elements upstream of the IP to pass through the detector region without hitting local surfaces.

For this discussion, synchrotron radiation generated by beam particles is separated into two categories:

- Radiation generated by a beam passing through a bending magnet or an offset quadrupole; this is referred to as *fan radiation.* The intensity and power density of the fan radiation are high, because all of the beam particles contribute.
- Radiation generated by a beam that is on-axis as it travels through a quadrupole; this is referred to as *quadrupole radiation.* The intensity and power density of quadrupole radiation are much lower than for fan radiation, because the radiation is dominated by beam particles that are some distance away from the beam centerline, usually by three or more rms beam widths ($\sigma_{x,y}$).

In general, quadrupole radiation contributes only about 1% of the power generated by fan radiation, and the power is spread out over a much larger surface area. All calculations of detector backgrounds reported here include both fan and quadrupole radiation. Power calculations and estimates of photon power density on surfaces, described in Section 4.2.2, include only fan radiation. Both types of calculations are based on the nominal beam currents: 1.48 A for the high-energy beam (HEB) and 2.14 A for the low-energy beam (LEB).

As shown in Fig. 4-41, the LEB is centered in the Q2 quadrupole, and the HEB is centered in both the Q1 and Q3 quadrupoles. This combination of offsets maximizes the separation of the beams as they travel through these magnets. The Q1 and Q3 quadrupoles are horizontally defocusing. Therefore, offsetting the LEB in these magnets produces substantial beam deflection. Because Q2 is horizontally focusing, offsetting the HEB in this quadrupole helps the beam separation by minimizing the beam deflection.

The apertures of the separation dipole magnet B1 and the quadrupoles Q1, Q2, and Q3 are large enough to accommodate at least 5 mm of radial space for a beam pipe and trim coils, while still maintaining 2 mm of free space between the beam pipe and either the synchrotron radiation fans or the 15σ envelope of the beam. (For determining beam-stay-clear apertures, we use the *uncoupled* horizontal emittance and the *fully coupled* vertical emittance, as discussed in Section 5.2.)

4.2.1.1 Synchrotron Radiation Fans. The LEB generates synchrotron radiation fans as it passes through the Q3, Q1, and B1 magnets on its way to the IP. Figure 4-42 shows the LEB radiation fans near the IP. The mask labeled AB in Figs. 4-41 and 4-42 is designed to prevent any of the synchrotron radiation (either fan or quadrupole) generated by the upstream magnets from directly striking the detector beam pipe. Surface A of mask AB is sloped such that incoming photons striking it cannot scatter into the detector beam pipe. To clear the radiation that goes by the AB mask tip, the Q1 magnet on the downstream side of the IP for the LEB, though centered on the high-energy beamline, is rotated with respect to the HEB axis by 22 mrad. As can be seen in Fig. 4-42, the AB mask absorbs all of the fan radiation from the upstream Q3 magnet. The fans generated by the two B1 magnets and by the downstream Q1 and Q3 magnets pass through the IR without striking any surfaces. The first surface that intercepts these fans is the "crotch mask" in front of the Q4 septum quadrupole, located 3.96 m from the IP (see Fig. 4-41).

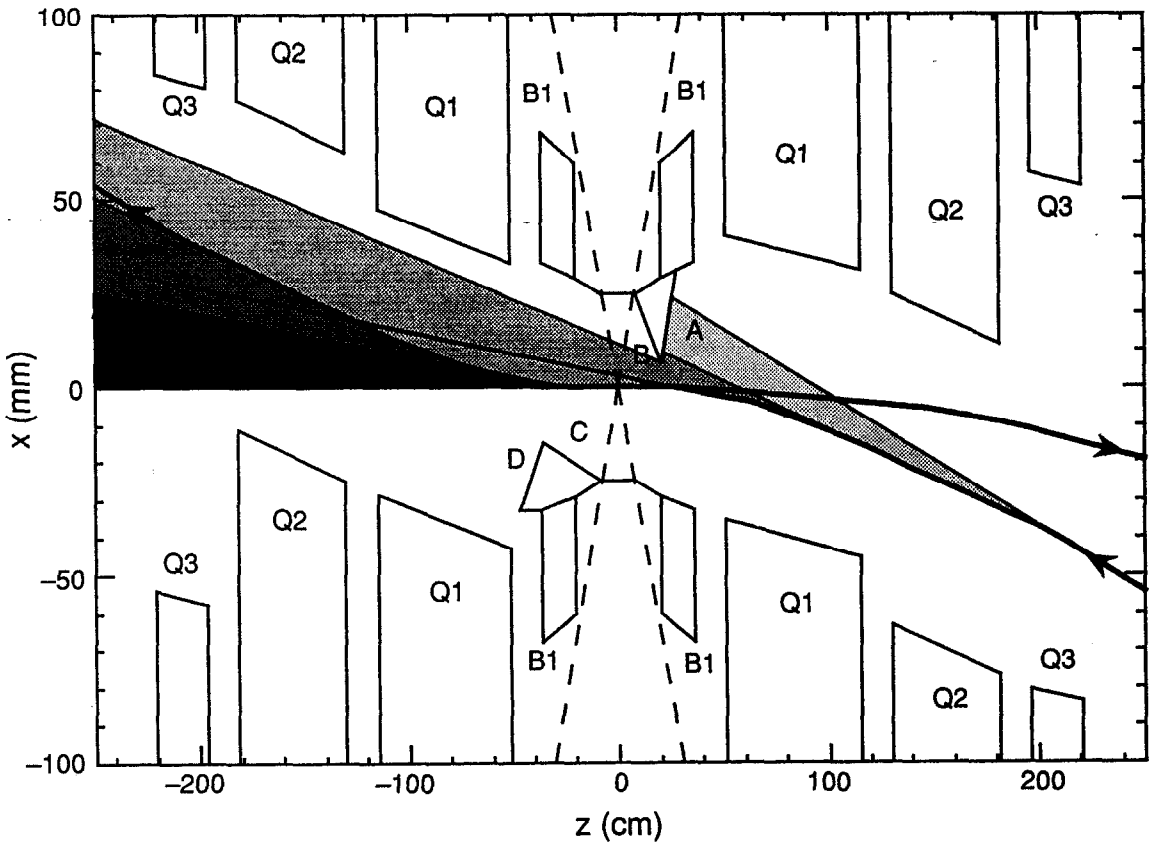

Fig. 4-42. Detail of the IR geometry, showing the radiation fans from the low-energy beam. The density of shading gives a crude indication of the relative photon intensity from the various radiation fans.

About 400 W of power is deposited on this mask from both of the LEB Q1 fans. Table 4-6 summarizes some of the properties of the LEB and HEB radiation fans.

The synchrotron radiation fans generated by the HEB as it passes through the Q2 and B1 magnets also pass through the detector region without striking any surfaces. Figure 4-43 shows the HEB radiation fans near the IP. The mask labeled CD in Figs. 4-41 through 4-43 is located to prevent quadrupole radiation produced by the HEB in Q5 and Q4 (the last major focusing elements for the HEB before the collision point) from directly striking the detector beam pipe. Again, surface D of mask CD is sloped such that scattered photons cannot reach the detector beam pipe. The CD mask tip is positioned 2 mm outside the Q2 radiation fan that passes through the IR. The first surface struck by the upstream Q2 fan is the crotch mask in front of the Q4 septum quadrupole (see Fig. 4-44). This crotch mask must be capable of absorbing 4.3 kW of power; a satisfactory design is described in Section 5.2.7.

Again, the Q1 magnet downstream of the IP for the HEB is tilted with respect to the HEB axis by 15 mrad, so it clears the synchrotron radiation fan generated by the upstream Q2 magnet.

As can be seen in Table 4-6, most of the synchrotron radiation power is generated by the HEB, and all but 4.3 kW of this power passes through the IR without striking any

Table 4-6. General properties of the fans of synchrotron radiation generated by the B1 magnets and the offset beams in the quadrupoles within ±3 m of the IP. The values are based on the nominal beam currents of 1.48 A for the HEB and 2.14 A for the LEB.

Magnet	Fan power (kW)	N_γ (10^{10})	ε_{crit} (keV)
LEB:			
Upstream Q3	0.84	3.1	2.3
Upstream Q1	0.83	5.4	1.3
Upstream B1	2.39	4.2	4.8
Downstream B1	2.39	4.2	4.8
Downstream Q1	0.96	5.2	1.4
Downstream Q3	0.91	3.1	2.4
Subtotal	8.3	13	
HEB:			
Upstream Q2	28.3	7.5	32.1
Upstream Q1	2.3	2.7	7.3
Upstream B1	13.8	2.9	40.4
Downstream B1	13.8	2.9	40.4
Downstream Q1	1.1	1.8	5.1
Downstream Q2	26.1	7.3	30.5
Subtotal	85.4	25	
Total	93.7	38	

local surfaces. A complete inventory of synchrotron radiation power striking various surfaces near the IP is presented in Section 4.2.2.

4.2.1.2 Detector Backgrounds from Synchrotron Radiation. To evaluate detector backgrounds from synchrotron radiation, a series of programs was used. A flow diagram corresponding to the description below is shown in Fig. 4-45. As a first step, a machine lattice file is produced in which magnet positions, lengths, and strengths are specified, as well the position of each beam in each magnet. This information is fed into two programs, MAGBENDS and FINBETAS. The MAGBENDS code produces a beamline geometrical layout and calculates the fan power distribution. The FINBETAS code is used to calculate beta functions, beam sigmas, and beam-stay-clear envelopes for both beams. Information from both of these programs is used to produce pictorial layouts of the IP region. In addition, outputs from these two programs are used to make the input file for SYNC_BKG, an enhanced version of the code QSRAD that was originally written to study synchrotron radiation backgrounds at PEP and that has also been used to model backgrounds at the final focus of the SLC.

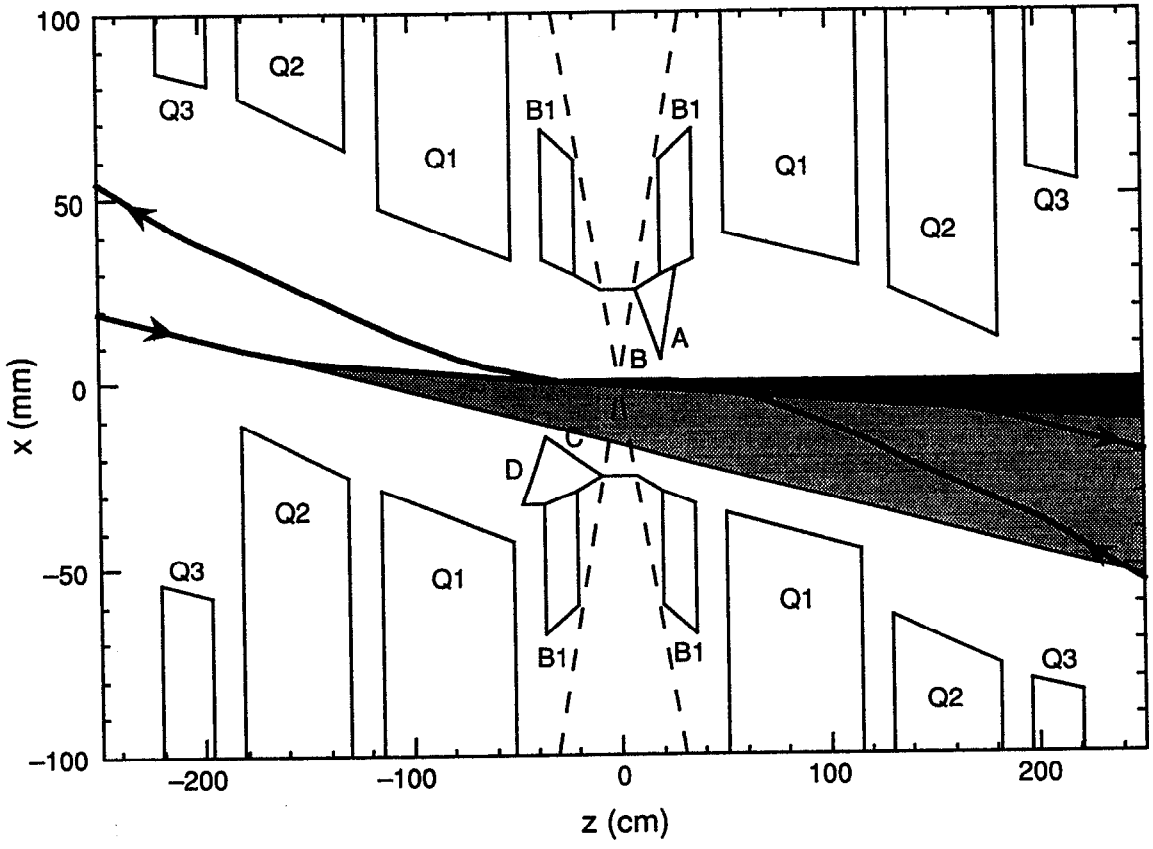

Fig. 4-43. Detail of the IR geometry, showing the radiation fans from the high-energy beam. The density of shading gives a crude indication of the relative photon intensity from the radiation fans. The tip of the CD mask is at least 2 mm outside the fan of radiation generated by the HEB as it goes through Q2.

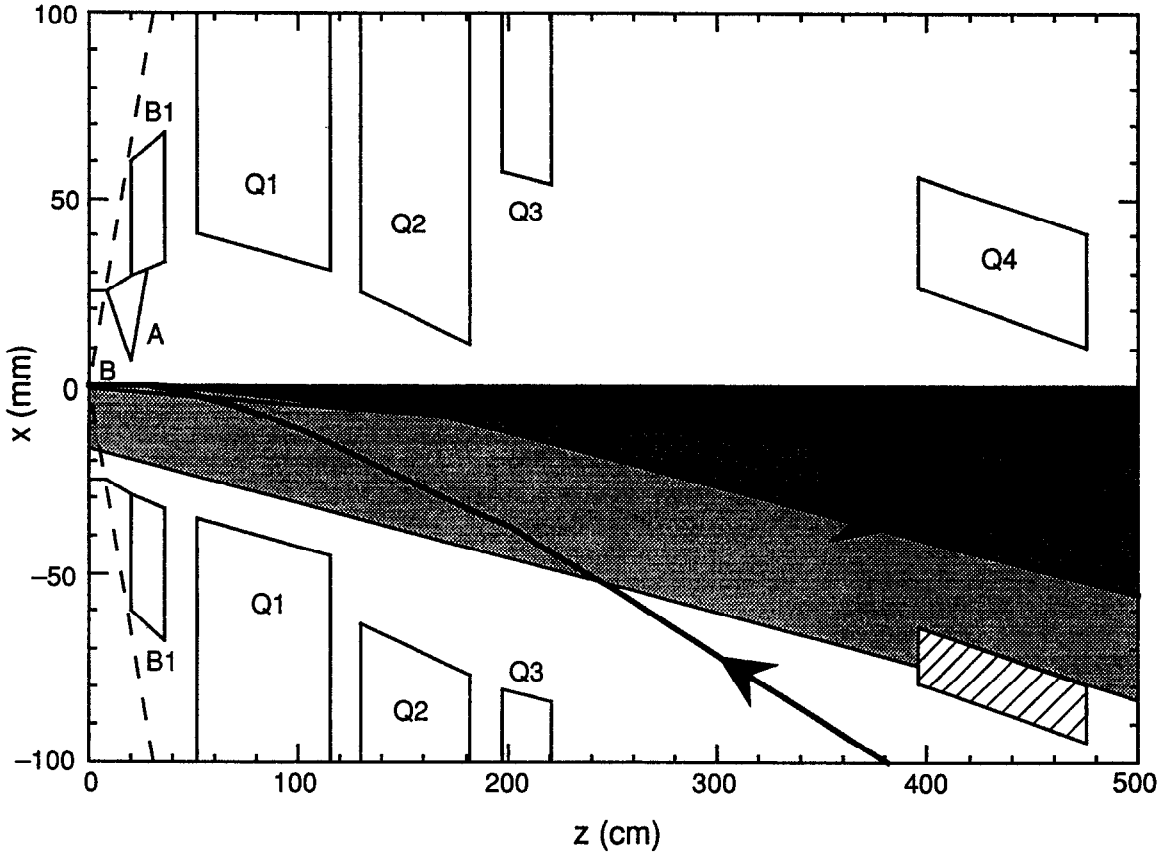

Fig. 4-44. The HEB synchrotron radiation fan from the upstream Q2 magnet that strikes the crotch mask (not shown) in front of Q4. The Q4 crotch is shown crosshatched.

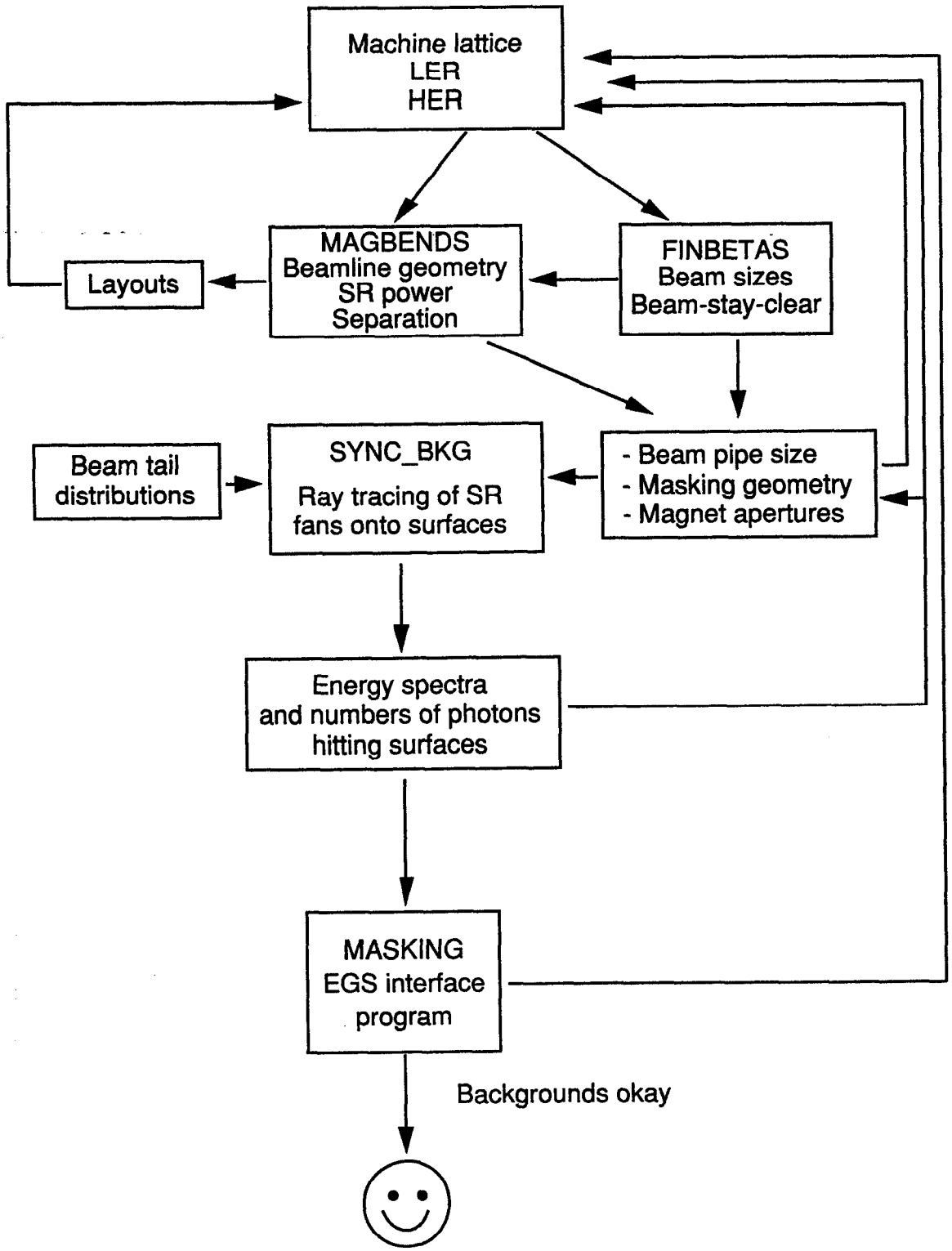

Fig. 4-45. Flow diagram of the procedure for calculating detector backgrounds from synchrotron radiation. At various stages in the procedure, a problem can be uncovered that forces a change in either the lattice or the masking geometry. This is represented by the various arrows returning to the lattice and masking geometry boxes. For any single design, many trips around these internal loops are needed before the design is either accepted or rejected.

The SYNC_BKG program traces rays for the entire beam profile through quadrupoles and produces synchrotron radiation fans that are "scored" on various user-supplied mask surfaces. SYNC_BKG tallies both the number of photons striking each surface and the photon energy distribution. In the case of the B Factory, the masking and beam pipe surfaces are designed so that the only nearby sources of photons that can reach the detector beam pipe are the tips of the masks AB and CD.

In addition to the beam pipe and masking geometry, SYNC_BKG also receives information about the transverse profile of the beam. Although its exact shape is not easily predicted, a non-Gaussian beam profile might result from, say, the beam-beam interaction. We include this possibility in our calculations by introducing a second Gaussian that has a larger rms width (σ) and a lower amplitude than that of the nominal beam core. Adding these two distributions together produces a non-Gaussian beam profile, with enhanced particle densities at large amplitudes. This parametrization of the beam tail yields two variables, the amplitude A of the distribution and the scaling factor S for the beam tail width. Figure 4-46 shows the beam distributions and the values of A and S used in this study; these values result from a previous study of synchrotron radiation backgrounds at PEP. To ensure that detector background rates are acceptable under all conditions, the beam-tail distributions are traced out to the limiting aperture of the ring. In the case under study, this means $10\sigma_{x0}$ and $35\sigma_{y0}$. We determined that our masking design is insensitive to the exact beam-tail distribution. Removing the tail distribution completely results in a very small (about 1%) change in detector background rates.

The information from SYNC_BKG is fed into an EGS [Nelson et al., 1985] interface program called MASKING. As indicated in Fig. 4-47, for a given incident photon energy spectrum, this program produces reflected, transmitted, and absorbed photon energy spectra. (A large selection of elements and compounds is available for the intercepting materials.) The EGS package includes K-shell photon fluorescence and Rayleigh scattering, but does not have provision for L-shell fluorescence. (Calculations of L-shell fluorescence suggest only small increases in the synchrotron radiation background rates we have computed.) MASKING uses an infinite-slab geometry to calculate the spectrum of photons that reflect from a surface or that penetrate through materials (for example, a beam pipe). In addition, a finite-slab geometry is available to study tip scattering. The files of reflection, transmission, and absorption coefficients thus produced are collected by another program (PHTALLY) and folded together to produce the background rates for various detector elements. These are displayed in Table 4-7. For comparison, Tables 2-5 and 2-6 indicate the maximum numbers of photons/μs that are permissible in terms of detector occupancy and radiation damage considerations. Figures 4-48 and 4-49 show the photon energy spectra for the HEB and LEB, respectively.

4.2.1.3 Tip Scattering. The scattered photons incident on the detector beam pipe are those that scatter through the tips of masks AB and CD. Figure 4-50 illustrates the mechanism of tip (as opposed to surface) scattering. The coordinate system in Fig. 4-50 is based on the direction-cosine axes for the incident photons. The tip-scattering effect is modeled by uniformly generating the incident photons along a line perpendicular to the edge of the material. The angular distribution of tip-scattered photons is azimuthally uniform in the UV plane (see Fig. 4-50a), but there is a preference for photons to scatter

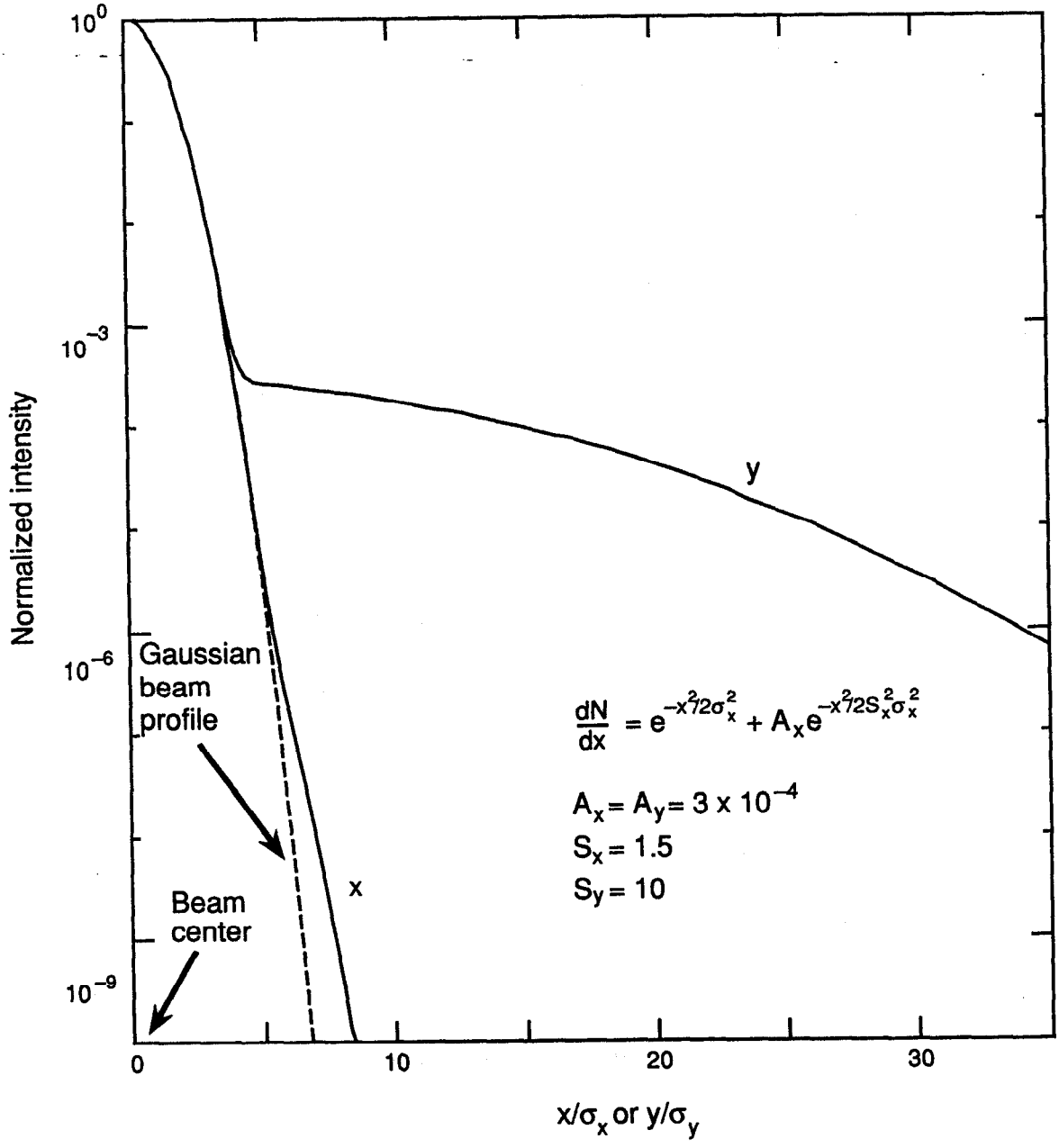

Fig. 4-46. Plot of the beam profiles assumed for the calculation of detector backgrounds due to synchrotron radiation. The integral of the background Gaussian is about 0.25% of the main beam Gaussian.

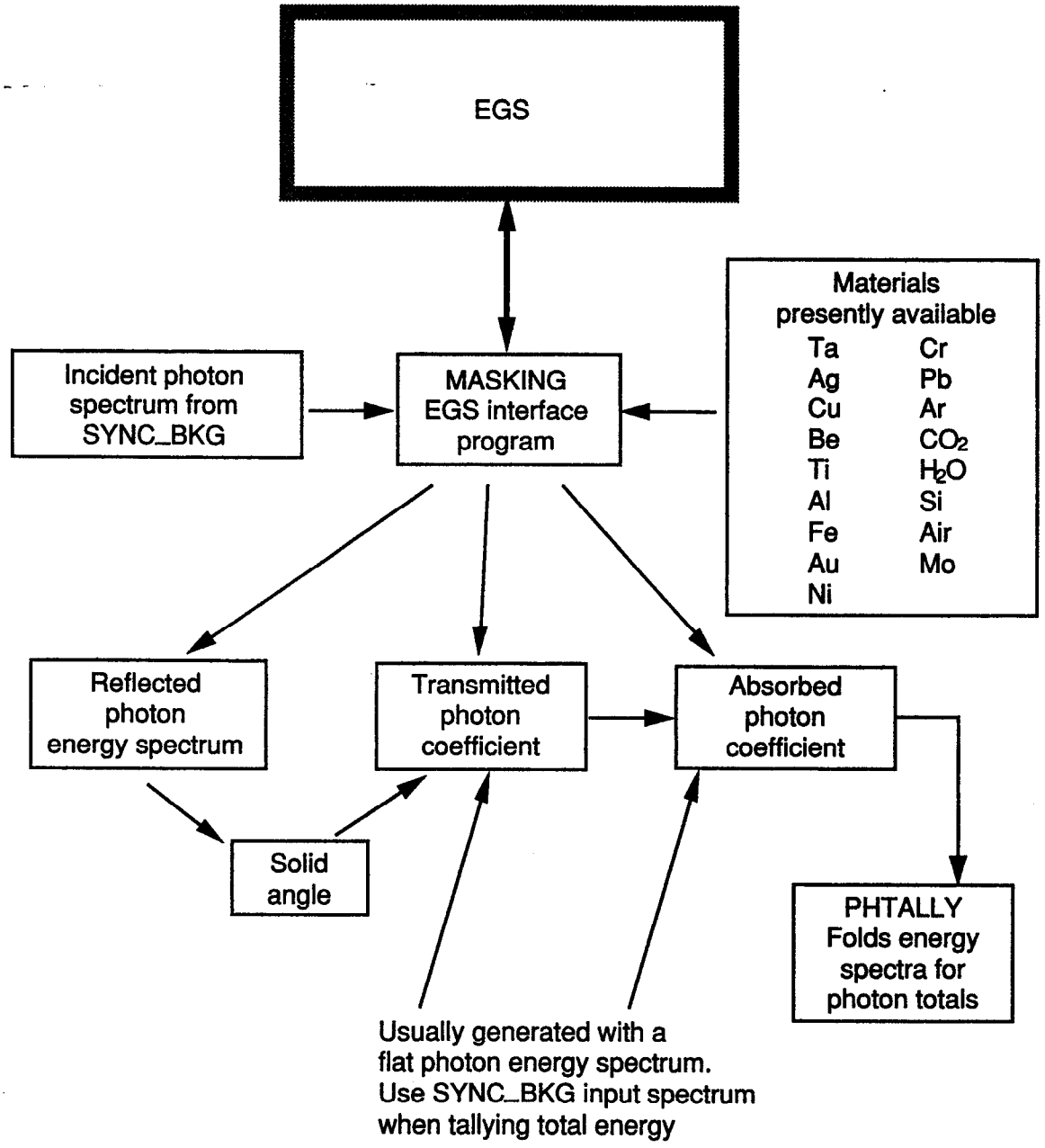

Fig. 4-47. Flow diagram of the procedure for producing reflection, transmission, and absorption coefficients and final photon spectra.

Table 4-7. Synchrotron radiation detector background predictions. The numbers are for each crossing. Multiply by 2.38×10^8 to get photons per second. The energies refer to the total energies of the indicated photons. The beam pipe materials are 25 μm of Cu and 1 mm of Be. The beam pipe inner radius is 2.5 cm with a 17-cm length for the Be section. The average angle of incidence is 100 mrad for the radiation striking the beam pipe from the tip of the CD mask and 200 mrad for the radiation striking the beam pipe from the AB mask tip. The silicon layers are 300 μm thick. The number of photons per crossing penetrating the beam pipe and incident on the first layer of silicon is 0.038. The total energy of these photons is 1.19 keV.

	Incident on Be pipe	Absorbed in first Si layer	Absorbed in second Si layer	Absorbed in third Si layer	Incident on drift chamber
			3.1-GeV beam		
$4 < E_\gamma < 100$ keV:					
Number of photons	0.39	1.0×10^{-3}	3.9×10^{-6}	3.4×10^{-7}	1.8×10^{-9}
Energy (keV)	2.48	9.4×10^{-3}	3.8×10^{-5}	3.4×10^{-6}	1.9×10^{-8}
$4 < E_\gamma < 20$ keV:					
Number of photons	0.39	1.0×10^{-3}	3.9×10^{-6}	3.4×10^{-7}	1.8×10^{-9}
Energy (keV)	2.48	9.4×10^{-3}	3.8×10^{-5}	3.4×10^{-6}	1.9×10^{-8}
			9.0-GeV beam		
$4 < E_\gamma < 100$ keV:					
Number of photons	0.65	0.017	6.6×10^{-4}	6.0×10^{-4}	1.5×10^{-4}
Energy (keV)	10.0	0.48	0.03	0.03	7.8×10^{-3}
$4 < E_\gamma < 20$ keV:					
Number of photons	0.52	6.4×10^{-3}	3.2×10^{-5}	9.4×10^{-6}	2.1×10^{-7}
Energy (keV)	5.20	0.075	4.1×10^{-4}	1.4×10^{-4}	3.7×10^{-6}
			Totals		
$4 < E_\gamma < 100$ keV:					
Number of photons	1.04	0.018	6.6×10^{-4}	6.0×10^{-4}	1.5×10^{-4}
Energy (keV)	12.5	0.49	0.03	0.03	7.8×10^{-3}
$4 < E_\gamma < 20$ keV:					
Number of photons	0.91	7.4×10^{-3}	3.6×10^{-5}	9.7×10^{-6}	2.4×10^{-7}
Energy (keV)	7.68	0.084	4.5×10^{-4}	1.4×10^{-4}	3.7×10^{-6}

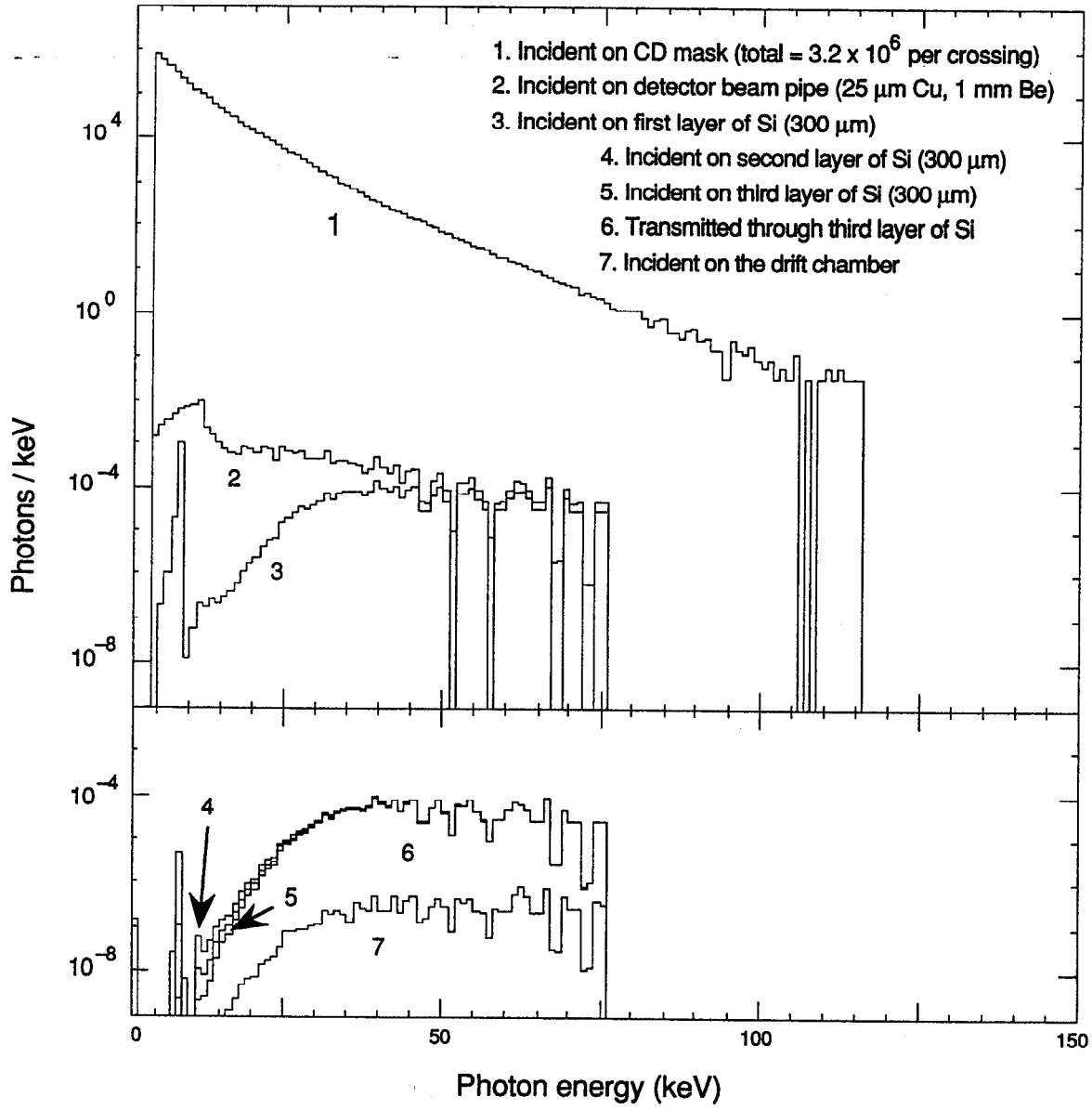

Fig. 4-48. Final photon spectra for the HEB. The initial photon spectrum is incident on the 500 μm of the CD mask nearest the edge. The second spectrum results from photons that have scattered through the tip of the CD mask.

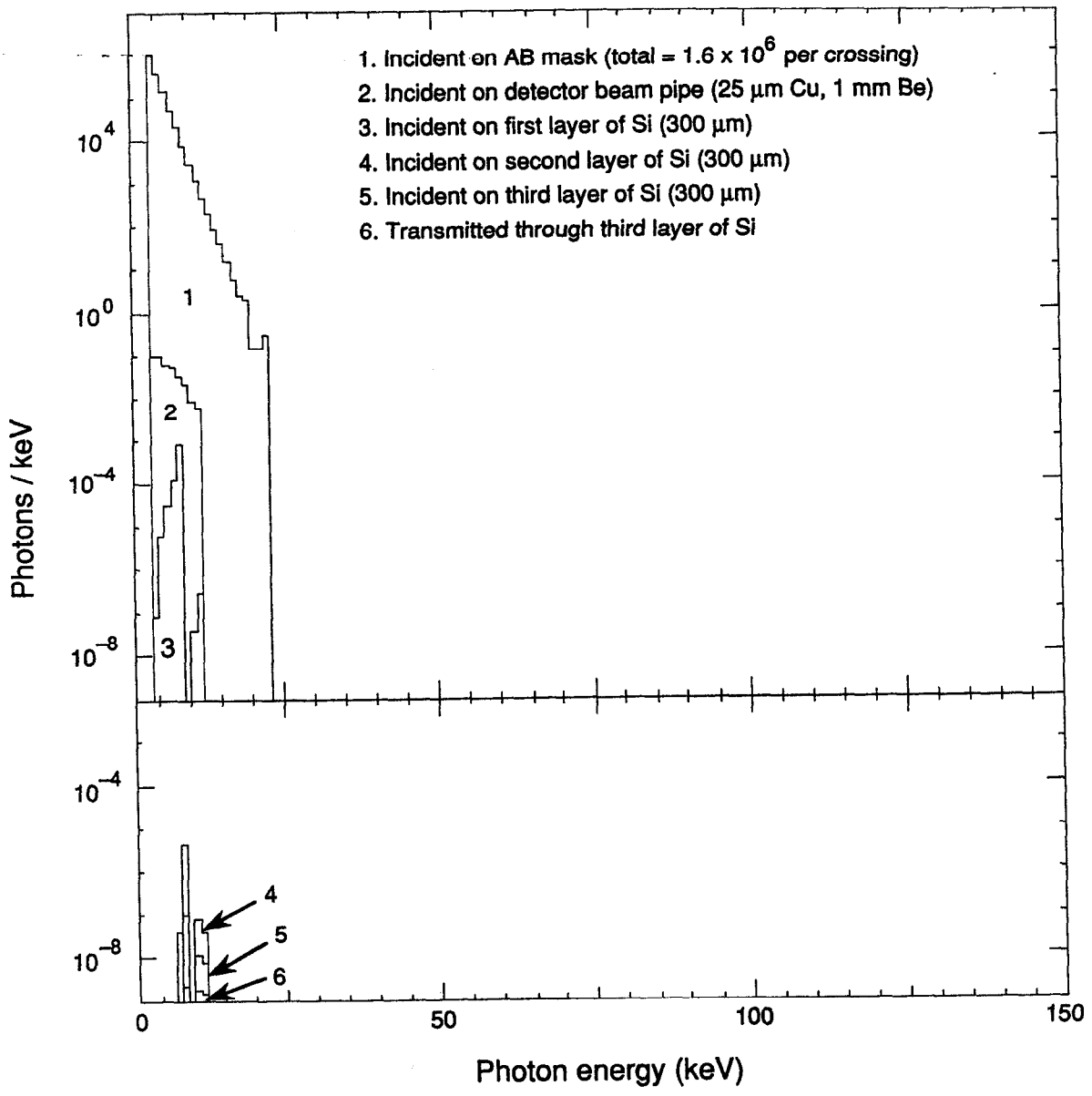

Fig. 4-49. Final photon spectra for the LEB. The initial photon spectrum is incident on the 500 μm of the AB mask nearest the edge. The second spectrum results from photons that have scattered through the tip of the AB mask.

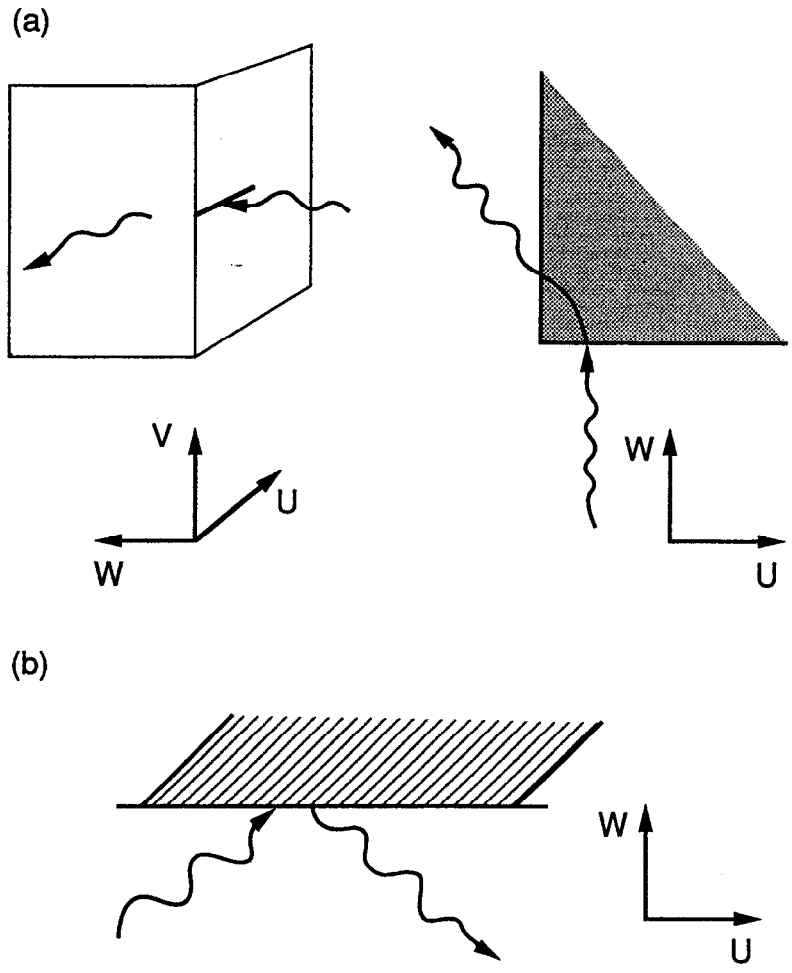

Fig. 4-50. Schematic illustration depicting the mechanisms of (a) tip scattering and (b) reflected scattering from a surface.

forward, thereby enhancing the number of photons with a direction-cosine close to that of the incident photon direction-cosine. Figure 4-51 is a plot of the distribution of W direction-cosines for photons that scatter through a mask tip when the incident-photon direction-cosine is equal to 1. The shaded region of the plot is the approximate angular region of the detector beam pipe seen from the mask tips. The number of photons in this forward direction is about 2.5 times higher than would result from an isotropic distribution. This increase is taken into account for determining photon rates that come from the mask tips.

Figure 4-52 shows a plot of the distribution of photons that scatter through a mask tip of gold, as a function of the distance from the edge of the mask. Nearly half of the scattered photons result from incident photons that are less than 1 μm from the edge. This calculation assumes a perfectly sharp mask edge; however, an actual mask tip will be somewhat rounded. Photons that strike the rounded surface can also reflect directly, as illustrated in Fig. 4-53; indeed, this direct reflection is more likely than tip scattering through the mask. If we assume that the corner of the mask has a 1-μm radius (which is

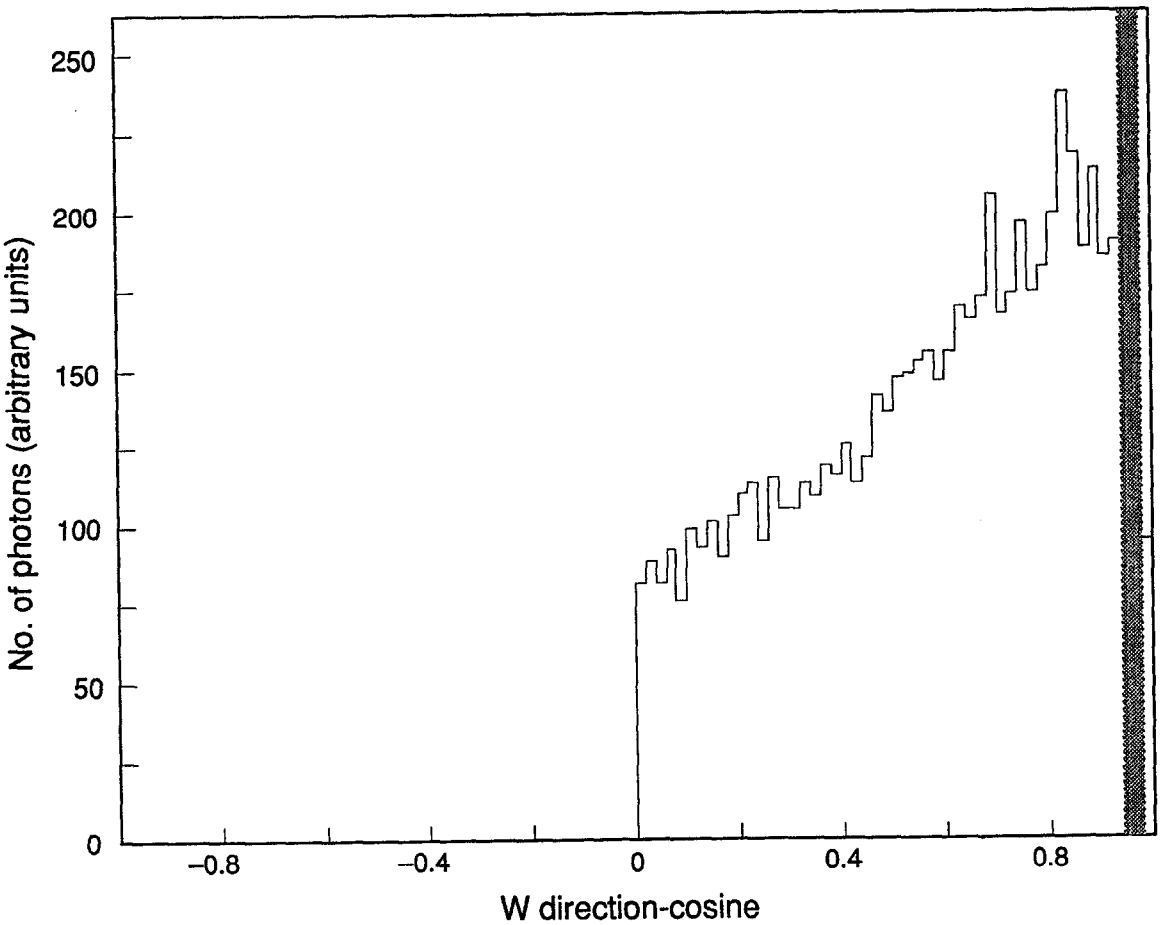

Fig. 4-51. Plot of the W direction-cosines for photons that scatter through the CD mask tip with an initial W direction-cosine of 1. The shaded region represents the approximate angular region occupied by the detector beam pipe.

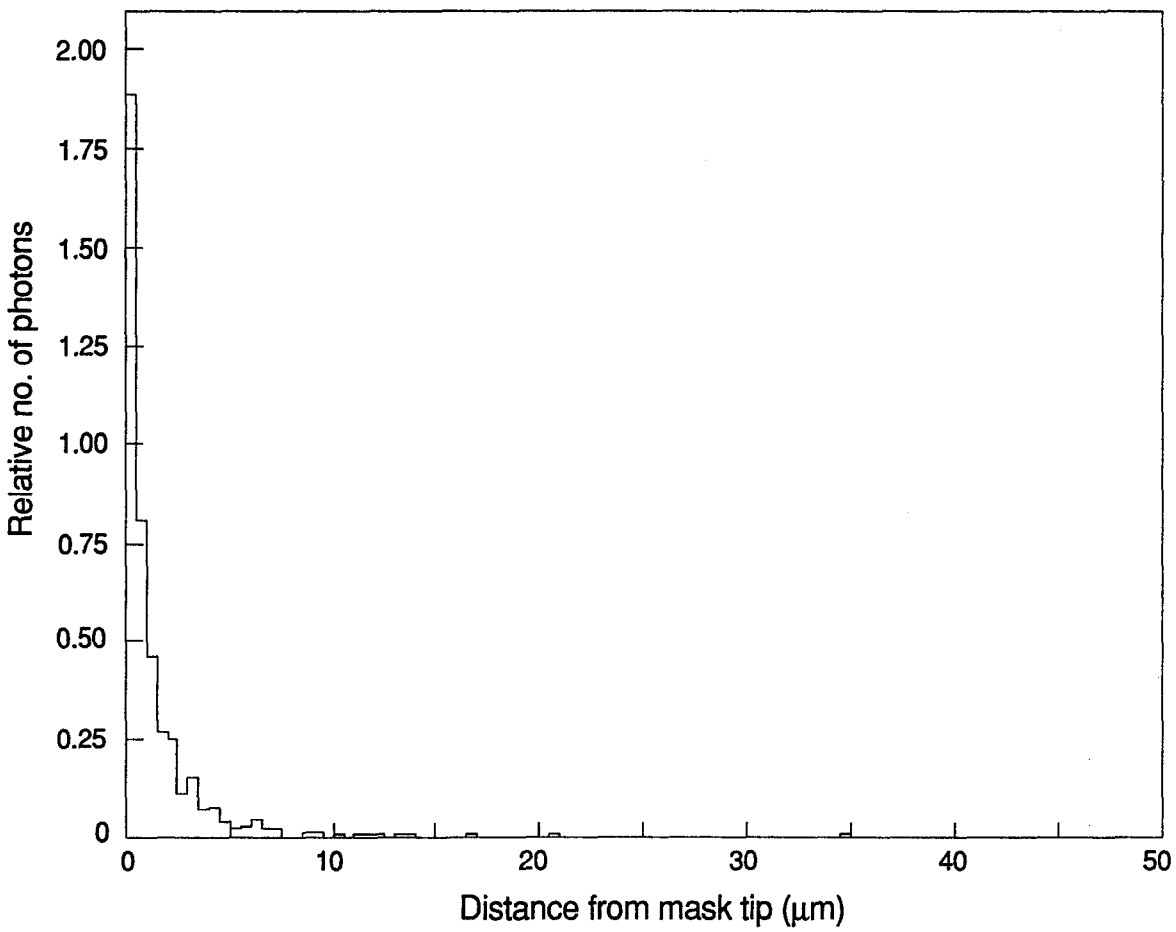

Fig. 4-52. Plot of the distribution of photons that scatter through a gold mask tip, as a function of the incident distance from the mask tip, for the CD mask.

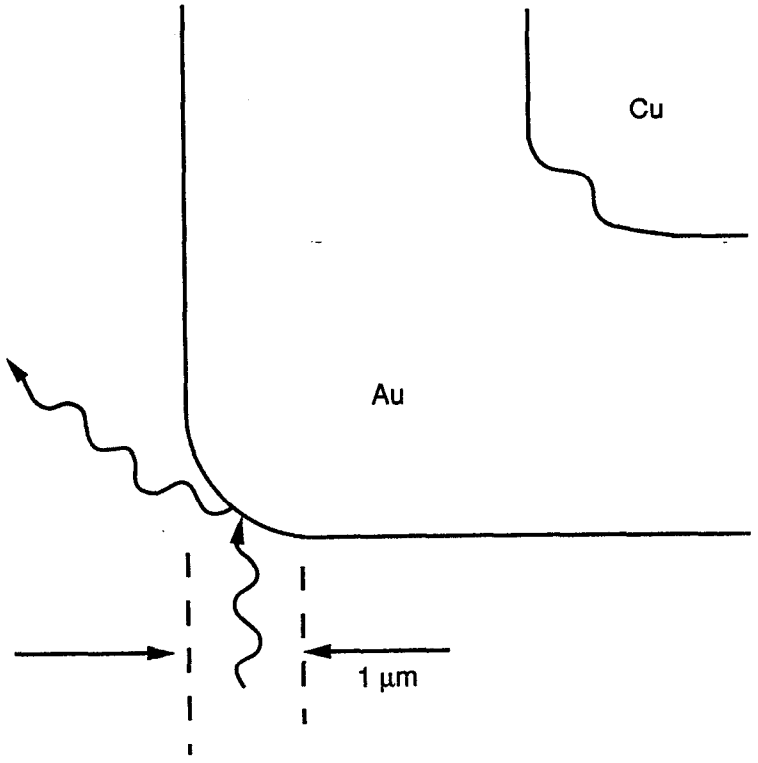

Fig. 4-53. Schematic illustration of direct reflection from a rounded mask tip.

not difficult to achieve), then, for the 9-GeV radiation on the tip of the CD mask, we can estimate the number of photons per crossing incident on the detector beam pipe from this source of background by taking the product of the number of incident photons/μm (above 4 keV), the surface-scattering probability of the mask material, and the solid-angle fraction subtended by the detector beam pipe:

$$6400 \text{ photons}/\mu\text{m} \times 0.007 \text{ (for Au)} \times 0.014 = 0.63 \text{ photons per crossing}$$

Similarly, for the 3.1-GeV radiation on the rounded AB mask tip we have

$$3200 \text{ photons}/\mu\text{m} \times 0.0016 \text{ (for Au)} \times 0.095 = 0.49 \text{ photons/crossing}$$

We therefore find that the background rates from a tip with a 1-μm radius and that from a perfect tip are comparable (see Table 4-7, which assumes a perfect tip).

4.2.1.4 Other Upstream Sources of Synchrotron Radiation

High-Energy Beamline. There are two bending magnets (B2 and B3, located 11 m and 40 m from the IP) in the high-energy beamline that generate radiation fans passing through the IR. These are very low-field, long bending magnets (ε_{crit} = 1 keV), but they nonetheless produce a large number of low-energy photons that strike the B side of the AB mask. The total synchrotron radiation power from these two magnets striking the AB

mask is 130 W, corresponding to 1.1×10^{10} photons per crossing. The low critical energy of these photons means that only 9.5×10^{8} photons have an energy greater than 1 keV. Of these, 7.9×10^{5} reflect from the mask surface. With a detector beam pipe solid-angle fraction of 0.019, we have 1.5×10^{4} photons above 1 keV incident on the beam pipe. Fortunately, the energy spectrum of these photons is so soft that only 1.1×10^{-2} photons per crossing are transmitted through the beam pipe and are incident on the first layer of the silicon vertex detector. This compares with 3.8×10^{-2} photons per crossing incident on the first layer of silicon from the tip-scattered photons. All of the photons transmitted through the beam pipe are completely absorbed in the first layer of silicon and do not increase the detector occupancy.

Low-Energy Beamline. There are two bending magnets in the low-energy beamline that bend the beam vertically into the horizontal plane upstream of the magnetic elements near the IP. Figure 4-54 shows elevation views of the LEB as it enters and leaves the IP region. The first vertical bending magnet, BV–, produces about 7.5 kW of synchrotron radiation power, but this is absorbed in a mask that spreads the power out over 2 m. None of this radiation reaches the detector beam pipe. The second vertical bending magnet, BV1, is a weaker magnet (ε_{crit} = 1 keV). It deposits about 100 W of power on the A side of the AB mask. Again, none of the photons from this source strikes the detector beam pipe.

4.2.1.5 Downstream Secondary Sources of Synchrotron Radiation. The radiation fan generated by the HEB as it passes through the upstream Q2 magnet strikes the downstream crotch mask in front of the Q4 septum quadrupole. Roughly 1×10^{10} photons per crossing strike this mask. Photons that backscatter out of the crotch mask have no direct line-of-sight to the detector beam pipe: The AB mask shields the beam pipe from this source of photons. Nonetheless, the intensity of this photon source is sufficiently high that one must ascertain that photons bouncing off the intervening beam pipe do not cause a background problem.

The mechanism of the "double bounce" of photons onto the detector beam pipe is illustrated in Fig. 4-55a. The simplified geometry shown in Fig. 4-55b permits the calculation of solid-angle fractions for various cylindrical sections of beam pipe between the detector beam pipe and the source. A calculation of the solid-angle fraction of the detector beam pipe seen by each cylindrical section of beam pipe can also be made. Summing the products of these two solid-angle fractions yields the probability that a photon can backscatter from the crotch mask and strike the detector beam pipe. The solid-angle fractions, along with their products, are displayed in Fig. 4-56; Table 4-8 lists the numerical solid-angle values.

As can be seen, the largest contribution to the solid angle comes from those beam pipe surfaces near the detector beam pipe and near the source. Assuming 1×10^{10} photons per crossing incident on a copper mask located 3 m from the IP, and assuming that the intervening beam pipe is coated with a high-Z element such as gold, then the number of photons per crossing incident on the detector beam pipe is given by the product of the photons per crossing incident on the mask, the reflectivity of the mask material, the solid angle for a double bounce, and the reflectivity of the beam pipe coating:

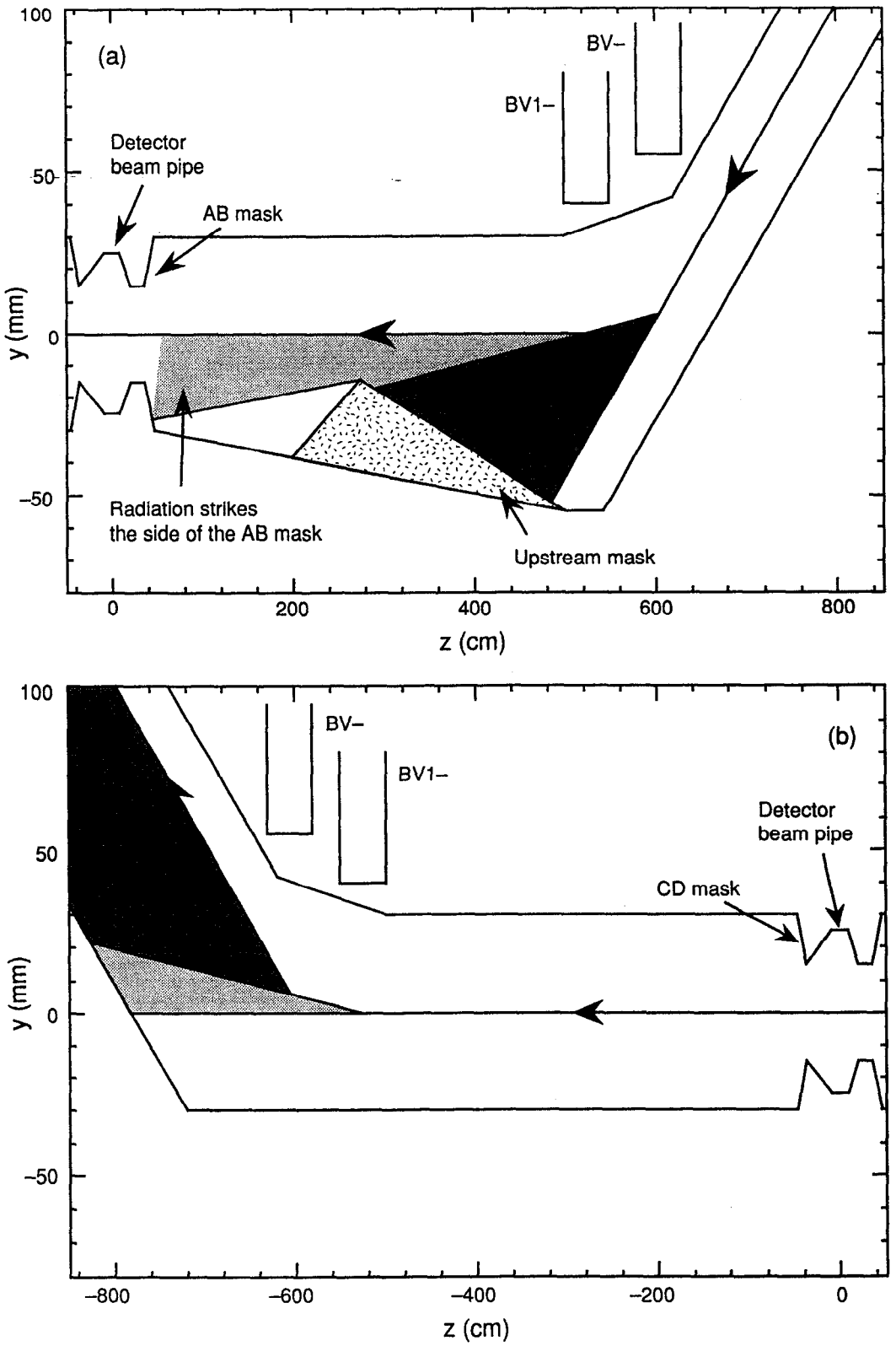

Fig. 4-54. Elevation views of the LEB as it (a) enters and (b) leaves the IR.

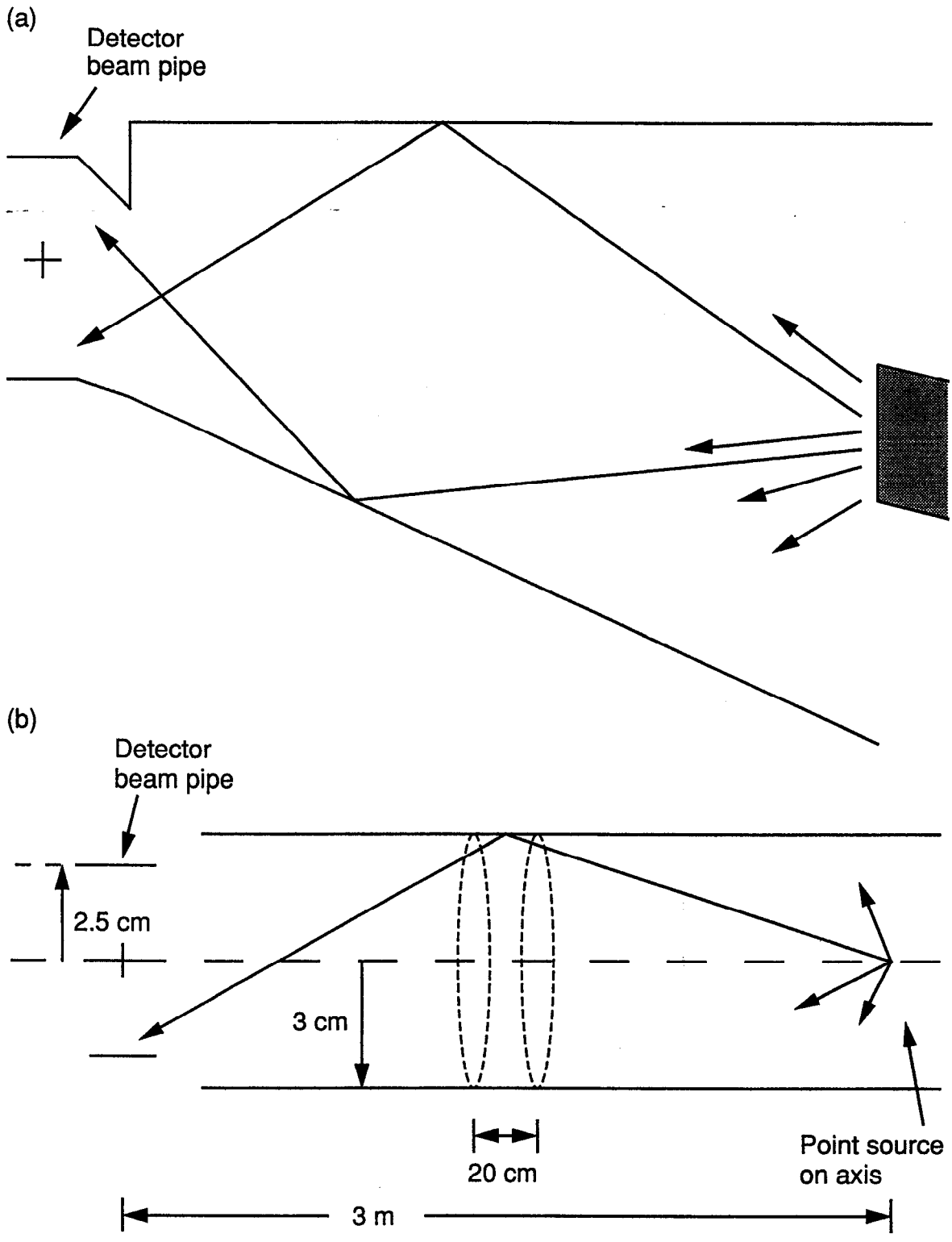

Fig. 4-55. (a) Schematic illustration of photons "double bouncing" to the detector beam pipe from a source of synchrotron radiation, and (b) a simplified geometry for the double-bounce problem. The typical dimensions shown in (b) were used to generate Table 4-8.

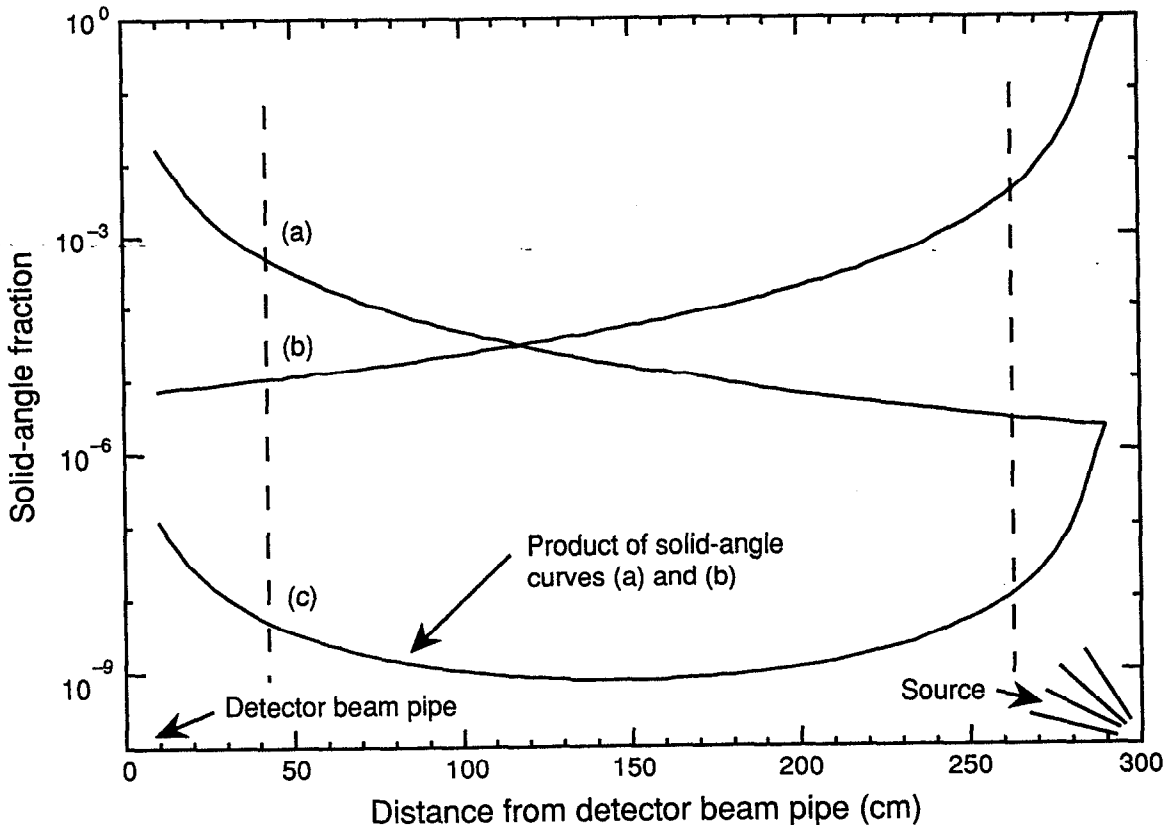

Fig. 4-56. Plot of (a) the solid-angle fraction of detector beam pipe as seen from the main beam pipe, (b) the solid-angle fraction of intervening beam pipe as seen from the source of radiation, and (c) the product of (a) and (b); the abscissa represents the distance from the detector beam pipe.

$$(1 \times 10^{10}) \times 0.06 \text{ (for Cu)} \times (2.2 \times 10^{-6}) \times 0.007 \text{ (for Au)} = 10 \text{ photons per crossing}$$

The AB mask effectively shields most of the detector beam pipe from photons reflected from the nearby portion of the intervening beam pipe. In addition, care has been taken to ensure that regions of the beam pipe within 50 cm of the source and within 50 cm of the detector beam pipe do not have any line-of-sight to the detector beam pipe. This reduces by two orders of magnitude the probability of backscattered photons striking the detector beam pipe (see Table 4-8). Furthermore, most of the photons that do strike the detector beam pipe have a very small angle of incidence (<25 mrad), which further reduces the probability that photons from this source will penetrate the detector beam pipe. Taken together, these factors make double-bounce photons from the crotch mask a negligible source of detector background.

Still another possible source of detector background is backscattered photons coming from the dump downstream of the IP in which most of the synchrotron radiation power from the IR is absorbed. These photons may backscatter directly onto the detector beam pipe. To estimate this effect, we assumed that the entire synchrotron radiation power is absorbed in a dump located 12 m from the IP. The solid-angle fraction of the detector

Table 4-8. Solid-angle fractions from a double-bounce source. The numbers between the two dashed lines correspond to the double-bounce solid angle for the 2 m of beam pipe centrally located between the source and the detector beam pipe.

Distance from detector beam pipe to intervening beam pipe (cm)	SA fraction of detector beam pipe as seen from intervening beam pipe segment (a)	SA fraction of intervening beam pipe segment as seen from source (b)	Product (c)
290	2.14×10^{-6}	0.9557	2.05×10^{-6}
270	2.64×10^{-6}	8.26×10^{-3}	2.18×10^{-8}
250	3.30×10^{-6}	1.55×10^{-3}	5.12×10^{-9}
230	4.21×10^{-6}	5.45×10^{-4}	2.29×10^{-9}
210	5.49×10^{-6}	2.53×10^{-4}	1.39×10^{-9}
190	7.34×10^{-6}	1.37×10^{-4}	1.01×10^{-9}
170	1.10×10^{-5}	8.28×10^{-5}	8.36×10^{-10}
150	1.45×10^{-5}	5.38×10^{-5}	7.80×10^{-10}
130	2.19×10^{-5}	3.69×10^{-5}	8.08×10^{-10}
110	3.52×10^{-5}	2.64×10^{-5}	9.29×10^{-10}
90	6.20×10^{-5}	1.95×10^{-5}	1.21×10^{-9}
70	1.25×10^{-4}	1.48×10^{-5}	1.85×10^{-9}
50	3.11×10^{-4}	1.16×10^{-5}	3.61×10^{-9}
30	1.18×10^{-3}	9.17×10^{-6}	1.08×10^{-8}
10	1.60×10^{-2}	7.40×10^{-6}	1.18×10^{-7}
		Total	2.22×10^{-6}
		Total for central 2 m	1.98×10^{-8}

beam pipe seen from this source is 6×10^{-8}. (This calculation assumes that there is no intervening AB mask to shield most of the detector beam pipe.) There are about 5×10^{10} photons per crossing incident on the dump mask. Taking a reflection coefficient for the dump mask material of 0.007, we get 22 photons per crossing incident on the detector beam pipe. In reality, the AB mask shields at least 90% of the detector beam pipe from this source. The small region of detector beam pipe still exposed can be easily shielded by a small lip (about 1 mm) near the edge of the beam pipe. In addition, the very small

angle of incidence on the beam pipe (about 2 mrad) eliminates the high-power downstream dump as a possible source of detector background.

4.2.1.6 Sensitivity of Backgrounds to Misalignments. The following misalignments were evaluated for their effects on detector backgrounds:

- Displacing the Q4 magnet ±1 mm in x and y for the HEB
- Displacing the Q2 magnet ±1 mm in x and y for both beams
- Displacing the Q1 magnet ±1 mm in x and y for both beams
- Displacing Q1, Q2, Q3, and Q4 ±3 mm in x for the HEB; this corresponds to a displacement of about 1σ for the beam
- Displacing Q1, Q2, and Q3 ±1.5 mm in x for the LEB; this also corresponds to about a 1σ beam displacement

The LEB background is the more sensitive to misalignments such as these. We see a 2.5-fold increase in the background rate for a 1-mm excursion in y for both Q1 and Q2. Likewise, the LEB background rate increases by a factor of about 2.25 for a 1-mm excursion in x for Q1 and Q2, and for a 1.5-mm displacement in all three inner magnets. The rest of the misalignment checks produced small (<25%) increases in backgrounds, with some settings producing rates that are actually below the nominal background rate.

4.2.2 Survey of Synchrotron Radiation Power in the Interaction Region

Here we discuss the power levels on all the surfaces near the IP. An extensive analysis of all sources of fan radiation that either travels through or comes close to the IP is included. The analysis follows the fan from each source of radiation, and a tally of all surfaces the fan strikes is maintained. Table 4-9 summarizes the power deposited on various surfaces near the IP. The letters in the table that identify the various surfaces are also shown in Figs. 4-57 through 4-60. As mentioned earlier, the power values are calculated using the nominal beam currents: 1.48 A for the HEB and 2.14 A for the LEB.

There are fourteen radiation fans, ten of which are produced within 3 m of the IP and four of which originate from upstream bending magnets. The radiation fans can be conveniently separated into four categories: upstream LEB sources, downstream LEB sources, upstream HEB sources, and downstream HEB sources.

4.2.2.1 Upstream LEB. These sources of radiation include two bending magnets, BV– and BV1–, and three magnets near the IP, Q3, Q1, and B1. As described earlier, the synchrotron radiation fan from BV– is stopped in a 2-m-long mask located well upstream of the IP (see Fig. 4-54a); the total power from this fan is 7.5 kW. The fans from BV1– and Q3 and part of the fan from Q1 strike the AB mask, giving a total power of 1.15 kW. Some of the Q1 fan strikes the downstream Q4 crotch mask, depositing 186 W. The rest of the Q1 fan goes into dumps located about 6 m from the IP in the LER beam pipe and 12–15 m from the IP in the HER beam pipe. The downstream dump in the HER beamline is referred to as the high-power downstream dump (HPDD). The B1 fan misses

Table 4-9. Power on surfaces near the IP. Each surface is identified by letter in Figs. 4-57 through 4-60. Radiation fans that strike a surface do not necessarily overlap; the surface power summary for each surface is the maximum power density for that surface. Quadrupoles Q1 and Q2 were split into pieces (A and B) to reflect the changing power levels as the offset beams travel through these magnets.

	Source	Surface power (W/mm)	Total power (W)
Surface struck:			
a. Beam pipe between Q4 and Q5 (4.76 – 5.25 m)			
	B3B	0.03	17
	B2B	0.13	65
		0.16	82
b. Bore of Q4, HEB side (3.76 – 4.76 m)			
	B3B	0.03	16
	B2B	0.04	35
	Q1A downstream	0.1	105
		0.17	156
c. Crotch mask, HEB side (3.76 m)			
	Q1A upstream	1.2	186
	Q1A downstream +	1.7	75
	Q1B downstream	1.1	122
		2.9	383
d. Beam pipe between Q3 and Q4, HEB side (2 – 3.76 m)			
	B3B	0.03	52
e. CD mask, D side (0.35 m)			
	B3B	0.36	9
	Q4 + Q5 quad. rad.	–	16
		0.36	25
f. AB mask, B side (0.2 m)			
	B3B	0.29	29
	B2B	0.84	99
		1.13	128
f. AB mask, A side (0.2 m)			
	BV1–	2.8	225
	Q3	17.	901
	Q1B	17.	138
		17.	1264
g. Crotch mask, LEB side (3.76 m)			
	B2A	0.9	99
	Q2B	41.	4330
		41.9	4429

all nearby surfaces and is absorbed entirely in the HPDD. The total B1 fan power is 2.4 kW. These radiation fans are shown as shaded regions in Fig. 4-57.

4.2.2.2 Downstream LEB. Three fans are generated by the downstream elements B1, Q1, and Q3. The B1 fan again misses all nearby surfaces and is absorbed in the HPDD (with a power of 2.4 kW). Part of the downstream Q1 fan strikes the crotch mask on the Q4 septum quadrupole, depositing 200 W of power, and some is deposited inside the beam pipe in Q4 (giving a power of 100 W over 0.8 m of length). The rest of the Q1 fan is absorbed in the HPDD and in the corresponding LER beamline dump. The Q3 fan is also absorbed in the LER dump. Figure 4-58 shows as shaded regions the fans generated by the downstream LEB elements.

4.2.2.3 Upstream HEB. For the HEB, there are four upstream sources of radiation fans, as shown in Fig. 4-59: Two emerge from the upstream B3 and B2 bending magnets and two from the Q2 and B1 magnets near the IP. Weak radiation fans (ε_{crit} = 1 keV) from the B2 and B3 bending magnets located at 11 m and 40 m, respectively, sweep through the entire IR. The B3 fan strikes the beam pipe between Q4 and Q5 (with 17 W of power), the inside of the Q4 beam pipe (16 W), the beam pipe between Q3 and Q4

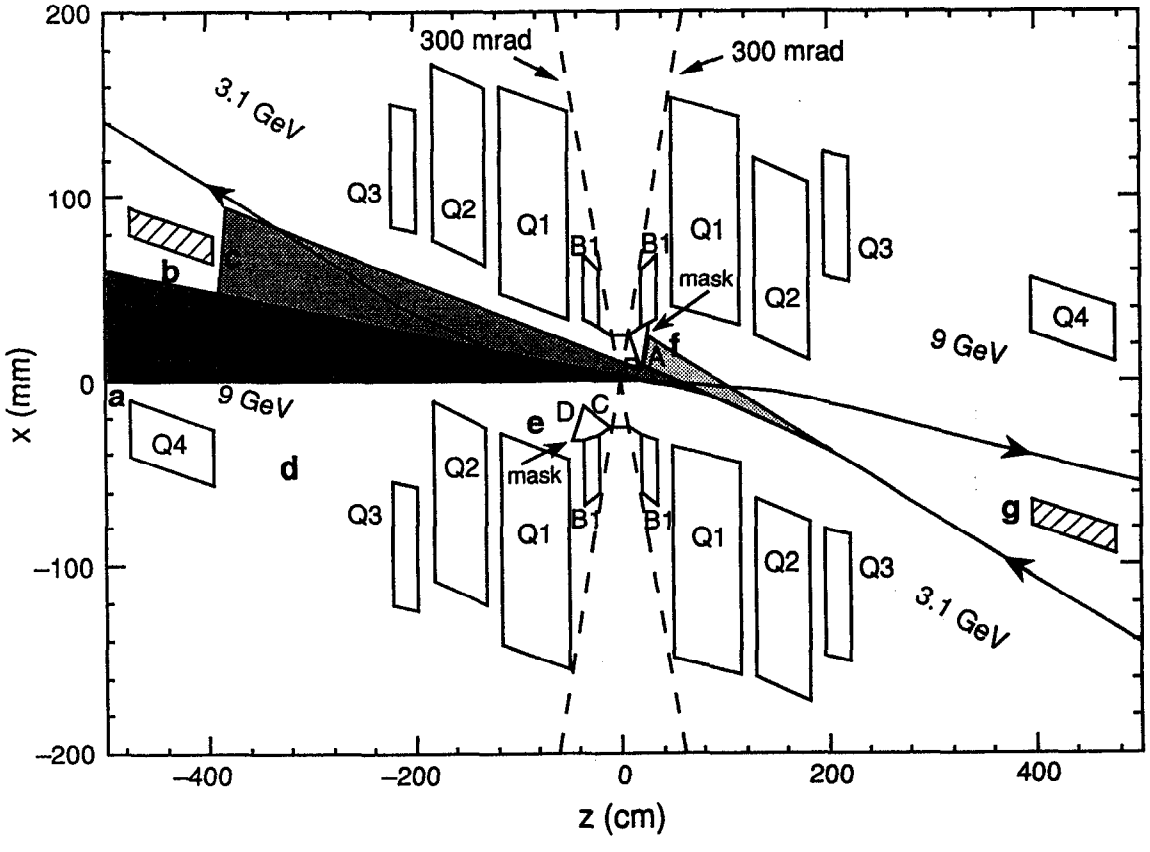

Fig. 4-57. LEB radiation fans produced upstream of the IP. The fan generated by the upstream Q3 magnet is absorbed by the AB mask. The lower-case lettering refers to surfaces in Table 4-9 that are struck by synchrotron radiation.

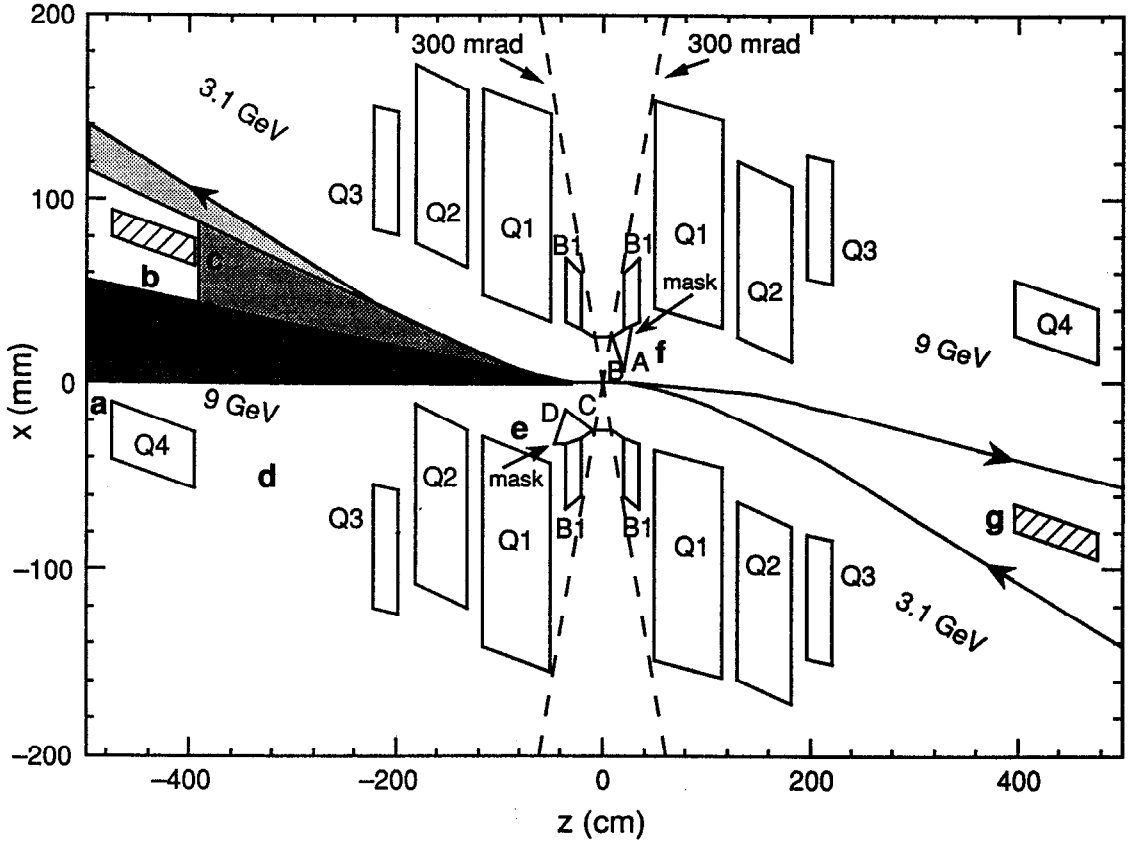

Fig. 4-58. LEB radiation fans produced downstream of the IP. The radiation fans from the downstream B1 and Q1 magnets overlap the upstream B1 and Q1 radiation fans (see Fig. 4-57).

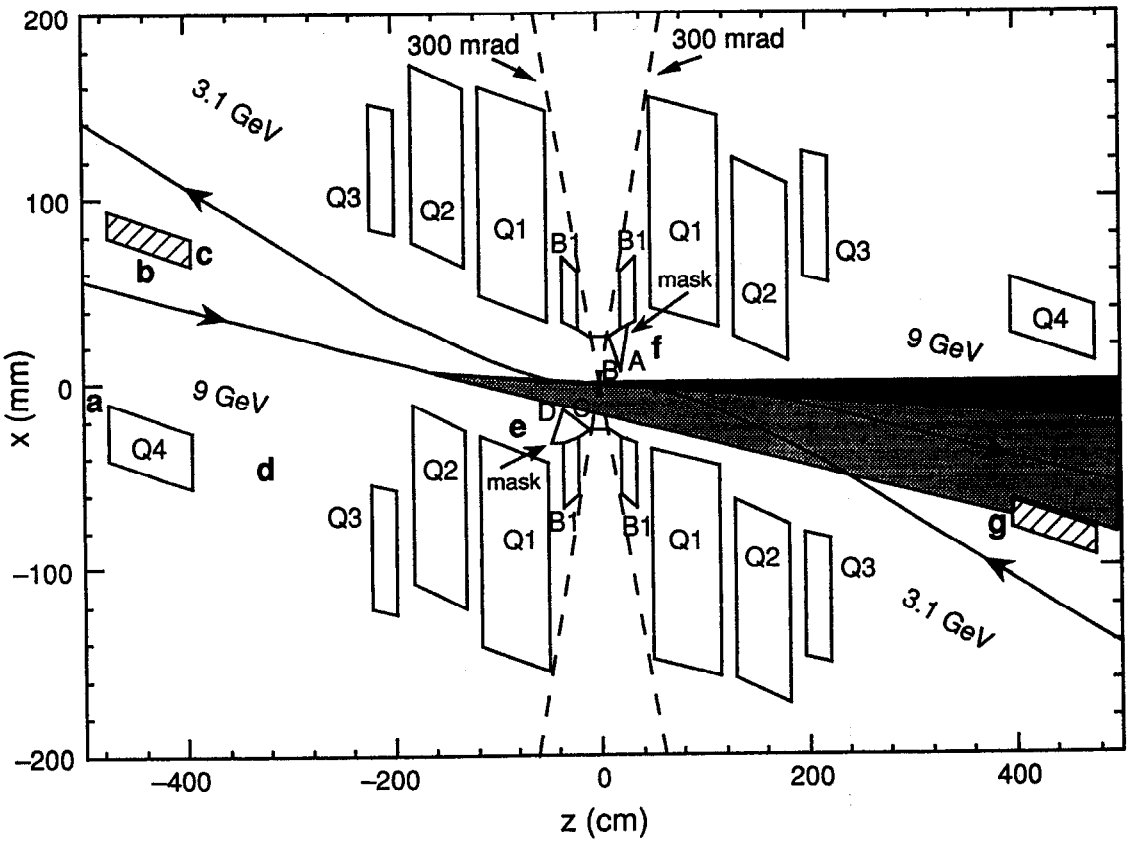

Fig. 4-59. HEB radiation fans produced upstream of the IP. The upstream Q2 fan strikes the downstream crotch mask in front of the Q4 septum, depositing about 4.5 kW of power.

(52 W), the CD mask (9 W), and the AB mask (29 W). The B2 fan strikes the beam pipe between Q4 and Q5 (65 W), the inside of Q4 (35 W), the AB mask (99 W), and the downstream Q4 crotch mask (99 W). Part of the intense fan of photons coming from the Q2 magnet strikes the downstream crotch mask in front of the Q4 septum quadrupole. A power of 4.33 kW is deposited on this mask, with the rest of the fan power going down the HER beam pipe, where it is absorbed by the HPDD. The B1 fan misses all nearby surfaces and is absorbed in the HPDD.

4.2.2.4 Downstream HEB. The two radiation fans from downstream HEB elements B1 and Q2 miss all nearby surfaces (see Fig. 4-60) and are absorbed in the HPDD.

The total amount of power that is absorbed in the upstream 12-m region of the HEB is 5.6 kW, and the HPDD absorbs 84 kW of power. The power absorbed in the downstream dump in the LER is 1.2 kW. No power is seen in the upstream beamline of the LER. In summary, nearly 90% of the synchrotron radiation power is absorbed in downstream dumps and thus causes no increase in detector background, either from backscattered photons or from beam-gas interactions. Of the remaining 10.5 kW, 5.6 kW are absorbed

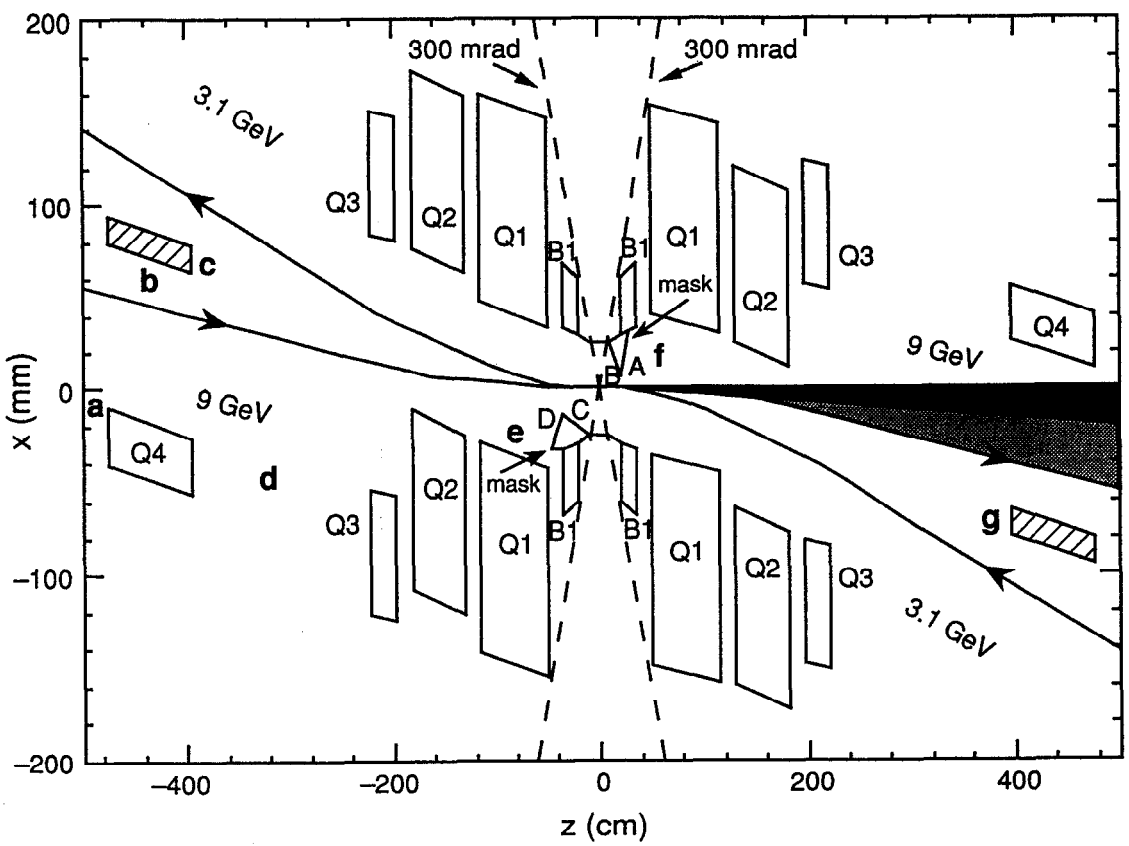

Fig. 4-60. HEB radiation fans produced downstream of the IP. The radiation fans from the downstream B1 and Q2 magnets overlap the upstream B1 and Q2 radiation fans (see Fig. 4-59).

in an upstream region of the HER 12 m from the IP, and most of the rest is absorbed on the crotch mask at Q4 and on the AB mask.

4.2.3 Detector Backgrounds from Lost Beam Particles

Bremsstrahlung and Coulomb scattering of beam particles from residual gas molecules in the beam pipe can lead to high-energy electrons and photons striking masks and the beam pipe near the IP. The resulting electromagnetic showers can cause excessive detector occupancy and lead to radiation damage. Here we discuss the methods used to simulate this process, the rates and locations of lost-particle hits, and the resulting detector backgrounds. Calculated rates are found to be 25–100 times lower than the acceptable limits (see Section 2.4, Tables 2-5 and 2-6) in the silicon microvertex detector and the CsI calorimeter, and about 15 times lower in the drift chamber.

In calculating the rates of bremsstrahlung and Coulomb scattering, both the high- and low-energy lattices are simulated for a distance of 185 m upstream of the IP (halfway around the arc). Bremsstrahlung scattering produces an electron and a photon whose combined energy is equal to the beam energy. The photon energy is restricted to a range between 0.02 and 0.99 of the beam energy; scattering events with a lower photon energy are found to contribute less than 1% to the energy deposited near the IP. Coulomb scattering gives an off-axis electron at the nominal beam energy; the scattering angle is restricted to lie between 1 and 500 mrad. (Electrons scattered at lower angles do not strike the beam pipe.)

The pressure in the beam pipe is assumed to be 1 nTorr of N_2 within 30 m upstream of the IP and 5 nTorr elsewhere.

The analysis was carried out using DECAY TURTLE [Carey et al., 1982], a modified version of TRANSPORT [Brown et al., 1977]. In this program, rays are scattered and transported until they either strike an aperture or pass through the IR. The location and direction of rays that strike near the IP are stored, together with a weighting factor corresponding to the probability of that scattering process occurring per beam crossing, for later use in a detailed EGS model. Approximately 230 beam crossings occur per microsecond; this is the relevant time interval, because 1 μs is typical of the live-time of most detector elements.

The rate of rays striking near the IP is reduced by the use of upstream masks at points of high dispersion. The masks are elliptical, with half-apertures in x and y given by the larger of 8 mm or $15\sigma_{x,y} + 2$ mm, where $\sigma_{x,y}$ is the transverse beam size at that point in the lattice. The dispersion in x and y of each beam and the location of the masks are shown in Fig. 4-61. These masks completely shadow the IR from LEB bremsstrahlung scattering events upstream of the outboard vertical bend (30 m upstream of the IP). Particles from upstream Coulomb scattering do strike the detector, but at a low rate. The masking is not quite as successful for the HEB. Figure 4-62 shows the energy of the scattered electrons that strike near the IP as a function of the bremsstrahlung scattering location (in meters upstream of the IP). There is a "window" for electrons having energies between 8.5 and 9 GeV that scatter 85–90 m upstream to hit the region near the IP. However, these rays constitute only 14% of the energy from the HEB deposited near the IP and thus do not dominate the background. A more sophisticated masking scheme

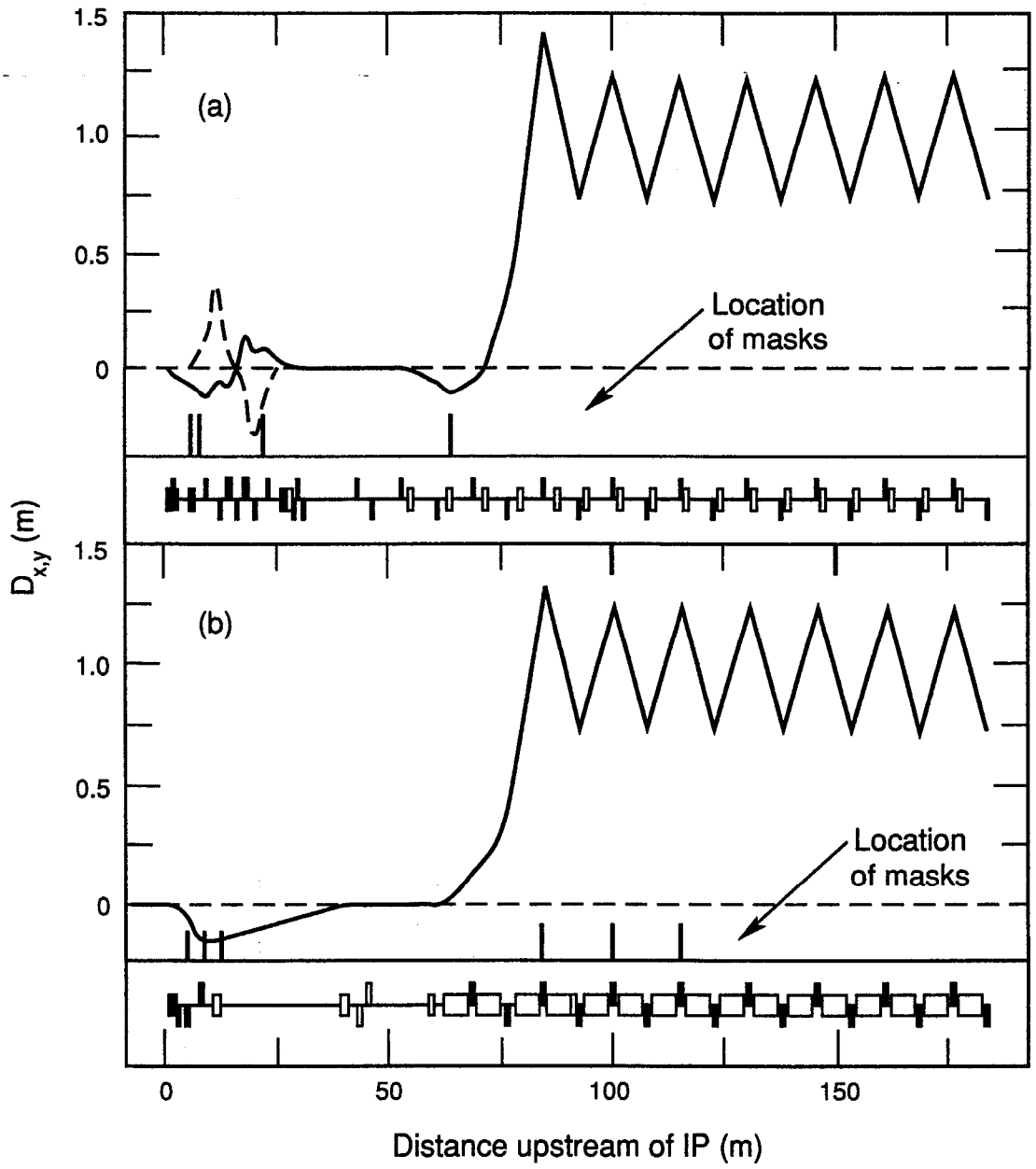

Fig. 4-61. Plots showing the dispersion and location of masks for (a) the low-energy beam and (b) the high-energy beam: solid line, horizontal dispersion; dashed line, vertical dispersion. The HER lies in a horizontal plane and therefore has no vertical dispersion.

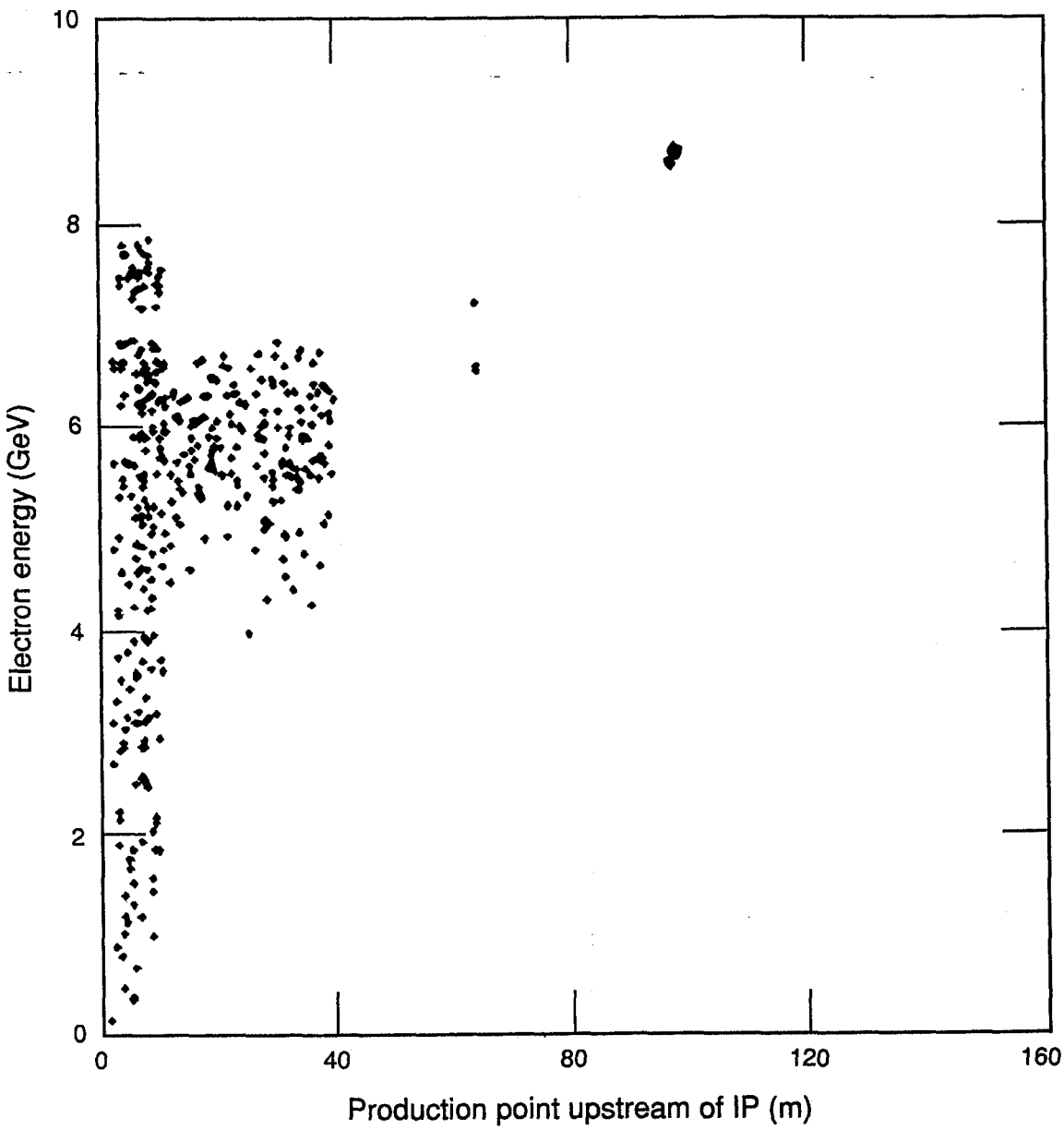

Fig. 4-62. Plot of the energy of bremsstrahlung-scattered electrons striking near the IP, as a function of the location of the scattering point (distance upstream of the IP), for the HEB. Scattering events 85–90 m upstream with 8.5 < E < 9.0 GeV are not completely masked.

could probably eliminate them. Coulomb scattering events of the HEB that take place more than 30 m upstream do not strike near the IP.

Because shower debris is expected to be roughly proportional to the incident energy, the rate of energy deposition on each aperture in the IR is given in Table 4-10 for each source and is displayed graphically in Fig. 4-63. For both the HEB and the LEB, the dominant sources of detector background are bremsstrahlung electrons deflected by the B1 magnet that strike the downstream synchrotron radiation mask. Note that Coulomb scattering contributes less than 6% of the deposited energy. Overall, a total energy of 5.7 GeV, from 3.1 rays per microsecond, is deposited near the IP from the LEB, while 19 GeV, from 4.4 rays per microsecond, originates from the HEB.

In our analysis, all rays that strike the IR were passed to an EGS simulation code that includes the geometry and material type of the beam pipe, masks, magnets, and detector components, as well as the final-focus optics and detector magnetic fields. The number of showers generated per incident ray is determined by its weighting factor from DECAY TURTLE. For the LEB backgrounds, 250,000 beam crossings (1100 μs of running) were simulated; 70,000 crossings (300 μs) were used for the HEB backgrounds. The EGS total energy cutoffs were 0.7 MeV for electrons and 0.01 MeV for photons.

All objects in the simulation are constructed from cylinders parallel to and centered on the z axis. The geometry is therefore specified by the extent in z and the inner and outer radii of each object (see Table 4-11). Note that the synchrotron radiation masks (masks AB and CD) were divided into five cylinders to better represent their tapered shape. The composition of each object is also shown in Table 4-11. Figure 4-64 shows the detector and IR geometry incorporated into the EGS simulation.

The actual layout of the IR (corresponding to the geometry used by TRANSPORT) is not cylindrically symmetric about the z axis. This is particularly true of the masks. Therefore, TRANSPORT rays are mapped from the correct geometry to the cylindrically symmetric EGS geometry [Nelson et al., 1985]. This is done so as to preserve the incident angle of the particle with respect to the surface, the azimuthal angle of the point of impact, and the distance (δ) of the impact point from the edge of the struck mask. Figure 4-65 shows an example of this mapping.

The EGS calculation finds the energy deposited in, and the number of photons and electrons entering, each object. Electrons are counted each time they loop through an object in the solenoid field. For this reason, the drift chamber is divided into a series of thin cylinders so that the number of electron crossings at each radius is accurately counted. Electrons produced by photon interactions in the gas are scored as electrons when they subsequently enter a new object (a drift chamber scoring cylinder, for example). The results of the EGS calculations for the B Factory IR are summarized in Table 4-12 for the LEB and HEB, both separately and combined.

Four plots characterizing the backgrounds in the drift chamber from the LEB are shown in Fig. 4-66. The backgrounds in the drift chamber are due primarily to low-energy photons from rays striking the HEB synchrotron radiation mask (CD); Fig. 4-67 shows the z location at the beam pipe of photons that enter the drift chamber. Backgrounds from the HEB are qualitatively similar, except that the LEB synchrotron radiation mask (AB) is the primary source. The probability that a photon interacts in the

Table 4-10. Number of rays and energy (given in parentheses in GeV) deposited on IR area apertures per microsecond.

Aperture	Coulomb	Brem e^-	Brem γ	All rays
Due to LEB:				
Q3	0.0 (0.0)	0.0 (0.0)	0.2 (0.07)	0.2 (0.07)
Q2	0.0 (0.04)	0.1 (0.31)	0.0 (0.0)	0.1 (0.35)
Q1	0.0 (0.02)	0.0 (0.02)	0.0 (0.01)	0.0 (0.05)
HEB SR mask	0.0 (0.04)	0.9 (2.39)	0.0 (0.0)	0.9 (2.43)
IP	0.0 (0.0)	0.0 (0.08)	0.0 (0.0)	0.0 (0.08)
LEB SR mask	0.0 (0.05)	0.0 (0.06)	0.8 (0.50)	0.8 (0.610)
B1	0.0 (0.0)	0.0 (0.02)	0.3 (0.15)	0.3 (0.18)
Q1	0.0 (0.01)	0.4 (1.16)	0.1 (0.07)	0.5 (1.24)
Q2	0.0 (0.01)	0.3 (0.65)	0.0 (0.01)	0.3 (0.68)
Q3	0.0 (0.0)	0.0 (0.01)	0.0 (0.0)	0.0 (0.01)
Total	0.0 (0.17)	1.7 (4.70)	1.4 (0.81)	3.1 (5.70)
Due to HEB:				
Q3	0.0 (0.0)	0.0 (0.01)	0.0 (0.0)	0.0 (0.01)
Q2	0.0 (0.05)	1.1 (6.3)	0.0 (0.0)	1.1 (6.35)
Q1	0.0 (0.01)	0.1 (0.24)	0.0 (0.0)	0.1 (0.25)
HEB SR mask	0.0 (0.01)	0.0 (0.20)	0.2 (0.44)	0.2 (0.66)
IP	0.0 (0.0)	0.0 (0.02)	0.0 (0.0)	0.0 (0.02)
LEB SR mask	0.0 (0.42)	0.5 (3.39)	2.1 (4.1)	2.6 (7.92)
B1	0.0 (0.0)	0.0 (0.0)	0.0 (0.0)	0.0 (0.0)
Q1	0.0 (0.0)	0.0 (0.07)	0.0 (0.07)	0.0 (0.07)
Q2	0.1 (0.59)	0.3 (2.78)	0.0 (0.0)	0.4 (3.37)
Q3	0.0 (0.0)	0.0 (0.0)	0.0 (0.0)	0.0 (0.0)
Total	0.1 (1.07)	2.0 (13.01)	2.3 (4.61)	4.4 (18.63)
Due to both beams:				
Q3	0.0 (0.0)	0.0 (0.01)	0.2 (0.07)	0.2 (0.08)
Q2	0.0 (0.09)	1.2 (6.61)	0.0 (0.0)	1.2 (6.70)
Q1	0.0 (0.03)	0.0 (0.26)	0.0 (0.01)	0.0 (0.30)
HEB SR mask	0.0 (0.05)	0.9 (2.59)	0.2 (0.44)	1.1 (3.03)
IP	0.0 (0.0)	0.0 (0.1)	0.0 (0.0)	0.0 (0.11)
LEB SR mask	0.0 (0.47)	0.5 (3.45)	2.9 (4.6)	3.4 (8.53)
B1	0.0 (0.0)	0.0 (0.02)	0.3 (0.15)	0.3 (0.18)
Q1	0.0 (0.01)	0.4 (1.23)	0.1 (0.14)	0.5 (1.31)
Q2	0.1 (0.6)	0.6 (3.43)	0.0 (0.01)	1.7(4.05)
Q3	0.0 (0.0)	0.0 (0.01)	0.0 (0.0)	0.0 (0.01)
Total	0.1 (1.24)	3.7 (17.71)	3.7 (5.42)	7.5 (24.33)

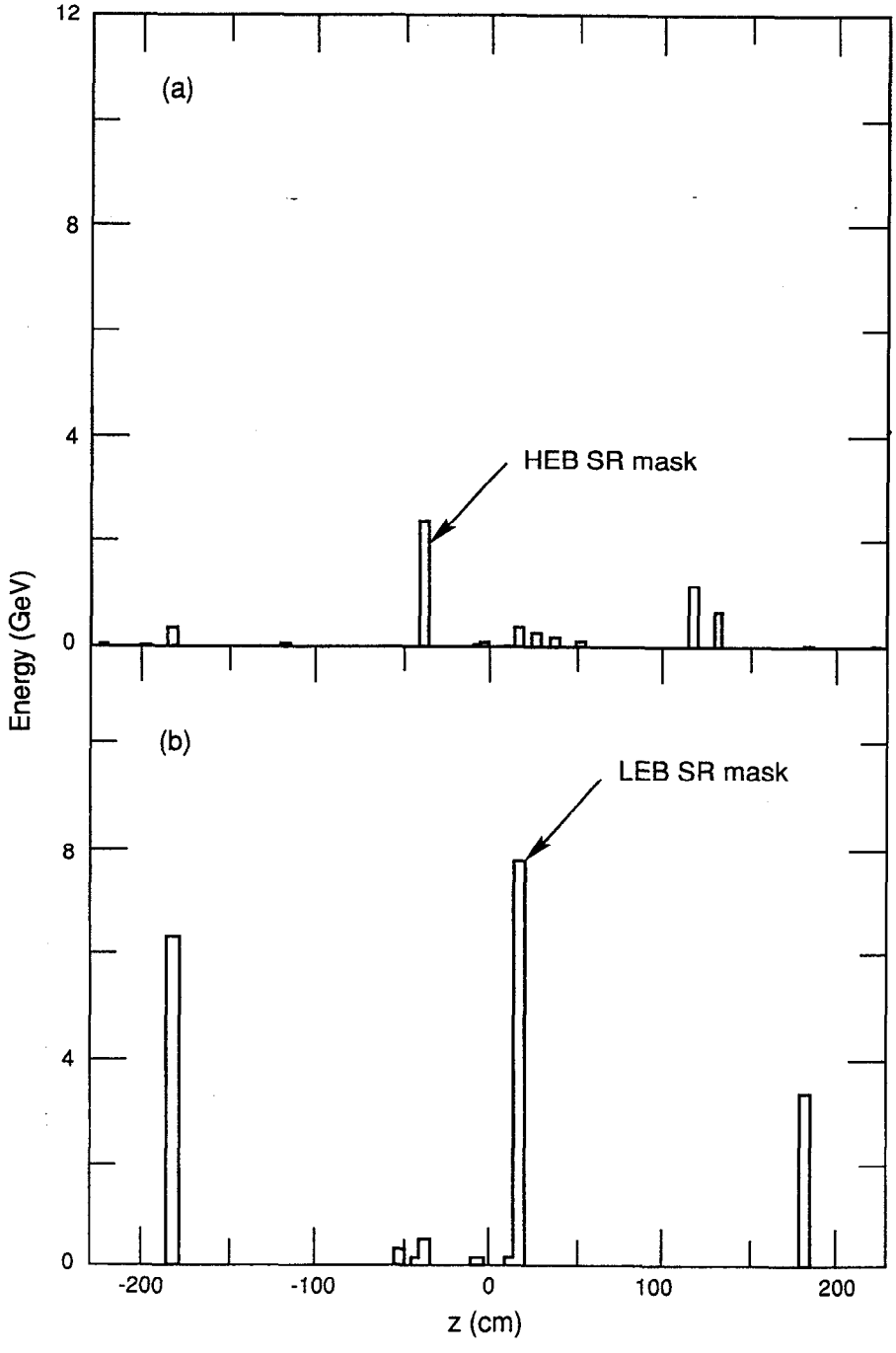

Fig. 4-63. Energy per microsecond incident on the IR due to scattering from (a) the low-energy beam and (b) the high-energy beam, as functions of location. The location plotted corresponds to the point where the ray strikes an aperture. The HEB travels in the direction of increasing z. The drift chamber covers the region $-150 < z < 150$ cm.

Table 4-11. Geometry and materials used in EGS simulation.

Object	Material	z (cm)	r (cm)
Support 2	Al	±60 to ± 900	16.8 to 18.0
Q3	Sm_2Co_{17}	±196.8 to ±220.8	6.1 to 13.2
Q2	Sm_2Co_{17}	±130.2 to ±181.8	3.6 to 11.0
Q1	Sm_2Co_{17}	±51.0 to ±115.2	3.3 to 14.6
B1	Sm_2Co_{17}	±20.0 to ±36.0	2.6 to 6.1
Beam pipe 3	Al	±115.2 to ±181.6	3.5 to 3.6
Beam pipe 4	Al	±181.8 to ±900	6.0 to 6.1
End cap	CsI	±150.0 to ±187.0	45.0 to 100.0
End cap shield 1	Pb	±187.0 to ±197.0	45.0 to 100.0
End cap shield 2	Pb	±150.0 to ±197.0	35.0 to 45.0
Mask E	W	±14.9 to ±20.0	2.6 to 4.6
Beam pipe 1	Be	–40.3 to +36.0	2.5 to 2.6
Beam pipe 2+	Al	+36.0 to +115.2	3.2 to 3.3
Beam pipe 2–	Al	–115.2 to –40.3	3.2 to 3.3
Mask A_1	Ta	+19.37 to +20.51	1.50 to 1.70
Mask A_2	Ta	+18.11 to +21.53	1.70 to 1.90
Mask A_3	Ta	+16.85 to +22.55	1.90 to 2.10
Mask A_4	Ta	+15.59 to +23.57	2.10 to 2.30
Mask A_5	Ta	+14.33 to +24.59	2.30 to 2.50
Mask C_1	Ta	–35.59 to –32.37	1.75 to 1.90
Mask C_2	Ta	–36.77 to –27.11	1.90 to 2.05
Mask C_3	Ta	–37.95 to –21.85	2.05 to 2.20
Mask C_4	Ta	–39.13 to –16.59	2.20 to 2.35
Mask C_5	Ta	–40.31 to –11.33	2.35 to 2.50
Mask F	W	–40.31 to –36.0	2.6 to 6.1
Support	Carbon fiber	–60.0 to +60.0	16.8 to 18.0
Si layer 1	Si	–4.5 to +4.5	2.80 to 2.83
Si layer 2	Si	–9.0 to +9.0	5.10 to 5.13
Si layer 3	Si	–9.0 to +9.0	7.40 to 7.43
Si layer 4	Si	±11.0 to ±11.03	2.80 to 8.50
Si layer 5	Si	±14.0 to ±14.03	2.80 to 8.50
DC inner wall	Al	–150 to +150	18.0 to 18.2
DC score 1	He/CO_2/Iso	–150 to +150	18.2 to 18.4
DC score 2	He/CO_2/Iso	–150 to +150	18.4 to 18.6
DC score 3	He/CO_2/Iso	–150 to +150	18.6 to 18.8
DC score 4	He/CO_2/Iso	–150 to +150	18.8 to 19.0
DC score 5	He/CO_2/Iso	–150 to +150	19.0 to 19.2
DC score 6	He/CO_2/Iso	–150 to +150	19.2 to 19.4

Table 4-11 continued.

Object	Material	z (cm)	r (cm)
DC score 7	$He/CO_2/Iso$	−150 to +150	19.4 to 19
DC score 8	$He/CO_2/Iso$	−150 to +150	19.6 to 19.8
DC score 9	$He/CO_2/Iso$	−150 to +150	19.8 to 20.0
DC score 10	$He/CO_2/Iso$	−150 to +150	20.0 to 20.2
DC score 11	$He/CO_2/Iso$	−150 to +150	20.2 to 20.4
DC score 12	$He/CO_2/Iso$	−150 to +150	20.4 to 20.6
DC other 1	$He/CO_2/Iso$	−150 to +150	20.6 to 30.0
DC score 13	$He/CO_2/Iso$	−150 to +150	30.0 to 30.2
DC other 2	$He/CO_2/Iso$	−150 to +150	30.2 to 40.0
DC score 14	$He/CO_2/Iso$	−150 to +150	40.0 to 40.2
DC other 3	$He/CO_2/Iso$	−150 to +150	40.2 to 50.0
DC score 15	$He/CO_2/Iso$	−150 to +150	50.0 to 50.2
DC other 4	$He/CO_2/Iso$	−150 to +150	50.2 to 60.0
DC score 16	$He/CO_2/Iso$	−150 to +150	60.0 to 60.2
DC other 5	$He/CO_2/Iso$	−150 to +150	60.2 to 70.0
DC score 17	$He/CO_2/Iso$	−150 to +150	70.0 to 70.2
DC other 6	$He/CO_2/Iso$	−150 to +150	70.2 to 79.3
DC score 18	$He/CO_2/Iso$	−150 to +150	79.3 to 79.5
DC outer wall	Al	−150 to +150	79.5 to 80.0
CRID	Vacuum	−150 to +150	80.0 to 94.0
Calorimeter	CsI	−150 to +150	94.0 to 131.0

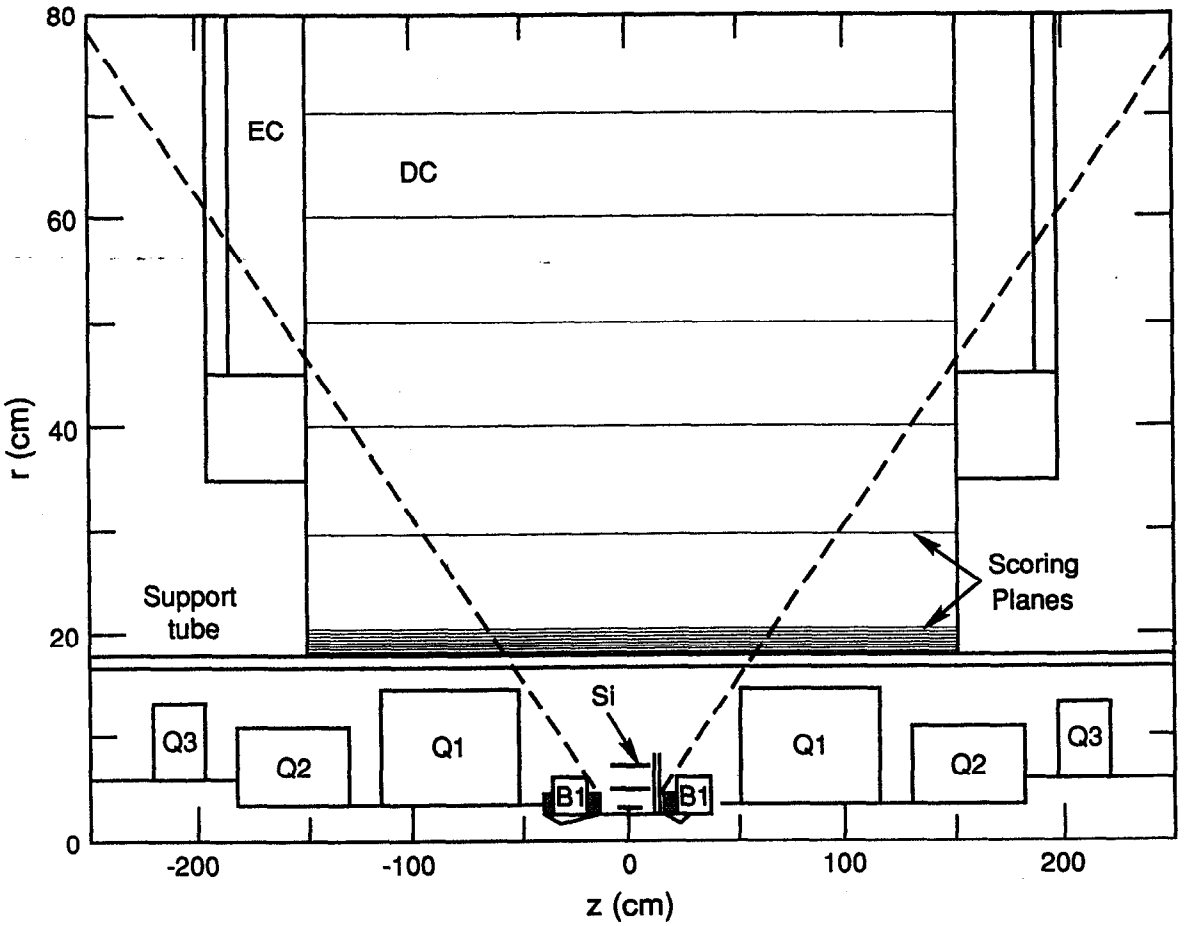

Fig. 4-64. Schematic of the detector and IR geometry used by EGS.

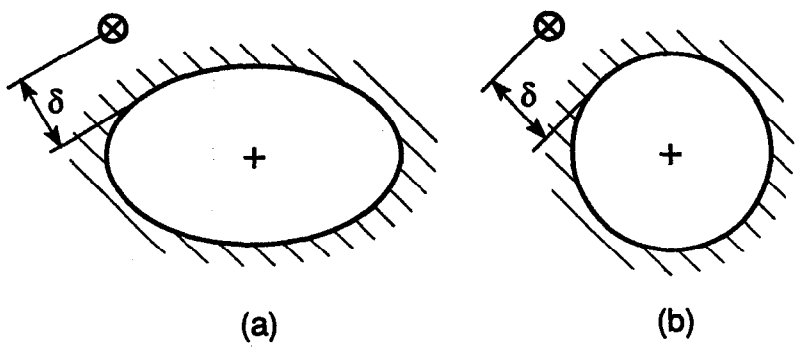

Fig. 4-65. Representation of the mapping of a noncylindrical geometry to the cylindrically symmetric EGS geometry. A ray striking a mask in DECAY TURTLE (a) is represented in EGS by a ray striking a cylinder (b). The distance δ is the same in both cases.

Table 4-12. Rate of energy deposition (in MeV/μs) as determined by EGS simulation.

Object	Energy deposited by LEB	Energy deposited by HEB	Total energy deposited
+z support 2	2.8	275.9	278.7
+z Q3	26.1	150.2	176.3
+z Q2	661.6	2251.3	2912.9
+z Q1	1788.5	933.9	2722.4
+z B1	119.1	860.5	979.6
+z beam pipe 3	35.2	78.7	113.9
+z beam pipe 4	1.0	44.8	45.8
+z end cap	2.2	38.2	40.4
+z end cap shield 1	0.03	0.41	0.44
+z end cap shield 2	3.6	26.1	29.7
+z mask E	52.3	1056.9	1109.2
–z support 2	38.9	10.3	49.2
–z Q3	4.4	37.5	41.9
–z Q2	18.9	6063.8	6082.7
–z Q1	300.0	334.5	634.5
–z B1	249.4	143.8	393.2
–z beam pipe 3	1.4	158.0	159.4
–z beam pipe 4	2.8	1.08	3.9
–z end cap	14.0	4.90	18.9
–z end cap shield 1	0.04	0.16	0.20
–z end cap shield 2	2.8	36.4	39.2
–z mask E	77.6	18.1	95.7
Beam pipe 1	8.6	84.0	92.6
Beam pipe 2+	23.8	41.5	65.3
Beam pipe 2–	13.2	13.8	27.0
Mask A_1	3.6	116.0	119.6
Mask A_2	9.0	283.6	292.6
Mask A_3	6.3	583.9	590.2
Mask A_4	11.4	767.3	778.7
Mask A_5	13.0	1175.2	1188.5
Mask C_1	252.5	132.8	385.3
Mask C_2	570.9	194.8	765.7
Mask C_3	617.4	131.4	748.8
Mask C_4	306.5	96.9	403.3
Mask C_5	163.0	86.7	249.7
Mask F	123.9	140.4	264.3
Support 1	0.54	1.16	1.70
Si layer 1	0.089	0.17	0.26

Table 4-12 continued.

Object	Energy deposited by LEB	Energy deposited by HEB	Total energy deposited
Si layer 2	0.063	0.21	0.27
Si layer 3	0.055	0.098	0.15
Si layer 4	0.024	0.088	0.11
Si layer 5	0.018	0.078	0.10
DC inner wall	2.5	5.69	8.2
DC score 1	0.0026	0.0059	0.0085
DC score 2	0.0025	0.0061	0.0086
DC score 3	0.0019	0.0047	0.0066
DC score 4	0.0019	0.0035	0.0054
DC score 5	0.0012	0.0033	0.0045
DC score 6	0.0011	0.0027	0.0038
DC score 7	0.0005	0.0024	0.0029
DC score 8	0.0005	0.0033	0.0038
DC score 9	0.0010	0.0014	0.0024
DC score 10	0.0007	0.0024	0.0031
DC score 11	0.0010	0.0008	0.0018
DC score 12	0.0010	0.0017	0.0027
DC other 1	0.033	0.134	0.167
DC score 13	0.0001	0.0019	0.002
DC other 2	0.036	0.118	0.154
DC score 14	0.0004	0.0008	0.0012
DC other 3	0.033	0.078	0.111
DC score 15	0.0010	0.0031	0.0041
DC other 4	0.038	0.044	0.082
DC score 16	0.0003	0.0006	0.0009
DC other 5	0.028	0.076	0.104
DC score 17	0.0007	0.0019	0.0026
DC other 6	0.025	0.070	0.095
DC score 18	0.0002	0.0008	0.0010
DC outer wall	4.39	10.32	14.71
CRID	0.0000	0.0000	0.0000
Calorimeter	102.9	230.2	333.1

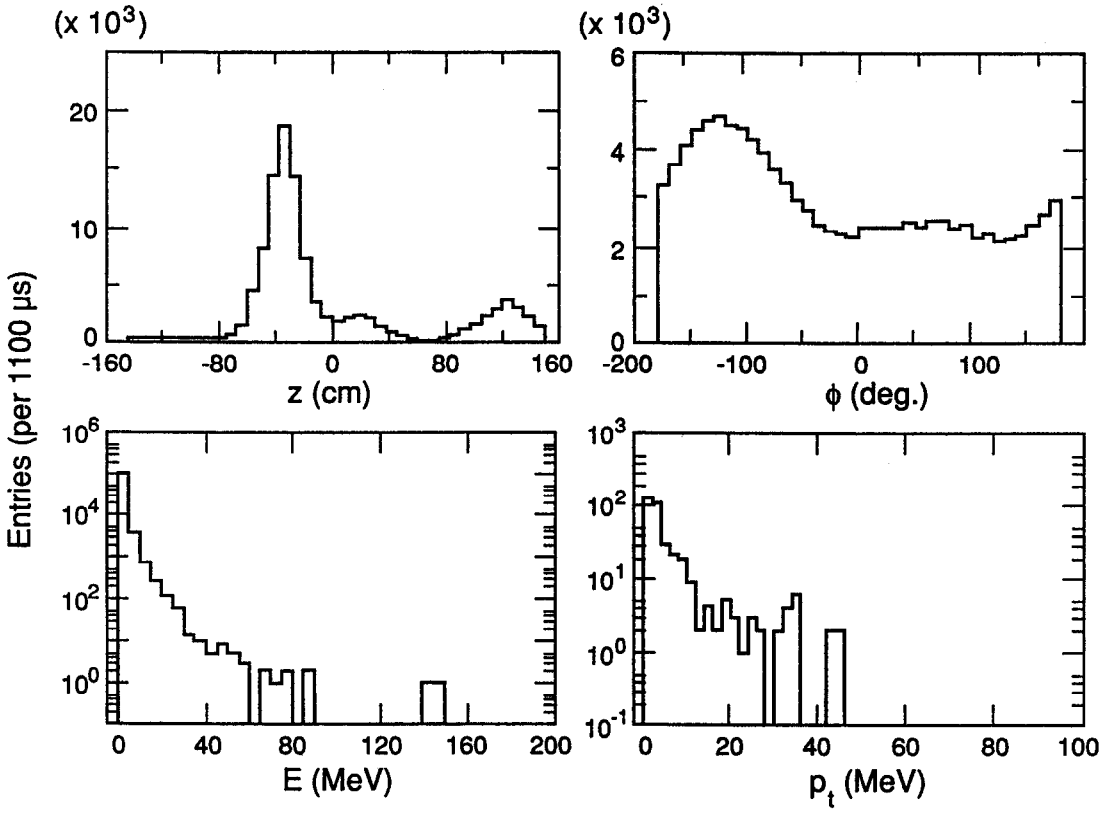

Fig. 4-66. Backgrounds due to the LEB in the first sense wire plane of the drift chamber ("drift chamber score 8" in Tables 4-11 through 4-13): (a) z; (b) the azimuthal angle ϕ, (c) energy of photons entering the scoring plane; and (d) the transverse momentum p_t of the electrons. The vertical scale represents entries per 1100 μs of running.

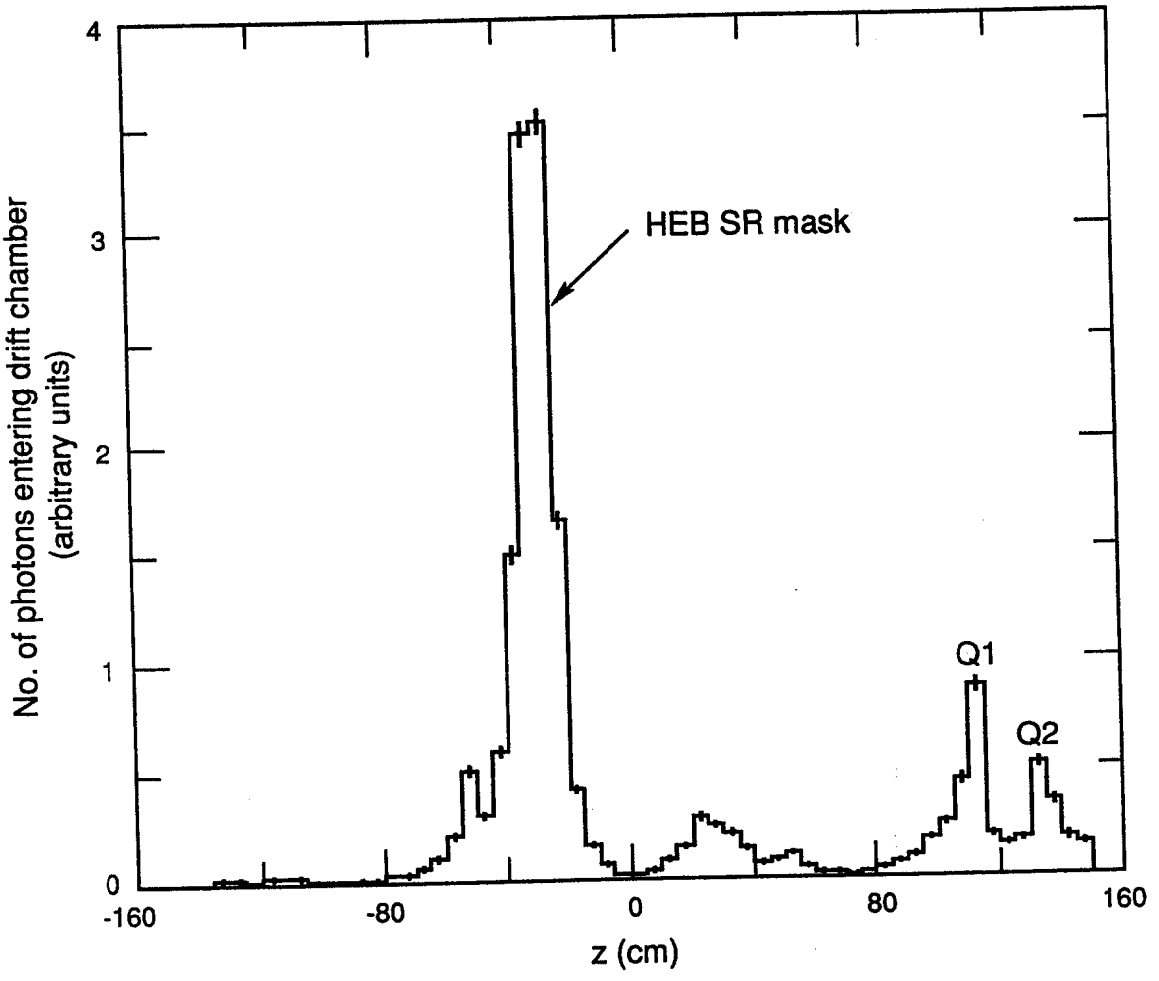

Fig. 4-67. Plot showing the origin of photons that enter the drift chamber due to beam particles lost from the LEB. The largest peak is due to showers originating at the synchrotron radiation mask CD.

drift chamber is of the order of 5×10^{-3}. The electrons entering the innermost drift chamber scoring layers are due to photon conversions in the inner wall. At larger radii—roughly 2–3 cm from the inner wall—the electrons are due to photon conversions in the gas. A low-density gas (He, 78%; CO_2, 15%; C_4H_{10}, 7%) is used. The number of photons, and hence the number of electrons, crossing each radius is essentially constant with radius (see Fig. 4-68). The number of electrons per area therefore falls as $1/r$. Note that the points in Fig. 4-68 have large statistical fluctuations, because a single electron can be counted as many as 100 times due to looping. Electrons deposit 3.0 keV per cm of path length in the gas. The average path length of an electron traversing a 2-mm-thick scoring cylinder is 5.2 mm. (Similarly, the path length of an electron traversing a 0.3-mm-thick silicon vertex detector layer is 0.8 mm.) Backgrounds elsewhere in the detector are similar to those in the drift chamber; that is, they are characterized by low-energy photons and low-p_t electrons.

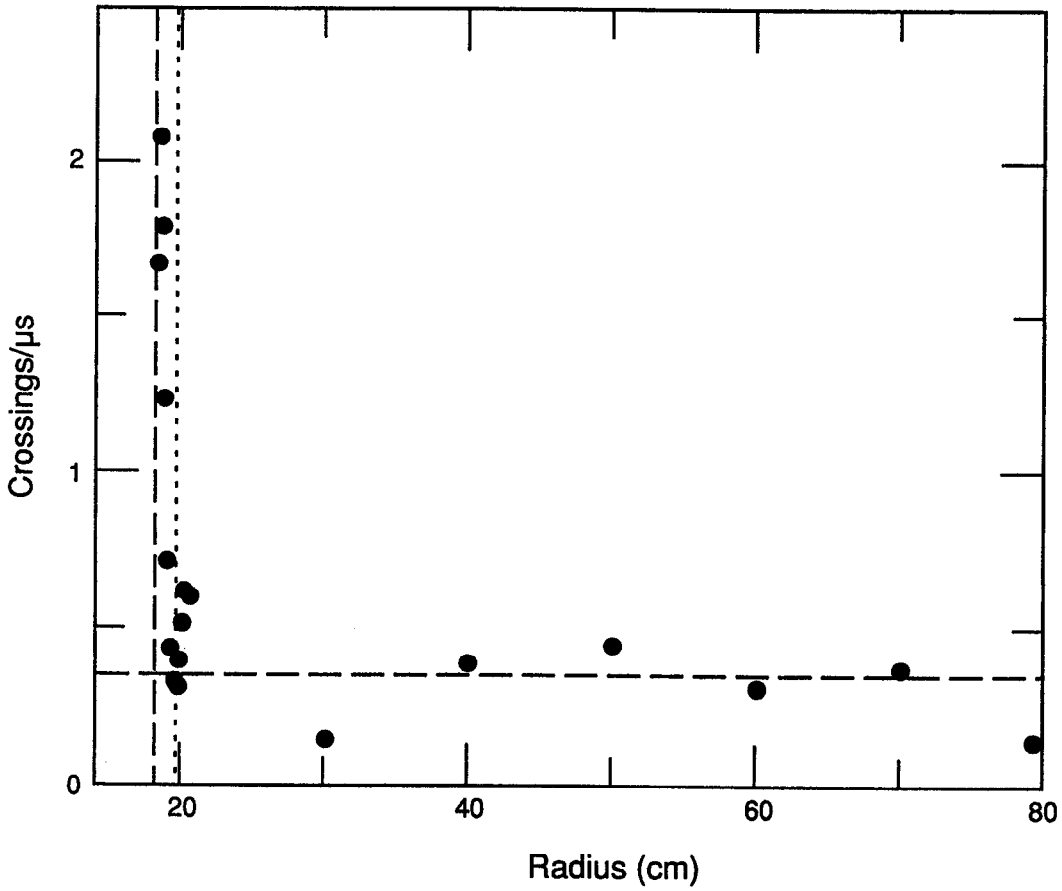

Fig. 4-68. Number of electrons crossing each drift chamber scoring plane as a function of radius. Electrons looping in the solenoid field are counted each time they cross the plane; electrons from photon conversions are counted as electrons. The peak at the inner wall (dashed line) is due to conversions in the wall. Charge deposited in the first centimeter beyond the wall will drift to the z strips rather than the first sense wire (dotted line).

Table 4-13 lists the calculated backgrounds in several detector components from the LEB and the HEB, along with the estimated allowable rates (see Chapter 2). The most stringent limit on silicon backgrounds comes from an allowed radiation dose of 100 krads in a 10^7-second operating year, rather than occupancy considerations. In the drift chamber, the most stringent limiting factor is the 10% occupancy allowed; the radiation damage limit of 0.5 C/cm is six times higher. In the calorimeter, the limit results from a radiation dose of 5000 rads per 10^7-second operating year.

We therefore see from comparing the calculated rates with the limits imposed by detector considerations (see Section 2.4) that, on average, the drift chamber dose is a factor of fifteen lower than the most stringent limit. Even the worst case, for the first sense wire, is a factor of six below the limit. Safety factors in the silicon vertex detector and the calorimeter are even better.

4.2.4 Summary

The B Factory lattice and masking designs produce detector synchrotron radiation backgrounds that are more than 100 times below the specified limits for radiation damage and detector occupancy. The design allows most of the synchrotron radiation to pass through the IR without striking any nearby surfaces. Backgrounds are insensitive to the beam-particle distribution at large amplitudes, making the design insensitive to details of the beam-beam interaction. The primary masks, labeled AB and CD in Fig. 4-41, shield the detector beam pipe from direct synchrotron radiation. Detector backgrounds result from photons that scatter through the tips of these masks. A careful analysis of tip-scattered photons using a realistic (rounded) tip edge shows that the background levels

Table 4-13. Summary of detector backgrounds per microsecond, due to lost beam particles; energy is given in MeV.

					Limits	
		LEB	HEB	Total	Occupancy	Radiation
Si 2	Energy	0.06	0.21	0.27	—	—
	$e^{\pm}$	0.20	0.61	0.81	200	—
	γ	1.9	10.1	12.0	—	—
	rads/yr	250	880	1130	—	10^5
DC 8	Energy	0.0005	0.0033	0.0038	—	—
1st sense	$e^{\pm}$	0.32	1.5	1.8	11	50
	γ	95	191	286	—	—
DC 15	Energy	0.0010	0.0031	0.0041	—	—
$r = 50$ cm	$e^{\pm}$	0.45	0.44	0.9	28	127
	γ	95	202	297	—	—
Barrel	Energy	103	230	333	—	—
calorimeter	γ	84	176	260	—	—
	rads/yr	2	4	6	—	5000

are essentially the same as those of a mask with a perfect tip. Sources of synchrotron radiation farther upstream (beyond 5 m) were also investigated. These sources do not increase detector occupancy and only increase the amount of energy absorbed in the first layer of silicon by 50%. A substantial amount of synchrotron radiation power strikes surfaces downstream of the IP. Photons that backscatter from these surfaces were studied and found not to contribute to detector background levels. The sensitivity of detector backgrounds to reasonable beam misalignments (±1 mm) is small (about a factor of two).

We made an exhaustive study of all radiation fans generated near the IP. Care was taken to ensure that all of this miscellaneous synchrotron radiation does not increase detector backgrounds. Nearly 90% of the 97 kW of power is absorbed in downstream dumps. This causes no increase in detector backgrounds, either from backscattered synchrotron radiation photons or from beam-gas interactions.

A detailed study of lost-particle backgrounds in the detector was also carried out. The dose in the drift chamber was found to be a factor of fifteen below its limit, on average, and a factor of six below its limit at the worst location (the first sense wire). For the silicon vertex detector and the calorimeter, even larger safety factors are available. Thus, the configuration adopted here is safely and conservatively designed from the viewpoint of detector backgrounds.

4.3 COLLECTIVE EFFECTS

In Chapter 3 we discussed the alternatives that might be considered in the design of a high-luminosity B Factory, and indicated the reasons for the choices we have made. The lattice design presented in Section 4.1 is based on these choices. Having fixed these parameters, it is necessary to investigate the influence of the various intensity-dependent effects on the actual performance of the accelerator.

The main parameters we must achieve in the B Factory include:

- Beam energies of 9 GeV (HER) and 3.1 GeV (LER)
- Beam currents of 1.48 A (HER) and 2.14 A (LER)
- Bunch length of 1 cm
- Beam emittances of approximately 50 nm·rad (HER) and 100 nm·rad (LER)
- Beam energy spread of $\sigma_E/E \leq 1 \times 10^{-3}$

In terms of collective effects, the dominant issue is the relatively high beam current that must be supported in each ring. As was discussed briefly in Chapter 3, and as will be covered in more detail in Section 4.4, this constraint is associated mainly with the fact that the beam-beam tune shift parameter is taken to be a design limit, which means that the high luminosity must come mainly from the combined benefits of low beta functions and high currents.

A beam circulating in a storage ring interacts with its surroundings electromagnetically by inducing image currents in the walls of the vacuum chamber and other "visible" structures, such as beam position monitor electrodes, kickers, RF cavities, bellows, valves, etc. This interaction leads, in turn, to time-varying electromagnetic fields that act on the beam and can give rise to instabilities. In most electron-positron colliders, single-bunch effects are the primary concern. However, different beam bunches can communicate through the narrow-band impedances in the ring, producing coupled-bunch instabilities.

The issues with which we must deal for the B Factory fall into the broad categories of single-bunch and multibunch phenomena. Single-bunch phenomena include:

- Longitudinal and transverse single-bunch instabilities
- Beam loss from intrabeam (Touschek) or beam-gas scattering
- Beam loss from beam-beam (Bhabha) scattering
- Higher-order-mode (HOM) heating
- Ion trapping

Multibunch phenomena can also be a serious issue. Wakefields deposited in various high-Q resonant objects can influence the motion of following bunches and can cause the motion to become unstable if the beam currents are too high. This effect is one of the most serious issues for a B Factory design.

For our B Factory design, we have opted for a situation in which the nominal beam currents of 1.48 A in the HER and 2.14 A in the LER are distributed in many (1658) bunches. Our reasoning is as follows: The multibunch instabilities are mainly driven by the total beam current, with little regard to how it is distributed in the ring. That is, once the bunch separation is small enough for bunches to fully see wakefields left by preceding bunches, the growth rates are independent of the details of the bunch pattern. Thus, if a high beam current is needed, coupled-bunch instabilities become almost unavoidable. If we choose a relatively small number of bunches to make up the high current, we do little to improve the situation with regard to coupled-bunch instabilities and simply make the single-bunch phenomena harder to manage—in effect requiring the accelerator designers to wage a two-front war. (This usually translates into impedance requirements for the ring that are difficult to meet.) It is true, of course, that the bandwidth requirements of a feedback system to deal with coupled-bunch motion are eased if the bunch spacing increases. However, we do not feel that this is a major limitation (see Section 5.6 for details) and it should not dominate the design decisions.

Given our decision to utilize many bunches, the parameters of the single bunches (emittances, bunch length, intensity) are not unusual—they are in the parameter regime in which PEP and many other colliders have run successfully for many years. This, in turn, means that heroic efforts at impedance reduction are not required to avoid problems with single-bunch effects.

4.3.1 Single-Bunch Issues

In this section, we focus on the issues of single-bunch instability thresholds, beam lifetime, and heating of the chamber due to parasitic HOM losses. We also discuss the issue of ion trapping and the means available to avoid or eliminate it. Before beginning, we digress briefly to define the beam impedances that drive the various instabilities.

4.3.1.1 Impedances. Beam instabilities can occur in either the longitudinal or transverse phase planes. Longitudinal instabilities are driven by voltages induced via interactions of the beam with its environment. The strength of the interaction can be characterized by the ring impedance $Z_{\|}(\omega)$, in ohms, which is defined by

$$V_{\|}(\omega) = -Z_{\|}(\omega)\, I_b(\omega) \tag{4-3}$$

where $V_{\|}(\omega)$ is the longitudinal voltage induced in the beam per turn arising from a modulation of the beam current $I_b(\omega)$ at some particular angular frequency ω.

Transverse instabilities arise from the transverse dipole wake field, which gives a force that increases linearly with transverse distance from the electromagnetic center of the vacuum chamber and is antisymmetric in sign about that center. The transverse impedance (in Ω/m) is defined by

$$Z_\perp(\omega) = \frac{-i\int_0^{2\pi R} F_\perp(\omega,s)\,ds}{e\Delta I_b(\omega)} \tag{4-4}$$

where $F_\perp$ is the transverse force, integrated over one turn, experienced by a charge e having transverse displacement Δ. Explicitly, $F_\perp$ is given by

$$F_\perp = e\hat{\theta}(E_\theta + B_r) + e\hat{r}(E_r - B_\theta) \tag{4-5}$$

In a typical storage ring, the impedance seen by the beam can be loosely characterized as being either broadband or narrow-band. Sharp discontinuities in the vacuum chamber act as local sources of wakefields. These fields have a short time duration, which means that they include many frequency components, and we refer to the corresponding impedance as broadband.

For instability calculations performed in the frequency domain (for example, with ZAP), such impedances are typically represented with a so-called $Q = 1$ resonator, whose analytical form is given below for the longitudinal and transverse cases, respectively:

$$Z_\parallel^{BB}(\omega) = \frac{R_S}{\left[1 + i\left(\frac{\omega_c}{\omega} - \frac{\omega}{\omega_c}\right)\right]} \tag{4-6}$$

$$Z_\perp^{BB}(\omega) = \left(\frac{\omega_c}{\omega}\right)\frac{R_T}{\left[1 + i\left(\frac{\omega_c}{\omega} - \frac{\omega}{\omega_c}\right)\right]} \tag{4-7}$$

This representation has convenient analytical properties and qualitatively exhibits the correct behavior for the actual impedance of a storage ring. In particular, the modulus of the longitudinal impedance, $|Z_\parallel|$, is proportional to frequency up to a cutoff frequency ω_c, after which it falls off as $1/\omega$ with increasing frequency. In the calculations of longitudinal instabilities described below, we make use not of $|Z_\parallel|$ but of the related quantity $|Z_\parallel/n|$, where $n \equiv \omega/\omega_0$ is the harmonic of the revolution frequency ω_0. This quantity remains essentially constant up to the cutoff frequency, beyond which it decreases as $1/\omega^2$. (The fall-off with frequency for the $Q = 1$ resonator is now believed to be somewhat more rapid than is true for the actual storage ring impedance. Nonetheless, a $Q = 1$ resonator impedance model is typically used for calculational convenience. In the B Factory parameter regime, the differences are not expected to be large.) As can be seen from inspection of Eq. 4-7, the frequency dependence of the transverse impedance follows that of $|Z_\parallel/n|$.

The other category of impedance-producing objects in a typical storage ring consists of cavitylike objects. Such objects can trap electromagnetic energy and exchange it with the beam. The wakefield from a cavity oscillates for a long time and thus gives a narrow

spectrum in the frequency domain. These impedances are represented in calculations as narrow-band (that is, high-Q) resonators:

$$Z_{\parallel}(\omega) = \frac{R_s}{\left[1 + iQ\left(\frac{\omega_r}{\omega} - \frac{\omega}{\omega_r}\right)\right]} \tag{4-8}$$

$$Z_{\perp}(\omega) = \left(\frac{\omega_r}{\omega}\right)\frac{R_T}{\left[1 + iQ\left(\frac{\omega_r}{\omega} - \frac{\omega}{\omega_r}\right)\right]} \tag{4-9}$$

Typical values for Q lie in the range of 10^2–10^5, with parasitic modes of the RF cavities being closer to the upper end of the range (unless special procedures, such as those discussed in Section 5.5, are used to de-Q them). As a result of the relatively long duration of these wakefields, trailing beam bunches feel the effects of the bunches that preceded them. The motion of the many bunches in the ring thus becomes coupled and can become unstable for certain patterns of relative phase between bunches. This topic is discussed in Section 4.3.2.

4.3.1.2 Longitudinal Microwave Instability. The first instability we consider is the longitudinal microwave instability, sometimes referred to as turbulent bunch lengthening. This instability, which has been seen in numerous proton and electron storage rings, is not a "fatal" instability, in the sense that it does not lead to beam loss. Instead, the instability causes an increase in both the bunch length and the momentum spread of a bunched beam. Its threshold (peak) current is given by

$$I_p = \frac{2\pi|\eta|\,(E/e)\,(\beta\sigma_p)^2}{\left|\frac{Z_{\parallel}}{n}\right|_{\text{eff}}} \tag{4-10}$$

where $|Z_{\parallel}/n|_{\text{eff}}$ is the effective broadband impedance of the ring and $\eta = \alpha - 1/\gamma^2$ is the phase-slip factor.

We refer to an "effective" impedance here to account for the fact that the bunch samples the storage ring impedance weighted by its power spectrum $h(\omega)$, which is the square of the Fourier spectrum of the bunch. As was shown by Zisman [1990a], a short bunch—one having a frequency spectrum that extends well beyond the cutoff frequency of the broadband impedance—does not sample the impedance fully. This reduction in effective impedance can be modeled in calculations by making use of the "SPEAR Scaling" ansatz [Chao and Gareyte, 1976] for $\sigma_\ell < b$:

$$\left|\frac{Z_{\parallel}}{n}\right|_{\text{eff}} = \left|\frac{Z}{n}\right|_0 \left(\frac{\sigma_\ell}{b}\right)^{1.68} \tag{4-11}$$

where b is the chamber radius. (In terms of the discussion above, the dependence on b in Eq. 4-11 results from our estimate of the cutoff frequency of the broadband impedance to

be $\omega_c = c/b$.) The result of the impedance roll-off for short bunches is that the bunch lengthening threshold increases. It is worth noting that the expression given in Eq. 4-11, which was determined phenomenologically, is in reasonable agreement with the behavior expected from a simple $Q = 1$ resonator.

As mentioned, the actual broadband impedance in a storage ring is not exactly a $Q = 1$ resonator shape, and so the actual roll-off of the broadband impedance in any ring depends on the details of the particular vacuum chamber hardware. Indeed, in modern storage rings that are specifically designed to minimize the broadband impedance, it may well be that the impedance is dominated by a few discrete items, making the concept of an amorphous broadband impedance somewhat suspect.

To estimate the growth from the longitudinal microwave instability, we must assume a value for the broadband impedance of the ring. For the B Factory HER, this value—usually dominated by the RF system in a high-energy storage ring—is expected to be lower than the value of $|Z/n| = 3\ \Omega$ obtained from measurements at PEP [Rivkin, 1987].

The equivalent broadband contribution to the impedance seen by the beam can be estimated, for a given RF system, following the approach of Zisman et al. [1986]. Basically, this involves estimating the frequency shift that would be induced in a long beam bunch by the aggregate of the many cavity HOMs, and then determining the strength of a $Q = 1$ broadband resonator that would produce the same effect. That is, we take

$$\left|\frac{Z_\parallel}{n}\right|_{\mathrm{BB,RF}} = \sum_{\mathrm{HOMs}} \left|\frac{Z_\parallel}{n}\right|_j = \sum_j \left(\frac{R_s\,\omega_0}{Q\,\omega_R}\right)_j \tag{4-12}$$

where R_s, ω_R, and Q are the shunt impedance, resonant angular frequency, and quality factor, respectively, of the jth HOM, and ω_0 is the particle (angular) revolution frequency. With this approach, we find that the present PEP RF system contributes an equivalent broadband component of $|Z/n| \approx 0.026\ \Omega$/cell. Applying the same prescription to the B Factory RF cavity (described in Section 5.5) yields an equivalent broadband contribution of $|Z/n| \approx 0.01\ \Omega$ for the first few trapped modes. If additional higher-frequency modes were included in our estimate, it is likely that the broadband impedance *per cell* would not differ markedly from PEP.

A more significant gain is made by producing the required voltage and providing the required power to the beam (to replenish the losses to synchrotron radiation) with many fewer RF cells than the 120 used now at PEP. In the design described in Section 5.5, the voltage is provided by only 20 RF cells in the HER or 10 cells in the LER. This decrease in the number of cells reduces, by about a factor of six, the broadband impedance in the ring that stems from the RF system (estimated in PEP to be about two-thirds of the total). Thus, we expect to reduce the RF contribution to the broadband impedance to about 0.3 Ω. Clearly, however, the broadband impedance from the other components in the beam path (valves, bellows, BPMs, etc.) must contribute to the total seen by the beam, and there will be additional hardware in the B Factory ring (for example, more powerful feedback kickers) that will have an effect.

A preliminary investigation of the impedance contributions from the various components in the rings was carried out by Heifets [1990b]. The results of this

investigation, summarized in Table 4-14, indicate a small impedance contribution from the non-RF hardware. Nonetheless, the actual PEP chamber has a broadband impedance of about 1 Ω, and it is prudent, for now, to take the larger value to account for those things that have not been considered yet. With this in mind, we have adopted a total broadband impedance of $|Z/n| = 1.5\ \Omega$ for the HER—half that of PEP. As we will see, even this fairly conservative assumption does not lead to any difficulties in the parameter regime in which the B Factory rings are designed to operate. Although the LER has less RF hardware than does the HER, we have assumed for simplicity that it is also characterized by a broadband impedance of 1.5 Ω.

Table 4-14. Preliminary B Factory impedance budget.

Item	Broadband impedance contribution (Ω)
Bellows	0.012
Clearing electrodes	0.072
Transition tapers	0.18
Feedback system	0.05
Interaction region	0.015
Total	0.35

To maintain bunch lengths in both rings that are short compared with the small β^* value of 1.5 cm in the LER, we adopt an RF voltage in the HER of 18.5 MV. As shown in Fig. 4-69, this voltage gives an rms bunch length of $\sigma_\ell = 1$ cm at the required single-bunch current of 0.9 mA. For the LER (see Fig. 4-70), a 1-cm bunch at the design current of 1.3 mA can be obtained with a voltage of 9.5 MV.

The expected bunch lengthening beyond threshold is shown in Fig. 4-71 for the HER, based on the threshold formula given in Eq. 4-10. We remain well below the threshold at the required single-bunch current of 0.9 mA. The situation for the LER is shown in Fig. 4-72; again we are well below threshold at the nominal 1.3 mA/bunch value. The curves in Figs. 4-71 and 4-72 are based on the so-called SPEAR Scaling ansatz, mentioned earlier. It is worth noting here that we have estimated the natural momentum spread of the low-energy beam to be 9.5×10^{-4}. This relatively large value is associated with the significant amounts of "extra" synchrotron radiation (generated in the wigglers) needed to achieve the proper emittance and to preserve the ability to reach equal damping decrement if need be.

Because the collider must be able to accommodate some energy variability, we have also considered the effects of moderate changes from the nominal operating energies of 9

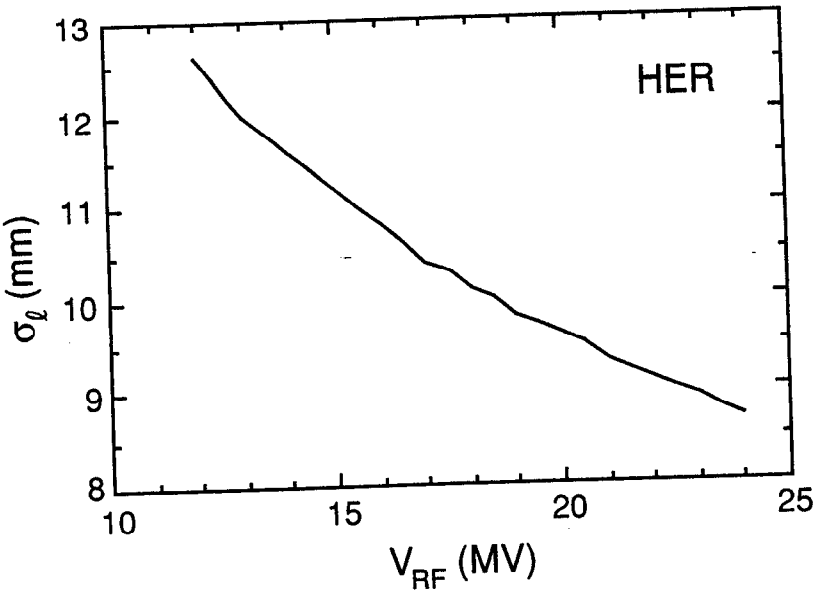

Fig. 4-69. Plot of HER bunch length as a function of RF voltage. A 1-cm bunch requires V_{RF} = 18.5 MV.

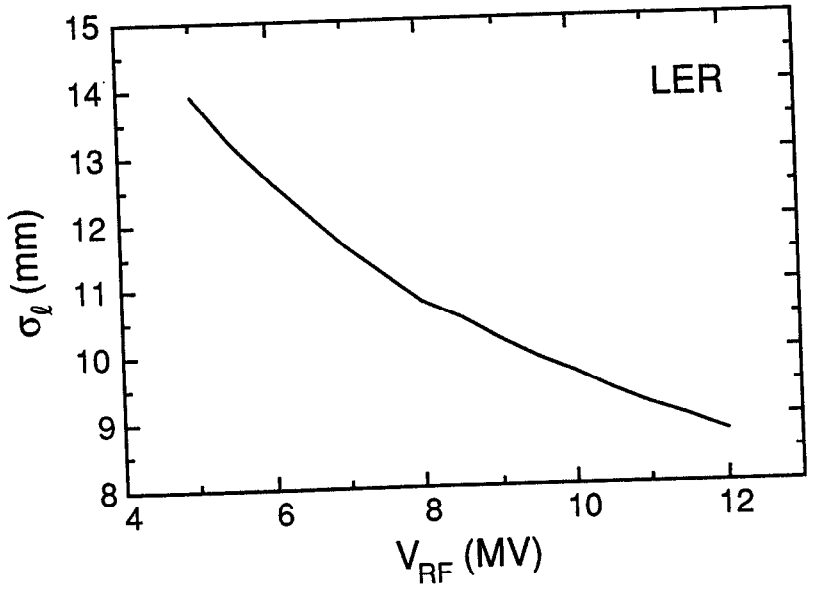

Fig. 4-70. Plot of LER bunch length as a function of RF voltage. A 1-cm bunch requires V_{RF} = 9.5 MV.

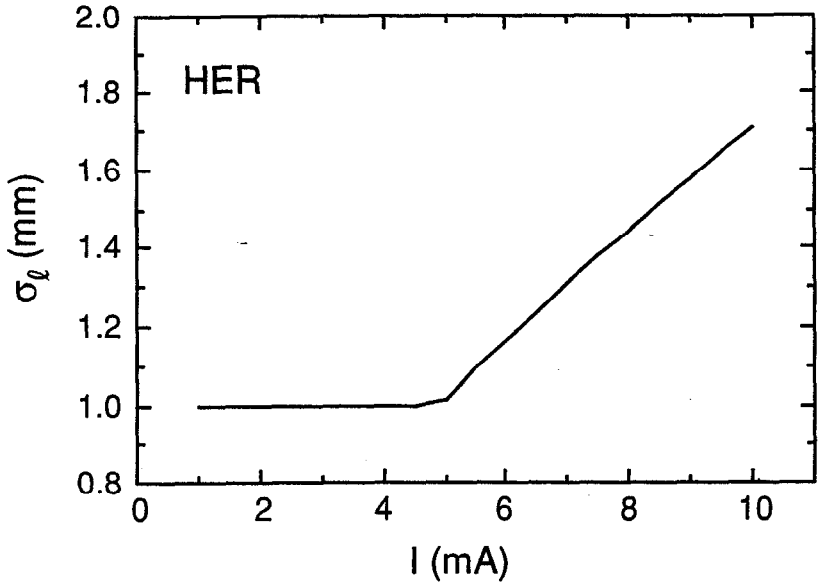

Fig. 4-71. Plot of HER bunch length as a function of current, showing the onset of bunch lengthening. Even above threshold, the bunch length increases only slowly with current.

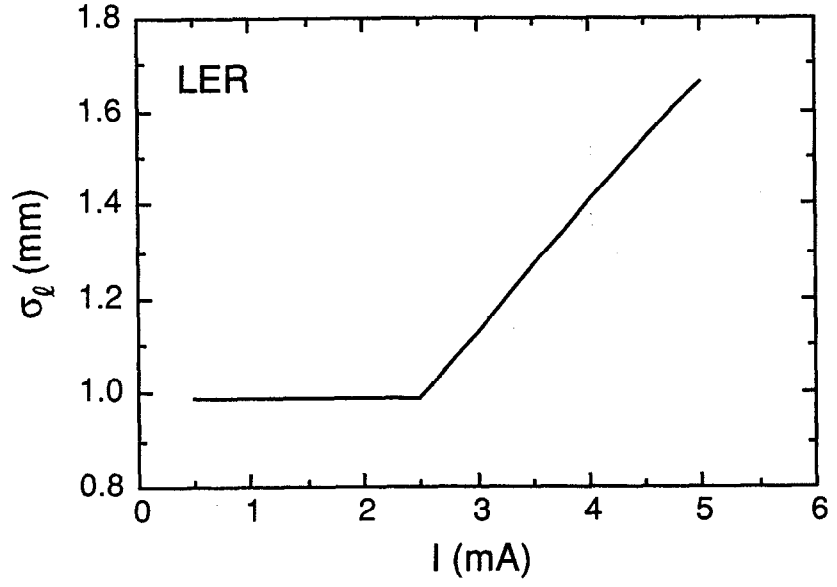

Fig. 4-72. Plot of LER bunch length as a function of current, showing the onset of bunch lengthening. The bunch length increases slowly with current above threshold.

GeV (HER) and 3.1 GeV (LER). In Figs. 4-73 and 4-74, we show the energy dependence of the microwave threshold current at the specified operating voltages for the two rings. The steepness of these curves is mainly due to the increase in natural momentum spread with energy (see Eq. 4-10). The dependence of the threshold current on voltage is shown for several different energies in Fig. 4-75 (HER) and 4-76 (LER). The preference for higher voltage is a consequence of the decrease in effective impedance as the bunch length decreases.

In our calculations we have ignored the effect of potential-well distortion, which—for short bunches—is predicted to reduce the bunch length; this effect is expected to be minor.

From these estimates, we conclude that there are no problems associated with the longitudinal microwave instability, provided the broadband impedance of each ring can be kept at or below 1.5 Ω.

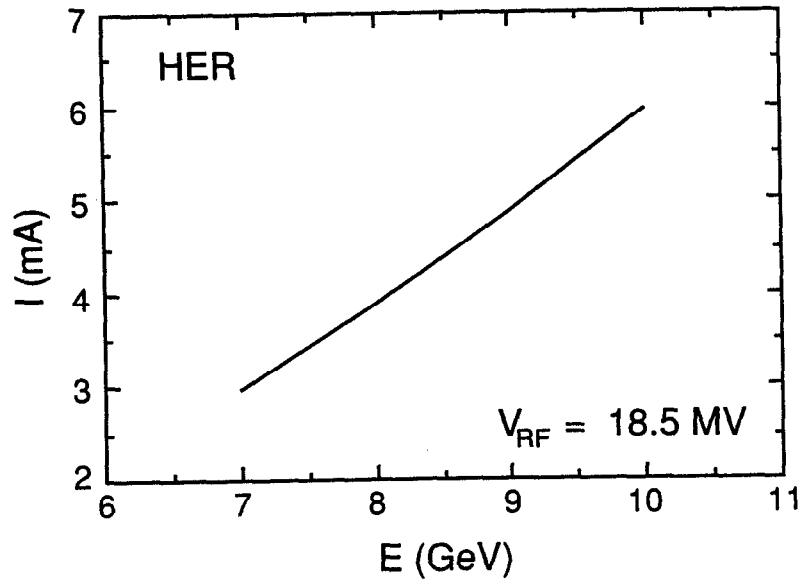

Fig. 4-73. Plot of the microwave threshold current in the HER as a function of energy, for V_{RF} = 18.5 MV. The required single-bunch current of 0.9 mA is well below the instability threshold in this energy range.

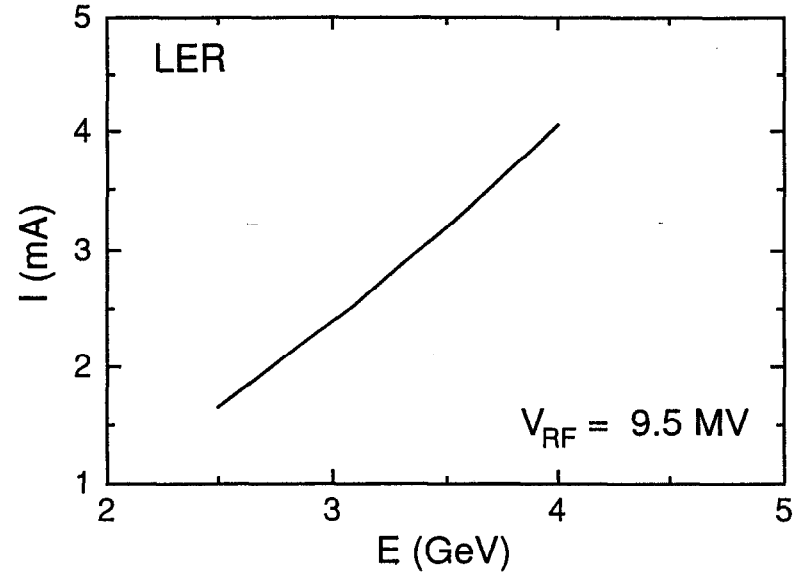

Fig. 4-74. Plot of the microwave threshold current in the LER as a function of energy, for V_{RF} = 9.5 MV. The required single-bunch current of 1.3 mA is below the instability threshold in this energy range.

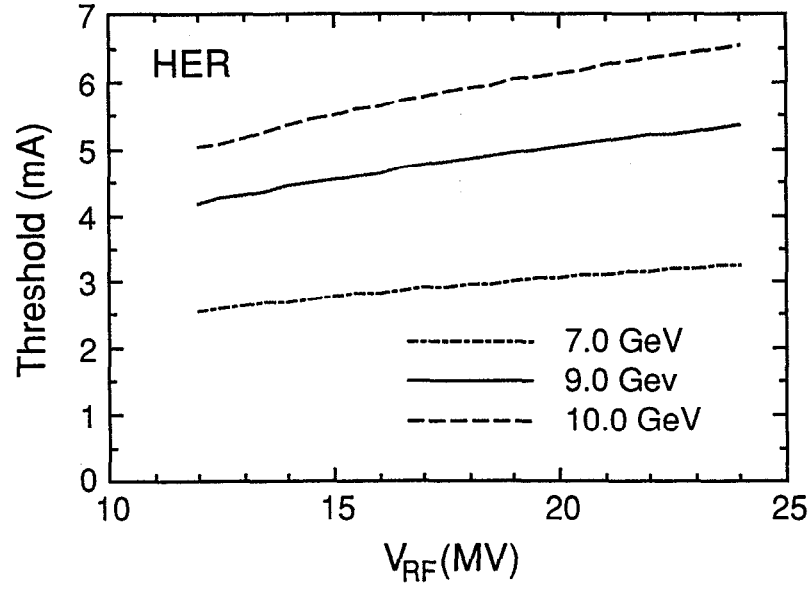

Fig. 4-75. Plot of the microwave threshold current in the HER as a function of RF voltage, for several energies. Throughout this parameter range, the threshold current is well beyond the required 0.9 mA.

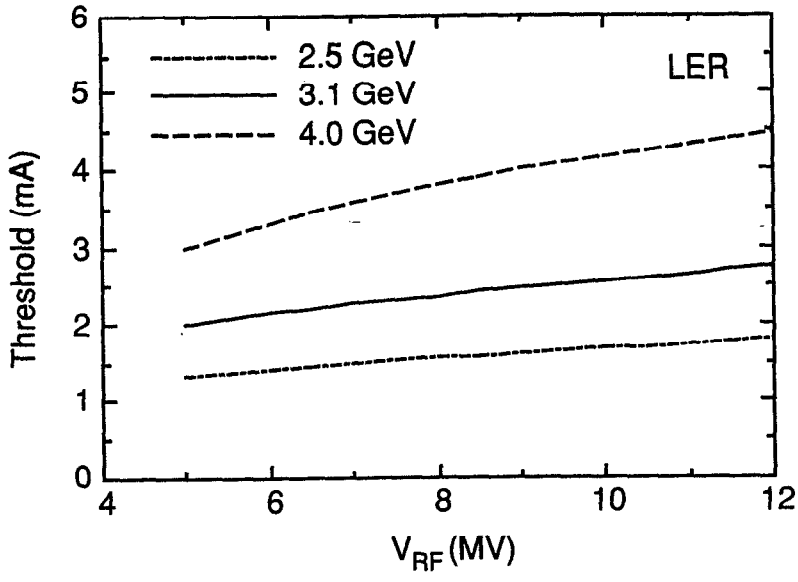

Fig. 4-76. Plot of the microwave threshold current in the LER as a function of RF voltage, for several energies. Only for the lowest energy and lowest voltage does the threshold current approach the required operating value of 1.3 mA.

4.3.1.3 Transverse Mode-Coupling Instability. Because the ring is large, we must also consider the transverse mode-coupling instability, which is known [Zisman et al., 1988] to limit the single-bunch current in PEP. This instability arises when the imaginary part of the transverse impedance $Z_\perp$ couples the frequency of the $m = 0$ and $m = -1$ synchrotron sidebands. For long bunches, the threshold is expected to scale as

$$I_b = \frac{4\,(E/e)\,\nu_s}{\langle \mathrm{Im}\,(Z_\perp)\,\beta_\perp \rangle\, R}\,\frac{4\sqrt{\pi}}{3}\,\sigma_\ell \qquad (4\text{-}13)$$

where ν_s is the synchrotron tune, $\beta_\perp$ is the beta function at the location of the impedance, and R is the average ring radius. Although the transverse impedance is expected to decrease for very short bunches [Zisman 1990a], we are operating in a regime where the mode-coupling threshold is more or less independent of bunch length. For the impedance presently expected for the HER, a simple scaling from measured PEP data based on Eq. 4-13, shown in Table 4-15, suggests that the transverse mode-coupling threshold should be somewhat higher for the B Factory than for PEP, even though both the HER and LER will have a lower beam energy than does PEP. The scaled threshold value for the LER, nearly 14 mA/bunch, is well beyond the required single-bunch current of 1.3 mA and should pose no problem.

To estimate the transverse mode-coupling threshold in each ring more reliably, we used the code MOSES [Chin, 1988]. Initially, we considered a $Q = 1$ resonator impedance having a cutoff frequency of 1 GHz and a transverse impedance of 0.5 MΩ/m.

Table 4-15. Scaling comparison for transverse mode-coupling threshold.

	Low-energy ring	PEP	High-energy ring
E [GeV]	3.1	14.5	9.0
$\beta_\perp$ [m]	20	87	20
R [m]	350	350	350
ν_s [10^{-2}]	5.0	4.6	5.3
$Z_\perp$ [MΩ/m]	0.5	0.8	0.5
Relative factor[a]	1.6	1	5.0
Observed [mA]	—	8.5	—

[a]Factor $= \dfrac{E\nu_s}{Z_\perp \beta_\perp R}$

The calculations take into account the effect of bunch lengthening at high currents, which is ignored in the simple scaling arguments presented in Table 4-15. The threshold currents, corresponding to the crossing of the mode $m = 0$ and mode $m = -1$ frequencies, are 37 mA for the HER (Fig. 4-77) and 10.6 mA for the LER (Fig. 4-78), in good agreement with the scaling estimates.

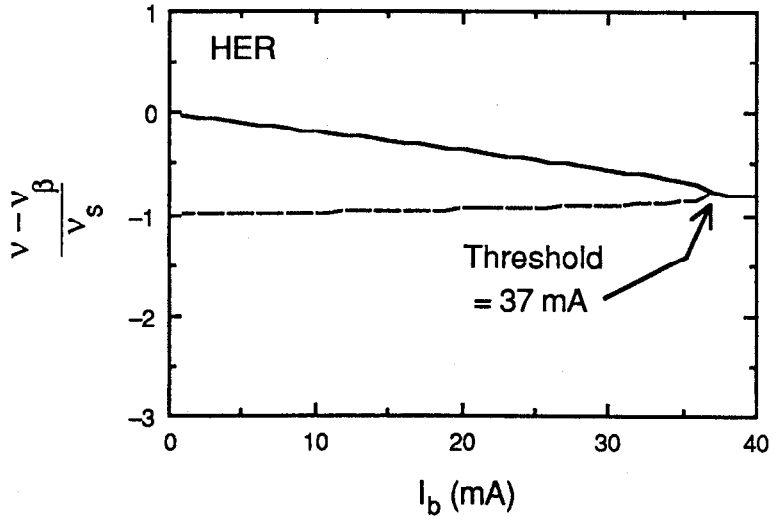

Fig. 4-77. Calculation of transverse mode-coupling instability threshold for the HER, assuming $Z_\perp = 0.5$ MΩ/m. The instability sets in when the $m = 0$ and $m = -1$ frequencies merge. This calculation represents a limitation in the horizontal plane; the vertical limitation is lower (see text).

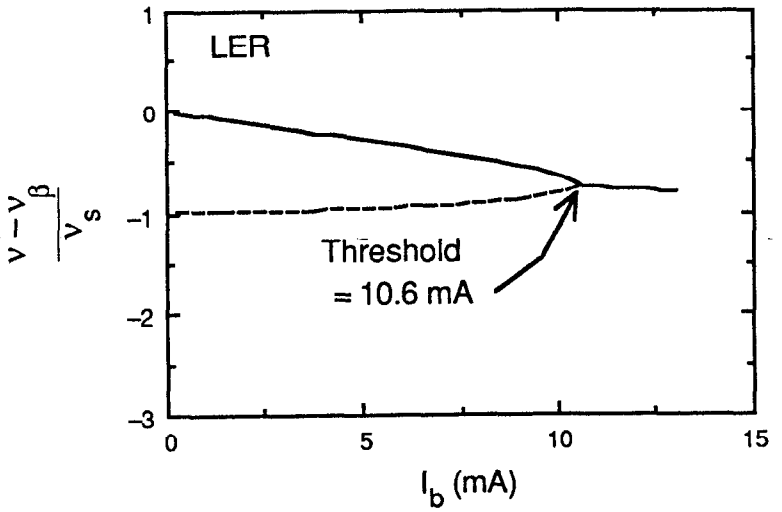

Fig. 4-78. Calculation of transverse mode-coupling instability threshold for the LER, assuming $Z_\perp = 0.5$ MΩ/m. The instability sets in when the $m = 0$ and $m = -1$ frequencies merge. This calculation represents a limitation in the horizontal plane; the vertical limitation is lower (see text).

Because the RF cavities are no longer expected to be the dominant impedance source, we have also considered the situation in which the transverse impedance comes mainly from the arc vacuum chamber hardware. In this case, the cutoff frequency for $Z_\perp$ increases to 1.9 GHz, and the strength of the impedance (weighted by the fraction of the circumference that consists of arc chambers, roughly 70%) increases to about 1.3 MΩ/m. For these parameters, MOSES predicts the transverse thresholds to be 6.5 mA for the HER and 2.2 mA for the LER.

To put these results in context, we note that the maximum allowable single-bunch current in the B Factory rings is 1.8 mA, corresponding to 3 A in 1658 bunches. Thus, the transverse mode-coupling instability is not expected to limit the performance of the B Factory.

Although the RF cavities are not the dominant contributors to the transverse impedance, it is still best to "hide" them in a low-beta region of the ring. This should be more easily accomplished in the B Factory HER than in PEP, because the total length of RF structure will be considerably shorter. Indeed, it would be possible, in principle, to adapt the focusing of the RF straight sections to permit very low beta functions in both planes.

4.3.1.4 Intrabeam Scattering. Although we are considering beams of fairly high energy, the requirements for relatively short bunches and relatively high peak currents make emittance growth from intrabeam scattering (IBS) a possible concern. IBS collisions occur because, in the bunch rest frame, not all particles are moving in the same direction. In general, the temperatures in the transverse phase planes (x and y) are higher than in the longitudinal plane. This results in small-angle multiple scattering occurring mainly in such a way as to transfer momentum from the transverse to the longitudinal plane. However, in dispersive regions of the lattice, this momentum change results in the

excitation of a betatron oscillation and thus gives rise to an increase in horizontal emittance.

To be sure this is not a concern, we performed calculations on each of the rings at the lowest energy now being considered: 7 GeV for the HER and 2.5 GeV for the LER. In the HER case, our estimates indicate that no growth is expected. In the LER case, the lower beam energy enhances the IBS growth rates, and the single-bunch current is higher than for the high-energy beam, so we might expect an observable growth. However, in the LER these aspects are compensated by the larger transverse emittance values. Thus, even here we predict no emittance growth from intrabeam scattering.

4.3.1.5 Beam and Luminosity Lifetime. For a high-energy electron beam, there are four main processes that lead to beam loss: Touschek and gas scattering for the single beams, and Bhabha ($e^+e^- \rightarrow e^+e^-$) and radiative Bhabha ($e^+e^- \rightarrow e^+e^-\gamma$) interactions for the beams in collision. For single beams at the B Factory, the first of these effects is not generally important, but the second one is. For the colliding beams, the radiative Bhabha interactions dominate the luminosity lifetime. Lifetimes presented in this section are quoted as mean (that is, $1/e$) values.

Touschek Scattering. The Touschek scattering mechanism is related to the IBS mechanism described above. The main difference is that we are concerned now with large-angle, single-scattering events that change the scattered particle's momentum sufficiently to make it fall outside the momentum acceptance of the accelerator.

The limit on the tolerable momentum deviation from the design value can come from several sources. There is a longitudinal limit from the potential well ("RF bucket") provided by the RF system. Particles deviating in momentum from the nominal value by more than this amount do not undergo stable synchrotron oscillations and are lost. There can also be a transverse limit on momentum acceptance, arising from the excitation of a betatron oscillation when the Touschek scattering event takes place in a dispersive region of the lattice. For large momentum deviations ($\delta p/p \approx$ several percent), the resultant betatron oscillation can either hit the vacuum chamber wall elsewhere in the lattice (physical aperture limit) or exceed the dynamic aperture of the machine. Because the lifetime for Touschek scattering increases approximately as $(\Delta p/p)^3$, where $(\Delta p/p)$ is the limiting momentum acceptance value, there is the potential for a strong degradation if the acceptance is too low.

For detector background reasons, we envision the possibility of installing collimators in the arcs that would restrict the particle amplitudes to about $10\sigma_x$ motion. To see how this affects the various lifetimes, ZAP has been modified to include this option.

The RF voltage in the HER, selected to be 18.5 MV so as to produce short beam bunches, actually provides too large an acceptance ($\Delta p/p = 1\%$) compared with the estimated limitation from the physical aperture ($\Delta p/p = 0.7\%$). This is not beneficial to the lifetime, since it results in a higher bunch density and thus a higher collision probability; this is the price we must pay to obtain short bunches. Fortunately, the Touschek lifetime is not a major concern in this parameter regime, as shown in Fig. 4-79. At 9 GeV, a Touschek lifetime of 870 hours is predicted for the HER based on the physical aperture limit. If a 10σ limit is applied, however, the lifetime decreases to 188 hours.

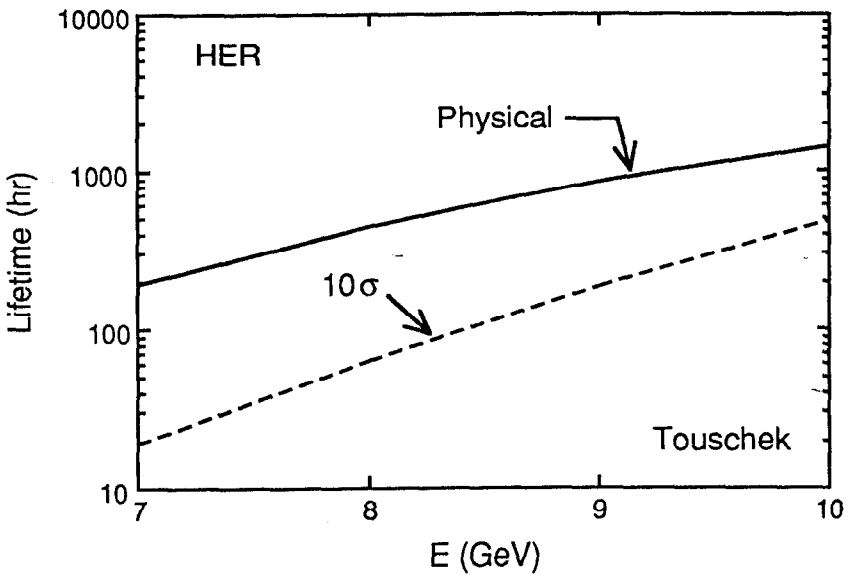

Fig. 4-79. Plot of Touschek lifetime as a function of beam energy in the B Factory HER. The solid line corresponds to taking the physical aperture of the vacuum chamber as the transverse limitation; the dashed line assumes a 10σ aperture restriction in the injection straight section.

In the LER, the physical momentum acceptance limit, $\Delta p/p \approx 1.3\%$, is almost the same as that of the RF bucket ($\Delta p/p \approx 1.7\%$). Although the energy is lower than in the HER, the large acceptance makes the Touschek lifetime about 270 hours, and thus not of concern. With a 10σ aperture restriction, the lifetime drops to 65 hours, which is still quite comfortable. We see (Fig. 4-80) that a 10σ aperture becomes quite noticeable at the lower energies, where the lifetime drops to below 10 hours.

Gas Scattering. Gas scattering involves collisions with residual gas nuclei present in the vacuum chamber. Such collisions can be either elastic or inelastic (bremsstrahlung). In the former case, particle loss results from the excitation of a betatron oscillation that exceeds the physical or dynamic aperture of the ring; in the latter case, the loss results from a momentum change that exceeds the momentum acceptance of the ring (see discussion above).

The HER must accommodate 1.48 A of circulating beam to reach a luminosity of 3×10^{33} cm^{-2} s^{-1}. This high beam current will give a large desorbed-gas load, and substantial pumping speed is needed to maintain a background gas pressure below 10 nTorr in the ring. The B Factory vacuum system is designed to produce a pressure of 5 nTorr under these conditions, so we base our lifetime estimates on this value (N_2 equivalent).

For the HER (see Fig. 4-81), the estimated lifetime from gas scattering—dominated by the bremsstrahlung process—is six hours at a pressure of 5 nTorr. This beam loss process is much more severe in its effects than the Touschek scattering process; therefore, we have placed great emphasis (see Section 5.2) on a vacuum system design capable of maintaining a good pressure in the presence of a large gas load from synchrotron-radiation desorption. It is worth noting here that our lifetime estimates are somewhat

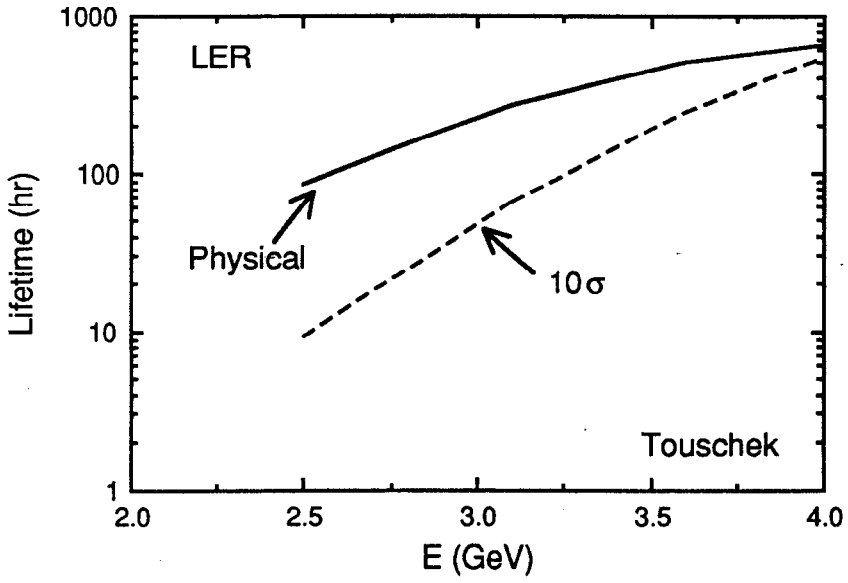

Fig. 4-80. Plot of Touschek lifetime as a function of beam energy in the B Factory LER. The solid line corresponds to taking the physical aperture of the vacuum chamber as the transverse limitation; the dashed line assumes a 10σ aperture restriction in the injection straight section.

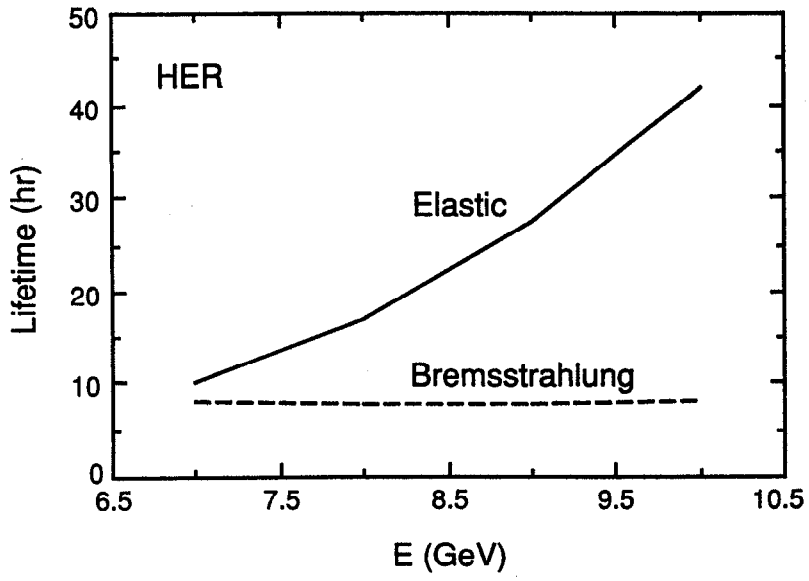

Fig. 4-81. Plot of gas-scattering lifetime as a function of beam energy for the HER. For the elastic scattering (solid line), an aperture restriction of 10σ was taken in each plane, with the vertical σ being calculated with the fully coupled vertical emittance. An average pressure of 5 nTorr (N_2 equivalent) was assumed.

pessimistic in that they are based on a fixed gas pressure. In reality the pressure will decrease as the beam current decreases, making the lifetimes longer than the values quoted here.

For the LER at a gas pressure of 6 nTorr (N_2 equivalent), the lifetime is roughly equally matched between elastic scattering and bremsstrahlung losses (see Fig. 4-82); the overall beam lifetime is 3.6 hr. Even for the LER, special care must be taken in the design of the vacuum chamber; this topic is discussed in Section 5.2.

Luminosity Lifetime. A potentially important contribution to beam lifetime is the loss of particles due to interactions between the individual particles in the two beams. In particular, we consider the loss of particles due to $e^+e^- \rightarrow e^+e^-$ and $e^+e^- \rightarrow e^+e^-\gamma$ interactions that scatter beam particles outside the accelerator acceptance.

If the e^+e^- cross section leading to loss of a particle from beam i is σ_i, then the loss rate depends on the luminosity according to

$$\frac{dN_i}{dt}(t) = -\sigma_i \mathcal{L}(t) \tag{4-14}$$

Each beam may consist of a number of bunches (not including gaps), n_{bi} with a number of particles per bunch, $N_{bi}(t)$. The subscript b is used to indicate that this is a quantity for a single bunch, and the subscript i refers to the beam (i = +,–). The total number of particles in a given beam is $N_i = n_{bi}N_{bi}$ We introduce the notation $N_{0,i} \equiv N_i(0)$, and we also use $\mathcal{L}_0 \equiv \mathcal{L}(0)$ to denote quantities evaluated at $t = 0$.

To determine the beam and luminosity lifetimes for the processes of interest, we need to know how the luminosity depends on the beam currents. This dependence is

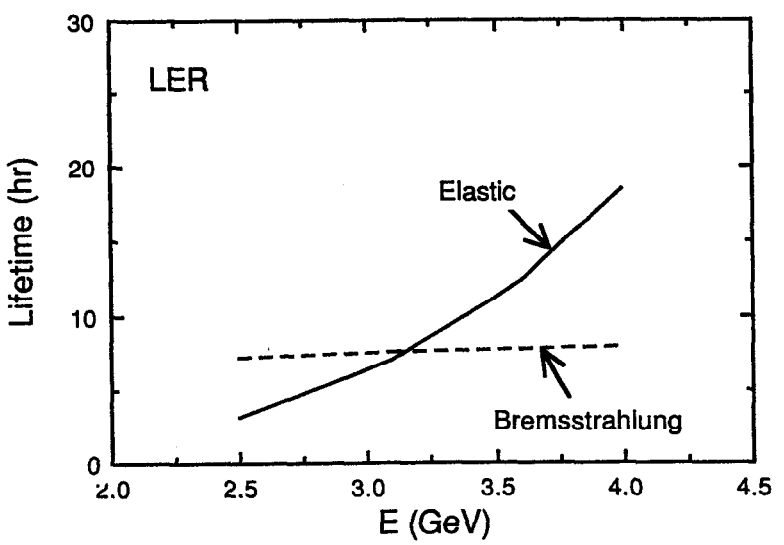

Fig. 4-82. Plot of gas-scattering lifetime as a function of beam energy for the LER. For the elastic scattering (solid line), an aperture restriction of 10σ was taken in each plane, with the vertical σ being calculated with the fully coupled vertical emittance. An average pressure of 6 nTorr (N_2 equivalent) was assumed.

determined to some extent by the operation of the storage ring. We adopt here a conservative model which assumes that the bunch sizes do not vary with time. Then the luminosity is given by

$$\mathcal{L}(t) = \frac{N_{b+}(t)N_{b-}(t)n_{bi}f_i}{2\pi\sqrt{\left(\sigma_{x,+}^{*2} + \sigma_{x,-}^{*2}\right)\left(\sigma_{y,+}^{*2} + \sigma_{y,-}^{*2}\right)}} \tag{4-15}$$

The $\sigma_{x,\pm}^*$ and $\sigma_{y,\pm}^*$ in this equation are the transverse rms spot sizes at the interaction point (IP). All time-dependent terms are explicitly indicated. It is assumed that the bunches are distributed such that all bunches meet opposing bunches at the IP (that is, bunches meet bunches and gaps meet gaps), hence $n_{b+}f_+ = n_{b-}f_-$ is the bunch collision frequency. Here, f_i is the revolution frequency for beam i. We also assume that any modifications to the above formula from considerations such as finite bunch lengths and nonzero crossing angles are time independent.

Equations 4-14 and 4-15 lead to two coupled differential equations in the beam currents:

$$\frac{dN_+}{dt} = -k\sigma_+ N_+ N_-$$

$$\frac{dN_-}{dt} = -k\sigma_- N_+ N_- \tag{4-16}$$

where

$$k \equiv \frac{\mathcal{L}_0}{N_{0,+}N_{0,-}} \tag{4-17}$$

The solution is

$$N_+(t) = N_{0,+}\frac{1-r}{e^{Gt} - r}$$

$$N_-(t) = N_{0,-}\frac{1-r}{1 - re^{-Gt}} \tag{4-18}$$

where

$$G \equiv \mathcal{L}_0\left(\frac{\sigma_+}{N_{0,+}} - \frac{\sigma_-}{N_{0,-}}\right) \tag{4-19}$$

and

$$r \equiv \frac{N_{0,+}\sigma_-}{N_{0,-}\sigma_+} \tag{4-20}$$

The $1/e$ beam lifetimes are given by

$$\tau_+ = \frac{1}{G}\ln\left[e + r(1-e)\right]$$

$$\tau_- = -\frac{1}{G}\ln\left[\frac{1}{r}(1-e+re)\right] \tag{4-21}$$

The time-dependence of the luminosity is

$$\mathcal{L} = \mathcal{L}_0 e^{Gt}\left(\frac{1-r}{e^{Gt}-r}\right)^2 \tag{4-22}$$

We define the luminosity lifetime τ to be the time it takes the luminosity to reach $1/e$ of its initial value:

$$\tau = \frac{1}{G}\ln\left\{\frac{e}{2}\left[(1-r)^2 + 2r/e + (1-r)\sqrt{(1-r)^2 + 4r/e}\right]\right\} \tag{4-23}$$

The more important mechanism of the two Bhabha processes considered here is loss due to bremsstrahlung ($e^+e^- \rightarrow e^+e^-\gamma$) of a photon, which can change the energy of a beam particle sufficiently to put it outside the energy acceptance of the accelerator. An excellent approximation for the cross section to lose a particle from beam i due to bremsstrahlung is [Altarelli and Buccella, 1964]

$$\sigma_{\text{brems } i} \approx \frac{16\alpha r_e^2}{3}\left[\left(\ln\frac{E_{\text{c.m.}}^2}{m_e^2} - \frac{1}{2}\right)\left(\ln\frac{E_i}{k_{\min i}} - \frac{5}{8}\right) + \frac{1}{2}\left(\ln\frac{E_i}{k_{\min i}}\right)^2 - \frac{3}{8} - \frac{\pi^2}{6}\right] \tag{4-24}$$

In this expression, $k_{\min i}$ is the minimum energy of a radiated photon that causes loss of a particle from beam i. Thus, $k_{\min i}/E_i$ can be taken as the fractional energy aperture of the machine for beam i. This cross section depends slowly on the energy aperture and on $E_{\text{c.m.}}$.

Table 4-16 shows the bremsstrahlung beam loss cross section calculated according to Eq. 4-24 for the Asymmetric B Factory. The fractional energy aperture is limited by the transverse aperture rather than by the RF voltage—we have used a value corresponding to ten times the rms energy spread of the beam.

The $1/e$ time for the low-energy beam is infinite; that is, the high-energy beam is completely destroyed before the low-energy beam drops by $1/e$ from its initial value. The asymptotic current in the low-energy beam is roughly 40% of its initial value. The instantaneous loss rate at $t = 0$ for the low-energy beam would correspond to a $1/e$ beam lifetime of 36 hours if the rate were constant.

We note that the large circumference of the B Factory rings (2200 m) helps to produce a comfortably large luminosity lifetime from this source. Even if future upgrades result in a higher luminosity, we do not have a problem. For example, suppose we anticipate a luminosity of 1×10^{34} cm^{-2}s^{-1}. As a "worst case," suppose further that

Table 4-16. Bremsstrahlung luminosity lifetime calculation.

Parameter	Symbol	High-energy ring	Low-energy ring
Fractional energy aperture	f_E	0.0061	0.0095
Min. energy in brems. integral [MeV]	$k_{\min}$	55.0	29.7
Brems. cross section for particle loss [cm^2]	$\sigma_{e^+e^-\gamma}$	3.0×10^{-25}	2.7×10^{-25}
Bremsstrahlung beam lifetime [hr]	$\tau_{\mathrm{Br}\,i}$	27.3	–
Bremsstrahlung luminosity lifetime [hr]	τ_{Br}	17.2	

this gain is achieved at the same beam currents as in our nominal design, either by reaching higher tune shifts or by focusing more strongly. In this case, the luminosity lifetime is inversely proportional to the luminosity, so 17.2 hours at 3×10^{33} cm^{-2} s^{-1} becomes 5.2 hours at 10^{34} cm^{-2} s^{-1}. This would still be acceptable, although it would then be comparable to the beam-gas luminosity decay rate.

Another loss mechanism, typically not as important as the bremsstrahlung considered above, is the loss due to Bhabha ($e^+e^- \rightarrow e^+e^-$) scattering at sufficiently large angles to escape the acceptance of the machine. To a good approximation for the small angles and high energies that we consider, the cross section to lose a particle from beam i is

$$\sigma_{\mathrm{Bhabha}\ i} \approx \frac{8\pi\alpha^2}{E_{\mathrm{c.m.}}^2}\,\frac{E_j}{E_i}\left(\frac{1}{\theta_{\min\,x;i}^2}+\frac{1}{\theta_{\min\,y;i}^2}\right) \tag{4-25}$$

where $\theta_{\min\,x,y;i}$ is the minimum horizontal or vertical scattering angle in the laboratory frame leading to particle loss, and $j = (-,+)$. Cross sections in units of GeV^{-2} may be converted to cm^2 by multiplying by 3.89×10^{-28} GeV^2 cm^2.

Table 4-17 summarizes the calculation for the present B Factory design. For the minimum angles, we have made our usual assumption that the limiting aperture is 10σ (using the uncoupled horizontal and the fully coupled vertical beam sizes). Because the Bhabha cross section to lose a beam particle is substantially smaller than the cross section in our earlier bremsstrahlung loss example, this is not a significant lifetime consideration.

We conclude that the luminosity lifetime from $e^+e^- \rightarrow e^+e^-$ and $e^+e^- \rightarrow e^+e^-\gamma$ will not be a significant limitation for the B Factory at a luminosity of $\mathcal{L} = 3 \times 10^{33}$ cm^{-2} s^{-1}. Even at a luminosity of 1×10^{34} cm^{-1} s^{-1}, the large circumference (and hence large number of particles per unit of beam current) of the B Factory rings ensures that these sources of beam loss will not seriously degrade the lifetime.

4.3.1.6 Higher-Order-Mode Losses. A complete specification of the thermal loading in the vacuum chamber must take into account the localized heating of beamline

Table 4-17. Bhabha luminosity lifetime calculation.

Parameter	Symbol	High-energy ring	Low-energy ring
Minimum angle in Bhabha integral [rad]	$\theta_{\min x}$	2.59×10^{-3}	5.17×10^{-3}
Minimum angle in Bhabha integral [rad]	$\theta_{\min y}$	9.14×10^{-3}	1.83×10^{-2}
Bhabha cross section for beam loss [cm^2]	$\sigma_{e^+e^-}$	2.60×10^{-28}	5.44×10^{-28}
Bhabha beam lifetime [hr]	$\tau_{\mathrm{Bh}\,i}$	90000	24000
Bhabha luminosity lifetime [hr]	τ_{Bh}	13373	

components due to the absorption of power generated by the beam in the form of HOM losses. We estimate the HOM power as

$$P_{\mathrm{HOM}} = 1.6 \times 10^{-10}\, N_b I k_\ell \ \text{[kW]} \tag{4-26}$$

where N_b is the number of particles per bunch, I (in A) is the total current, and k_ℓ (in V/pC) is the loss factor for the ring due to its broadband impedance. For the design parameters of the B Factory, the HOM power in the HER is given by [Heifets, 1990a]

$$P_{\mathrm{HOM}} = 10\, k_\ell \ \text{[kW]} \tag{4-27}$$

The equivalent value for the LER is

$$P_{\mathrm{HOM}} = 20\, k_\ell \ \text{[kW]} \tag{4-28}$$

To estimate the loss factor, we consider a broadband impedance of the form

$$\frac{Z(\omega)}{n} = \begin{cases} \dfrac{Z}{n} & \text{for } \omega \le \omega_c \\ \dfrac{Z}{n}\left(\dfrac{\omega_c}{\omega}\right)^{3/2} & \text{for } \omega > \omega_c \end{cases} \tag{4-29}$$

This form of broadband impedance has a frequency dependence similar to that of the commonly used $Q = 1$ resonator (see Eq. 4-6) at low frequencies, but it falls off more slowly above the cutoff frequency $\omega_c = c/b$, where b is the beam pipe radius. The loss factor is defined as

$$k_\ell = \frac{1}{\pi}\int_0^\infty Z(\omega)\, e^{-(\omega\sigma_\ell/c)^2} d\omega \tag{4-30}$$

For the impedance of Eq. 4-29, the loss factor is dominated by the contribution from the high-frequency tail and has been estimated by Heifets [1990a] to be

$$k_\ell = \frac{1}{6000}\left(\frac{Z}{n}\right)\left(\frac{R}{b}\right)\frac{R}{\sqrt{b\sigma_\ell}}\quad\left[\frac{\mathrm{R}}{\mathrm{pC}}\right] \tag{4-31}$$

where (Z/n) is the broadband impedance (in Ω), R is the mean ring radius (in meters), b is the chamber height (in meters), and σ_ℓ is the rms bunch length (in meters). For (Z/n) = 1 Ω, we find from Eq. 4-31 that k_ℓ is about 60 V/pC. If we evaluate the loss factor numerically, however, we find that Eq. 4-31 overestimates its value by about 50%. Thus, a better estimate is k_ℓ = 40 V/pC for a 1-Ω broadband impedance. It is worth mentioning here that the impedance in Eq. 4-29 results in a considerably higher loss factor than would be calculated using an equivalent Q = 1 resonator impedance, for which the loss factor is only k_ℓ = 16 V/pC for (Z/n) = 1 Ω.

The HOM heating resulting from our choice of broadband impedance is P_{HOM} = 400 kW for the HER and P_{HOM} = 800 kW for the LER. We expect this power to be generated mainly at the various tapers in the rings, as these have the highest loss factors [Heifets, 1990a]. In addition to these losses, there will be HOM power deposited in the RF cavities. Taking the equivalent broadband impedance of the RF system into account, we expect this additional loss in each ring to be about 130 kW.

Based on the work of Heifets, we can estimate the overall loss factor for the various components close to the IP as k_ℓ = 0.06 V/pC, which gives P_{HOM} = 1.8 kW for the high- and low-energy beams together. Of this, about 90 W is expected to be deposited in the beryllium beam pipe at the IP. The means to remove this power is described in Section 5.2.7.6.

4.3.1.7 Ion Clearing. The trapping of positively charged ions produced by collisions between electrons in the beam and background gas molecules has degraded the performance of many electron storage rings. The present theory of ion trapping is quite simple. When one of the electron beam bunches passes near an ion, the ion experiences a restoring force towards the beam axis. This force results in a change in the transverse velocity of the ion. Between bunch passages, the transverse velocity produces a change in the transverse position of the ion. This pattern is repeated for each passage of an electron bunch.

To estimate the ion motion, it is useful to consider the case in which the transverse charge density of the electron beam is uniform inside an ellipse with rms width and height σ_x and σ_y, respectively. Because the width of the beam is much greater than its height, ion trapping can be described by the motion of the ion in the vertical plane only; this is the motion we consider here.

The equation of motion for an ion in the electron bunch is given by

$$\ddot{y} + \hat{\omega}^2 y = 0 \tag{4-32}$$

where

$$\hat{\omega}^2/c^2 = \frac{4\hat{I}}{I_p A \sigma_y(\sigma_x + \sigma_y)} \tag{4-33}$$

with $\hat{I}$ the peak current in the bunch, c the speed of light, $I_p = m_p c^3/e = 3.1 \times 10^6$ A the Budker current of the proton, and A the ion mass number. The bunch cross section varies around the ring, but for purposes of estimation, we can take $\sigma_x = 1$ mm, $\sigma_y = 0.2$ mm, an ion mass of 20, and a peak current of 100 A. This yields $\omega = 5 \times 10^8$ rad/s. The bunch length τ and the interbunch spacing Δt are 30 ps and 4.2 ns respectively. Since both the quantities $\omega\tau$ and $\omega^2\tau\,\Delta t$ are much less than one radian, we can neglect the bunch structure of the beam, and the average ion motion can be obtained from Eq. 4-32 by replacing the peak current in Eq. 4-33 by the average current $\bar{I} = 1.48$ A. The ion effectively sees a continuous electron beam and oscillates with an average frequency of $\bar{\omega} = 6 \times 10^7$ rad/s. For a continuous bunched beam, the ions will be trapped in the electron beam unless measures are taken to remove them.

One method of removing trapped ions that has been used effectively is to turn on a fast kicker or "pinger" for a few turns and allow the ions to escape while the beam is moved away. However, the ionization rate is such that to reach a few percent neutralization again takes only of the order of milliseconds, so the beam would need to be kicked at a rate of nearly 1 kHz to keep it free of ions. If this method of ion clearing were used, the lifetime of the colliding beams and the detector backgrounds could be seriously affected.

Another method often used to clear the ions is to periodically excite the electron beam near the ion frequency. However, the ion frequency depends upon the amplitude of ion motion as well as upon the average current and transverse size of the electron beam, both of which vary around the ring and change during colliding beam running. This technique would potentially require a complicated control system to be useful during colliding beam conditions, and it might have a detrimental effect upon the beam lifetime and detector backgrounds. Moreover, the success of this method has been mixed.

A vertical DC electric field also may be used to clear the ions. The vertical clearing field E_c must be greater than the trapping field, that is,

$$E_c > \frac{Z_0 \bar{I}}{\pi(\sigma_x + \sigma_y)} \tag{4-34}$$

where $Z_0 = 377\ \Omega$ is the impedance of free space and $\bar{I}$ is the average beam current. For an average current of 1.48 A, this would require a clearing field in excess of 1.4 kV/cm. While this is a possible solution, it has the drawback of requiring additional electrodes in the vacuum chamber structure. These increase the impedance seen by the beam and therefore increase the difficulty of controlling beam instabilities. In addition, it will not be possible to have the transverse electric field everywhere around the circumference of the ring, so there could still be pockets of trapped ions.

The most desirable solution—and the one that we have chosen to use—is to leave a gap in the electron bunch train. This gap need only be a few percent of the total ring

circumference, so that only a small increase in the single-bunch current is necessary to achieve the same luminosity obtained for the continuous bunch train. An ion will be linearly unstable whenever the gap satisfies the following condition:

$$\Delta T > \frac{2}{\bar{\omega}} \cot\left[\frac{\bar{\omega}(T-\Delta T)}{2}\right] \tag{4-35}$$

where T is the revolution period and ΔT is the gap period. For $T = 7\ \mu s$, the total ion oscillation during the passage of the bunch train is given by $\bar{\omega}(T - \Delta T) \approx 400$ rad, and a gap of a few percent is sufficient to allow the ions to be cleared.

There is the worry that for a particular combination of current, beam cross section, and ion mass, the ion would perform nearly an exact number of half-integer oscillations during passage of the bunch train. This would result in a large value for the cotangent on the right-hand side of Eq. 4-35. Because the beam cross section varies around the ring, there may be locations where ions can be trapped. These locations would move as the current decays and the beam cross section changes. Similarly, the alternating magnetic fields in the wigglers could produce a "magnetic bottle" that can trap ions. We do not expect such localized pockets to contain sufficient ions to disturb the electron beam. This view is supported by the observation that many storage rings have demonstrated the ability to eliminate ion trapping problems by having a beam gap such as we envision. The more serious question, which we are now investigating with simulations, is how the amplitude dependence of the ion oscillation frequency affects the ion trapping, for example, whether an ion that is linearly unstable remains unstable at a large amplitude.

One of the disadvantages in this method of ion clearing is that the use of a gap in the bunch train will have an effect upon the control circuitry of the RF system. However, this is a problem that needs to be considered anyway, since the RF system must be designed to function with uneven bunch population during the filling process. The solution to this problem is discussed in Section 5.5.4.

4.3.2 Coupled-Bunch Instabilities

As mentioned earlier, wakefields in high-Q resonant structures in a storage ring cause different beam bunches to interact. In general, such high-Q resonances result from the HOMs of the RF cavities. For certain values of relative phase between bunches, the coupled-bunch motion can grow and become unstable, leading to beam loss. In addition to the relative phase between bunches, the instabilities are characterized by their motion in longitudinal (synchrotron) phase space. Longitudinally, the $a = 0$ mode (corresponding to no motion) cannot be unstable, so the lowest longitudinal instabilities are characterized by $a = 1$ (dipole) synchrotron motion. In the *transverse* case, the $a = 0$ motion can also become unstable (referred to as "rigid-dipole" motion).

In the case of the B Factory, we require a relatively large number of RF cells, both to generate the voltage needed to produce the short bunches and to replace the beam power lost to synchrotron radiation each turn. Combined with the required very high average beam currents, the substantial RF system can produce extremely rapid growth of coupled-bunch instabilities. In the cases studied here, the most severe growth comes from the

lowest modes, that is, $a = 1$ longitudinally and $a = 0$ transversely.

We have estimated the growth rates for both longitudinal and transverse instabilities for typical B Factory parameters, that is, 1746 bunches having a total current of 1.48 A (HER) or 2.14 A (LER). This bunch number, which ignores the gap for clearing ions, is necessary for calculations performed with ZAP in the frequency domain.

Two different cases, based on the cavity design described in Section 5.5, were studied:

Case A: Undamped cavities; 20 cells (HER) or 10 cells (LER)

Case B: As in A, but with HOMs damped to $Q = 70$; 20 cells (HER) or 10 cells (LER)

In Case A, we examined the behavior of a standard B Factory cavity with no HOM damping. This cavity has a high shunt impedance for the fundamental while having reasonable values for the HOMs. Case B represents what happens when the higher-order RF modes of the single-cell system are heavily de-Qed by external means, such as the waveguides described in Section 5.5.

Predictions of longitudinal growth times (for the fastest-growing mode) for both RF scenarios considered are summarized in Tables 4-18 and 4-19. The undamped cavity (Case A) gives $a = 1$ growth times below 0.1 ms. Substantial de-Qing (Case B) does help slow down the growth considerably, to times on the order of 5 ms. Note that the feedback system power required to counteract these instabilities will scale as the square of the growth rate, so the change associated with damping the cavity HOMs is very significant.

Although not shown in Tables 4-18 and 4-19, we have also observed that the fundamental mode of the RF system is capable of causing instability for selected coupled-bunch normal modes. This problem is handled via feedback on the cavity itself, as

Table 4-18. Longitudinal coupled-bunch growth times for the B Factory HER (9 GeV; $\tau_E = 18.4$ ms) at a beam current of 1.48 A.

(A) Undamped	
$\tau_{a=1}$	0.04 ms
$\tau_{a=2}$	1.3 ms
(B) Damped to $Q = 70$	
$\tau_{a=1}$	5.1 ms
$\tau_{a=2}$	242 ms

Table 4-19. Longitudinal coupled-bunch growth times for the B Factory LER (3.1 GeV; τ_E = 18.4 ms) at a beam current of 2.14 A.

(A) Undamped	
$\tau_{a=1}$	0.03 ms
$\tau_{a=2}$	1 ms
(B) Damped to $Q = 70$	
$\tau_{a=1}$	3.8 ms
$\tau_{a=2}$	180 ms

described in Sections 5.5 and 5.6. Transverse results, summarized in Tables 4-20 and 4-21, are similar to those for the longitudinal case. Here too, we find for Case A that the two lowest synchrotron modes, $a = 0$ and $a = 1$, have growth times much shorter than the radiation damping time. We again note the benefits of substantial de-Qing (Case B) in slowing down the growth rates to more manageable levels.

Although the feedback system design (Section 5.6) is based on detailed simulations of the multibunch growth rates, the simple estimates made here already justify the effort that has gone into designing an effective HOM damping system for the RF cavities (described in Section 5.5).

4.3.3 Summary of Findings

Total beam current limitations in both rings will depend upon the ability of the vacuum system to maintain an acceptable pressure, about 5 nTorr, in the presence of about 2 A of circulating beam. Neither bunch lengthening and widening due to the longitudinal microwave instability (which places a limit on the allowable broadband impedance), nor

Table 4-20. Transverse coupled-bunch growth times for the B Factory HER (9 GeV; τ_x = 37.2 ms) at a beam current of 1.48 A.

(A) Undamped	
$\tau_{a=0}$	0.2 ms
$\tau_{a=1}$	8.4 ms
(B) Damped to $Q = 70$	
$\tau_{a=0}$	1.1 ms
$\tau_{a=1}$	302 ms

Table 4-21. Transverse coupled-bunch growth times for the B Factory LER (3.1 GeV; $\tau_x = 36.4$ ms) at a beam current of 2.14 A.

(A) Undamped		
	$\tau_{a=0}$	0.1 ms
	$\tau_{a=1}$	4.8 ms
(B) Damped to $Q = 70$		
	$\tau_{a=0}$	0.65 ms
	$\tau_{a=1}$	184 ms

current limitations arising from the transverse mode-coupling instability are predicted to be constraints in the multibunch scenario considered here.

We have seen here that the performance of both high- and low-energy rings is likely to be limited mainly by coupled-bunch instabilities. Our choice of specially designed single-cell RF cavities helps to reduce the longitudinal HOM impedance by permitting the voltage to be produced with relatively few cells and by permitting the cavity HOMs to be effectively damped. Feedback systems able to deal with the remaining growth have been designed; they are described in Section 5.6.